

The Manufacture and Characterisation of Microscale Magnetic  
Components

David Flynn

A dissertation submitted for the degree of Doctor of Philosophy

Heriot-Watt University

School of Engineering and Physical Sciences

March 2007

This copy of the thesis has been supplied on condition that anyone who consults it is understood to recognise that the copyright rests with its author and that no quotation from the thesis and no information derived from it may be published without the prior written consent of the author or of the University (as may be appropriate).

## Abstract

This thesis presents the work undertaken by the author within the Microsystems Engineering Centre in the School of Engineering and Physical Sciences at Heriot-Watt University, Edinburgh.

This research has focused on the manufacture and characterisation of microscale magnetic components, namely microinductors and transformers for DC-DC converter applications. The development of these components has involved an investigation into manufacturing processes for microscale magnetic components, a study into suitable magnetic materials and methods of tailoring their electric and magnetic properties, the development of models within ANSYS to aid the understanding of current and flux density distribution within components, experimental characterisation of fabricated devices and the development of an optimal design process.

Micromachined inductors and transformers with solenoid and pot-core geometries utilizing a variety of magnetic cores have been fabricated on glass using micromachined techniques borrowed from the LIGA process.

Components were characterised over the 1-10MHz frequency range with a low frequency impedance analyser. The performance of prototype components was then improved via an optimal design process. Analytical, experimental and simulated data was used to develop some of the most state-of-the-art components to date with efficiencies in excess of 90% and high power densities greater than 100 W/cc. Results have indicated that electrodeposited alloys out performed the commercial alloy for high frequency operation. With the cost effective production of thin film laminate core layers and magnetic material development fundamental to the success of future magnetic components.

## Dedication

*To my family*

*Your love and support gives me strength to endeavour against all that life tests me with  
and inspiration so that I may push myself to be all that I can be.*

*In Loving Memory of*

*Steven Flynn and Mark Flynn*

## Acknowledgements

I would like to express my gratitude for the support, encouragement and guidance provided by my academic supervisor Professor Marc Desmulliez. I would also like to thank Dr Resham Dhariwal for his advice and guidance and for being the second reader of this thesis. Thanks also to Professor Philip Prewett for serving as the external examiner of this thesis.

I would like to acknowledge the financial and technical support of Raytheon Systems Limited. In particular the time and effort dedicated to the project by Mr Anthony Toon and Mr Les Allen.

I would also like to acknowledge the financial support of both the Engineering and Physical Sciences Research Council (EPSRC) the Scottish Manufacturing Institute (SMI). I would also like to thank the Institution of Engineering and Technology (IET) for their support in the form of the Robinson Scholarship and Leslie H Paddle Scholarship.

Finally, I would also like to extend my thanks to my colleagues and friends within the Microsystems Engineering Centre and School of Engineering and Physical Sciences for their support, advice and assistance in the course of my research.



# Table of Contents

Page

## Chapter 1

Motivation Behind the miniaturisation of microscale components and thesis outline	1
1.1 Introduction, main objectives and aim	1
1.2 Motivation of microscale magnetic component	2
1.2.1 Market trends of passive power components	4
1.2.2 Technology drivers of passive power components	5
1.3 The challenges of miniaturising magnetic components	8
1.4 Thesis layout	8

References

## Chapter 2

Basics of power components Fundamental design equations and material properties	13
2.1 Introduction	13
2.2 Fundamental design equation	13
2.3 Introduction to magnetic material	19
2.3.1 Magnetisation and magnetic materials	20
2.3.2 Eddy current phenomena within thin films	25
2.3.3 Origins of anisotropy	26
2.4 Magnetic materials for DC-DC converters operating in the MHz frequency range	30
2.5 Summary	32

References

## Chapter 3

Literature review of power magnetic components	37
3.1 Introduction	37
3.2 Basics of passive power inductive components	37
3.2.1 Inductors	37
3.2.2. Transformers	42
3.3 Introduction to switch mode power supplies	46
3.3.1 DC-DC converter configurations	48

3.3.1.1 Buck converter	50
3.3.1.2 Boost converter	50
3.3.1.3 Buck-Boost converter	51
3.3.1.4 Flyback converter	52
3.3.2 Frequency effect on passive components	53
3.4 Fabrication of power inductive components	55
3.4.1 Review of conventional fabrication	55
3.4.1.1 Review of conventional core materials	60
3.4.2 Review of micromachined fabrication approach	63
3.5 Summary of deposition techniques	67
3.6 Review of state of the art power magnetic components	68
References	
<b>Chapter 4</b>	
Electrodeposition of Nickel-Iron	76
4.1 Introduction to Electrodeposition	76
4.1.1 Basics of Electrodeposition	76
4.2 Electrolyte Systems for Nickel-Iron deposition	79
4.2.1 Sulphate and chloride electrolytes	79
4.2.2 Sulfamate electrolytes	81
4.2.3 Periodic deposition of Nickel-Iron Alloys	82
4.3 Anomalous Deposition	83
4.4 Magnetic field annealing during electrodeposition	86
4.5 Experimental results for DC Nickel-Iron electrodeposition	88
4.5.1 DC Plating Cell	88
4.5.2 Experimental analysis of DC Ni-Fe	90
4.5.2.1 White light interferometer analysis	91
4.5.2.2 SEM-EDX Analysis	93
4.5.2.3 AFM and XDA Analysis	95
4.5.2.4 Electrical and magnetic characterisation	99
4.5.2.5 Magnetic field Annealing	105
4.6 Summary	109
References	
<b>Chapter 5</b>	
Design of Experiments for electrodeposition of nickel-iron	113
5.1 Introduction	113

5.2 Rationale for using DOE for nickel-iron electrodeposition	113
5.3 Experimental Set-up & Waveforms Generated by the DOE	115
5.4 Structural properties of DOE samples	119
5.5 Electrical Properties of DOE samples	127
5.6 Magnetic Properties of DOE Samples	129
5.7 Summary	133
References	
<b>Chapter 6</b>	
Design of Microscale Magnetic Components	136
6.1 Introduction	136
6.2 Microfabricated Component Design	136
6.2.1 Basic geometry	140
6.3 Winding design	143
6.3.1 Skin and proximity effect	148
6.4 Core loss in micro-inductors and transformers	151
6.5 Component design: the solenoid approach	155
6.5.1 Solenoid anisotropic core	159
6.5.2 Solenoid air-gap	160
6.6 Thermal dissipation & electromigration	162
6.7 Pot core micro-inductors and transformers	162
6.8 Review of circuit parameters on component design	164
6.8 Influence of magnetic component on circuit operation	168
6.9 Summary	170
References	
<b>Chapter 7</b>	
Microfabrication of Power Inductors and transformers	173
7.1 Introduction	173
7.2 Mask Design	173
7.2.1 Transferring acetate mask to titanium on glass	175
7.3 Micro-fabrication & assembly of solenoid microinductor	176
7.3.1 Preparation of the substrate	176
7.3.2 Deposition of sacrificial layer	177
7.3.3 Deposition of a titanium seed layer	179
7.3.4 Photoresist deposition and UV photolithography	182
7.3.5 Electrodeposition of copper and nickel	186

7.3.6 Electrodeposition of gold	188
7.3.7 AZ stripping and seed layer etching	190
7.3.8 Flip-chip assembly of the micro-inductor	195
7.4 Fabrication of other microscale magnetic components	200
7.5 Other magnetic alloys investigated	204
7.6 Summary	205
References	
<b>Chapter 8</b>	
Characterisation of Micro-Inductors and Transformers	207
8.1 Introduction	207
8.2 Low frequency impedance measurement	207
8.3 Measurement results of the microinductors	208
8.3.1 Solenoid micro-inductor: winding & dielectric assessment	208
8.3.1.1 Solenoid microinductor: resistance test	210
8.3.1.2 Solenoid micro-inductor: inductance & Q-factor test	214
8.3.1.3 Solenoid microinductor: anisotropic test	218
8.3.1.4 Solenoid micro-inductor: air-gap & core area tests	220
8.3.1.5 Solenoid micro-inductor: DC bias test	222
8.3.1.6 Solenoid micro-inductor: efficiency & power density	224
8.4 Pot-core micro-inductor	229
8.5 Pot-core micro-transformer	232
8.6 Summary	239
References	
<b>Chapter 9</b>	
Modeling-based component optimization	242
9.1 Introduction	242
9.2 Modeling of the solenoid micro-inductor	242
9.3 Computer modeling of a one-turn pot-core micro-inductor	248
9.4 Optimization & Characterization of the Solenoid Micro-Inductor	258
9.5 Conclusions	262
References	
<b>Chapter 10</b>	
Conclusions and future work	265
10.1 Conclusion	265
10.2 Future Work	271



## List of Tables

Table 2.1 The fundamental equations governing inductor and transformer operation: Faraday's Law, Ampere's Law and Lenz's Law	18
Table 2.2: Relationship between magnetic parameters in cgs and S.I. units	19
Table 2.3 Core losses for various commercial ferrite materials	31
Table 2.4 Properties of Permalloy and a Typical High Performance MnZn Power Ferrite	32
Table 3.1 Advantages of planar magnetic components	58
Table 3.2 A comparison of deposition methods for micromachined power magnetic components	68
Table 4.1 Electrolyte composition of Nickel-Iron	89
Table 4.2 Magnetic and Electrical Properties of DC $Ni_{80}Fe_{20}$	104
Table 4.3 Anisotropic and Isotropic $Ni_{80}Fe_{20}$ film properties	108
Table 5.1 Pulse Reverse waveform parameters and associated equations	116
Table 5.2 DOE PR waveform parameters	118
Table 5.3 SEM-EDX analysis results for PR waveform deposits fabricated from the DOE	119
Table 5.4 Comparison of DC and PR $Ni_{80}Fe_{20}$ properties	134
Table 6.1 Physical parameters of the solenoid micro-inductor	157
Table 6.2 Summary of analytical equations used to define the performance of the micro-inductor	159
Table 6.3 Details of the pot core microscale magnetic components	163
Table 6.4 Buck specifications	164
Table 6.5 Permalloy characteristics	166
Table 6.6 Buck (CCM) converter	167
Table 6.7 Buck (ZVS) converter	167
Table 7.1 Spin cycle parameters for various AZ9260 thicknesses	183
Table 7.2 Baking procedures for various AZ thicknesses	183
Table 7.3 Nickel plating solution composition	186

Table 7.4 Copper plating solution composition	187
Table 7.5 Operation condition for gold plating	190
Table 7.6 Composition of Ti etchant	191
Table 7.7 Pot-core components and dimensions	203
Table 7.8 Properties of electrodeposited and commercial alloys incorporated into the solenoid micro-inductor	204
Table 7.9 Electroplating solution and conditions of CoFeCu	205
Table 8.1 Measured and analytical saturation current values for the alloys investigated	224
Table 8.2 Power density and efficiency of electrodeposited and commercial alloys at 250 kHz	226
Table 8.3 Power density and efficiency of electrodeposited and commercial alloys at 500 kHz	226
Table 8.4 Performance values of the race-track and spiral micro-inductor performance at 50 kHz	232
Table 8.5 Power Density and efficiency of the micro-transformer at 50 kHz	239
Table 9.1 Micro-Inductor model dimensions	243
Table 9.2 Inductor model dimensions	250
Table 9.3 Material properties used in the modelling	250
Table 9.4 Performance of optimized and prototype components with CoFeCu cores operating at 500 kHz	259
Table 9.5 Performance of laminated core inductors	262

## List of Figures

Figure 1.1(a) Evolution of the size of telecommunication power modules	3
Figure 1.1(b) The increase in frequency has reduced the size of the bulky passive components	3
Figure 1.2 “A 5-Year Power technology Roadmap”, PMSA	5
Figure 1.3 Estimation of the output power, voltage and current for a single buck converter supply in handheld electronic products	7
Figure 1.4 Synopsis of the thesis	11
Figure 2.1 (a) Uniform magnetic field of magnitude H, (b) Electrical analogy	13
Figure 2.2(a) Uniform flux density of magnitude B, (b) Electrical analogy	15
Figure 2.3 Faraday’s Law: a magnetic field changing in time creates a proportional emf	15
Figure 2.4 Lenz’s Law: Induced flux opposing changing flux	16
Figure 2.5 Ampere’s Law: For any closed loop path, the sum of the length, $l_m$ , Times the magnetic field, H, in the direction of the length element is equal to the permeability times the electric current enclosed in the loop	17
Figure 2.6 Review of basic magnetic relationships	19
Figure 2.7 Schematic illustration of the break up of magnetisation into domains (a) single domain, (a) single domain, (b) two domains, (c) four domains and (d) closure domains	21
Figure 2.8 The hysteresis loop of a ferromagnetic material	22
Figure 2.9 Determination of relative permeability from the hysteresis response of a magnetic medium	24
Figure 2.10 Plot of the saturation magnetostriction vs. NiFe composition	28
Figure 3.1 Frequency response of the impedance of an ideal inductor and a practical inductor	39
Figure 3.2 General equivalent circuit of an inductor	40
Figure 3.3 Q-factor response of a practical inductor with frequency	40
Figure 3.4 Schematic Diagram of a Transformer	42
Figure 3.5 Model of an ideal transformer	44
Figure 3.6 Model of a practical transformer	45
Figure 3.7 Equivalent circuit of a high frequency transformer	45



Figure 3.8 Inductor response to constant current	48
Figure 3.9 Inductor response to increasing current	49
Figure 3.10 Inductor response to decreasing current	49
Figure 3.11 The duty cycle is defined as the ratio between the pulse duration and the period (T) of a rectangular waveform	49
Figure 3.12 Circuit diagram of a buck converter	50
Figure 3.13 Circuit diagram of a boost converter	51
Figure 3.14 Circuit Diagram of the buck-boost converter	51
Figure 3.15 Flyback converter (a) The inductor of the buck-boost converter is replaced with a transformer, (b) the isolated output is clarified by removal of the common reference of the input and output circuits	53
Figure 3.16 Construction of an inductor using two ER cores, a plastic bobbin and two clips	56
Figure 3.17 Examples of core geometries commonly utilised in wound magnetic components	57
Figure 3.18 Planar magnetic component	58
Figure 3.19 Representation of the area indicative of energy storage within a magnetic material	61
Figure 3.20 A schematic of a planar meander wound inductor enclosed by two NiZn ferrite thin plates	64
Figure 3.21 A two layer vertically stacked spiral type micro-inductor with ferrite composite core: (Dimensions 2mm x 2mm x 50mm)	65
Figure 3.22 Cross section through a fabricated micro-transformer showing turns of copper conductors sandwiched between a two-layer, laminated magnetic core of Nickel-Iron	66
Figure 3.23 Fabricated micromachined inductor with DC electroplated nickel-iron core	67
Figure 3.24 Previous power magnetic components: power density vs. device volume	69
Figure 4.1 Schematic representation of a simple electrodeposition bath	77
Figure 4.2 Illustration of (a) Direct Current, (b) Pulse and (c) Pulse Reverse waveforms used in electrodeposition	78
Figure 4.3 Solution composition vs. deposit composition	85
Figure 4.4 Current Density vs. Deposit composition	85

Figure 4.5 Current Density vs. Current Efficiency	86
Figure 4.6 Behaviour of magnetisation with field applied in the easy-axis direction	87
Figure 4.7 Behaviour of magnetisation with field applied in the hard-axis direction	87
Figure 4.8 Ni-Fe electroplating cell (a) Electroplating cell positioned on top of a hot-plate and stirrer with a DC power supply, (b) Image of the cathode wafer holder, background, and sacrificial nickel anode, foreground	89
Figure 4.9 Deposition rate of Ni at varying values of current density. The deposition rate of Ni is used as a guide to the deposition rate of Ni-Fe	91
Figure 4.10 Zygo NewView images of DC electroplated $Ni_{80}Fe_{20}$	92
Figure 4.11 Illustration of the current crowding phenomena that occurs due to non-uniform distribution of current density	92
Figure 4.12 SEM images of $Ni_{80}Fe_{20}$ samples from the same wafer as Fig 4.10	93
Figure 4.13 EDX spectrum of the $Ni_{80}Fe_{20}$	94
Figure 4.14 Anomalous co-deposition effect of DC electroplated Ni-Fe	95
Figure 4.15 (a) AFM data of a Ni-Fe sample fabricated at $13\text{mA}/\text{cm}^2$ , and (b) a 3D plot of the surface profile of a $10\mu\text{m} \times 10\mu\text{m}$ area of the same sample	97
Figure 4.16 Grain Size vs. Fe content of the Ni-Fe samples	98
Figure 4.17 XRD analysis of Ni-Fe samples ranging in composition from (1) 65:35, (2) 80:20, and (3) 90:10	99
Figure 4.18 Resistivity measurements	100
Figure 4.19 Schematic of the VSM	101
Figure 4.20 (a) A schematic of three coils configured as a second-order gradiometer is used as superconducting detection coils in SQUID magnetometer. (b) Edinburgh Universities SQUID with the sample holder and detection coil chamber encircled	103
Figure 4.21 Hysteresis response of DC electroplated $Ni_{80}Fe_{20}$ recorded from the VSM	104
Figure 4.22 Saturation Flux Density (T) vs. Fe content of the Ni-Fe samples	105
Figure 4.23 Coercivity vs. Fe content of the Ni-Fe samples	105
Figure 4.24 Schematic of the Core geometry with magnetic easy and hard axis indicated	107

Figure 4.25 Anisotropic Ni-Fe after magnetic field annealing in DC field of 300 A/m	108
Figure 5.1 The Pulse Rectifier is connected to an oscilloscope displaying a pulse reverse waveform (PR)	115
Figure 5.2 Pulse Reverse Waveform with the 5 factors highlighted; (a) cathodic current intensity amplitude, (b) cathodic pulse duration on time, (c) anodic current intensity amplitude, (d) anodic pulse duration on time, and (e) represents the off-time of the pulse	116
Figure 5.3 Fe content in percentage as a function of average current density	120
Figure 5.4 Fe Content as a function of cathodic pulse density and anodic pulse densities expressed in mA/cm <sup>2</sup>	121
Figure 5.5 Pit count as a function of the off-time and average current density expressed in mA/cm <sup>2</sup>	122
Figure 5.6 Zygo image of the deposit generated by waveform Doe13	123
Figure 5.7 Zygo image of current crowding effects on deposit profile	123
Figure 5.8 Profile of deposit surface generated by PR waveform Doe 2	124
Figure 5.9 (a) AFM data of a Ni-Fe sample fabricated at 50mA/cm <sup>2</sup> , & (b) a 3D plot of the surface profile	125
Figure 5.10 DC and PR grain size vs. Fe content	126
Figure 5.11 Grain size (nm) as a function of Fe content and cathodic pulse Density	126
Figure 5.12 Resistivity of PR DOE and DC deposits vs. Fe content	127
Figure 5.13 Intercrystalline Volume Fraction as a function of Grain size	128
Figure 5.14 Excess resistivity vs intercrystalline volume fraction	129
Figure 5.15 Saturation flux density of DC and PR deposits vs. Fe content	130
Figure 5.16 Coercivity of DC and PR deposits vs Fe content	130
Figure 5.17 Coercivity, H <sub>c</sub> , vs. grain size, D, for various soft magnetic alloys	131
Figure 5.18 Relative permeability vs. Fe content	133
Figure 6.1 Solenoid inductor with a magnetic core	137
Figure 6.2 Simple rectangular one-turn micro-inductor	139
Figure 6.3 (a) Top view displaying the exposed copper contacts & (b) Side view showing the enclosed magnetic path	140

Figure 6.4 Simplified pot-core component	141
Figure 6.5 Pot-core with magnetic core enclosing the windings	143
Figure 6.6 Layout of a spiral winding	144
Figure 6.7 The parameters for the calculation of mutual inductance between two sections of windings	145
Figure 6.8 Solenoid winding	147
Figure 6.9 Meander windings	147
Figure 6.10 Optimum width of windings	150
Figure 6.11 Hysteresis loop of a magnetically soft material	152
Fig 6.12 An illustration for a core model	154
Figure 6.13(a) Illustration of the solenoid micro-inductor of size 2mmx5mmx250 $\mu$ m (WxLxT). 33 windings wrap around the core, (b) The closed magnetic core dimensions	156
Figure 6.14 flowchart of analytical equations used to determine component efficiency and power density	158
Figure 6.15 The inclusion of an air-gap in the flux path of the core	161
Figure 6.16 Buck (CCM) converter	164
Figure 6.17 Buck (ZVS) converter	165
Figure 6.18 Efficiency drop in converter performance as a result of DC winding resistance, R <sub>dc</sub> .	169
Figure 7.1 Acetate mask for the fabrication of the core of the solenoid micro-inductor	174
Figure 7.2 Fabrication process of transferring acetate mask on to Ti/glass mask	175
Figure 7.3 A wafer holder containing 5 3-inch glass wafers is placed within a beaker of Decon 90 cleaning solution diluted with deionised water	177
Figure 7.4 Isotropic thermal cracking of a wafer with 10 $\mu$ m thick AZ 9260 layer after the deposition of Ti within the E-beam	178
Figure 7.5 Isotropic thermal cracking of a wafer consisting of a sacrificial AZ layer, Ti seed layer and patterned photoresist layer	179
Figure 7.6(a) E-Beam Evaporation with control unit and power supply, (b) Schematic of E-beam evaporation chamber	180
Figure 7.7 Overview of AZ 9260 deposition and UV photolithography	182
Figure 7.8 Tamarack UV aligner	185
Figure 7.9 AZ9260 patterned with UV photolithography	186

Figure 7.10(a) The patterned AZ 9260 prior to electroplating, and (b) after DC electrodeposition of 90 $\mu$ m thick Ni	187
Figure 7.11(a) 3D plot of AZ 9260 patterned to form electroplating cavities for electrodeposition of Cu: Au interconnection bumps, and (b) intensity image of the winding layer	188
Figure 7.12 Potassium sulphite based gold plating bath set-up	189
Figure 7.13(a) A 3D plot of the lower winding layer, (b) The lower winding layer with 90 $\mu$ m Cu windings, Cu: Au bumps 25 $\mu$ m and 5 $\mu$ m respectively, etched Ti/Ni layer, and 10 $\mu$ m AZ insulation layer	191
Figure 7.14 The upper winding layer with 90 $\mu$ m Cu windings, Cu: Au bumps 25 $\mu$ m and 5 $\mu$ m respectively, etched Ti/Ni layer, and 10 $\mu$ m AZ insulation layer	192
Figure 7.15(a) Glass wafer with 120 functional lower winding layers. The winding layers are now chips that can be flip-chip bonded together with alternative core samples, and (b) a released chip positioned on a 5 pence coin	193
Figure 7.16 Summarised fabrication process of the electrodeposited core samples	194
Figure 7.17 Flip-chip bonding machine Karl SUSS FC6	196
Figure 7.18 Cross-section of the thermo-compression flip-chip bonding process	197
Figure 7.19 Pre-set bonding profile for temperature and force as a function of time	198
Figure 7.20 Flip-chip bonded solenoid microinductor	199
Figure 7.21 Released solenoid micro-inductor of size 2mmx5mmx 250 $\mu$ m (WxLxT)	200
Figure 7.22 Solenoid micro-inductor showing the interconnection between the upper and lower winding layers	200
Figure 7.23 Fabrication process of the pot-core planar windings	201
Figure 7.24 Assembly process of the pot-core spiral inductor	202
Figure 7.25 Pot-Core 3T “race-track” micro-inductor	203
Figure 8.1 Winding Resistance versus Frequency	209
Figure 8.2 Winding resistance versus frequency	210
Figure 8.3 Micro-inductor resistances as a function of frequency	211

Figure 8.4 Comparison of core and winding resistances as a function of frequency	212
Figure 8.5 Winding resistance and core eddy current resistance as a function of frequency	213
Figure 8.6 Analytical winding resistance as a function of frequency and number of winding layers	214
Figure 8.7 Analytical and commercial values of the inductance of the commercial alloy Vitrovac	215
Figure 8.8 Electrodeposited alloys inductance vs. Frequency. NiFe* indicates the anisotropic Ni-Fe	216
Figure 8.9 Effective relative permeability of the NiFe alloy as a function of Frequency	217
Figure 8.10 Impedance vs. frequency for the solenoid microinductor with NiFe core	218
Figure 8.11 Q-Factor vs. frequency for commercial and electrodeposit alloys	218
Figure 8.12 Inductance vs. frequency for magnetically anisotropic Ni-Fe with HARD and EASY axes	219
Figure 8.13 Q-factor vs. frequency for magnetically anisotropic Ni-Fe with HARD and EASY axis	219
Figure 8.14 Inductance vs. frequency for Vitrovac and NiFe with a 50 $\mu$ m air-gap	220
Figure 8.15 Inductance vs. frequency for a single Vitrovac layer and a three-layer laminated core	221
Figure 8.16 Inductance vs. Frequency for a single Ni-Fe layer and a three layer laminated core	222
Figure 8.17 Inductance as a function of DC bias for NiFe with a 50 $\mu$ m air-gap	223
Figure 8.18 Inductance as a function of DC bias for NiFe with a closed magnetic path	223
Figure 8.19 Contribution of power loss mechanisms at 250 kHz	228
Figure 8.20 Contribution of power loss mechanisms at 500 kHz	228
Figure 8.21 Inductance value of the race-track micro-inductor vs. frequency	229
Figure 8.22 Q-factor value of the race-track micro-inductor vs. frequency	230
Figure 8.23 Value of the inductance for the spiral micro-inductor vs. frequency	230

Figure 8.24 Values of the Q-factor of a spiral micro-inductor vs. frequency	231
Figure 8.25 Inductance vs. frequency of primary windings. An open circuit winding test generated the measured results	233
Figure 8.26 Core resistance vs. frequency. An open circuit winding test generated the measured results	234
Figure 8.27 Inductance vs. frequency of secondary windings. An open circuit winding test generated the measured results	234
Figure 8.28 Winding resistance vs. frequency	235
Figure 8.29 Primary and secondary winding leakage inductance vs. frequency	237
Figure 8.30 Mutual inductance vs. frequency	238
Figure 9.1 Computer model of the solenoid micro-inductor	243
Figure 9.2 H field distribution in the solenoid inductor at $f=1\text{MHz}$	244
Figure 9.3 Current density in the inductor	245
Figure 9.4 The analytical, measured and simulated values of the inductance for the solenoid inductor with $10\mu\text{m}$ Ni-Fe core material	246
Figure 9.5 The analytical, simulated and experimental values of the inductance for the solenoid inductor with $20\mu\text{m}$ 6025v core material	246
Figure 9.6 Analytical, simulated and experimental values of the Q-factor for the inductor with a Vitrovac core	247
Figure 9.7 The inductance of a single layer Ni-Fe core and a 5-layer Ni-Fe core	248
Figure 9.8 Schematic of a simple one-turn inductor	249
Figure 9.9 Schematic cross-section of the inductor model	249
Figure 9.10 Inductance vs. Frequency for the model of a 1-turn pot-core $\text{Ni}_{80}\text{Fe}_{20}$ micro-inductor	251
Figure 9.11 Flux line distribution in the core (a) $f=1\text{Hz}$ and (b) $f=10\text{MHz}$	251
Figure 9.12 (a): The inductor model. (b): The current density distribution in the inductor. (c): Current density in part of the core	252
Figure 9.13 Total Joule loss as function of the frequency	253
Figure 9.14 Q-factor vs. Frequency	253
Figure 9.15 FEA Model with air gaps	254
Figure 9.16 Flux lines in and around the inductor with, (a) no gap in the core, (b) single $50\mu\text{m}$ gap, and (c) ten $5\mu\text{m}$ gaps	254

Figure 9.17 Inductance of inductors with gaps	255
Figure 9.18 (a) Losses in the conductor. (b) Losses in the magnetic core	255
Figure 9.19 Q-factor values of inductors with and without magnetic gaps as a function of frequency	256
Figure 9.20 The inductance value is a function of the gap spacing of the ten-gap model	257
Figure 9.21 The gap-distance dependent Q values of of an inductor with ten-gaps	258
Figure 9.22 Fabrication and assembly process of the laminated core	260
Figure 9.23 Footprint of a laminate layer	261
Figure 9.24 Inductance vs. Frequency for laminated hand wound inductors	261
Figure 10.1 Comparison of performance of prototype laminated inductors with prior work (components 1&2 have been circled)	269



## List of Authors Publications

### Journal publications:

1. D. Flynn, R.S. Dhariwal, M.P.Y. Desmulliez, "Study of a solenoid microinductor operating in the MHz frequency range," *IoP Journal of Microengineering and Micromechanics*, vol 16, pp. 1811-1818, 2006.
2. D. Flynn, A. Toon, M.P.Y. Desmulliez, "A comparison of various magnetic thin films for the application of microscale magnetic properties," *IEEE Proc. of Integrated MEMS 2006*, Biopolis, Singapore, May 2006.
3. D. Flynn, T. Toon, M.P.Y. Desmulliez, "Manufacture, characterisation and test of a DC-DC power converter," *Journal of Microsystems Technology*, MST ref. n. 675, Publisher Springer Verlag, 2006.
4. D. Flynn, A. Toon, M.P.Y. Desmulliez, "Manufacture and characterisation of micro-engineered DC-DC power converter using UV-LIGA process," *IEE Electronics Letters*, vol. 41, no. 24, pp. 1351-1353, 2005.
5. D. Flynn, R.S. Dhariwal, M.P.Y. Desmulliez, "Microscale magnetic components for the application of DC-DC converters," *IoP Conference Series Journal of Microengineering*, vol. 34, pp.112-117, 2006.
6. D. Flynn, A. Toon, L. Allen, R. Dhariwal, M.P.Y. Desmulliez, "Characterisation of core materials for microscale magnetic components operating in the MHz range," *IEEE Journal Trans. On Magnetism*, 2007.

### Conference publications:

1. D. Flynn, A. Toon, M.P.Y. Desmulliez, "Microscale magnetic components for the application of DC-DC converters operating in the 1-10 MHz range," *IEEE Proc. of Electronic Materials and Packaging (EMAP) Conference*, Tokyo, Japan, pp. 192-198, 2005
2. D. Flynn, A. Toon, M.P.Y. Desmulliez, "Fabrication process of a micro-inductor utilising a magnetic thin film core," pp. 38-43, ISBN 2-84813-0357-1, *IEEE Proc. of DTIP of MEMS and MOEMS*, 01-03 June 2005.
3. D. Flynn, M.P.Y. Desmulliez, "Microscale Magnetic Components," *IMAPs System in Package (SiP)*, Cambridge, March, 2006.

4. D. Flynn, M.P.Y. Desmulliez, "Microscale Magnetic Components for DC-DC Converter Applications," MEMs Sensors and Actuators (IEE), London, April, 2006.
5. H. Lu, D. Flynn, C. Bailey and M.P.Y Desmulliez, "Computer Modelling of a Micro-manufactured One-turn Inductor," IEEE Proc. of High Density Packaging Conference, Shanghai, June, 2006.
6. H. Lu, D. Flynn, C. Bailey and M.P.Y Desmulliez, "An Analysis of a Microfabricated Solenoid Inductor," IEEE Proc. Electronics System-integration Technology Conference (ESTC), Dresden, Sept. 2006.
7. H. Lu, D. Flynn, C. Bailey and M.P.Y Desmulliez, "Assessment of MicroInductors for DC-DC Converters" IEEE Proc. of Electronic Materials and Packaging (EMAP) Conference, Hong Kong, 2006.
8. A. J Walton, D. Flynn, J.T.M. Stevenson, I. Underwood, J.G. Terry, S. Smith, W. Parkes, C. Dunare, H. Lin, Y. Li, R. Henderson, D. Renshaw, K. Muir, M. Desmulliez, A. F. Murray, T.B. Tang, Integration of IC technology with MEMS: Silicon technology for the future, Invited Paper *MEMs Sensors and Actuators (IET)*, London, April, 2007.

# Chapter 1

## Motivation behind the miniaturisation of magnetic components and thesis outline

### 1.1 Introduction, main objective and aims

There is an increasing demand for miniaturised power inductors and transformers that can be operated at high frequency either on a chip or on a module [1.1-1.4]. These power inductive components have applications in the area of powering hand-held mobile electronic systems, locally distributed Points of Load (PoL) or in power conversion electronic systems. The trend towards the miniaturisation of these components has resulted in developing surface-mount devices that are lower in profile than traditional bulk components. However, since these surface mount devices are inherently developed from existing conventional bulk technology, the ability to produce further improvements is limited in terms of component profile, increased power density, level of integration, etc. The intent of this work is to develop a fabrication technology for high power density, low profile, and highly efficient passive inductive components utilising MEMS (Micro-Electro-Mechanical-Systems) fabrication processes.

This chapter outlines the following:

- (a) The main objective of this thesis;
- (b) The motivation for microscale magnetic components;
- (c) The thesis general layout.

**The main objective of this thesis is to research and develop novel fabrication processes for the assembly of microscale magnetic components.** This work involves design, manufacturing, assembly, packaging and test of the resulting micro-components.

In order to satisfy these objectives, the thesis has the following aims:

- to identify the main motivation of microscale magnetic components;
- to perform literature research into the state of the art microscale magnetic components;
- to investigate suitable core materials for the development of microinductors and microtransformers;

- to research the effect of electrodeposition parameters on the magnetic and electrical properties of magnetic thin film alloys;
- to study the loss mechanisms that affect the performance of transformers and inductors
- to develop an optimal design procedure to produce microscale magnetic components with maximised power density and efficiency;
- to perform the experimental characterisation of the fabricated microscale magnetic component prototypes and discuss the experimental results with modelled and analytical data.

## **1.2 Motivation of microscale magnetic component**

While the physical size of digital and analogue electronic circuits has been drastically reduced over the past 20 years, the size of their associated power supplies has been reduced at a much slower rate. As a result, the power supply represents an increasing proportion of the size and cost of electronic equipment. One of the main difficulties in the miniaturization of power conversion circuits such as DC-DC converters is the construction of inductors and transformers. As expressed as far back as 1988, “magnetic design is the main bottleneck to the successful reduction of the overall converter size and weight” [1.5] and remains a technological obstacle today.

Recent efforts to miniaturise the overall size of DC-DC power converters, has resulted in an increase in switching frequency of the power circuit from the 100-500 kHz range to the 1-10MHz range. This effort has led to a reduction of the size of the energy storage components that dominate the converter volume, as demonstrated within Fig 1.1(a) & 1.1(b) [1.4]. Chapter 3 will expand on the theory behind the influence of frequency on the size of passive components. Several problems arise when frequencies are pushed into the MHz region. Core materials commonly used in the 20-500 kHz region such as MnZn ferrites, have rapidly increasing hysteresis and eddy current losses as the frequency is increased. Furthermore, eddy current losses in windings can also become a severe problem, as the skin depth in copper becomes small in relation to the cross section of wire used. Even if these problems are adequately dealt with, the resulting transformer/inductor is still one of the physically largest and most expensive components in the circuit.

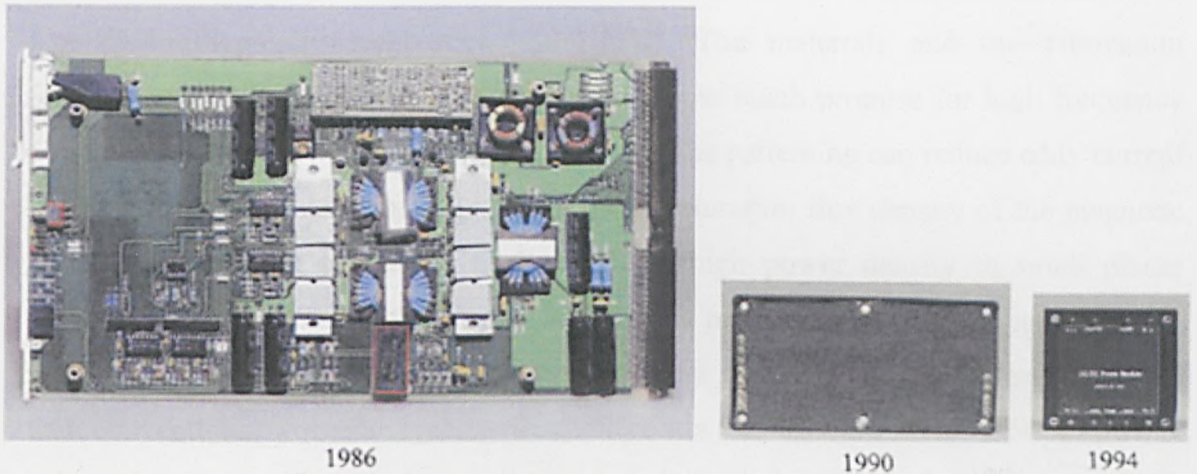


Figure 1.1(a) Evolution of the size of telecommunication power modules. The modules shown operate at the same power and voltage levels. Large energy storage elements required at lower frequencies have given way to smaller elements as frequencies have increased allowing reduced physical size.

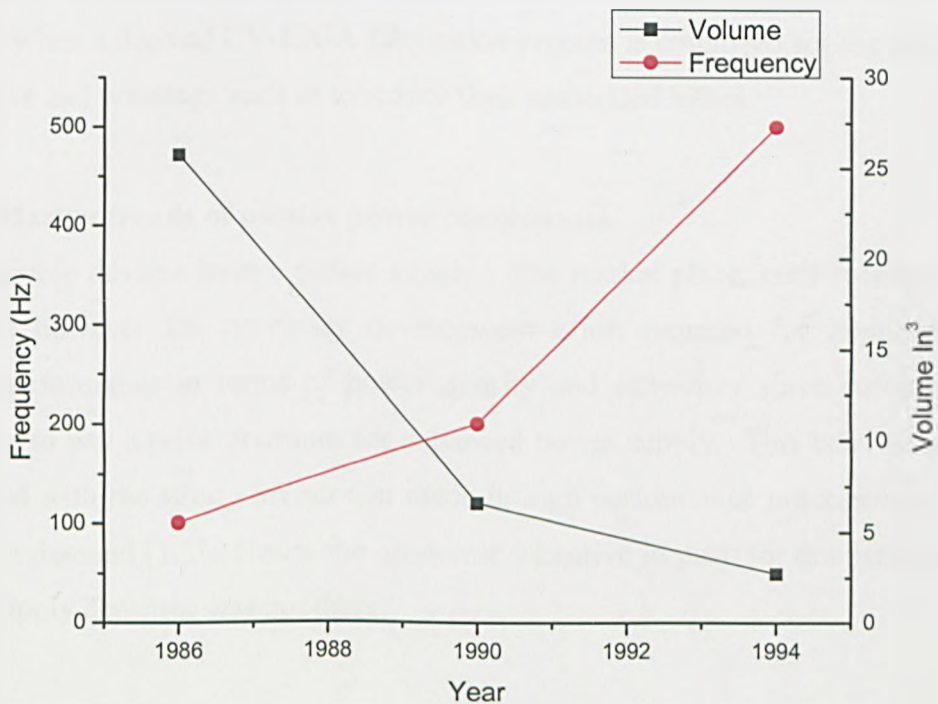


Figure 1.1(b) The increase in frequency has reduced the size of the bulky passive components.

In the magnetic recording head industry, thin-film metal alloys have replaced ferrites as the material of choice for inductive read-write heads, particularly where high density and high frequency are required. These materials have high saturation flux density and

the use of thin films controls eddy current losses at frequencies up and above 100 MHz [1.6-1.8]. Structures with very small feature size are fabricated with integrated-circuit-like photolithography techniques [1.9-1.13]. The materials and the fabrication techniques used for magnetic recording heads show much promise for high frequency power conversion. The ability to fabricate very fine patterning can reduce eddy current losses in both cores and windings. The higher saturation flux density of the magnetic alloys, as compared to that of ferrites, allows high power density in small planar devices. While costs may initially be high, batch processing techniques can bring the cost down substantially, and mass-produced devices may be significantly less expensive than conventional wound magnetic circuit elements. In any case the cost breakdown is very different from that of conventional magnetic devices as it is related to the number of layers and substrate area, rather than the number of turns.

To summarise, the motivation of this thesis is to investigate the issues involved in the manufacturing of miniaturised magnetic components for DC-DC converters, employing both theoretical analysis and experimental measurements. Gains in magnetic component efficiency and power density with increasing switching frequency are possible when a derived UV-LIGA fabrication process is employed for the manufacture of the core and windings such as to reduce their associated losses.

### **1.2.1 Market trends of passive power components**

All electronic devices have a power supply. The market place, until recently, did not stimulate however the necessary development effort required for improved power supply performance in terms of power density and efficiency since customers were unwilling to pay a price premium for enhanced power supply. This behaviour is to be contrasted with the strong investment made in high performance processors as a result of market demand [1.3]. Hence the economic incentive to push for dramatically higher power-supply densities was not there.

Today consumer products are driving the majority of the electronics industry growth. The increasing functionality of electronic products and demands for increased operation time have produced an insurgence in power density requirement. More and more, portable electronic products prioritise power over performance due to their reliance on battery operation. Physically small DC/DC converters may be the key enablers in powering high performance loads, and there is now a growing economic incentive to

invest in the needed technology improvements. Frost and Sullivan (F & S) predict that the entire power supply industry will grow at a compound annual growth rate (CAGR) of 6.5% through 2009, bringing revenues of \$15.6 billion. By 2009 the revenue share of the DC-DC modules within this market will grow to 41.7% from 35.6% in 2002 [1.14].

Addressing consumer needs will require price competitive components but initial markets for miniaturised converters are in equipment whose size and weight must be minimised, such as for satellites and aircraft. These aerospace products are produced in low volume, and their performance and reliability take precedence over cost, especially for military applications.

### 1.2.2 Technology drivers of passive power components

A number of scientific studies have addressed the question of the technological requirements that changing market trends will have on the power supply of the future. The findings of the Power Sources Manufacturers Association (PSMA) [1.15] are presented in Fig 1.2. They concluded that solutions would lie in the categories of packaging, circuits and technology, passive components and semiconductors.

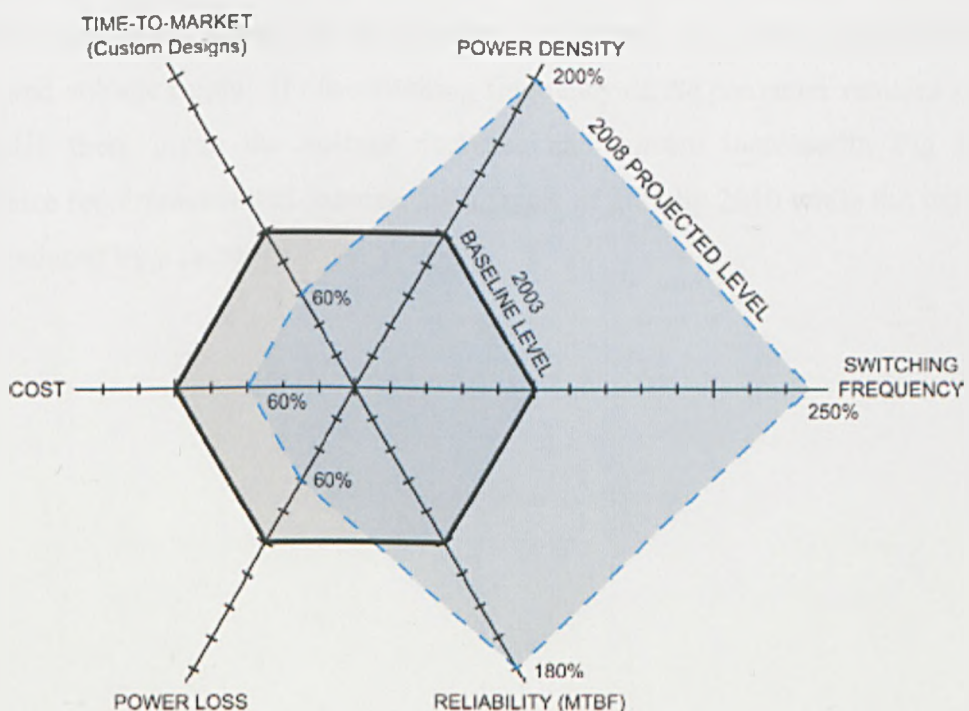


Figure 1.2 “A 5-Year Power technology Roadmap”, PMSA [1.16].



In reference to Fig 1.2, cost will be reduced through optimal topologies, more integration, innovative design and manufacturing techniques. Time-to-market will be shortened through integration and design software. Power density will increase with higher frequency, more integration, lower losses, better components and thermal design. The growth in switching frequency will be via better components, lower losses, thermal design and development of new materials. Reliability will be improved with better design, better components and thermal design. A clear resultant of this will be reduced power loss, achieved with optimal topologies, better components and power semiconductors.

Another study, the International Technology Roadmap for Semiconductors (IRTS Roadmap), confirms a similar trend outlined by the PSMA in reference to the hand-held electronic product sector [1.3]. Based on this roadmap, the graph in Fig. 1.3 plots the estimated trends in output power, voltage and current for a single buck DC-DC converter supplying power to the digital section of a handheld electronic product. The general trend is an increase in power consumption up to 3W, with a decrease in voltages (down to 0.8V in 2010) resulting in an increase in the output current from 2 to 5A [1.3]. For illustration purposes, given the estimates for DC-DC converter power, current and voltage, it is relatively easy to determine, for a given switching frequency, the inductance and capacitance values required to satisfy any given specifications for current and voltage ripple. If the switching frequency of the converter remains constant at 1 MHz then, given the voltage decrease and current increase in Fig 1.3, the capacitance requirements will increase by a factor of 2.25 by 2010 while the inductance will be reduced by a factor of 2.



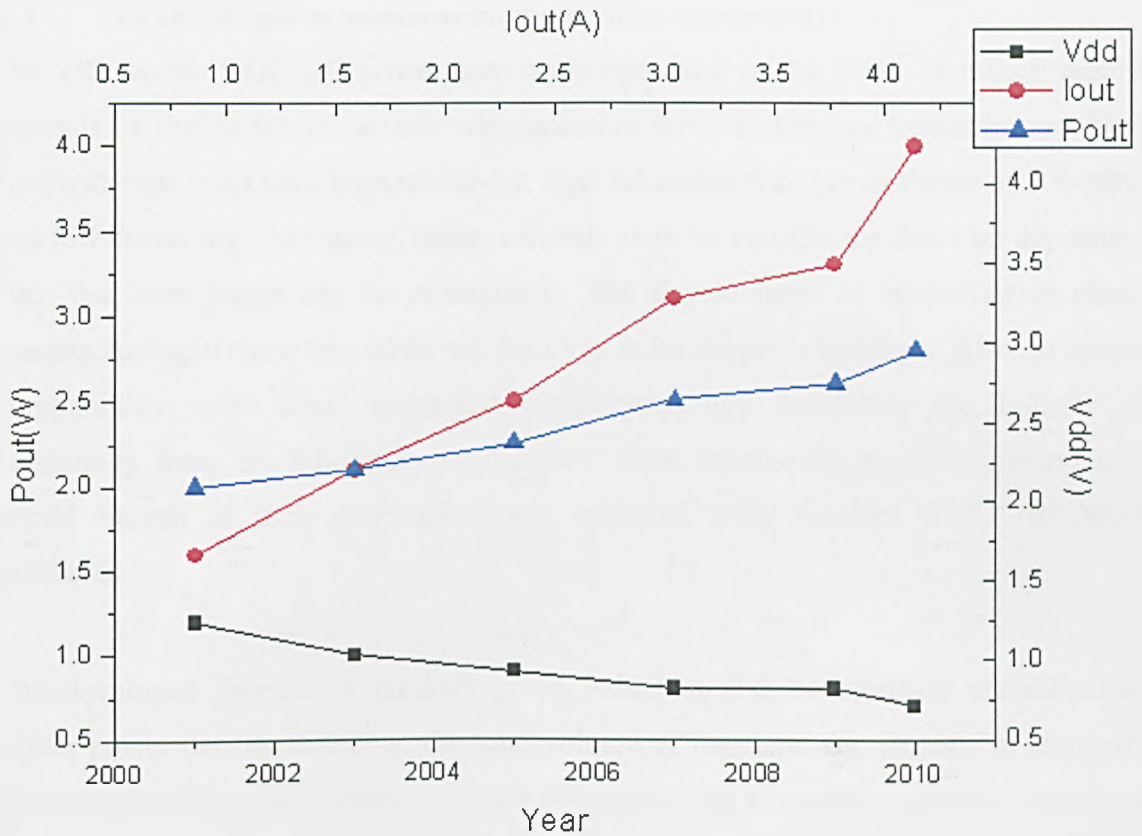


Figure 1.3 Estimation of the output power, voltage and current for a single buck converter supply in handheld electronic products. All data is based on the ITRS2003 roadmap.

Clearly, to achieve miniaturization, a decrease in both the capacitor and inductor values will address this increase in the converter switching frequency. Once suitable switches are available, the next limitation in going to higher switching frequencies is the magnetic components within the circuit. Since switching frequency stalled in the few hundred kHz range [1.3, 1.4], magnetic core manufacturers focused their development efforts on developing core materials with reduced loss in this frequency range. Ferrites appeared to have reached maturity in terms of higher frequency operation at reasonable loss levels. Therefore new core materials applicable at frequencies of 10MHz and beyond need to be developed. Another concern in the area of magnetic components is the windings. With increasing frequency the magnetic component becomes smaller, AC resistance losses increase alongside the current handling capability that the windings are being required to satisfy.

### 1.3 The challenges of miniaturising magnetic components

The efficiency of DC-DC power converters operating in the MHz frequency regime depends on the choice of suitable core materials for inductors and transformers. New core materials must have high resistivity, high saturation flux, permeability of 100-3000 and low coercivity. Moreover, these materials must be suitable for thin film deposition such that core losses can be minimized. The development of cost-effective mass-manufacturing of these thin films will be a key technological challenge. Also, to ensure compatibility with other integrated components and accelerate the transfer of technology from the laboratory to industry, these microscale magnetic components would benefit if their fabrication was achieved with standard CMOS/BiCMOS processes.

The developed fabrication technology of inductors and transformers should allow higher power density to reduce the total volume of magnetic components in compact-power application with practical power handling ( $\geq 1W$ ), and low profile of devices ( $\leq 1mm$ ) with reasonable fabrication complexity.

### 1.4 Thesis layout

The layout of this thesis is presented schematically in Fig 1.4.

**Chapter 1** outlines the main objective of this thesis, its aims and introduces inductor and transformer operation. It also highlights the market trends driving the evolution of magnetic components, provides an overview of the challenges encountered when miniaturising magnetic components and introduces the proposed solution that is to be pursued in this thesis.

**Chapter 2** presents the fundamental magnetic design equations and background theory on magnetic materials outlining the desirable properties for power magnetic components. An explanation of hysteresis and eddy current phenomena within thin films is provided, along with a description of anisotropy within magnetic thin films.

**Chapter 3** presents the requirements of magnetic components operating within DC-DC converters and is accompanied by a description of how the three most common types of DC-DC converters operate. A review of conventional components, including

component structure, materials and fabrication processes is also carried out. A study into current state of the art techniques of fabricating microscale magnetic components is presented. Finally, the performance of conventional and prior micromachined components is presented in order to assess the performance of the components fabricated within this thesis.

**Chapter 4** explains the theory behind the process of electrodeposition and the various waveforms that can be applied. The composition of electrolyte solutions for the deposition of nickel-iron alloys is provided and the theory behind magnetic field annealing during electrodeposition is described. The preliminary experimental analysis of nickel-iron alloys with a description of the analytical tools is presented. An explanation of anomalous deposition is provided via modelled and experimental data.

**Chapter 5** explains briefly the Design Of Experiments (DOE) carried out in the manufacturing of magnetic alloys and the parameters utilised within the DOE. The effect of alloy properties generated via deposition conditions is examined in terms of the electric and magnetic properties of the thin film. Other magnetic thin film alloys incorporated into prototype magnetic components are introduced.

**Chapter 6** examines the basic loss mechanisms of the component and derives the equations that impact on the performance. Various component geometries are described and assessed since the design of the component is application specific. The impact of the component's performance on the operation of the converter is also reviewed in this chapter.

**Chapter 7** details the fabrication process of the microinductors and microtransformers.

**Chapter 8** explains the experimental procedure used to characterise the components. Results of the characterisation of all the fabricated components are presented, and analysis of the data is provided.

**Chapter 9** provides an overview of ANSYS and a description of the methodology of the developed models. A comparison between analytical, experimental and simulated data is performed and conclusions provided.

**Chapter 10** gathers the collated data from prior chapters on the performance of the prototype components. A comparison of the optimised component performance is made with components from the literature review provided in Chapter 3. Conclusions are presented covering the performance of the prototype components in comparison to prior work, the fabrication processes used in their assembly and the deposition of the magnetic alloys. A section on future work will describe areas for component improvement and how this may be achieved.

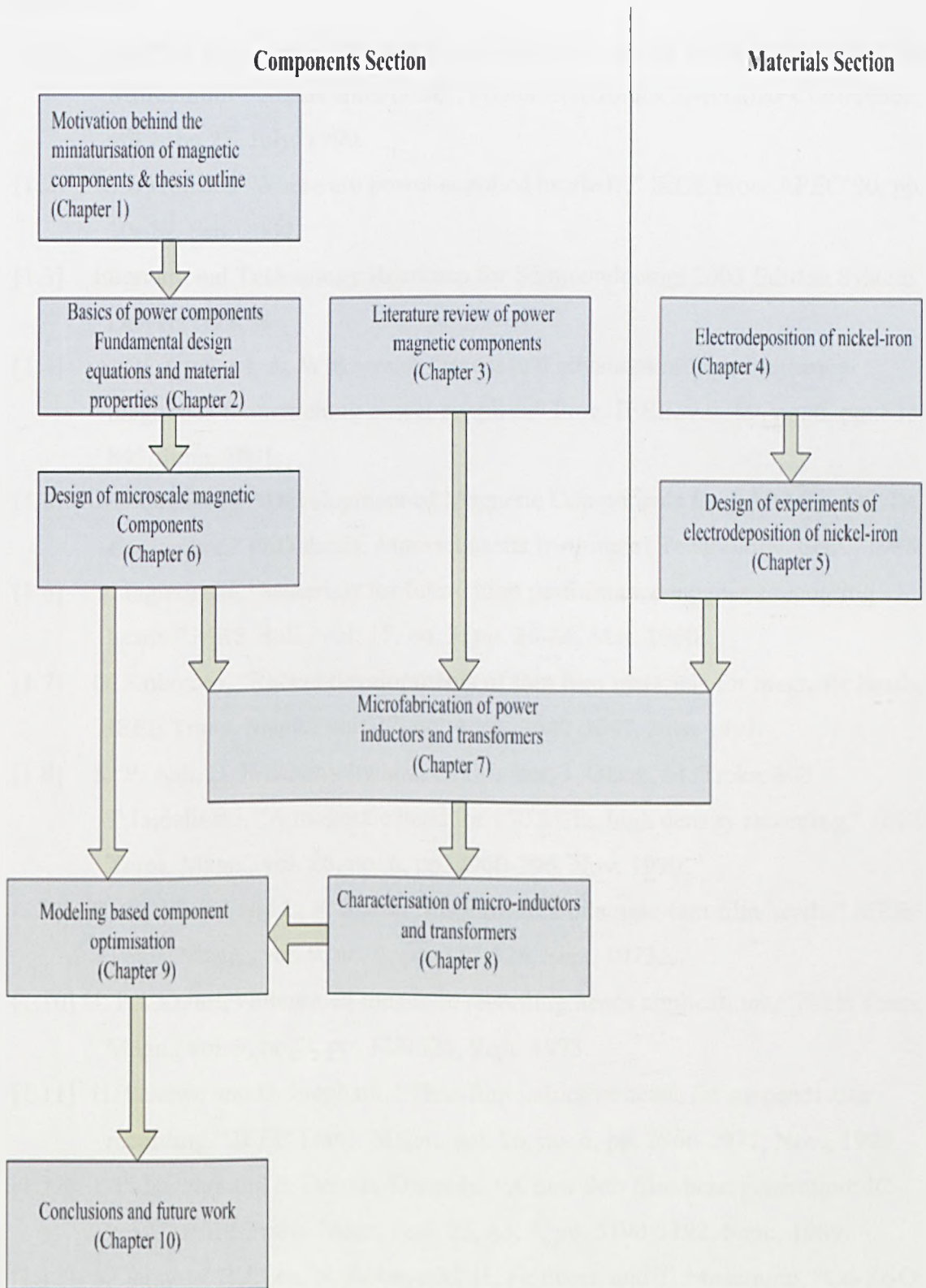


Figure 1.4 Synopsis of the thesis.

## References

- [1.1] Van Wyk J.D., Lee F., "Power Electronics Technology at the Dawn of the New Millennium – Status and Future", Power Electronics Specialists Conference, vol.1, pp.27, July, 1999.
- [1.2] R. J. Huljak., "Where are power supplies headed?," IEEE Proc. APEC'00, pp. 10–17, Feb, 2000.
- [1.3] International Technology Roadmap for Semiconductors 2003 Edition System Drivers (ITRS)
- [1.4] A. W. Lotfi, M. A. Wilkowski, "Issues and advances in high-frequency magnetics for switching power supplies," Proc. IEEE, vol. 89, no. 6, pp. 833-845, June, 2001.
- [1.5] A.F Goldberg, "Development of Magnetic Components for 1-10 MHz DC/DC Converters," PhD thesis, Massachusetts Institute of Technology, Sept., 1988.
- [1.6] T. Jagielinski, "Materials for future high performance magnetic recording heads," MRS Bull., vol. 15, no. 3, pp. 36-44, Mar. 1990.
- [1.7] O. Kohmoto, "Recent developments of thin film materials for magnetic heads," IEEE Trans. Magn., vol. 27, no. 4, pp. 3640-3647, July, 1991.
- [1.8] K. P. Ash, D. Wachenschwanz, C. Brucker, J. Olson, M. Trcka, and T.Jagielinski, "A magnetic head for 150 MHz, high density recording," IEEE Trans. Magn., vol. 26, no. 6, pp. 2960-296, Nov. 1990.
- [1.9] E. P. Valstyn and L. F. Shew, "Performance of single-tum film heads," IEEE Trans. Magn., vol. 9, no. 3, pp. 317-326, Sept. 1973.
- [1.10] J. P. Lazzari, "Integrated magnetic recording heads applications," IEEE Trans. Magn., vol. 9, no. 3, pp. 322-326, Sept. 1973.
- [1.11] H. Schewe and D. Stephani, "Thin-film inductive heads for perpendicular recording," IEEE Trans. Magn., vol. 26, no. 6, pp. 2966-2971, Nov., 1990.
- [1.12] J. P. Lazzari and P. Deroux-Dauphin, "A new thin film head generation: IC head," IEEE Trans. Magn., vol. 25, no. 5, pp. 3190-3192, Sept., 1989.
- [1.13] S.Ohnuma, H.J.Lee, N. Kobayashi, H. Fujimori, and T. Masumoto, "Co-Zr-O Nano-Granular Thin Films with Improved High Frequency Soft Magnetic Properties," IEEE Trans. Magn., vol. 37, no. 4, July, 2001.
- [1.14] F. K. Wong, "High Frequency Transformer for Switching Mode Power Supplies," PhD thesis, Griffith University, Brisbane, Australia, March, 2004.
- [1.15] PSMA Power Technology Roadmap (2000). [Online]. Available: [www.pσμα.com](http://www.pσμα.com)

## Chapter 2

### Basics of power components Fundamental design equations and material properties

#### 2.1 Introduction

This chapter provides an introduction to magnetism and properties of magnetic materials. Section 2.2 presents units and fundamental design equations that underline transformer and inductor operation. The process of magnetization in a ferromagnetic medium is outlined in section 2.3. Hysteresis, eddy current phenomena and residual loss are reviewed. Magnetic anisotropy and its influence on the response of the magnetic material is discussed. Lastly, section 2.4 compares the properties of ferrite with thin film alloys, with particular reference to nickel-iron.

#### 2.2 Fundamental design equations

Inductor and transformer operation are described by three fundamental equations: Ampere's Law, Faraday's Law, and Lenz's Law [2.1-2.5]. These three equations, coupled with the core geometry, material characteristics, and the various conductors' electrical characteristics, are used to derive the necessary equations for transformer and inductor design. This section introduces the units and fundamental equations.

To assist in the understanding of inductor and transformer operation the basic units used are explained by taking an electrical analogy. Magnetomotive force (mmf) is the strength of a magnetic field in a coil of wire, illustrated in Fig 2.1.

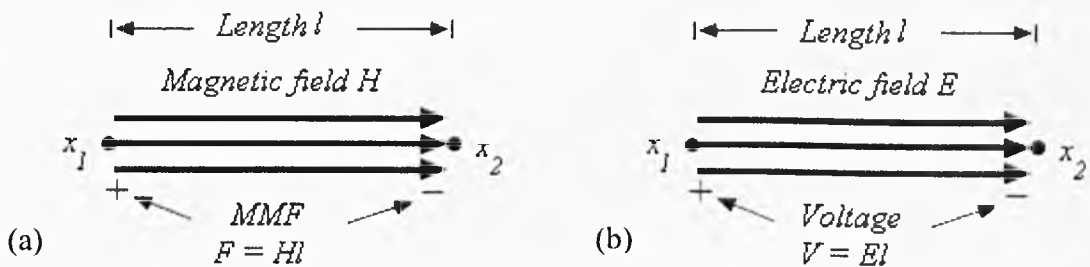


Figure 2.1 (a) Uniform magnetic field of magnitude  $H$ , (b) Electrical analogy

The mmf between points  $x_1$  and  $x_2$ , Fig 2.1(a), is related to the magnetic field  $H$  according to:

$$F = \int_{x_1}^{x_2} H \cdot dl \quad (2.1)$$

This is analogous to an electric field strength,  $E$ , that induces the voltage (emf)  $V$  as shown in Fig 2.1(b). Moving from the straight conductor of Fig 2.1 to a typical winding geometry with turns, the mmf is dependent on the amplitude of current in the turns of coil according to Eq (2.2). The more current, the stronger the magnetic field; the more turns of wire, the more concentrated the lines of force. The current times the number of turns of the coil is expressed in units called "ampere-turns":

$$F = NI \quad (2.2)$$

The magnetic flux is a measure of quantity of magnetism and this quantity takes into account the strength and the extent of a magnetic field. The total magnetic flux passing through a surface of area  $A_c$  is related to the flux density  $B$  according to:

$$\Phi = \int_{\text{surface } S} B \cdot dA \quad (2.3)$$

The magnetic flux is analogous to electrical conductor current density of magnitude  $J$ , which leads to total conductor current  $I$ . Fig 2.2 displays this comparison.



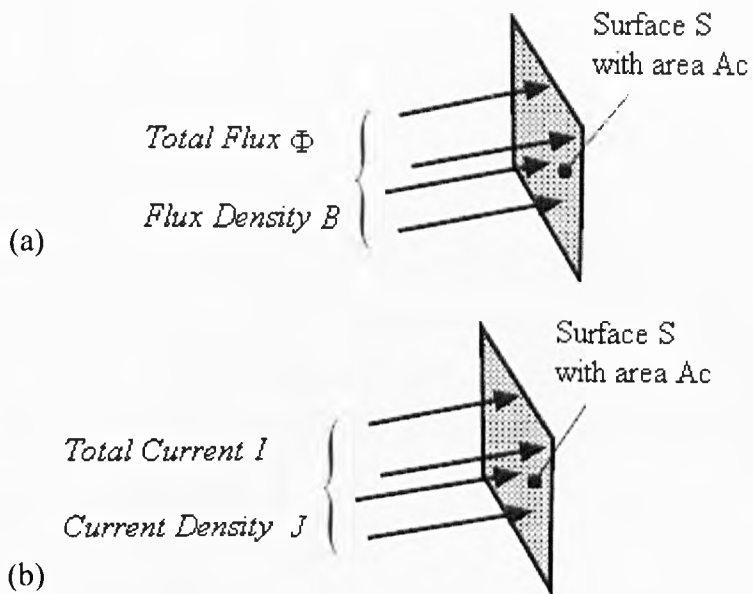


Figure 2.2(a) Uniform flux density of magnitude  $B$ , (b) Electrical analogy

With the basic quantities defined an introduction to Faradays Law, Lenz's Law, and Ampere's Law follows.

Faradays law of induction states that a magnetic field changing in time creates a proportional electromotive force, illustrated in Fig 2.3

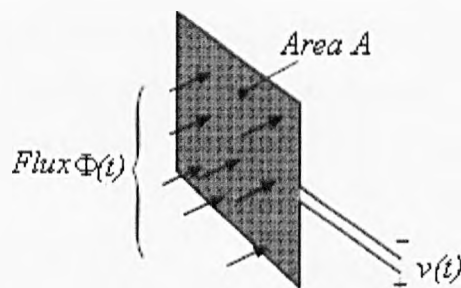


Figure 2.3 Faradays Law: a magnetic field changing in time creates a proportional emf.

Therefore the voltage  $v(t)$  is induced in a loop of wire by change in the total flux  $\Phi(t)$  passing through the loop, according to:

$$v(t) = \frac{d\Phi(t)}{dt} \tag{2.4}$$

For a uniform flux distribution:  $\Phi(t) = B(t)A_c$ , and hence:

$$v(t) = A_c \frac{dB(t)}{dt} \quad (2.5)$$

Lenz's law gives the direction of the induced emf resulting from electromagnetic induction. The emf induced,  $v(t)$ , in an electric circuit always acts in such a direction that the current it drives around a closed circuit produces a magnetic field which opposes the change in magnetic flux. Fig 2.4 displays Lenz's law via a shorted loop of wire.

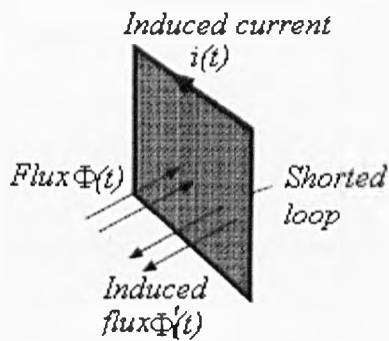


Figure 2.4 Lenz's Law: Induced flux opposing changing flux.

Changing flux  $\Phi(t)$  induces a voltage  $v(t)$  around the loop. This voltage, divided by the impedance of the loop conductor, provides the current  $i(t)$ . This current induces a flux  $\Phi'(t)$ , which opposes changes in  $\Phi(t)$ .

Ampere's law, states that the net mmf around a closed path is equal to the total current,  $I$ , passing through the interior of the path:

$$\oint_{\text{closed-path}} H \cdot dl = I \quad (2.6)$$

In reference to Fig 2.5, consider a magnetic core with current carrying wire passing through the core window. The dark region illustrates the main flux lines around the interior of the core. Ampere's Law relates the magnetic field strength,  $H(t)$ , to the winding current,  $i(t)$ . Winding currents are sources of mmf, the total mmf around the

core,  $F(t) = H(t)l_m$ , is equal to the winding current mmf  $i(t)$ . The total mmf around a closed loop, accounting for winding current mmf, is zero.

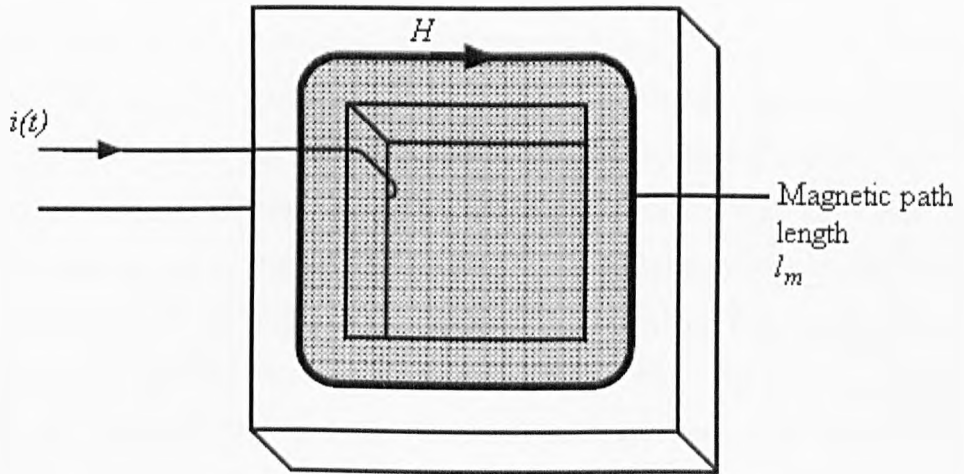


Figure 2.5 Ampere's Law: For any closed loop path, the sum of the length,  $l_m$ , times the magnetic field,  $H$ , in the direction of the length element is equal to the permeability times the electric current enclosed in the loop.

The resistance that current experiences travelling through a conductive medium is analogous to a magnetic field experiencing reluctance when travelling through a magnetic medium. Magnetic reluctance is the resistance of a material to a magnetic field. It is defined as the ratio of mmf to magnetic flux. The definition can be expressed as:

$$\mathfrak{R} = \frac{F}{\Phi} \quad (2.7)$$

where  $\mathfrak{R}$  is the reluctance in ampere-turns per Weber (a unit that is equivalent to turns per Henry),  $F$  is the mmf in ampere turns and  $\Phi$  is the magnetic flux in Webers.

The reluctance of a uniform magnetic circuit can be calculated as:

$$\mathfrak{R} = \frac{l_m}{\mu_o \mu_r A_c} \quad (2.8)$$

Where  $l_m$  is the length of the circuit in metres,  $\mu_o$  is the permeability of free space ( $4\pi \times 10^{-7}$  H/m),  $\mu_r$  is the relative magnetic permeability of the material (dimensionless), and  $A_c$  is the cross sectional area of the circuit in square metres.

The three fundamental equations are summarized in Table 2.1. In the study of magnetism there are two systems of units currently in use: the mks (metres-kilograms-seconds) system, which has been adopted as the S.I. units and the cgs (centimetres-grams-seconds) system, which is also known as the Gaussian system. These units and conversion factors are contained in Table 2.2. The basic components of inductor and transformer operation are displayed in Fig 2.6. Fig 2.6 relates the electric and magnetic properties of the winding and core to the overall function of the device. The windings are normally aligned to the core such that the induced magnetic field within the core, generated by the flow of current through the winding, follows a closed magnetic path within the core. The core, due to its relative permeability to free space, amplifies the flux density therefore inductance. An introduction to magnetic materials follows in section 2.2.

	Equation	Description
Faraday's Law	$v(t) = \frac{d\Phi(t)}{dt}$	A magnetic field changing in time creates a proportional emf.
Lenz's Law	$v(t) = -\frac{d\Phi(t)}{dt}$	The emf induced in an electric circuit always acts in such a direction that the current it drives around a closed circuit produces a magnetic field which opposes the change in magnetic flux.
Ampere's Law	$\oint_{\text{closed-path}} H \cdot dl = I$	The net mmf around a closed path is equal to the total current, $I$ , passing through the interior of the path

Table 2.1 The fundamental equations governing inductor and transformer operation: Faraday's Law, Ampere's Law and Lenz's Law.

Quantity	Gaussian(cgs units)	S.I units	Conversion Factor (cgs to S.I)
Magnetic Induction (B)	G	T	$10^{-4}$
Applied Field (H)	$O_e$	$\text{Am}^{-1}$	$10^3 / 4\pi$
Magnetisation ( $M_s$ )	$\text{emu.cm}^{-3}$	$\text{Am}^{-1}$	$10^3$
Permeability	Dimensionless	$\text{Hm}^{-1}$	$4\pi \cdot 10^{-7}$
Relative Permeability	Dimensionless	Dimensionless	-
Susceptibility (X)	$\text{emu.cm}^{-3} O_e^{-1}$	Dimensionless	$4\pi$

Table 2.2: Relationship between magnetic parameters in cgs and S.I. units.  
(Where: G = Gauss,  $O_e$  = Oersted, T = Tesla)

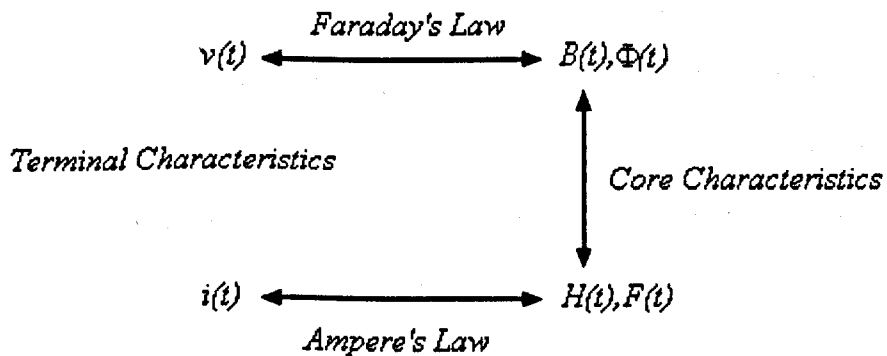


Figure 2.6 Review of basic magnetic relationships

### 2.3 Introduction to magnetic materials

To optimize a magnetic component it is important to understand the process of magnetization and the properties of the material that influence this process. A description of the magnetization process and properties of ferromagnetic materials are presented. When referring to ferromagnetic materials only magnetically soft magnetic materials and not hard magnetic materials i.e. permanent magnets, are considered. The magnetic characteristics of "soft" are superior to "hard" for this given application [2.6-2.8]. The three magnetic core loss mechanisms, hysteresis, eddy current phenomena and residual loss, are discussed. An overview of the thin film properties on the magnetization process follows. Lastly, an equivalent circuit model summarizing inductor and transformer operation is provided.

### 2.3.1 Magnetisation and magnetic materials

Magnetic materials get their properties from the electrons of the atoms in the material. The electrons in each atom, as governed by the rules of quantum mechanics, interact to give rise to a magnetic moment for each atom [2.2]. Depending on the way these magnetic moments interact with each other, a material can exhibit one of five different types of magnetism: diamagnetism, paramagnetism, antiferromagnetism, ferrimagnetism and ferromagnetism. Ferromagnetic materials present a magnetization much larger than other materials. Ferromagnetism arises from the strong coupling between the magnetic dipoles in the material [2.3].

Ferromagnetic materials get their magnetic properties not only because their atoms carry a magnetic moment but also because the material is made up of small regions known as magnetic domains. The theory of magnetic domains is integral to the understanding of ferromagnetic materials and optimisation of film properties. The concept of magnetic domains was proposed by Weiss in order to explain the fact that ferromagnetic materials with spontaneous magnetisation could exist in the demagnetised state [2.9]. Weiss built on earlier work carried out by Ampère, Weber and Ewing suggesting their existence. The findings of this work revealed that within a domain large numbers of atomic moments are aligned, typically  $10^{12}$ - $10^{18}$ .

Ferromagnetic materials become magnetized when the magnetic domains are aligned. This can be done by placing the material in an external magnetic field or by passing electrical current through the material [2.1]. When all domains are aligned the material is magnetically saturated. A uniformly magnetised material is shown in Fig 2.7 and has large magnetostatic energy associated with it. A definition of magnetostatic is provided in section 2.3.3. Magnetic domains exist in order to reduce the energy of the magnetic material system. From the convention adopted for the definition of the magnetic moment for a magnetic dipole the magnetisation within the specimen points from the south-pole to the north-pole, while the direction of the magnetic field points from north to south. Therefore, the demagnetising field,  $H_d$ , is in opposition to the magnetisation of the specimen. The magnitude of  $H_d$  is dependent on the geometry and magnetisation of the specimen. In general if the sample has a high length to diameter ratio, and is magnetised in the long axis, then the demagnetising field and the magnetostatic energy will be low.

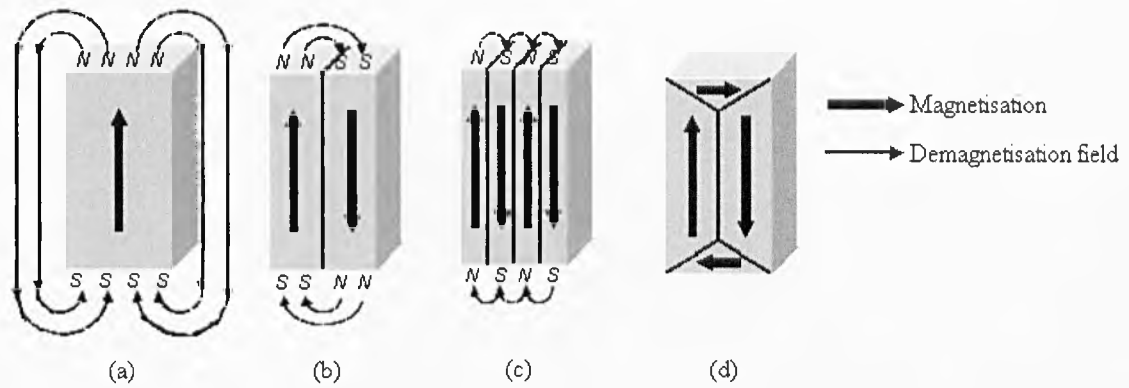


Figure 2.7 Schematic illustration of the break up of magnetisation into domains (a) single domain, (a) single domain, (b) two domains, (c) four domains and (d) closure domains.

The break-up of the magnetisation into two domains as illustrated in Fig 2.7(b) reduces the magnetostatic energy by half. In fact if the magnetic material breaks down into  $N$  domains then the magnetostatic energy is reduced by a factor of  $1/N$ , hence Fig 2.7(c) has a quarter of the magnetostatic energy of Fig 2.7(a). Figure 2.7(d) shows a closure domain structure where the magnetostatic energy is zero; however, this is only possible for materials that do not have a strong uniaxial anisotropy.

The introduction of a domain raises the overall energy of the system, therefore the division into domains only continues while the reduction in magnetostatic energy is greater than the energy required to form the domain wall. The energy associated with a domain wall is proportional to its area. A minimum energy can therefore be achieved with a specific number of domains within a specimen. This number of domains will depend on the size and shape of the sample, which will affect the magnetostatic energy, and the intrinsic magnetic properties of the material, which will affect the magnetostatic energy and the domain wall energy.

In reference to domain alignment, Fig 2.7, when a ferromagnetic material is magnetized in one direction, it will not relax back to zero magnetization when the imposed magnetizing field is removed. It must be driven back to zero by a field in the opposite direction. If an alternating magnetic field is applied to the material, its magnetization will trace out a loop called a hysteresis loop, as illustrated in Fig 2.8. The hysteresis loop is generated by the magnetic domains, for once the magnetic domains are

reoriented energy is required to turn them back again. Therefore the area enclosed by the hysteresis loop is regarded as lost energy.

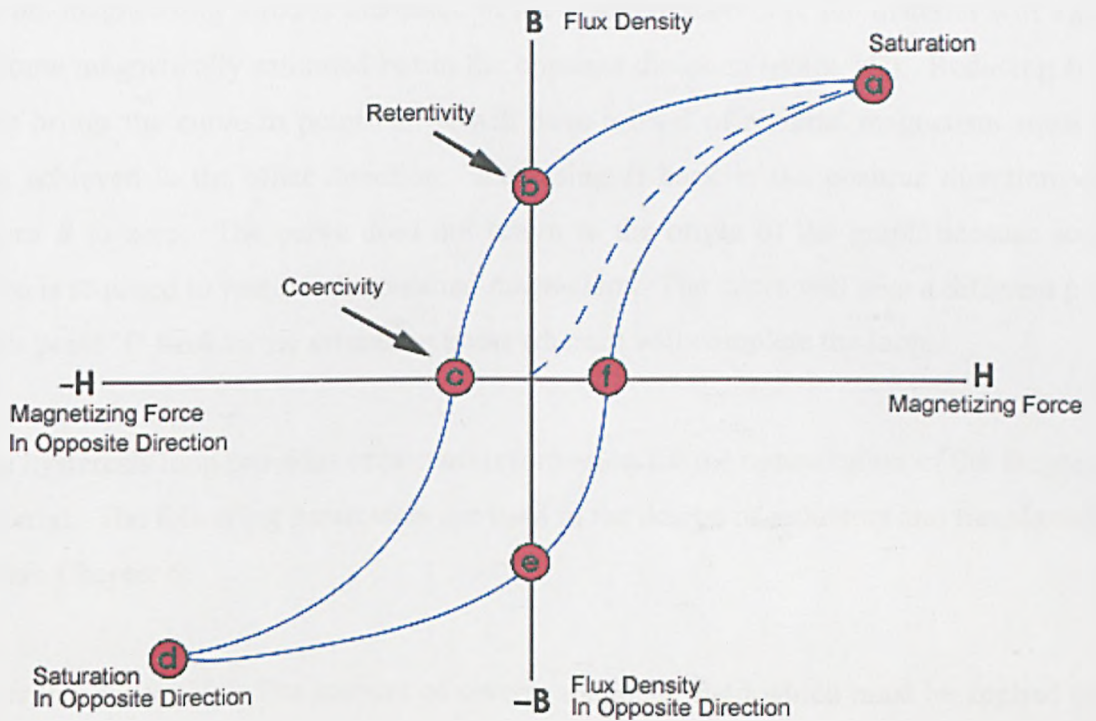


Figure 2.8 The hysteresis loop of a ferromagnetic material [2.5].

The hysteresis loop is recorded by measuring the magnetic flux,  $B$ , while the magnetizing force,  $H$ , is changed. A ferromagnetic material that has never been previously magnetized or has been thoroughly demagnetized will follow the dashed line as  $H$  is increased. As the line demonstrates, the greater the amount of current applied ( $H+$ ), the stronger the magnetic field in the component ( $B+$ ). At point "a" almost all of the magnetic domains are aligned and an additional increase in the magnetizing force will produce very little increase in magnetic flux. The material has reached the point of magnetic saturation. When  $H$  is reduced back down to zero, the curve will move from point "a" to point "b." At this point, some magnetic flux remains in the material even though the magnetizing force is zero. This is referred to as the point of retentivity on the graph and indicates the remanence or level of residual magnetism in the material due to some of the magnetic domains remaining aligned. As the magnetizing force is reversed, the curve moves to point "c", where the flux has been reduced to zero. This is called the point of coercivity on the curve. The reversed magnetizing force has flipped enough of the domains so that the net flux within the material is zero. The force



required to remove the residual magnetism from the material, is called the coercive force or coercivity of the material.

As the magnetizing force is increased in the negative direction, the material will again become magnetically saturated but in the opposite direction (point "d"). Reducing  $H$  to zero brings the curve to point "e." It will have a level of residual magnetism equal to that achieved in the other direction. Increasing  $H$  back in the positive direction will return  $B$  to zero. The curve does not return to the origin of the graph because some force is required to remove the residual magnetism. The curve will take a different path from point "f" back to the saturation point where it will complete the loop.

The hysteresis loop provides important information for the optimization of the magnetic material. The following parameters are used in the design of inductors and transformers within Chapter 6.

1. **Coercive force,  $H_c$**  - The amount of reverse magnetic field which must be applied to a magnetic material to make the magnetic flux return to zero. Indicated by the value of  $H$  at point C on the hysteresis curve. This value defines the width of the hysteresis loop and as a result the area within the loop. This area is "hysteresis loss"; hence it is advantageous to minimize this value. The formula for hysteresis loss is derived in Chapter 6.

2. **Relative permeability,  $\mu_r$** - The permeability,  $\mu$ , is a material property that describes the ease with which a magnetic flux is established in a magnetic medium. It is the ratio of the flux density to the magnetising field, represented by Eq (2.9).

$$\mu = \frac{B}{H} \quad (2.9)$$

Eq (2.9) describes the slope of the curve at any point on the hysteresis loop. The permeability value used to evaluate the material is the relative permeability. The relative permeability,  $\mu_r$ , is recorded as the slope of the B/H curve taken from the point where a straight line from the origin is tangent to the B/H Curve, illustrated by Fig 2.9.

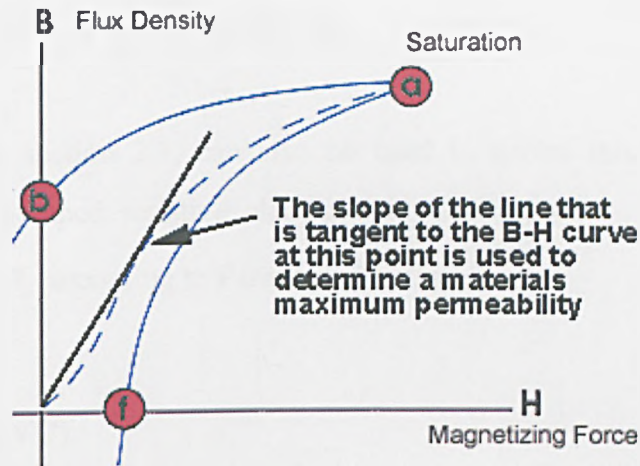


Figure 2.9 Determination of relative permeability from the hysteresis response of a magnetic medium.

The relative permeability is derived by taking the ratio of the medium's permeability to the permeability in free space,  $\mu_o = 1.256 \times 10^{-6}$  (H/m), as shown by Eq (2.10)

$$\mu_{relative} = \frac{\mu_{material}}{\mu_o} \quad (2.10)$$

Relative permeability is used to determine the number of turns for a given inductance, calculation of skin depth, therefore frequency of operation, and saturation current.

3. **Saturation flux density,  $B_{sat}$**  – for a magnetic medium, saturation is the state when the material cannot absorb a stronger magnetic field, such that an increase of magnetization force produces no significant change in magnetic flux density. Recalling from Ampere's Law that the current induces the magnetic field, the saturation point along with the medium's geometry determines the maximum current prior to saturation or required core area. This is demonstrated in Chapter 6.

### 2.3.2 Eddy current phenomena within thin films

Besides hysteresis loss, the second type of core loss is due to eddy currents, which are induced in the core material by time-varying flux,  $d\Phi/dt$ . Recall from section 2.1, according to Lenz's Law a changing flux induces a current that itself induces a flux in

opposition to the initial flux. The eddy current flows in the conductive core and produces  $I^2R$  or  $V^2/R$  power loss [2.10].

Faraday's Law, section 2.1, can also be used to derive this effect. A core can be modelled as a lumped resistive element with resistance  $R_c$ , then the voltage  $v'(t)$  induced across  $R_c$  according to Faraday's Law is

$$\frac{d\Phi}{dt} = A_c \cdot \frac{dB}{dt} = v'(t) \quad (2.11)$$

where  $A_c$  is the cross-sectional area of the core. The power loss in the core due to eddy currents is

$$P_{\text{eddy-current}} \approx \frac{v'(t)^2}{R_c} \quad (2.12)$$

Eq (2.12) indicates that a material with high resistivity will minimise eddy current power loss [2.11]. With low resistivity materials such as magnetic alloys laminated core structures are used [2.12-2.14]. This power loss is proportional to the square of the rate of change of flux in the core. Since the rate of change of flux is directly proportional to the applied voltage, the power loss due to eddy currents increases as the square of the applied inductor voltage and directly with its pulse width:

$$P_{\text{eddy-current}} \approx \frac{V_L^2}{R_c} \cdot \frac{t_{\text{applied}}}{T} \quad (2.13)$$

where  $V_L$  is the voltage applied to the inductor,  $t_{\text{applied}}$  is the on or off time, and  $T$  is the switching period. A detailed derivation of the eddy current loss is contained in Chapter 6.

Two forms of magnetic loss have so far been distinguished, namely hysteresis and eddy current loss. When flux density and frequency are equal to zero the total loss of the magnetic material is not zero. The remainder is called residual loss, sometimes referred

to an excess loss. Recording residual loss requires a thin magnetic sample so that the bulk of eddy current loss is negligible. The flux density must also be reduced so that hysteresis loss is negligible, the remainder is then the residual loss. With the requirement of high frequency operation at maximum flux density residual loss will be omitted.

### 2.3.3 Origins of anisotropy

Magnetic anisotropy is an important property of magnetic materials. Magnetic anisotropy affects the shape of hysteresis loops and controls the coercivity and remanence [2.15]. Knowledge and understanding of the origins of magnetic anisotropy is necessary if the properties of the magnetic alloy are to be tailored. To create a tailored magnetic material, which is the focus of Chapter 5, it is necessary to minimize these intrinsic properties during manufacturing.

Several factors contribute to the anisotropy energy of the magnetic material. These include exchange energy  $E_{ex}$ , Zeeman energy  $E_H$ , magnetoelastic energy  $E_{EA}$ , crystalline anisotropy energy  $E_{ca}$ , and magnetostatic energy  $E_D$  (demagnetisation energy) [2.16-2.18]. Therefore the total energy,  $E$ , can be expressed as:

$$E = E_{ex} + E_H + E_{EA} + E_{ca} + E_D \quad (2.14)$$

These effects have been reviewed in depth for applications ranging from biology to data storage e.g. magnetic random access memory (MRAM), magnetic tweezers [2.19-2.25]. Their findings are summarized below.

Exchange energy is a measure of the strength of electrons spin-spin exchange coupling, which is ultimately responsible for ferromagnetism. Exchange coupling tends to keep magnetic moments parallel to each other, which means that uniform magnetism would have the minimum exchange energy. The exchange energy,  $E_{ex}$ , can be written as

$$E_{ex} = -2 \sum_{-2} J_{ij} S^2 \cos \theta_{ij} \quad (2.15)$$

where  $J_{ij}$  is the exchange integral,  $S$  is the spin associated with each atom, and  $\theta_{ij}$  is the angle between adjacent spin orientations. For ferromagnetic materials,  $J$  is positive, and the minimum-energy state occurs when the spins are parallel to each other ( $\theta_{ij} = 0$ ).

The Zeeman energy  $E_H$  is often referred to as the magnetic potential energy, which is simply the energy of the magnetization in an externally applied magnetic field. The Zeeman energy is always minimized when the magnetization is aligned with the applied field and can be expressed as

$$E_H = -M \cdot H \quad (2.16)$$

where  $H$  is the external field vector and  $M$  is the magnetization vector.

The magnetoelastic energy  $E_{EA}$  is used to describe the magnetostriction effect, which relates the influence of stress, or strain, on the magnetization of a material [2.26]. Control of film composition can be used to avoid this [2.27]. Fig 2.12 displays the saturation magnetostriction,  $\lambda_s$ , as a function of composition for nickel-iron films. Higher nickel content results in tensile stress with higher iron content producing compressive stress. A composition of 80% nickel and 20% iron results in zero magnetostriction. The varying material properties with composition, Fig 2.10, highlight the importance of composition control during the manufacture of magnetic alloy.

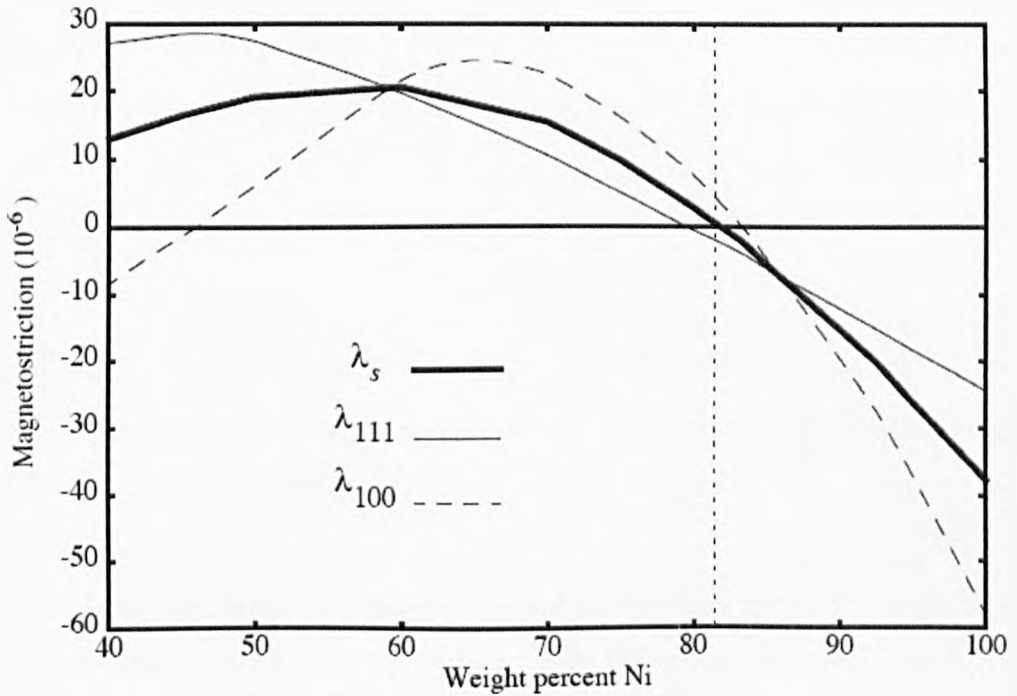


Figure 2.10 Plot of the saturation magnetostriction versus NiFe composition. Taken from Bozorth [2.28].

The last two terms in Eq (2.13), the crystalline anisotropy energy  $E_{ca}$  and the magnetostatic energy (or demagnetization energy)  $E_D$ , describe the dependence of the total free energy on the direction of the magnetization with respect to lattice orientation and the shape of the sample, respectively.

Most magnetic materials have preferred magnetisation direction, which is called magnetocrystalline anisotropy or crystalline anisotropy. The electron spin is coupled to the electronic orbital (spin orbital coupling) and influenced by the local environment (crystalline electric field). Due to the arrangement of atoms in crystalline materials, magnetization along certain orientations is energetically preferred. Therefore magnetocrystalline anisotropy is closely related to the structure and symmetry of the material.

The magnetostatic energy, mentioned in section 2.2, can be referred to as shape anisotropy of the magnetic material. If a rod-shaped object is magnetized with a north pole at one end and a south pole at the other, the field lines emanate from the north-pole and end at the south-pole. Inside the material the field lines are oriented from the north-pole to the south-pole and hence are opposed to the magnetization of the material, since the magnetic moment points from the south pole to the north pole. Thus, the magnetic

field inside the material tends to demagnetize the material and is known as the demagnetizing field  $H_d$ . Stated formally, the demagnetizing field acts in the opposite direction from the magnetization  $M$  that creates it, and is proportional to it, namely

$$H_d = -N_d M \quad (2.17)$$

where  $N_d$  is the demagnetizing factor.  $N_d$  is dependent on the shape of the body, but can only be calculated exactly for an ellipsoid where the magnetization is uniform throughout the sample [2.16].

Magnetic field annealing is a process utilised in the fabrication of alloys to produce films with desirable hysteresis properties. The annealing field must be of sufficient strength to overcome the anisotropy energy, Eq (2.14), and align the magnetic moments along the field direction. A theoretical description of this process is outlined in section 4.4. However, the interactions of stress and shape anisotropy can destroy the induced film properties; therefore it is important to recall the anisotropy factors mentioned within this section.

Another parameter that affects the magnetic response of the material is the Curie temperature [2.28]. The Curie temperature is the temperature at which the exchange energy between magnetic moments becomes smaller than the thermal energy and ferromagnetic order disappears. Therefore the Curie temperature is the thermal limit of operation.

Examples of magnetic materials and a comparison of their main electrical and magnetic properties are given in the next subsection.

## **2.4 Magnetic materials for DC-DC converters operating in the MHz frequency range**

The point of reference for a discussion of magnetic materials for high frequency power applications is ferrite. Its high resistivity makes it desirable for high frequency applications as the high resistivity reduces eddy current losses to very low levels.

However it is not the most desirable material for microfabrication. The high sintering temperatures of standard high quality ferrites are difficult to combine with other steps of microfabrication techniques [2.29]. Eddy current losses in magnetic alloys can be controlled by using alloys in thin-film form. Furthermore ferrites can only be run at relatively low flux levels, because they have low saturation flux densities (less than 0.1T) and rapidly increasing hysteresis losses at frequencies near 1 MHz or higher [2.30]. Table 2.3 contains the details of various modern ferrite materials at high switching frequencies [2.31-2.35]. Magnetic alloys used in recording heads have saturation flux densities over 1T, and usually can be operated close to this level without a disproportionate loss penalty. The ability to handle high flux is important in any power application. However it becomes essential in a thin film microinductor or transformer device.

There are a variety of thin film magnetic alloys but probably the most common and best-understood alloy is permalloy, a NiFe alloy, in the range of about 79-82% Ni concentration [2.37-2.38]. Table 2.4 compares the properties of thin film permalloy to a typical MnZn power ferrite, Magnetics K. Perhaps the most important property is the hysteresis loss. Whereas in ferrite, this is a salient limitation, the hysteresis loss in NiFe films can be, in principle, zero with magnetic field annealing. This will be explained in detail in section 5.3. Permalloy has a saturation flux density of approximately 1.0 T at room temperature and due to the relatively high Curie temperature (500-520 °C) the saturation flux density degrades little at high temperature. It decreases 10% at 130°C an advantage compared to ferrites that typically have Curie temperature around 240°C leading to a decrease in saturation flux density of about 35% at the same temperature. NiFe has a resistivity of approximately  $20\mu\Omega\cdot\text{cm}$  and permeability similar to power ferrites. In terms of manufacture, NiFe can be deposited by electroplating allowing the substrate to be kept at a low temperature unlike the high sintering temperatures of ferrite.



Frequency	Material	Core loss, W/m <sup>3</sup> for various peak flux density, mT						
		200	100	80	60	40	20	10
100 kHz	Ferroxcube 3C96	370	45	22				
	Ferroxcube 3F4		200	100	40			
	Magnetics K	700	95	42	20	5		
200 kHz	Ferroxcube 3C96		170	95	42			
	Ferroxcube 3F4		430	230	100	30		
	Magnetics F	2000	380	200	95	30		
500 kHz	Ferroxcube 3C96		1400	800	380	135		
	Ferroxcube 3F4		1000	520	70			
	Magnetics K		900	410	180	42	5	
700 kHz	Magnetics F				1850	750	180	40
	Ferroxcube 3F4			2000	1000	350	53	
	Magnetics K			2050	950	250	30	4
1 MHz	Ferroxcube 3F4					2000	400	85
	Ferroxcube 3F45					1100	250	55
	Magnetics K					4200	500	70
3 MHz	Ferroxcube 3F4						2000	400
	Ferroxcube 3F45						1100	250
	Magnetics K						4200	500
5 MHz	Ferroxcube 4F1						1200	300
10MHz	Ferroxcube 4F1							850

Table 2.3 Core losses for various commercial ferrite materials [2.31-2.35]

Property	Nickel-Iron (NiFe)	Magnetics "K"
Hysteresis loss	Near Zero	30 W/cm <sup>3</sup> at 1 MHz 0.2T*
Resistivity	$20 \times 10^{-8} \Omega /m$	20 $\Omega/m$
Relative Permeability	2000	1500
$B_{sat}$	1 T	0.46 T
Bsat at High Temperature (130°C)	-10%	-35%
Useable flux density at High Frequency	1 T > 20 MHz*	40 mT at 1 MHz

Table 2.4 Properties of Permalloy, NiFe [2.15], and a Typical High Performance MnZn Power Ferrite (Magnetics K [2.36])

The desirable characteristics of magnetic core materials for power inductor and transformer components can be summarised as follows: high saturation flux density to obtain a high power density device; reasonable relative permeability, 100-2000, to obtain high inductance with reduced number of winding turns, limiting the contribution of winding loss due to short wire length; high core resistivity to reduce eddy current loss at high frequency; low hysteresis loss for improved efficiency; ease of deposition; and capability of integrated fabrication with ICs. The aforementioned material properties indicate the potential advantages of electroplated alloys versus ferrite. The disadvantage of the alloys in comparison to ferrite is low resistivity. Potential solutions to this problem in the form of deposition parameters and thin film lamination are investigated in Chapters 5, 6, 8 and 9.

## 2.5 Summary

The fundamental design equations, quantities and units have been introduced. The magnetic properties and behaviour of ferromagnetic materials has been outlined. Ferrite and thin film alloys have been compared and it is apparent that thin films have the necessary prerequisite to improve component efficiency. The limited operational flux density of ferrite and increasing hysteresis loss restricts further increases in frequency of operation. With limited flux density, <0.2T, relatively large core areas are required with reducing power density.

Eddy current loss is related to film resistivity and permeability, frequency of operation and volts per turn. Therefore, the ability to tailor the resistivity via lamination and permeability via magnetic field annealing is an advantageous benefit of thin films versus ferrite.

## References

- [2.1] P. Hammond, "Electromagnetism for Engineers," 4<sup>th</sup> edition, Oxford Science Publications, 1997.
- [2.2] D. Jiles, "Introduction to magnetism and magnetic materials," Chapman and Hall, 1991.
- [2.3] A. Aharoni, "Introduction to the Theory of Ferromagnetism," Oxford University Press, New York, 1996.
- [2.4] D. H. Lloyd., MAG-100A Unitrode Magnetics Design Handbook, 1999.
- [2.5] J. K. Watson, "Applications of Magnetism," John Wiley & Sons, 1980.
- [2.6] K.P. Ash, D. Wachenschwanz, C. Brucker, J. Oslon, M. Treka, and T. Jagielinski, "A magnetic head for 150 MHz, high density recording," IEEE Trans. On Magn., vol. 26, pp.2960-296, Nov. 1990.
- [2.7] M. Yamaguchi, K. Ishihara and K. I. Arai, "Application of thin film inductors and LC passive filters," IEEE Trans on Magn., vol. 29, no. 6, pp. 3222-3225, 1993.
- [2.8] H. T. Kim, S. J. Kim, S. H. Han, Hi Jung Kim, "Soft Magnetic Properties of permalloy multilayered films with ceramic intermediate layers," IEEE Trans. On Magn., vol. 31, no. 6, pp.4100-4102, Nov. 1995.
- [2.9] M. E. McHenry, "Amorphous and nanocrystalline materials for applications as soft magnets," Progr. Mater. Sci., vol. 44, no. 4, pp.291-435, Nov. 1999.
- [2.10] E. E. Kriezis and J. A. Tegopoulos, "Eddy Currents: Theory and Applications," Proc. IEEE, vol. 80, no. 10, pp. 1559-1589, Oct. 1992.
- [2.11] M. K. Kazimierczuk, G. Sancineto, G. Grandi, U. Reggiani, A. Massarini, "High frequency Small-Signal Model of Ferrite Core Inductors," IEEE Trans. Magnetics., vol. 35, no.5, pp. 4185-4189, Sept 1999.
- [2.12] J. W. Park and M. G. Allen, "Ultra low-profile micromachined power inductors with highly laminated Ni/Fe cores: Application to low-megahertz DC-DC converters," IEEE Trans. Magn., vol. 39, no. 5, pp. 3184-3186, Sept. 2003.
- [2.13] M. Brunet, T. O'Donnell, J. O'Brien, P. McCloskey, C. O'Mathuna, "Design Study and Fabrication Techniques for High Power Density Micro-Transformers", IEEE Applied Power Electronics Conf., pp. 1189-1195, 2001.
- [2.14] L. Daniel, C.R. Sullivan, "Design of microfabricated inductors", IEEE Trans on Power Electronics, vol. 14, no. 4, pp.709-723, July 1999.

- [2.15] C.R. Sullivan, S. R. Sanders "Design of microfabricated transformers and inductors for high-frequency power conversion", IEEE Trans on Power Electronics, vol. 11, no. 4, pp. 228-238, July 1997.
- [2.16] L. Sun, "Tuning the properties of magnetic nanowires," IBM J. RES & DEV. vol. 49, no. 1, Jan. 2005.
- [2.17] W. F. Brown, "Micromagnetics," Wiley, New York, 1963.
- [2.18] R. D. Cullity, "Introduction to Magnetic Materials," Addison- Wesley, Reading, MA, 1972.
- [2.19] W. Andra and H. Nowak, "Magnetism in Medicine," Eds., Wiley, Berlin, 1998.
- [2.20] A. R. Bausch, W. Moller, and E. Sackmann, "Measurement of Local Viscoelasticity and Forces in Living Cells by Magnetic Tweezers," Journal of Biophys., vol. 76, pp.573-579, 1999.
- [2.21] C. Haber and D. Wirtz, "Magnetic Tweezers for DNA Micromanipulation," Rev. Sci. Instrum., vol. 71, pp.4561-4570, 2000.
- [2.22] O. Kohmoto, "Recent Developments of thin film materials for magnetic heads," IEEE Trans. On Magn., vol. 27, pp.3640-3647, July 1991.
- [2.23] K.P. Ash, D. Wachenschwanz, C. Brucker, J. Oslon, M. Trcka, and T. Jagielinski, "A magnetic head for 150 MHz, high density recording," IEEE Trans. On Magn., vol. 26, pp.2960-296, Nov. 1990.
- [2.24] K. Tamura, E. Nagao, and Y. Ohdoi, "Development of a 48-turn thin film head," Journal of Applied Physics, vol. 67, pp.4857-4859, May 1990.
- [2.25] H. Schewe and D. Stephani, "Thin film inductive heads for perpendicular recording," IEEE Trans. On Magn., vol. 26(6):2966-2971, Nov.1990.
- [2.26] E. C. Stoner and E. P. Wohlfarth, "A Mechanism of Magnetic Hysteresis in Heterogeneous Alloys," IEEE Trans. Magn. 27, 3475-3518 (1991).
- [2.27] R. M. Bozorth, "Ferromagnetism," New York: IEEE Press, Reissue, 1993.
- [2.28] M. K. Senesky, "Electromagnetic Generators for Portable Power Applications," PhD thesis, UCLA, 2005.
- [2.29] E.C. Snelling, "Soft Ferrites, Properties and Applications," Butterworths, 2<sup>nd</sup> edition, 1988.
- [2.30] F. K. Wong, "High Frequency Transformer for Swicthing Mode Power Supplies," PhD thesis, Griffith University, Brisbane Australia, March. 2004.
- [2.31] Soft Ferrites and accessories, 2002 e-version, Ferroxcube/Philips Magnetics.
- [2.32] Magnetics Ferrites 2003, Magnetics, 2003.
- [2.33] MMG-Neosid Magnetic Components, MMG-Neosid, 1997.

- [2.34] Siemens Ferrites and Accessories Data Book 1990/91, Siemens, 1990.
- [2.35] Ferrite Cores, e-version, TDK Electronics Co., Ltd. 2002.
- [2.36] Magnetic Division of Spang and Co., Butler PA, Ferrite Cores, 1992
- [2.37] J. Mallinson, "Magneto-Resistive Heads-Fundamentals and Applications," Academic Press, New York (1996).
- [2.38] W. P. Taylor, "A NiFeMo Electroplating Bath for Micromachined Structures," Electrochemical and Solid-State Letters, vol. 2, pp.624-626, 1999.

## Chapter 3

### Literature review of power magnetic components

#### 3.1 Introduction

This chapter presents a literature review of power magnetic components. Section 3.2 builds on the overview of Faraday's law, Ampere's Law and Lenz's law and provides a more detailed description of inductor and transformer operation using equivalent circuit models. An introduction to Switch Mode Power Supply (SMPS) is presented in section 3.2. The operation of the most common forms of DC-DC converter, namely the buck, boost, buck-boost and flyback are described in section 3.3. The fabrication of conventional power magnetic devices is then preceded with a review of some of the most recent research activities and developments in state-of-the-art microscale magnetic components, section 3.4. Section 3.5 presents a summary of the deposition techniques for fabricating thin film alloys and presents the case for electrodeposition. Lastly, section 3.6 reviews the most recent high performance magnetic components.

#### 3.2 Basics of passive power inductive components

This section builds on the overview of Faraday's law, Ampere's Law and Lenz's law and provides a more detailed description of inductor and transformer operation using equivalent circuit models.

##### 3.2.1 Inductors

An inductor is a circuit element that consists of an electrically conductive wire commonly in the form of a coil. Coil-wound inductors usually possess a core around which the wires are wound; the type of core and winding geometry categorises them [3.1, 3.2]. The core material, reviewed in Chapter 2 for this particular application, is ferromagnetic. The basic operating principles of inductors are as follows: a current passing through a coil of wire will produce a magnetic field whose variation induces an electromotive force (emf) that opposes the field producing current. Thus, the coil tends to impede changes of current. The important parameters of inductors are reviewed briefly [3.3-3.5]. The inductance ( $L$ ) of inductors is defined as

$$L = \frac{\lambda}{i} \quad (3.1)$$

where  $\lambda$  is the flux linkage and  $i$  is time-varying current. Any inductor will have some direct current resistance,  $R_{DC}$ , and induces ohmic losses in its coils. When an alternating current is passed through the inductor, an additional resistance, called winding resistance  $R_{winding}$ , occurs from the skin effect inside the coils. As the core is also lossy, the resistance generated from hysteresis,  $R_{hysteresis}$ , eddy currents  $R_{eddycurrent}$ , and excess loss  $R_{residual}$  are present [3.6-3.8]. These losses can be explained by the impedance measured across the coils in response to AC sinusoidal excitation. The impedance of the inductor,  $Z_{inductor}$ , at any given frequency can be expressed as:

$$Z_{inductor} = R + j 2\pi f L \quad (3.2)$$

Where  $R$  is the real part of the impedance, which acts like resistance and contributes to power dissipation in the form of Joule heating;  $f$  is the frequency of the excitation, and  $L$  is the inductance. This single equivalent resistance ( $R$ ), which represents the sum of all losses in the inductor, is called the effective resistance  $R_{effective}$  of the inductor, and is expressed as [3.9]:

$$R_{effective} = R_{winding} + R_{core} \quad (3.3)$$

$$R_{core} = R_{eddycurrent} + R_{residual} + R_{hysteresis} \quad (3.4)$$

The quality factor, Q-factor, of an inductor is a measure of its relative losses and is defined as:

$$Q = \frac{X_L}{R_{effective}} = \frac{2\pi f L}{R_{effective}} \quad (3.5)$$

Where  $X_L$  is the reactance of the inductor. Here, both  $X_L$  and  $R_{effective}$  are functions of frequency. At low frequencies,  $X_L$  usually increases with frequency at a rapid rate, but at high frequencies  $X_L$  decreases rapidly due to the reduction of  $L$  by the eddy current, parasitic capacitance, and other effects. On the other hand, at low frequencies,  $R_{effective}$  increases with frequency at a slow rate due to a combination of effects from  $R_{winding}$  and



$R_{core}$ , and at high frequency  $R_{effective}$  increases at a rapid rate due to the dominant effects of  $R_{core}$ . Fig 3.1 displays the frequency response of the impedance of an ideal and practical inductor.

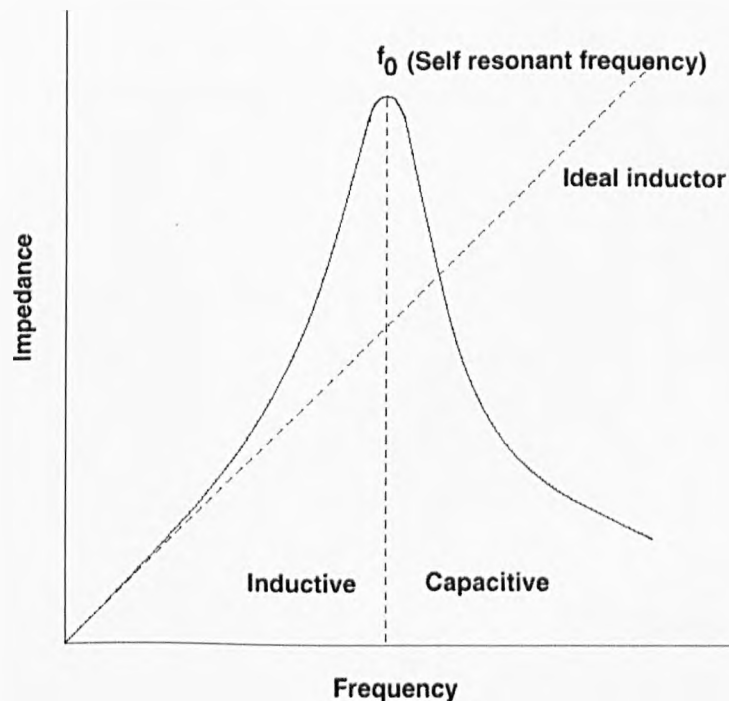


Figure 3.1 Frequency response of the impedance of an ideal inductor and a practical inductor.

In a real inductor, each turn of wire acts as a capacitor, and the combined effect of turn-to-turn and winding-to-core capacitance can be represented as a single capacitance, called distributed capacitance  $C_d$ , in parallel with the inductor. The parallel combination of inductance and distributed capacitance resonates at some frequency called the self-resonant frequency,  $f_o$ , (SRF). At this frequency the inductor will act as a pure resistor; beyond that frequency, the capacitive reactance becomes dominant. Therefore, a high self-resonance frequency is desirable in order to increase the operating frequency of the inductor. This can be achieved by reducing the distributed capacitance through careful winding design. The inductor equivalent circuit representing inductance, effective resistance, and distributed capacitance is shown in Fig 3.2 [3.1]. Therefore, Q usually increases with frequency at low frequency and decreases at high frequency. Figure 3.3 illustrates the Q-factor response of a practical inductor with frequency. A detailed analysis of Q can be found in Chapters 8 and 9.

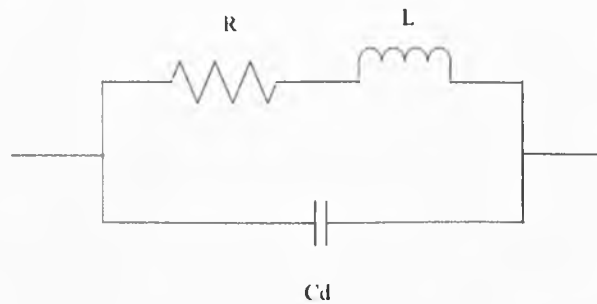


Figure 3.2 General equivalent circuit of an inductor

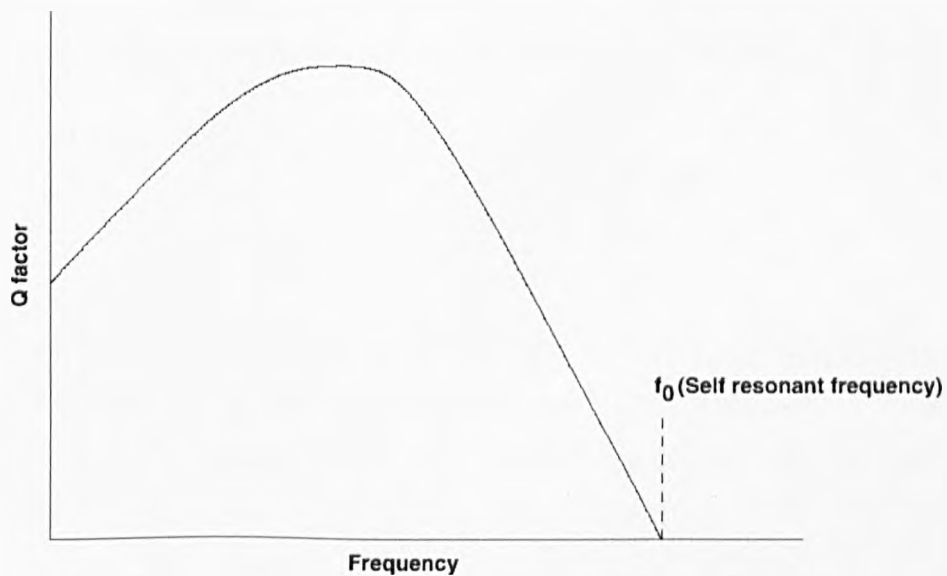


Figure 3.3 Q-factor response of a practical inductor with frequency

As the current through the coil of the inductor is increased, the flux density within the core increases until saturation is reached, at which point the inductance decreases. Once the core starts saturating, the inductance drops off rapidly with further increase in current. DC saturation current,  $I_{80\%}$ , is generally defined as the current at which the inductance value falls by 20% of the original inductance value from the measured inductance without the applied DC current [3.10].

The power density of an inductor in a switching mode power supply is an important parameter. This value can be determined via the magnetic energy stored in an inductor in a steady magnetic field [3.11]. An alternative method is via Faraday's law;

$$V = L \frac{di}{dt} \quad (3.6)$$

With,  $V$ , the induced voltage across the component, and  $\frac{di}{dt}$  the time varying current through the inductor windings. Taking the integral of each side of Eq (3.6), this becomes;

$$VT = LI \quad (3.7)$$

With the interval,  $T$ , being proportional to the inverse of the frequency;

$$T = \frac{1}{f} \quad (3.8)$$

With known values of inductance,  $L$ , and applied current,  $I$ , the induced voltage at a particular frequency of operation can be calculated. The optimal output power can be obtained through the measurements of  $V_{out}$  and  $I_{out}$ , output voltage and current, respectively:

$$P = V_{out} \times I_{out} \quad (3.9)$$

In order to determine the efficiency of the device, the dissipation of power due to core loss and winding loss must be calculated. The power loss due to residual loss,  $R_{residual}$ , is negligible within the frequency range under consideration [3.6]. Therefore core loss is considered as the sum of the hysteresis and eddy current loss. Through the calculated winding resistance,  $R$ , and known applied current, the power loss due to the windings,  $P_{Cu}$ , can be found:

$$P_{cu} = I^2 R \quad (3.10)$$

The overall efficiency,  $\eta$ , of the microinductor is then given by:

$$\eta = \frac{P_{out}}{(P_{out} + P_{core} + P_{Cu})} \quad (3.11)$$

### 3.2.2 Transformer

Transformers are inductors that are coupled by a shared magnetic circuit, that is, two or more windings that link some common flux, shown in Fig 3.4. The input current flowing through the primary winding generates a time varying magnetic flux, and this time varying flux will induce an output voltage coming out from the secondary winding of the transformer [3.11-3.17].

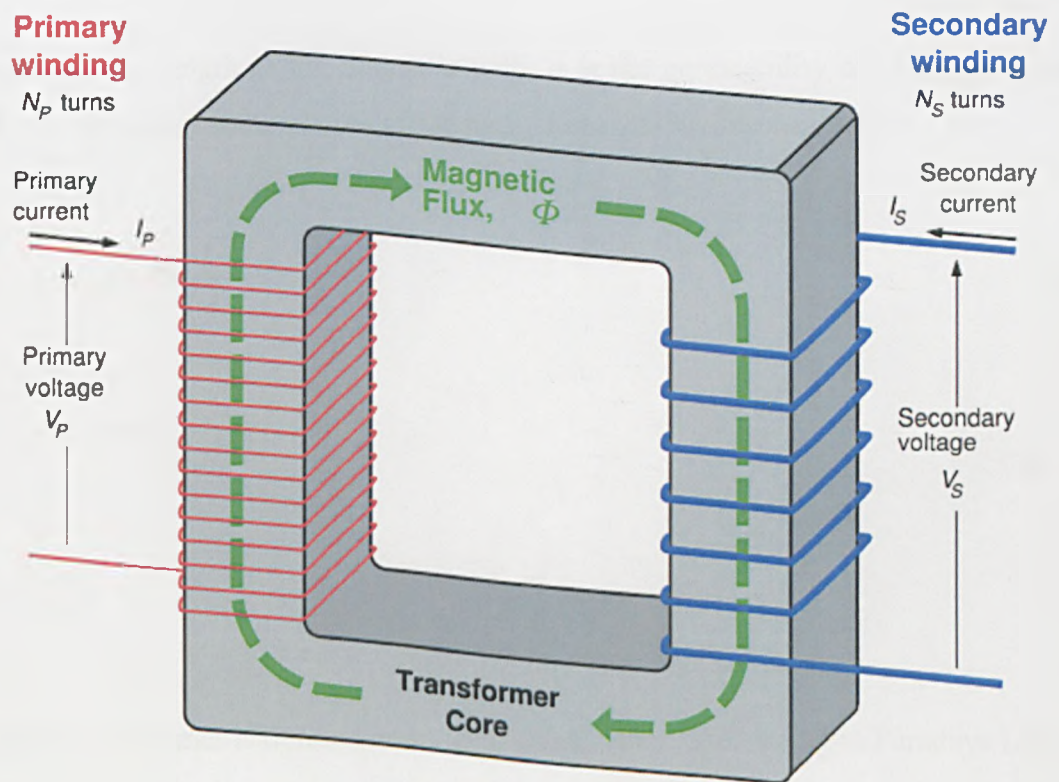


Figure 3.4 Schematic Diagram of a Transformer

A transformer is an alternating-current device that transforms voltages, currents, and impedances. For the closed path in the magnetic circuit, shown in Fig 3.4, traced by magnetic flux, the magnetic circuit can be expressed as:

$$N_p i_p - N_s i_s = \Phi \mathfrak{R} \quad (3.12)$$

Where  $\Phi$  is the magnetic flux,  $\mathfrak{R}$  is the reluctance for the magnetic path,  $N_p i_p$  and  $N_s i_s$  are the number of turns and the current in the primary and secondary windings, respectively.

According to Lenz's law, the induced magnetomotive force (mmf) in the secondary winding, opposes the flow of the magnetic flux created by the mmf in the primary winding [3.18]. The reluctance is defined as,

$$\mathfrak{R} = \frac{l}{\mu A_c} \quad (3.13)$$

Where  $l$  is the length of the magnetic path,  $\mu$  is the permeability of the core material, and  $A_c$  is the cross sectional area of the path. Substitution into Eq (2.4):

$$N_p i_p - N_s i_s = \Phi \frac{l}{\mu A_c} \quad (3.14)$$

If  $\mu \rightarrow \infty$ , then

$$\frac{i_p}{i_s} = \frac{N_s}{N_p} \quad (3.15)$$

And this transformer is defined as an ideal transformer. According to Faradays Law,

$$v_p = N_p \frac{d\Phi}{dt} \quad (3.16)$$

$$v_s = N_s \frac{d\Phi}{dt} \quad (3.17)$$

then the ratio of the voltages across the primary and secondary windings of an ideal transformer is equal to the turns ratio, i.e.

$$\frac{v_p}{v_s} = \frac{N_p}{N_s} \quad (3.18)$$

The coefficient of coupling, which is dependent on the portion of the total flux lines that cuts both primary and secondary windings, is defined as:

$$K = \frac{L_{ps}}{\sqrt{L_{sp}L_{ss}}} \quad (3.19)$$

Where  $L_{ps}$  is the mutual inductance,  $L_{sp}$  is the primary self-inductance and  $L_{ss}$  is the secondary self-inductance. The coupling coefficient is equal to 1, if  $L_{ps} = \sqrt{L_{sp}L_{ss}}$ , this would only occur if there were no leakage inductance. The model of an ideal transformer is shown in Fig 3.5.

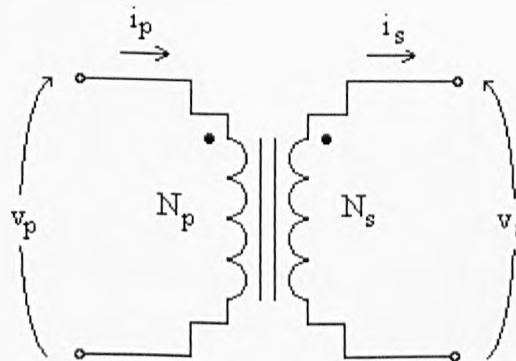


Figure 3.5 Model of an ideal transformer

A practical model of a transformer is shown in Fig 3.6. In a practical transformer, there are some additional elements, such as primary leakage inductance, secondary leakage inductance, equivalent magnetising inductance of primary, primary winding resistance, secondary winding resistance, and equivalent resistance corresponding to core losses.

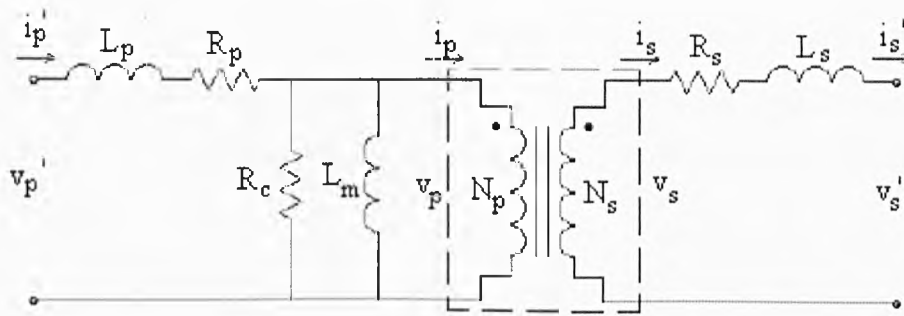


Figure 3.6 Model of a practical transformer

The voltages of the practical transformer can be expressed as:

$$v'_p = L_{sp} \frac{di'_p}{dt} - L_{ps} \frac{di'_s}{dt} \quad (3.20)$$

$$v'_s = L_{ps} \frac{di'_p}{dt} - L_{ss} \frac{di'_s}{dt} \quad (3.21)$$

The coefficient of coupling,  $K$ , is less than 1, as  $L_{ps} < \sqrt{L_{sp}L_{ss}}$ .

For high frequency applications the equivalent circuit of a transformer becomes more complex with the consideration of parasitic capacitances. Fig 3.7 shows the equivalent circuit of a high frequency transformer.

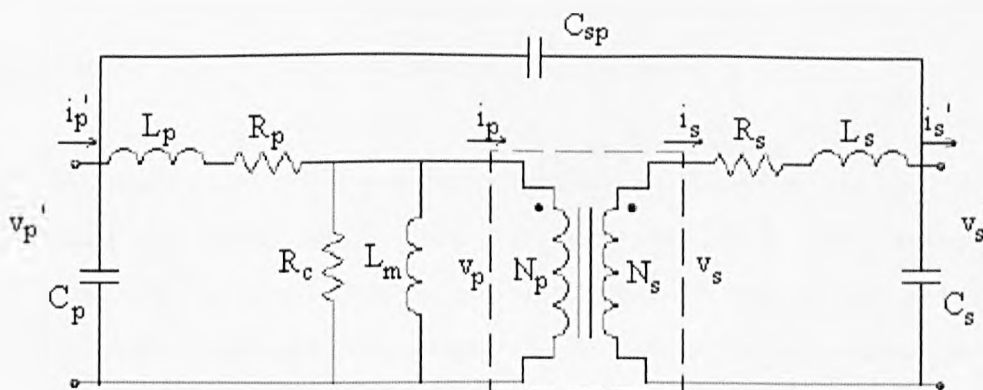


Figure 3.7 Equivalent circuit of a high frequency transformer

$C_p$ ,  $C_s$  and  $C_{sp}$  are the primary shunt and distributed capacitor, secondary shunt and distributed capacitor, and primary to secondary inter-winding capacitance, respectively. As with the inductor the power density of the transformer can be determined via Eq (3.11).

In summary, inductors and transformers operate based on the same fundamental principles. Both incur DC winding resistance and induced AC resistive losses, emanating from the winding and core, parasitic capacitance and leakage inductance as a result of the winding configuration. Even though the focus of this thesis is on the design of magnetic components, effective design requires an understanding of the application that is considered in the following section.

### **3.3 Introduction to switch mode power supplies**

A switch mode power supply (SMPS) is an electronic power supply unit that incorporates a switching regulator. The switching regulator is an internal control circuit that switches the load current rapidly on and off in order to stabilise the output voltage. Dependent on the output waveform, SMPS are categorized under one of the four headings [3.19-3.21];

- (1) AC-DC also called rectifier;
- (2) DC-DC or DC-DC converter;
- (3) AC-AC or frequency changer,
- (4) DC-AC or inverter.

There are two main types of regulated power supplies available, SMPS and linear. The advantages and disadvantages are summarized as follows;

- (1) *Size and weight*: linear power supplies use a transformer operating at the mains frequency 50/60 Hz. This component is larger and heavier than the corresponding transformer of the SMPS, which operates at a higher frequency.
- (2) *Efficiency*: linear power supplies regulate their output by using a higher voltage in the initial stages and then expending some of it as heat to improve the power quality. This power loss is necessary to the circuit. Resulting in a typical efficiency of 30%-60%. SMPS draw current at full voltage based on a variable



duty cycle, and can increase or decrease their power consumption to regulate the load as required. Consequently, a well designed SMPS will be more efficient.

- (3) *Heat/power dissipation*: A linear supply must generate more heat to power the same electrical load. Therefore, a SMPS will produce less heat.
- (4) *Electronic noise*: SMPS generally do have noisier outputs than linear PSUs; this is due to their higher frequency of operation.

SMPS are the current state of the art in high efficiency power supplies. Conventional series-regulated linear power supplies maintain a constant voltage by varying their resistance to cope with input voltage changes or load current demand changes. The linear regulator can, therefore, be very inefficient. The SMPS, however, uses a high frequency switch with varying duty cycle to maintain the output voltage. The output voltage variations caused by the switching are filtered out by an LC filter.

In general, there are four different types of magnetic components for the typical SMPS. They include the output transformer, output inductor, input inductor and the current sense transformer.

1. *The output transformer or "main" transformer* takes the input voltage that is supplied to its primary winding and then transforms the input voltage to one or more voltages that are the output of the secondary winding or windings.
2. *The output inductor* is used to filter the output voltage so that the load "sees" a filtered DC voltage.
3. *The input inductor* filters out the noise generated by the switching transistors so that this noise is not transmitted back to the source.
4. *The current sense transformer* is used to help regulate the SMPS so that when the load changes, the SMPS adjusts the power it is delivering to the load accordingly.

The work in this thesis does not focus on a specific type of transformer or inductor but aims to improve the primary functions of these components; maximise power density and efficiency, optimise the achievable inductance for a minimal component foot-print.

DC-DC converters are important in portable electronic devices, such as mobile phones, laptops, and satellites, which are supplied with power from batteries. Such devices often contain sub-circuits that require varying levels of voltage from those supplied by

the battery. Additionally, the battery voltage declines as its stored power is drained. DC-DC converters offer a method of generating multiple controlled voltages from a single variable battery voltage, thereby saving space instead of using multiple batteries to supply different parts of the device. An overview of four configurations of DC-DC converter is provided in section 3.3.1.

### 3.3.1 DC-DC converter configurations

DC-DC converters convert one DC voltage level to another by applying a DC voltage across an inductor, or transformer, for a period of time which causes current to flow through it and store energy magnetically, Eq (3.22).

$$E = \frac{1}{2}LI^2 \quad (3.22)$$

Where  $E$  is the stored energy,  $L$  is the inductance and  $I$  is the applied current.

When the current flow is constant, an ideal inductor has no effect on the circuit other than to store energy in the magnetic field in the inductor, illustrated in Fig 3.8.

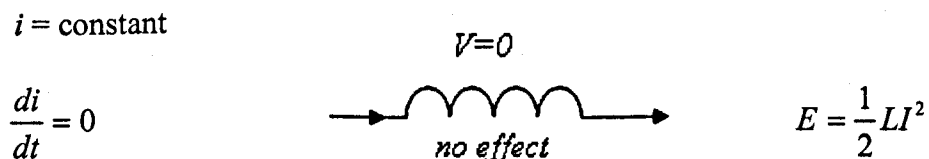
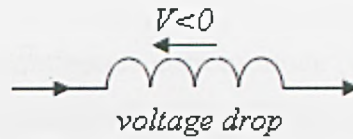


Figure 3.8 Inductor response to constant current

Whenever the current is increasing, an inductor acts like a choke in that it impedes the flow of current by producing a back emf, Fig 3.9. In this case the inductor acts like a resistance in a circuit in that it causes a voltage drop across the inductor. Some of the energy of the current goes into creating a magnetic field in the inductor.

$i = \text{increasing}$

$$\frac{di}{dt} > 0$$



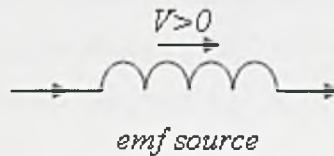
$E$  increases

Figure 3.9 Inductor response to increasing current

Whenever the current is decreasing, an inductor acts like a source of emf, Fig 3.10. The energy in the magnetic field is converted to a positive potential creating an additional current flow.

$i = \text{decreasing}$

$$\frac{di}{dt} < 0$$



$E$  decreases

Figure 3.10 Inductor response to decreasing current

Transformers replace inductors when multiple outputs or isolations between the source and the load are required. Multiple secondary windings with the required turns-ratio can provide the various outputs.

The variation of the current being applied or removed by the switch leads to the introduction of converter duty cycle. Duty cycle is the pulse duration divided by the pulse period and is shown in Fig 3.11. For a pulse train in which the pulse duration is  $1\mu\text{s}$  and the pulse period is  $4\mu\text{s}$ , the duty cycle is 0.25.

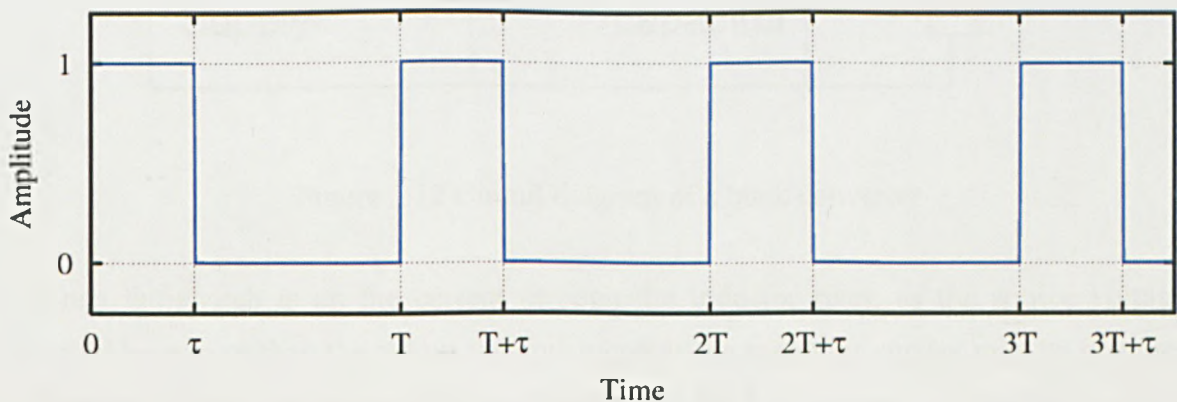


Figure 3.11 The duty cycle is defined as the ratio between the pulse duration and the period ( $T$ ) of a rectangular waveform.

All converters can operate in continuous current mode (CCM) or discontinuous current mode (DCM) [3.11]. In CCM the current through the inductor never falls to zero. In some cases the amount of energy required by the load is small enough to be transferred in a time lower than the whole commutation period. In this case, the current through the inductor falls to zero during part of the period and is termed DCM. The only difference in comparison to CCM is that the inductor is completely discharged at the end of the cycle. Chapter 6 highlights from a design perspective the impact of mode of operation on inductor geometry.

The various topologies of DC-DC converter can generate voltages higher, lower, higher and lower or negative of the input voltage [3.21]. Four fundamental topologies are the buck, boost, buck-boost and flyback converters. The operations of these converters are explained in sections 3.2.1.1-3.2.1.4.

### 3.3.1.1 Buck converter

The circuit for the buck converter is shown in Fig 3.12. The buck converter consists of an inductor and two switches (usually a transistor and a diode) that control the inductor. The switch alternates between connecting the inductor to source voltage to store energy in the inductor and discharging the inductor into the resistor, the load.

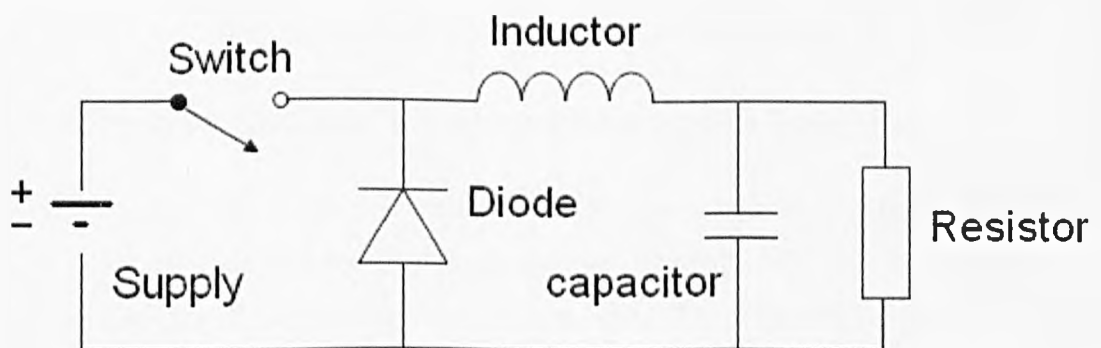


Figure 3.12 Circuit diagram of a buck converter

When the switch is on the current through the inductor rises, as the source voltage would be greater than the output voltage, whereas the capacitor current may be in either direction, depending on the inductor current and the load current. When the inductor current rises, the energy stored in it increases. During this state, the inductor acquires energy. When the switch is off and the diode is on the inductor current free-wheels

through the diode and the inductor supplies energy to the RC network at the output. The energy stored in the inductor falls in this state. In this state, the inductor discharges its energy and the capacitor current may be in either direction, depending on the inductor current and the load current. When it has discharged all its energy, its current falls to zero and tends to reverse, but the diode blocks conduction in the reverse direction. In this state both the switch and diode are off, the capacitor discharges its energy and the inductor is at rest, with no energy stored in it. The inductor does not acquire energy or discharge energy in this state.

### 3.3.1.2 Boost converter

The circuit for the boost converter is shown in Fig 3.13. A boost converter is a power converter with an output DC voltage greater than its input DC voltage.

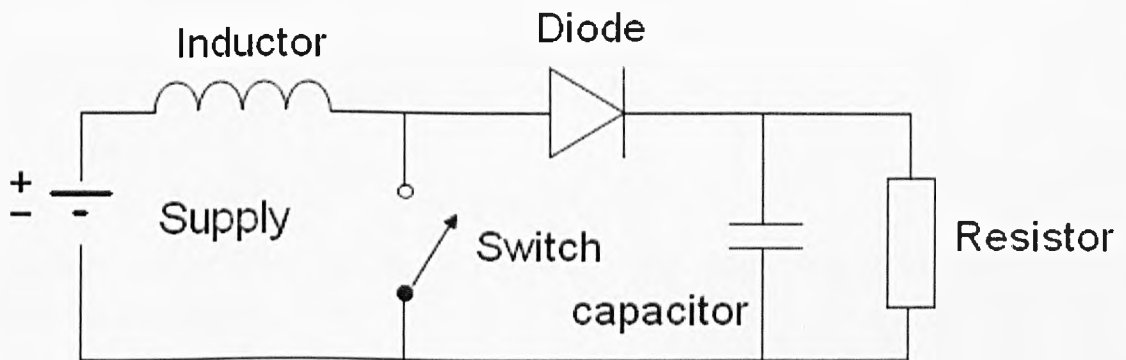


Figure 3.13 Circuit diagram of a boost converter

The basic operation principle of a boost converter consists in 2 distinct states:

- (1) In the on-state, the switch is closed, resulting in an increase in inductor current.
- (2) In the off-state, the switch is open and the only path offered to inductor current is through the diode, the capacitor, and the load (R). This results in transferring the energy accumulated during the on-state into the capacitor.

### 3.3.1.3 Buck-boost converter

The buck-boost converter is a type of DC-DC converter that has an output voltage magnitude that is either greater than or less than the input voltage magnitude. It has a similar circuit topology to the boost converter and the buck converter. The output voltage is based on the duty cycle of the switch. The converter is shown in Fig 3.14.

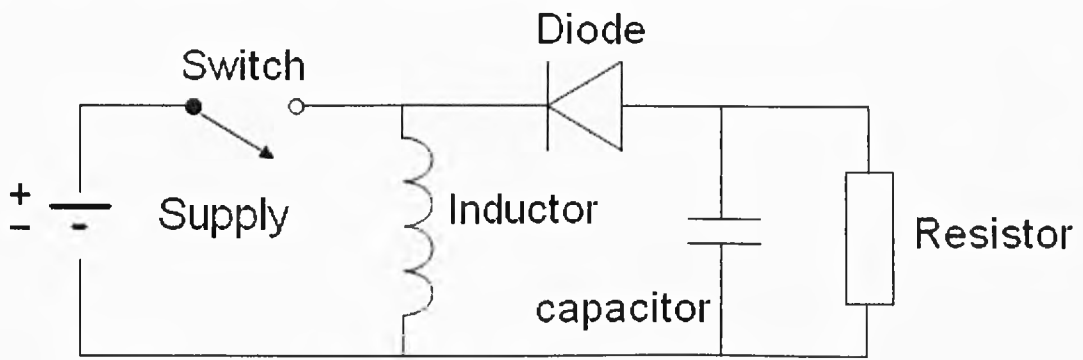


Figure 3.14 Circuit Diagram of the buck-boost converter

The operating principles of the buck-boost converter are as follows:

- (1) In the on-state, the input voltage source is directly connected to the inductor. This results in accumulating energy in the inductor. In this stage, the capacitor supplies energy to the output load.
- (2) In the off-state, the inductor is connected to the output load and capacitor, such that energy is transferred from the inductor to the capacitor and to the load resistor.

Compared to the buck and boost converters, the characteristics of the buck-boost converter are mainly:

- (1) Polarity of the output voltage is opposite to that of the input
- (2) The output voltage can vary continuously from 0 to  $-\infty$ , for an ideal lossless converter.

#### 3.3.1.4 Flyback converter

The previous converters have all utilised an inductor but the role of a transformer in DC-DC converters has not yet been demonstrated. In many DC-DC applications, multiple outputs are required and output isolation may need to be implemented depending on the application. The flyback converter, which is an adaptation of the buck-boost converter, is used for this purpose; the circuit diagram is shown in Fig 3.15.

As mentioned in section 3.2.3 the buck-boost converter works by storing energy in the inductor during the on phase and releasing it to the output during the off phase. With the transformer the energy storage is in the magnetisation of the transformer core. If increased energy storage is required an air gap is included in the core. The output of the ideal transformer depends on the turns-ratio. All transformers provide DC isolation

between isolated windings. Specific isolation transformers also include shielding and tailored winding configurations to prevent capacitive coupling between the windings. Capacitive coupling can carry high frequency noise from the primary to the secondary and vice versa [3.22].

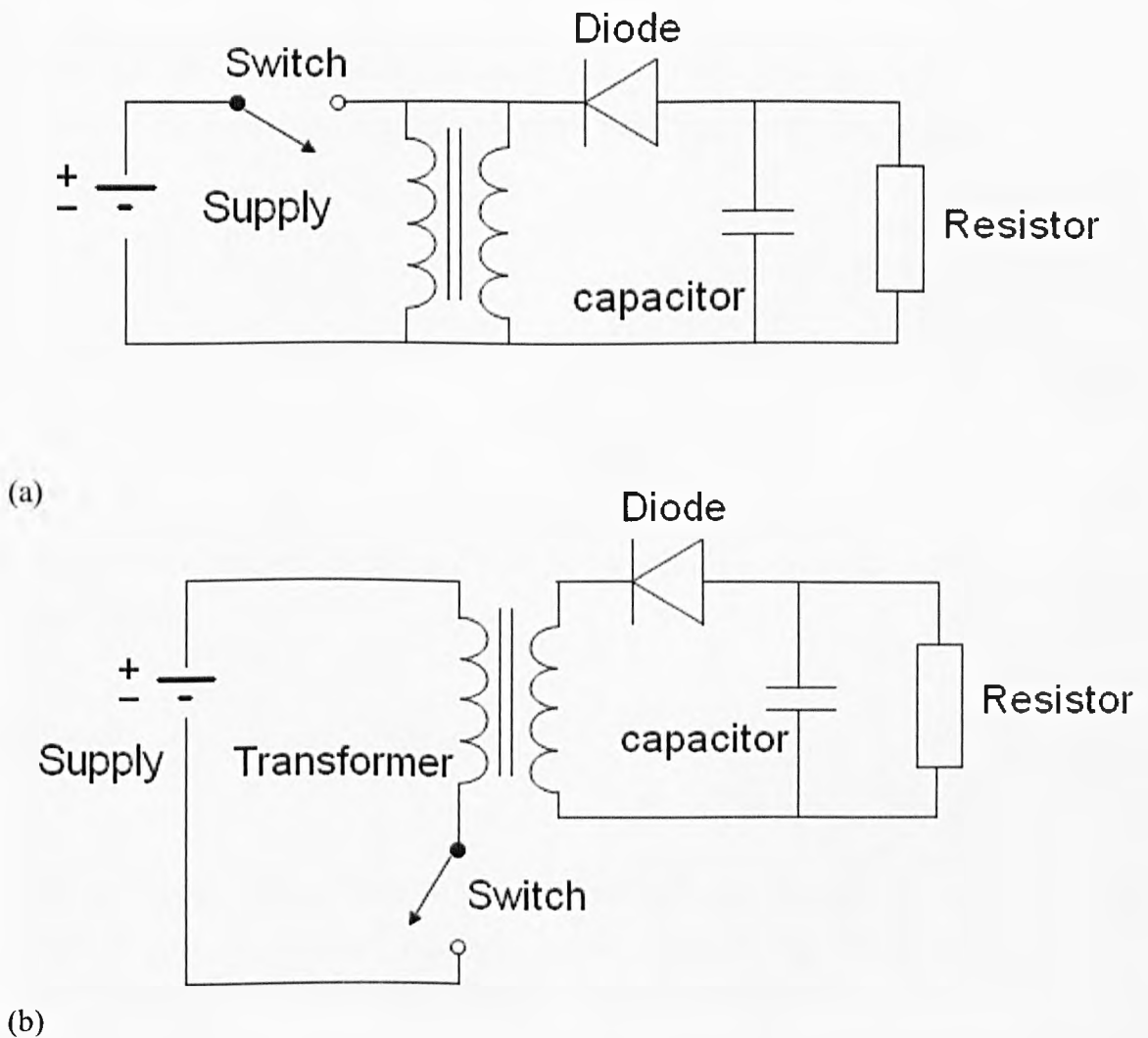


Figure 3.15 Flyback converter (a) The inductor of the buck-boost converter is replaced with a transformer, (b) the isolated output is achieved by removing the common reference of the input and output circuits.

Overviews of four basic DC-DC converters have been presented. The transformer and inductor within the converters are typically the largest components on the printed circuit board (PCB). The effect of increased switching frequency on the size of these magnetic components is discussed in section 3.3.2.

### 3.3.2 Frequency effect on passive components

The correlation between the physical size of a converter inductor and its switching frequency is as follows:

Size is a function of inductance. The inductance value of an inductor is a function of the component physical parameters, Eq (3.23). The number of turns, magnetic path length and core cross-sectional area is dependent on the inductance required. Therefore the area of the component is decreased with a reduction in the required inductance.

$$L = \frac{\lambda}{i} = \frac{N\Phi}{i} = \frac{NBA}{i} = \frac{NA}{i} \mu_o \mu_r \frac{Ni}{l}$$
$$L = \frac{\mu_o \mu_r N^2 A_c}{l} \quad (3.23)$$

The inductance required to produce a voltage is inversely proportional to the switching frequency. For a given current and voltage the required inductance is determined from Faradays Law.

$$V = L \frac{di}{dt} \quad (3.24)$$

Where,  $dt$  is the off-time and  $di$  is the ripple current going through the inductor. Ripple current is normally fixed in a design as a certain percentage of the full-load output current, typically 5%. Rearranging Eq (3.23) for the inductance;

$$L = V \frac{dt}{di} \quad (3.25)$$

For a given ripple current and output voltage  $V$ , the focus moves to bringing down the necessary value of  $L$  by reducing the off-time  $dt$  via a shorter switching period. Therefore, a decrease in the switching period, increase in the frequency, is the mathematical key to reducing the required inductance. The reduction in transformer size is also demonstrated by Faraday's Law;



$$V = N \frac{d\Phi}{dt} \quad (3.26)$$

In a different form:

$$VT = NA_c B \quad (3.27)$$

Rearranging Eq (3.27);

$$NA_c = \frac{VT}{B} \quad (3.28)$$

Therefore the area of the component can be traded off against the number of turns. Eq (3.28) also highlights the advantage of operating at increased flux density.

### 3.4 Fabrication of power inductive components

The power level, 1-20W, that micromachined inductive components need to handle is approaching that of low-power conventional magnetic components in order to meet the power requirements of compact power applications. This implies that some of the technologies utilised in the manufacture of conventional devices could effectively be combined with micro-machining technologies to realize micro-machined devices. Within this section, a general overview of conventional fabrication is presented followed by suitable micro-machining approaches.

#### 3.4.1 Review of conventional fabrication

Conventional transformers and inductors consist of a wound bobbin and magnetic core. A typical example of their assembly is illustrated in Fig 3.16. There are various core structures that can be utilised such as toroidal, U and C shaped cores, E cores etc [3.23, 3.24], examples of which are displayed in Fig 3.17. If the core is not toroidal and consists of more than one segment i.e. EI, ER, the core will require assembly with either a clip or high temperature glue. Cost comparisons between clipping and gluing are complex and involve numerous factors such as material cost, manual labour, curing and batch processing of glued parts, repair-ability etc. In a high-volume production

environment clipping can be automated and typically turns out to be the more cost-effective solution.

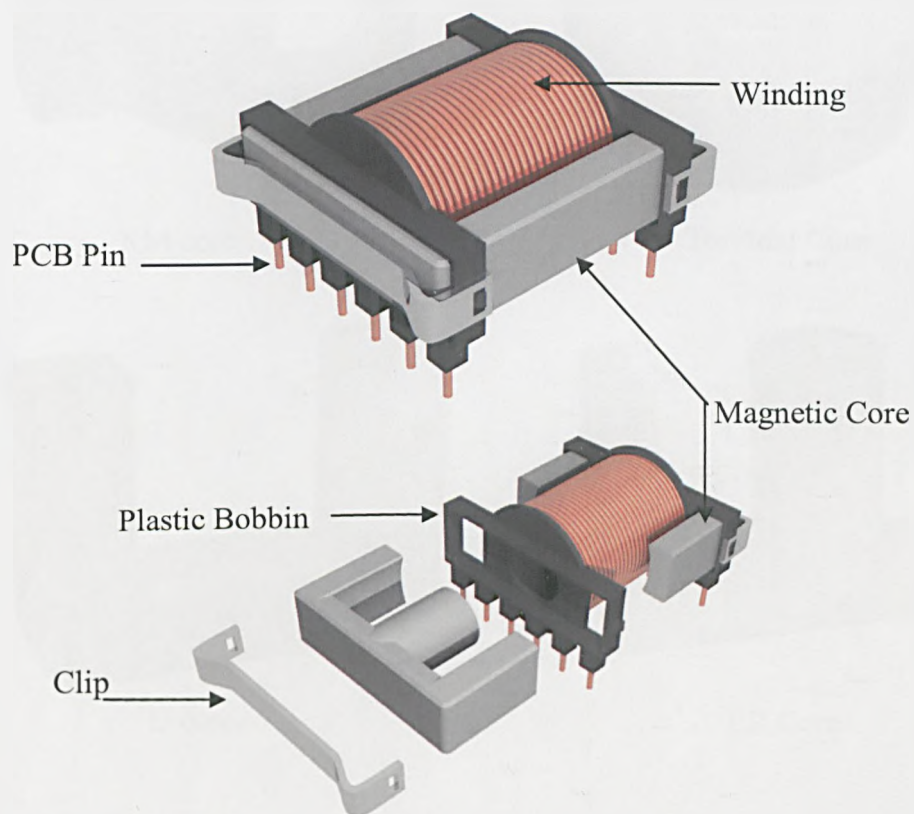
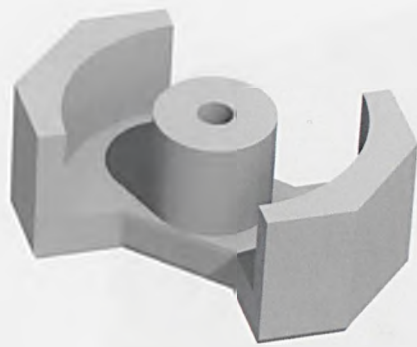


Figure 3.16 Construction of an inductor using two ER cores, a plastic bobbin and two clips. The bobbin has pins to be soldered to a printed circuit board (PCB).

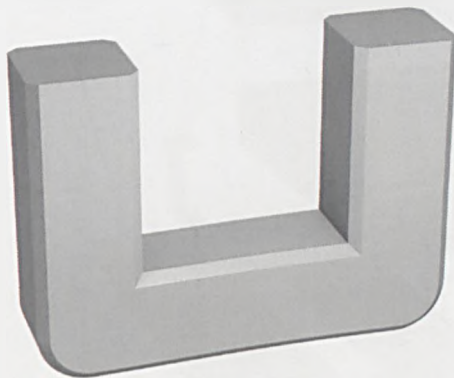
The windings are typically hand wound insulated cylindrical copper wire. The components can be integrated as stand alone components that are “off-the-shelf” or tailored for a particular application. The drive towards higher power densities and overall lower profile in switch mode power supplies has however exposed a number of limitations in the use of these conventional magnetic structures. As mentioned in Chapter 1, to achieve higher power densities an increase in the converter switching frequency was necessary to achieve passive component size reduction. The increase in frequency has led to a problem of increased winding loss due to the skin and proximity effects in the round conductors particularly at frequencies above 100 kHz.



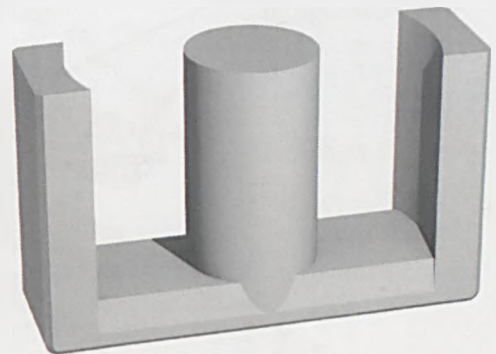
RM core



Toroidal Core



U core



ER Core

Figure 3.17 Examples of core geometries commonly utilised in wound magnetic components.

Planar magnetics emerged as a solution to the problem of increased winding loss and reduced profile. The base elements of a planar magnetic assembly consist of a low-profile core set, thin printed-circuit-board (PCB) windings and mechanical hardware to secure the PCBs in the core set and to hold the core pieces together. Fig 3.18 is an exploded view of a typical planar transformer using E-I style cores. Flexible circuits, copper and Kapton laminates, and stamped-copper foils are other popular techniques for planar magnetic construction [3.25].

The earlier applications of planar magnetics demonstrated the use of flat wide conductors to reduce skin and proximity losses in windings (compared to round wire) [3.26-3.29], and illustrated the control of other parasitics such as leakage inductance. The repeatability of component characteristics also proved of considerable importance, particularly for use in resonant topologies being used for converters switching in the 1-10 MHz range [5, 6]. The main advantages of planar components are summarised within Table 3.1[3.30-3.34].



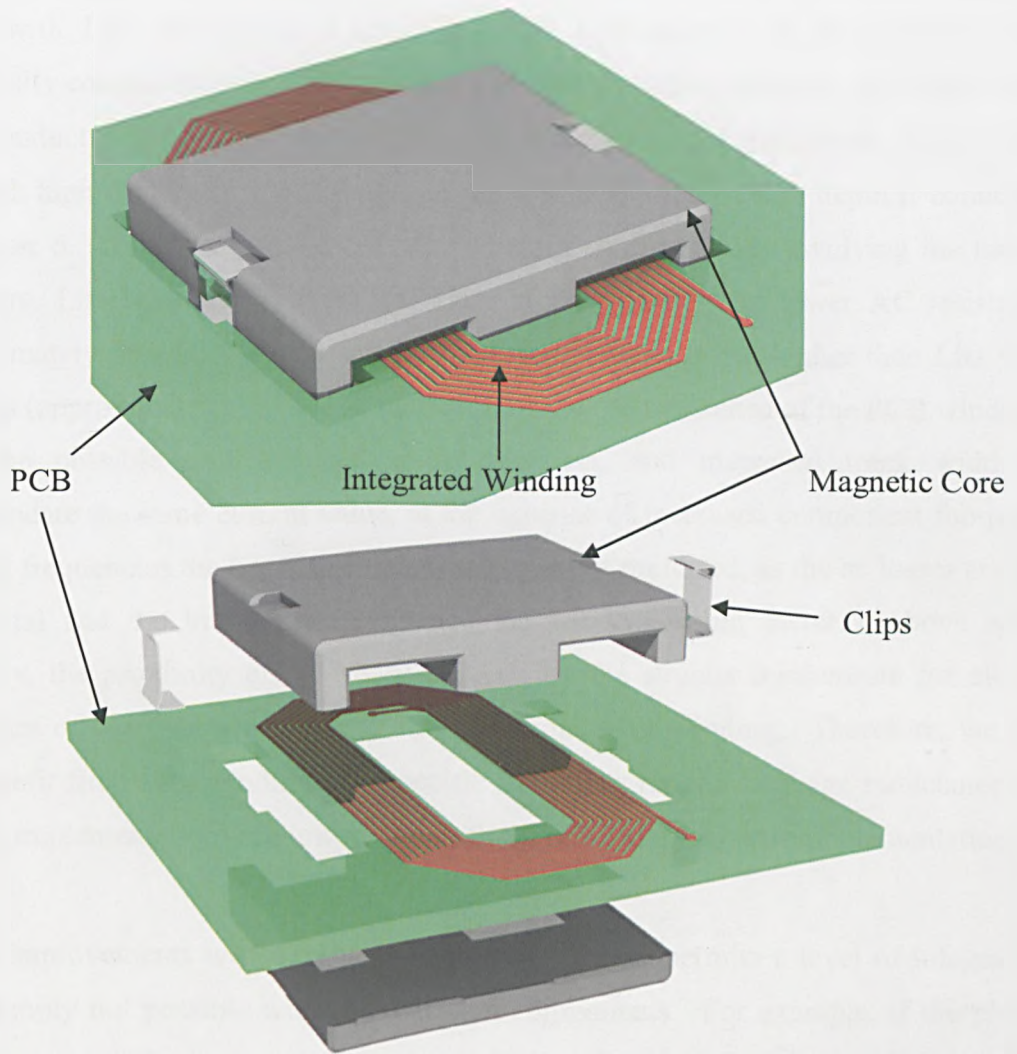


Figure 3.18 Planar magnetic component. The windings are fabricated within the PCB enabling a reduction in high frequency winding loss and reduced component profile in comparison to wire wound bobbin components.

Planar magnetic advantages	Description
High Power Density	Higher surface area to volume ratio than conventional components
High Current Capability	200A per PCB layer winding
High Efficiency	Typically 98% for most medium power designs
Good thermal Conduction	Greater surface area for thermal transfer
Low Leakage Inductance	Interleaving of windings
High Parameter Repeatability	Precise fabrication
Low EMI Emission Possible	Closed core designs with internal winding shield
Application Frequency Range	20kHz-2MHz

Table 3.1 Advantages of planar magnetic components

To reduce increases in winding resistance conventional components are sometimes wound with Litz wire [3.11, 3.35-3.37]. Litz wire consists of many thin wires, individually coated with an insulating film and braided, thus increasing the surface area of the conductor and thereby reducing the skin effect and associated power losses when used with high-frequency applications. A detailed definition of skin depth is contained in Chapter 6. In an analysis of different winding configurations involving the use of solid wire, Litz wire and PCB at 500 kHz, PCB windings had lower AC resistance (approximately 85 - 90 %) than similar solid wire windings but higher than Litz wire windings (approximately 115%). A reduction in the AC resistance of the PCB windings would be possible with reduced track thickness, and increased track width to accommodate the same current value, at the expense of increased component footprint. At lower frequencies the benefit of Litz winding is not preferred, as the ac losses are not detrimental and the braided wires reduce the window-filling factor. Above some frequency, the proximity effect losses induced by the strands compensate for all the advantages of the Litz winding over the solid conductor winding. Therefore, we can only benefit from Litz winding in a specific frequency range. Leakage inductances of the PCB implementations are lower than both the solid and Litz wire implementations.

Despite improvements with Litz wire, planar fabrication permits a level of integration that is simply not possible with conventional components. For example, if the planar magnetic is to be mounted to a user motherboard with other electronics, it often becomes very cost-effective to place the windings of the magnetic in the layers of the motherboard rather than an external multi-layer PCB to house the windings. Compared to their conventional wire-wound counterparts, PCB planar magnetic components can lead to a significant reduction in size while still meeting international safety standards.

Planar magnetics have however some drawbacks. Although improving thermal performance, planar magnetics have larger footprint area. The fact that windings can be placed close together thus reducing leakage inductance has the usually unwanted effect of increasing parasitic capacitance. The repeatability of characteristics obtained from PCB windings also comes at the price of having a greater portion of the winding window filled with dielectric material, thus reducing copper fill factor and limiting the number of turns. The window utilization factor can be quite low (typically 0.25 – 0.3 compared to 0.4 for conventional magnetics) due to a typical inter-turn spacing of 150  $\mu\text{m}$  and minimum dielectric thickness of 100  $\mu\text{m}$ . In summary, planar magnetic components have superseded conventional magnetic components for high frequency,

high power density, low profile DC-DC converter applications. The following section introduces the typical magnetic core materials utilised in wire wound and planar magnetic components.

#### **3.4.1.1 Review of conventional core materials**

Magnetic components are typically comprised of metal alloy tape wound cores, composite powdered cores and ferrite cores [3.11]. Metal alloy tape wound cores, using alloys such as nickel-iron, exhibit high relative permeability of 60,000, high saturation flux density (0.9 T) and insignificant energy storage. Unfortunately, the resistivity of these metal alloys is quite low, normally  $\leq 20\mu\Omega\text{cm}^2$ . To minimise losses due to induced eddy current, these cores are built up with very thin tape wound laminations typically  $\geq 15\mu\text{m}$ . These thin tapes are normally fabricated via a rapid solidification and cold rolling process [3.38-3.40].

Tape wound core applications are for 50, 60 and 400 Hz frequencies. At today's SMPS frequencies ( $\geq 100$  kHz), eddy current losses are too great even with extremely thin tape thickness. However, in SMPS filter inductor applications, gapped tape-wound cores are sometimes used. With their properties suited to low frequency applications they are normally included within conventional wire wound components.

Powder cores are made in three varieties: molypermalloy, high flux and KOOL MU. The manufacturing process is similar for all three types. An alloy material is first ground to a fine powder. The powder is mixed with an insulating material that separates each particle from the next, thus increasing resistivity. The powder is then pressed into toroidal shapes; the cores are then annealed and painted.

Composite powdered-metal cores, such as powdered iron, Kool M $\mu$ , and permalloy powdered cores do store considerable energy, and are therefore used in inductor and flyback transformer applications. However, energy is not stored in the very high permeability magnetic metal portions of the composite, but in the non-magnetic regions between the magnetic particles – in the binder that holds the cores together. Essentially, these composite cores store their energy in a non-magnetic gap that is distributed throughout the entire core. These cores are manufactured and categorised by their effective permeability, defined as the permeability of a hypothetical homogenous core material with the same characteristics as the actual composite. Different effective

permeabilities in the range of 15-200 are achieved by varying particle size and the amount of magnetically inert material in the composite mix.

Composite powered metal cores are not normally used in true transformer applications because their relatively low permeability results in high magnetising current and energy storage. Similar to tape wound cores, at SMPS frequencies powdered metal cores are quite lossy. Rounding of the B-H characteristic is another problem of composite powered cores, and ferrites [3.11]. An ideal magnetic material exhibits a square hysteresis loop characteristic with very high permeability and insignificant stored energy until finally driven into saturation. This is called a "sharp saturation" characteristic. A rounded or soft saturation characteristic exhibits a gradual reduction of incremental permeability until finally the core is completely saturated. In composite powdered metal cores, non-magnetic gaps exist between the discrete magnetic particles. Similar non-magnetic inclusions occur among the sintered particles in ferrite cores. These distributed non-magnetic regions cause significant rounding of the B-H characteristic and increasing the area between the y-axis and vertical component of the hysteresis curve resulting in energy storage within the core, Fig 3.19.

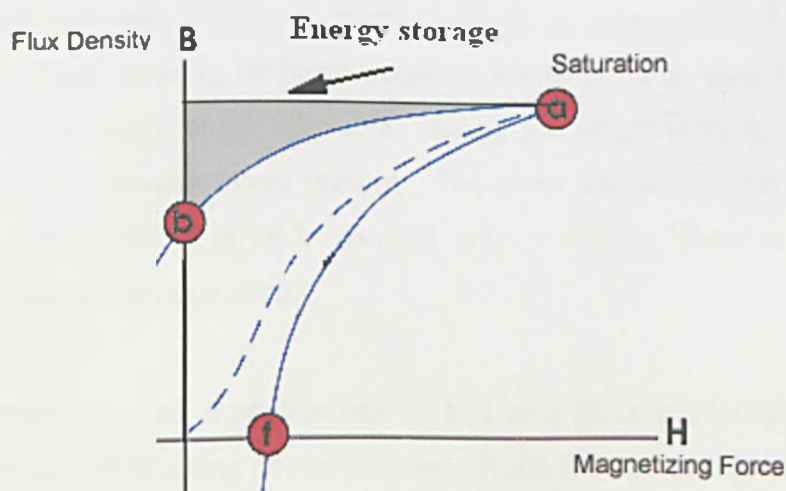


Figure 3.19 Representation of the area indicative of energy storage within a magnetic material

The particulate structure of these core materials has two main effects: First, the distributed reluctance of these tiny "gaps" causes the flux and the flux change to be distributed across the entire core, rather than as a discrete flux change boundary moving from inside to outside as depicted in an airgap core. Second, at low flux

densities, flux tends to concentrate in the paths of lowest reluctance, where the magnetic particles are in close proximity. As the flux density increases these paths areas are the first to saturate. Those portions of the magnetic particles that saturate first become nonmagnetic, making these paths less "easy". Only by reducing the operational flux density of the core can these two effects be avoided.

Therefore, the incremental inductance decreases substantially as the DC operating point is raised. Typically, the inductance may be halved at an operating flux density of 0.4T, only half way to saturation. The much greater saturation flux density,  $B_{sat}$ , of the powdered metal cores compared to ferrite (0.8T vs. 0.3T) would permit a much smaller inductor as a gapped ferrite for the same application, but at 100kHz and above, this is seldom fulfilled because of the restrictions imposed by losses and rounding. Composite powdered cores tend to be restricted to low frequency SMPS filter inductor applications.

SMPS typically have inductors and transformers with ferrite cores. Ferrites are manufactured from oxides of various metals such as iron, manganese, and zinc. Oxides normally act as insulators and, therefore, ferrites have higher resistivity than magnetic alloys, permitting them to function at much higher frequencies. The raw materials are mixed and fired in a presintering kiln. They are then broken up into uniform particles, and pressed into one of the many shapes desired, as shown in Fig 3.17. Since sintered cores are a hard ceramic, further processing has to be done with a diamond grinding wheel. The sintering process involves raising the temperature to 1300°C in about 3 hours, with 15 percent oxygen present. The cores are cooled slowly without oxygen present to about 200°C in 20 hours after entry. A 15% linear and 40% by volume shrinkage occurs during sintering.

MnZn ferrites are used in applications up to 1 or 2 MHz and include the power ferrite materials used in switching power supplies. NiZn ferrites have lower permeability and greater resistivity, and are used for frequencies  $\geq 1$  MHz [3.40,3.41]. The relative permeability of power ferrite materials is in the range of 1500 to 3000. A ferrite core will store a small amount of energy. This undesired magnetising energy must be subsequently dealt with in a snubber or clamp [3.11]. Ferrites popularity in SMPS applications is due to the lower cost and core loss than the materials previously discussed. A disadvantage of ferrite is its ceramic core, which is less robust than other materials and not suitable for high shock environments, such as space and military applications. Saturation flux density,  $B_{sat}$ , of ferrite is much less than tape wound or



powdered metal cores: 0.3T vs. 0.8T approximately. The amount of current that can be applied prior to saturation is therefore limited. An air gap may be required for increased current or increased magnetic path i.e. core area. Until recently the low saturation flux density,  $B_{sat}$ , was not viewed as an actual disadvantage. Beyond 100 kHz core losses within tape wound or powdered metal cores dominated core material selection. However, thin film deposition techniques can now restrict the onset of core loss via the fabrication of thin film laminates. Another drawback of ferrite is the high sintering temperature, 1300°C, which is not compatible with IC integration. The application of tape wound alloys, composite cores and ferrite cores in transformers and inductors are reviewed in the following section.

### **3.4.2 Review of micromachined fabrication approach**

Previous attempts to develop microscale magnetic components utilizing thin film alloys have demonstrated improvements in device performance. However, these development efforts have suffered from the slow and expensive deposition of the magnetic alloy [3.42], limited bandwidth of operation due to film thickness, high relative permeability [3.43] or low saturation flux density [3.44]. In the light of these developments an investigation into efficient component design, fabrication issues and challenges and desirable material properties is appropriate in order to aid future research towards more effective and cost effective device manufacturing.

The deposition methods of previously developed micro-machined power inductors and transformers can be categorised as follows: (1) Hybrid fabrication with ferrite plate, (2) Screen-printing of polymer/ferrite composite, (3) Sputtering of magnetic alloys, (4) electroplating of conductive metallic alloy. Each of these methods is explained and examples referenced.

#### *(1) Hybrid fabrication with ferrite plate*

In 1993, a planar power inductor using NiZn ferrite thin plates as a magnetic material was fabricated in the size of 10mm x 10mm x 2mm and was applied to a 10W DC-DC buck converter operating at 2 MHz, Fig 3.20 [3.45]. NiZn plates fabricated by conventional high temperature sintering were used as a magnetic substrate and were combined with sputtered copper fabrication technology in a hybrid manner. The efficiency of the component at 2 MHz was 82%. Windings of spiral or meander geometry instead of toroid were used because this permitted direct deposition onto the

magnetic substrate. Note that a spiral or a meander winding can be simply attached or fabricated on top of a magnetic substrate, since it is basically a 2D structure, while a toroidal winding is a 3D structure having a magnetic core inside. The ferrite core and winding structure is similar to that commonly used in planar magnetic components. However integrated fabrication with electronic circuitry is more difficult because of the high temperature required for ferrite sintering. Furthermore, low magnetic saturation flux density ( $B_{sat} = 0.3T$ ) of ferrite results in an overall large device volume. The vertical profile of these components is typically  $\geq 2\text{mm}$ .

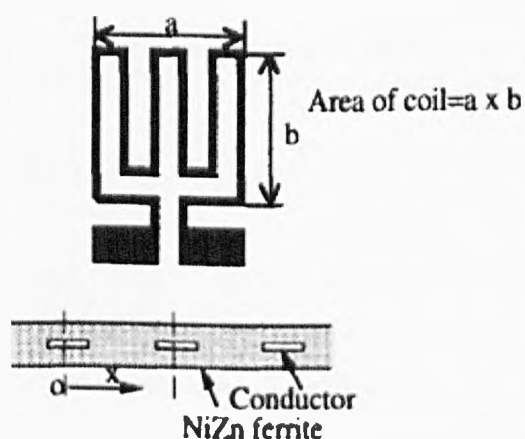


Figure 3.20 A schematic of a planar meander wound inductor enclosed by two NiZn ferrite thin plates. Component dimensions 10mm x 10mm x 2mm [3.45].

(2) *Screen printing of polymer/ferrite composite*

In 1997, a ferrite-based integrated planar inductor was fabricated using screen-printed polymer/ferrite composites and electroplated copper coils, Fig 3.21 [3.44]. Screen-printed ferrites were cured at  $<300^{\circ}\text{C}$ , which is more compatible with IC fabrication than the sintering temperature of standard ferrite fabrication. However, magnetic relative permeability ( $\mu_r = 33$ ) and saturation flux density ( $B_{sat} = 0.3T$ ) of these ferrites are inferior to the properties of typical magnetic alloys, ( $\mu_r > 500$ ,  $B_{sat} \geq 0.7T$ ). In 2005 a similar approach was used to fabricate a magnetic core for a MEMS actuator [3.46]. The magnetic properties exhibited no marked improvement; relative permeability ranged from 15-25 and saturation density range from 0.4-0.5T.

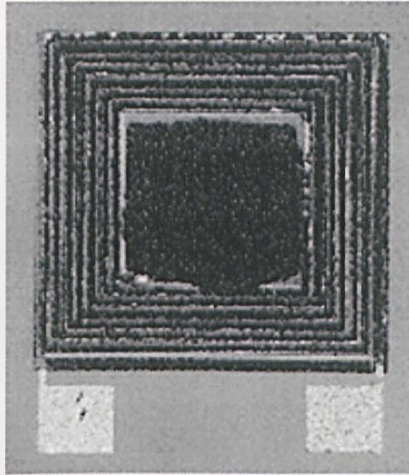


Figure 3.21 A two layer vertically stacked spiral type micro-inductor with ferrite composite core: (Dimensions 2mm x 2mm x 50mm) [3.44].

### *(3) Sputtering of magnetic alloys and lamination technology*

Magnetic alloys have been more widely explored than ferrites in realising micromachined magnetic components due to their high saturation flux density and relative permeability as well as fabrication compatibility with IC. Sputtered alloys for micromachined magnetic components include various Co-based and Fe-based alloys such as CoNbZr [3.47], CoFeSiB [3.47], NiFe [3.13], FeTaN [3.48] and FeBN [3.49]. In 1990, an integrated planar microtransformer with a magnetic core of CoZrRe was fabricated on a silicon substrate using a low temperature dry process [3.50]. A 5  $\mu\text{m}$  thick CoZrRe layer was deposited by sputtering and patterned by nitrogen ion beam etching. In 1996, this transformer was integrated monolithically with Schottky diodes on a silicon substrate to be used in a switching converter [3.51]. To reduce eddy current loss at high frequency, the magnetic alloy core was laminated by sputtered thin  $\text{SiO}_2$  insulation layers. The fabricated switching converter operating at 15MHz showed 0.3W output at 35% efficiency. In 2000, an integrated thin-film inductor with sputtered 9 $\mu\text{m}$  thick CoHfTaPd was fabricated on a 4 x 5mm power IC that included a PWM controller and MOSFETs [3.52]. The sputtered core was annealed in a vacuum at 400°C under a 48 kA/m DC magnetic field to introduce uniaxial magnetic anisotropy to reduce hysteresis loss. An output power of 1W was achieved with 76% efficiency by the DC/DC converter module. This method of thin film deposition has a critical disadvantage. Since electrical resistivity of most of these alloys is not high enough, lamination is required for thick cores to suppress eddy current. Vacuum deposition is relatively slower than other deposition methods; this technique requires a long process time resulting in possible high fabrication cost. In addition the internal stress of vacuum

deposited thin films tends to be high which can result in mechanical stability problems. Patterning multi-layered films into the required core shape presents difficulties such as the delamination of each film during wet etching. Ion beam etching can be used for patterning films [3.51], however this is a slow and therefore expensive process for thick films. Another consideration is the effect of typical high temperatures that ensue during deposition that may degrade the magnetic properties of the film. A recent application of the sputter deposition technique, shown in Fig 3.22, was used to fabricate a micro-transformer with a race track winding sandwiched between two nickel-iron layers. This component operated with an efficiency of 40% at 2MHz with a power density of 1.2 W/cm<sup>2</sup>. Most sputtered alloy approaches for micromachined magnetics have reported output power of less than 1.5 W and total thicknesses of magnetic core of less than 15  $\mu\text{m}$ .

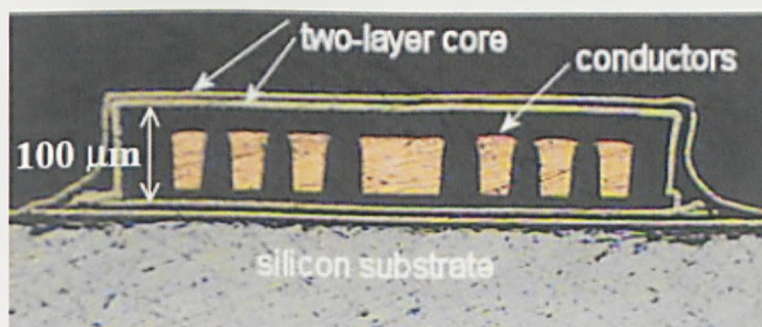


Figure 3.22 Cross section through a fabricated micro-transformer showing turns of copper conductors sandwiched between a two-layer, laminated magnetic core of Nickel-Iron. The inductor footprint is 5.7 mm<sup>2</sup> [3.53].

#### (4) Electroplating of Alloys

Electroplating is a common fabrication technique in the manufacture of microscale magnetic components because of advantages like precise dimensional control with a patterned photoresist, high deposition rate, ease of deposition, cost effectiveness, and ability to alter material properties via additives or waveform parameters/shape. In 1994, integrated planar inductors with electroplated NiFe cores were reported, and have inductances of 0.4~0.1 $\mu\text{H}$  and sizes of 4mm by 1mm, Fig 3.23 [3.54, 3.55]. In 1996 switching boost converters operating at 300 kHz were demonstrated using these inductors with power output of less than 1mW [3.56]. The performance of these inductors degraded at higher frequencies due to eddy currents within the core. Better



performance in the MHz switching frequency required lamination of the core. The disadvantage of creating horizontal laminations is the repeated deposition of insulation layers, seed layers, deposition and patterning of photoresist for the proceeding magnetic layer. The fabrication time for such a process would be unacceptably long and with numerous varying deposition steps would become problematic. In 2002 a sacrificial layer approach was developed to overcome this problem. Alternating layers of nickel-iron and copper were electrodeposited, the copper layers were subsequently wet etched leaving the nickel-iron layers attached to a nickel-iron frame [3.57]. Use of this inductor in a regulated DC-DC boost converter circuit (7-12 V) operating at 2.2 MHz yielded 1.9 W power output at 71% efficiency [3.58].

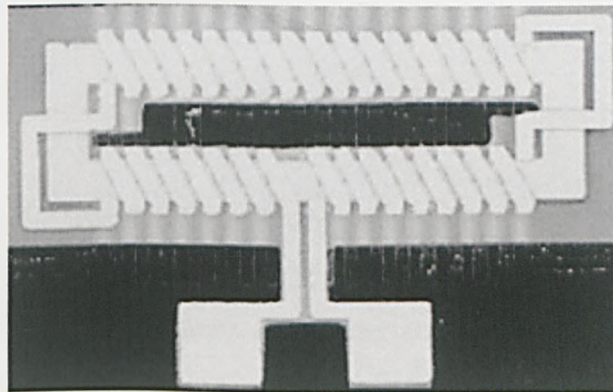


Figure 3.23 Fabricated micromachined inductor with DC electroplated nickel-iron core. The core is seen enclosed by the windings. The dimensions of the inductor are 4mm x 1mm x 0.13mm, length, width and height respectively [3.54].

### 3.5 Summary of deposition techniques

The important properties of the deposition methods related to the fabrication of micromachined power inductive components are compared in Table 3.2.

Properties	Ferrite plate	Ferrites-polymer composite	Electroplated alloys	Sputtered alloys
Material cost	Low	Low	Low	High (1,2)
Deposition rate	-	-	20 A/s	1-10 A/s
Deposition thickness	-	-	Few hundreds of microns	Few tens of microns (3)
Power density (4)	Low	Low	High	High
Integrated fabrication with IC	No	Yes	Yes	Yes
Lamination requirement	No	No	Yes	Yes/No (5)

Table 3.2 A comparison of deposition methods for micromachined power magnetic components

- (1) The price of common base materials like cobalt is 4 times higher than that of nickel
- (2) There is material wastage through the patterning process
- (3) Patterning difficulty in addition to film stress issues limits the thickness
- (4) According to magnetic saturation of materials
- (5) Some high resistivity sputtered material do not require lamination of core [3.59].

In reference to Table 3.2, electrodeposition is viewed as the more favourable fabrication process and will be investigated within this thesis.

### 3.6 Review of state of the art power magnetic components

Previous power magnetic components that have been developed for miniaturised DC-DC converters are compared in Fig 3.24. The solid reference line shown in Fig 3.24 indicates a power density of 40mW/mm<sup>2</sup>. Largest power handling (10W) was achieved in the case of the ferrite plate approach using a similar fabrication process to that of the conventional technology for ferrite cores. However, the volume of the device tends to be bulky due to the material utilised. The highest power density is observed in the sputtered alloy approach. However, the material cost in this approach is generally expected to be higher than other magnetic materials. Maximum deposition thickness is also limited to few tens of microns due to patterning difficulty and internal film stress issues. Components using electroplated alloy cores have suffered from high eddy current loss resulting in poor power density. A resolution to the eddy current issue,

electroplated alloys are expected to be a promising magnetic material for high power, small volume magnetic components in high frequency DC-DC converter applications.

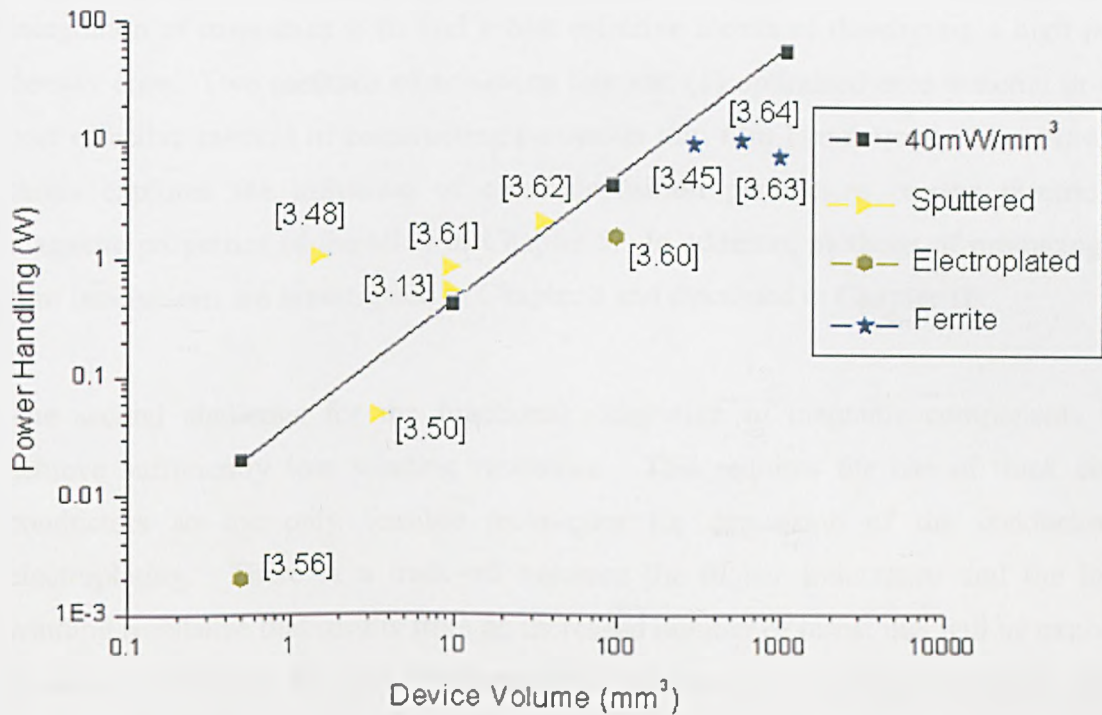


Figure 3.24 Previous power magnetic components: power density vs. device volume. The straight line indicates a constant power density of 40mW/mm<sup>3</sup>. Electroplated [3.56, 3.60], Sputtered [3.62, 3.61, 3.50, 3.13, 3.48], and ferrite [3.45, 3.64, 3.63].

Over the last 15 years, the majority of the research work on thin film magnetics, has focused on the integration of inductors into low power, non isolated converters. Among the most significant contributions to this research has been the work of Sullivan [3.12, 3.13, 3.35, 3.59] and Allen [3.14, 3.54-3.58]. Currently most of the research has focused on the integration of magnetics for low power converters with currents typically less than 1 A. With the predicted trends in power density growth as discussed in Chapter 1, components will have to operate efficiently at far greater applied current levels. Sullivan investigated the use of integrated inductors for the power supply of microprocessors, where the overall current requirements may be of the order of hundreds of amps. Single “V-groove” inductors were developed with an inductance of 6nH and designed to carry up to 7 Amps [3.59]. Unfortunately the current handling capability of this structure is offset by its low inductance value; many applications within the 1-20 MHz range require inductance in the order of  $\mu$ H.

It is clear that significant improvements are required in the development of microscale magnetic components. To maintain compatibility with IC processing, fabrication temperatures must be low (e.g., less than 450°C), which rules out the use of sintering techniques, and thus ferrites, for the magnetic material. The main challenge for the integration of magnetics is to find a cost effective means of developing a high power density core. Two methods of achieving this are: (1) optimised core material or (2) a cost effective method of constructing numerous thin film laminations. Therefore, this thesis explores the influence of electrodeposition parameters on the electric and magnetic properties of the alloy in Chapter 5. In addition, methods of producing thin film laminations are investigated in Chapter 8 and discussed in Chapter 10.

The second challenge for the functional integration of magnetic components is to achieve sufficiently low winding resistance. This requires the use of thick copper conductors so the only feasible techniques for deposition of the conductors is electroplating. There is a trade-off between the higher inductance and the higher winding resistance that results from an increased number of turns; this will be explained in detail in Chapter 6. The challenge is to achieve low winding resistance so that current handling can be increased while at the same time achieving high inductance.

With an optimised microinductor or transformer fabricated via high volume batch processing it may be cost effective to connect several components, in parallel or series to meet current or inductance requirements for certain applications.

In summary, current capacity of microscale magnetic components must be increased, but not at the expense of power density and achievable inductance. New core materials and new fabrication techniques need to be investigated to enable power microscale magnetic components. Component efficiency for transformers and inductors, in order to rival planar components, must be in excess of  $\geq 90\%$ . Electrodeposition has been proven to be the favourable method of thin film deposition and will be described in the next chapter.



## References

- [3.1] C. H. Ahn and M. G. Allen, "Micromachined Planar Inductors on Silicon Wafers for MEMS Applications," *IEEE Trans., Industrial Electronics*, vol. 45, no. 6, pp.886-876, Dec. 1998.
- [3.2] R. C. Dorf, J. A. Svoboda, "Introduction to Electric Circuits", 3<sup>rd</sup> edition, John Wiley & Sons, Inc., 1996.
- [3.3] J.K.Watson, "Applications of Magnetism," John Wiley & Sons, Inc., 1980
- [3.4] B.K.Bose, "Modern Power electronics, Evolution, Technology and Applications," IEEE Press, Jan 1992.
- [3.5] C. J. Kaiser, "The inductor handbook", Olathe, KS: CJ Publishing, 1996
- [3.6] E.C. Snelling, "Soft Ferrites, Properties and Applications," Butterworths, 2<sup>nd</sup> edition, 1988.
- [3.7] M. Brunet, T. O'Donnell, J. O'Brien, P. McCloskey, C. O'Mathuna, "Design Study and Fabrication Techniques for High Power Density Micro-Transformers," *IEEE Trans. On Magnt.*, pp. 1189-1195, 2001.
- [3.8] U. Reggiani, G. Grandi, G. Sancineto, M.K. Kazimierczuk, and A. Massarini, "High-frequency behavior of laminated iron-core inductors for filtering applications," *Proc. IEEE APEC*, pp. 654-660, 2000.
- [3.9] M. Bartoli, A. Reatti, and M. K. Kazimierczuk, "Minimum copper and core losses power inductor design," 31<sup>st</sup> industry applications conference, pp. 1369-1376, 1996.
- [3.10] D. Flynn, M. P. Y. Desmulliez, R. Dhariwal, "A design study of microscale components for operation in the MHz frequency range," *IOP, J. Micromech. Microeng.*, vol.16, pp. 1811-1818, 2006.
- [3.11] D. H. Lloyd., *MAG-100A Unitrode Magnetics Design Handbook*, 1999.
- [3.12] C. R. Sullivan and S. R. Sanders. "Measured Performance of a High-Power-Density Microfabricated Transformer in a DC-DC Converter." *IEEE Power Electronics Specialists Conference*, pp. 287-294, June 1996.
- [3.13] C. R. Sullivan and S. R. Sanders. "Microfabrication Process for High-Frequency Power-Conversion Transformers," *IEEE Power Electronics Specialists Conference*, pp. 658-664, June 1995.
- [3.14] M. G. Allen and J. Y. Park, "Packaging-compatible Microinductors and Microtransformers with Screen-printed Soft Ferrite Using Low Temperature Processes," 7<sup>th</sup> IEEE Joint MMM-Intermag Conference, 1998.
- [3.15] M. G. Allen, L. K. LaGorce, J. Y. Park, "Ferrite-based Integrated planar Inductors and Transformers Fabricated at Low Temperature," *IEEE Trans. Magn.*, vol. 33, no. 5, pp. 3322-3324, 1997.

- [3.16] M. Brunet, T. O'Donnell, L. Baud, N. Wang, J. O'Brien, P. McCloskey, and S.C.O' Mathuna, "Electrical Performance of Microtransformers for DC-DC Converter Applications," *IEEE Trans. Magn.*, vol. 38, no. 5, pp. 3174-3176, Sept. 2002.
- [3.17] W. M. Flanagan, "Handbook of transformer design and applications," New York, NY: MacGraw-Hill, Inc., 1993.
- [3.18] P. Hammond, "Electromagnetism for Engineers," 4<sup>th</sup> edition, Oxford science publications, 1997.
- [3.19] Applications of Magnetism, J.K.Watson, 1980 by John Wiley & Sons, Inc.
- [3.20] Modern Power electronics, Evolution, Technology and Applications, B.K.Bose, IEEE Press.
- [3.21] J. D. Lenk, "Simplified Design of Switching Power Supplies," EDN Series for Design Engineers, Butterworth-Heinemann, MA, 1995.
- [3.22] B. Lynch, K. Huess, "Under the Hood of Low-Voltage DC/DC Converters," Texas Instruments Incorporated 2003.
- [3.23] I. Gottlieb, "Practical Transformer Handbook," Woburn, MA: Newnes, 1998.
- [3.24] A. I. Pressman, "Switching power supply design," 2<sup>nd</sup> edition, McGraw-Hill International, 1999.
- [3.25] M. T. Quirke, J. J Barrett, M. Hayes, "Planar magnetic component technology - a review," *Trans. on Components, Hybrids, Manufacturing Technology*, vol.15, no. 5, pp. 884-892, Oct. 1992.
- [3.26] N. Dai, A. W. Lotfi, G. Skutt, W. Tabisz, F. C. Lee, "A comparative study of high frequency low profile planar transformer technologies," *Applied Power Electronics Conference (APEC)*, vol. 1, pp. 226-232, 1994.
- [3.27] R. Prieto, O. Garcia, R. Asensi, J. A. Cobos and J. Uceda, "Optimizing the performance of planar transformers," *Applied Power Electronics Conference (APEC)*, vol. 1, pp. 415-421, March 1996
- [3.28] G. Skutt, F. Lee, R. Ridley and D. Nicol, "Leakage inductance and termination effects in a high-power planar magnetic structure," *Applied Power Electronics Conference (APEC)*, vol. 1, pp. 295-301, Feb. 1994
- [3.29] K. D. T. Ngo, R. P. Alley and A. J. Yerman, "Fabrication method for a winding assembly with a large number of planar layers," *IEEE Transactions on Power Electronics*, vol. 8, pp. 55-61, Jan. 1993.
- [3.30] C. Quinn, K. Rinne, T. O'Donnell, M. Duffy and C. O. Mathuna, "A review of planar magnetic Techniques and technologies," *Applied Power Electronics Conference (APEC)*, vol. 2, pp. 1175-1138, 2001.

- [3.31] S. Ramakrishnan, R. Steigerwald, J. A. Mallick, "A comparison study of low-profile power magnetics for high frequency high density switching converters," Applied Power Electronics Conference (APEC), vol. 1, pp. 388-394, 1997.
- [3.32] G. Bloom, "Multi-chambered planar magnetics design techniques," Power Electronics Specialists Conference (PESC), vol.1, pp. 295-301, June 2000.
- [3.33] J. T. Strydon, J. A. Ferreira, J. D. van Wyk, I. W. Hofsajer and E. Waffenschmidt, "Power electronic subassembly with increased functionality based on planar sub-components", Power Electronics Specialists Conference (PESC), vol. 3, pp. 1273-1278, June 2000.
- [3.34] M. Rascon, J. Ara, R. Madsen, J. Navas, M. Perez and F. San Miguel, "Thermal analysis and modelling of planar magnetic components," Applied Power Electronics Conference (APEC), vol. 1, pp. 97-101, March 2001.
- [3.35] C. R. Sullivan, "Optimal choice for number of strands in a litz-wire transformer winding," IEEE Trans., on Power Electronics, vol. 14, pp. 283-291, March 1999.
- [3.36] F. Tourkhani and P. Viarouge, "Accurate analytical model of winding losses in round litz wire windings," IEEE Transactions on Magn., vol. 37, pp. 538-543, Jan. 2001
- [3.37] M. Bartoli, N. Noferi, A. Reatti and M. K. Kazimierczuk, "Modeling litz-wire winding losses in high-frequency power inductors", Power Electronics Specialists Conference (PESC), vol. 2, pp. 1690-1696, June 1996.
- [3.38] R. Groningen, "Magnetic properties of nanocrystalline materials for high frequency applications," PhD thesis, University of Groningen, Netherlands, Nov. 2003.
- [3.39] Hitachi Metals, "Nanocrystalline soft magnetic material-FINEMET", Jun. 2004.
- [3.40] A Critical Comparison of Ferrites with Other Magnetic Materials, Magnetics Technology Center, 1990.
- [3.41] Soft Ferrites: A Users Guide, Magnetic Materials Producers Association, 1998.
- [3.42] S. Ohnuma, H.J. Lee, N. Kobayashi, H. Fujimori, and T. Masumoto, "Co-Zr-O Nano-Granular Thin Films with Improved High Frequency Soft Magnetic Properties," IEEE Trans. Magn., vol. 37, no 4, pp. 2251-2254, July 2001.
- [3.43] O. Dezuari, S.E. Gilbert, E. Belloy, M.A.M. Gijs, "High inductance planar transformers", Sensors and Actuators, vol. 81, pp. 355-358, 2000.
- [3.44] J. Y. Park, L. K. Lagorce and M. G. Allen, "Ferrite-based integrated planar inductors and transformers fabricated at low temperature" IEEE Trans. Magn., vol. 33, no. 5, pp. 3322-3324, Sept. 1997.

- [3.45] I. Sasada, T. Yamaguchi, K. Harada, and Y. Notohara, "Planar inductors using NiZn Ferrite thin plates and the application to high-frequency DC-DC converters," *IEEE, Trans. Magn.*, vol. 29, no. 6, pp. 3231-3233, 1993.
- [3.46] A. C. Hartely, "Magnetic MEMs Actuator", PhD Thesis, University of Leeds, 2006.
- [3.47] K. Yamaguchi, S. Ohnuma, H. Matsuki, and K. Murakami, "Characteristics of a thin film microtransformer with circular spiral coils," *IEEE Trans. Magn.*, vol. 29, no.5, pp. 2232-2237, 1993.
- [3.48] D. Shin, C. Kim, C. Lee, S. Nam, and H. Kim, "Fabrication of double rectangular type FeTaN film inductor," *IEEE Trans. Magn.*, vol. 35, no.5, pp. 3511-3513, 1993.
- [3.49] K. Kim, J. Kim, H. Kim and S. Han, "A MHz switching DC/DC converter using FeBN thin film inductor," *IEEE Trans. Magn.*, vol. 38, no. 5, pp. 3162-3164, Sept. 2002.
- [3.50] M. Mino, T. Yachi, A. Tago, K. Yanagisawa, and K. Sakakibara, "A new planar microtransformer for use in micro-switching converters," *IEEE Trans. Magn.*, vol.28, no. 4, pp. 1969-1973, 1992.
- [3.51] M. Mino, T. Yachi, A. Tago, K. Yanagisawa, and K. Sakakibara, "Planar microtransformer with monolithically-integrated rectifier diodes for micro-switching converters," *IEEE Trans. Magn.*, vol.32, no. 2, pp. 291-296, 1996.
- [3.52] Y. Katayama, S. Sugahara, H. Nakazawa, and M. Edo, "High-power-density MHz-switching monolithic DC-DC converter with thin-film inductor," 31<sup>st</sup> Annu. Power Electron. Specialists Conf., pp. 1485-1490, 2000.
- [3.53] M. Brunet, T. O'Donnell, L. Baud, N. Wang, J. O'Brien, P. McCloskey and S. C. O'Mathuna, "Electrical Performance of Microtransformers for DC-DC Converter Applications," *IEEE Trans. Magn.*, vol.38, no. 5, Sept. 2002.
- [3.54] C. H. Ahn, Y. J. Kim, and M. G. Allen, "A fully integrated planar toroidal inductor with a micromachined nickel-iron magnetic bar," *IEEE Trans. Component and packaging and Manufacturing Technology*, vol. 17, no.3, pp. 463-469, Sept. 1994.
- [3.55] C. H. Ahn, and M. G. Allen, "A new toroidal-meander type integrated inductor with a multilevel meander magnetic core," *IEEE Trans. Magn.*, vol.30, no.1, pp. 73-79, 1994.
- [3.56] C. H. Ahn, Y. J. Kim, and M. G. Allen, "A comparison of two micromachined inductors (bar and meander type) for fully integrated boost DC/DC power converters," *IEEE Trans. Power Electron.*, vol. 11, no.2, pp. 239-245, 1996.

- [3.57] J. W. Park, F. Cros, and M. G. Allen, "A Sacrificial Layer Approach to Highly Laminated Magnetic Cores," *IEEE Trans. Magn.*, pp. 380-383, 2002.
- [3.58] J. W. Park and Mark G. Allen, "Ultra low-profile micromachined power inductors with highly laminated Ni/Fe Cores: Application to low-Megahertz DC-DC converters," *IEEE Trans. Magn.*, vol. 39, no. 5, pp. 3184-3186, Sept. 2003.
- [3.59] S. Prabhakaran, C.R.Sullivan, C.G.Levey, and K. Venkatachalam. "Fabrication of Thin Film V-Groove Inductors using Composite Magnetic Materials." IMAPS Advanced Technology Workshop (ATW) on Passive Integration, June 2002.
- [3.60] M. Ludwig, M. Duffy, T. O. Donnell, and C. O. Mathuna, "PCB integrated inductors for low power DC/DC converter," 17<sup>th</sup> Annu. Applied Power Electron. Conf. pp.319-325, 2002.
- [3.61] T. Sato, T. Inoue, H. Tomita, S. Yatabe, K. Nishijima, Y. Tokai, M. Nameki, N. Saito, and T. Mizoguchi, "5 MHz switching micro DC-DC converter using planar inductor," 18<sup>th</sup> International telecommunications Energy Conference, pp. 485-490, 1996.
- [3.62] M. Mino, K. Tsukamoto, K. Yanagisawa, A. Tago, T. Yachi, "A compact buck-converter using a thin-film inductor," 11<sup>th</sup> Annu. Applied Power Electron. Conf. and Exposition, pp. 422-426, 1996.
- [3.63] J. M. Lopera, M. J. Prieto, A. M. Pernia, F. Nuno, M. J. M. Graaf, J. W. Waanders, and L. A. Baric, "Design of integrated magnetic elements using thick-film technology," *IEEE Trans. Power Electron.*, vol.14, no. 3, pp. 408-414, 1999.
- [3.64] M. J. Prieto, A. M. Pernia, J. M. Lopera, F. Nuno, "Design and analysis of thick-film integrated inductors for power converters," *IEEE Trans. Industry applications.*, vol.38, no. 2, pp. 543-552, 2002.

## Chapter 4

### Electrodeposition of Nickel-Iron

#### 4.1 Introduction to Electrodeposition

This chapter introduces the process of electroplating. Electrodeposition is used for the fabrication of the magnetic core and windings. Therefore, it is necessary to review the theory of the electrodeposition process. Section 4.1.1 contains an overview of the governing principles of electroplating and the analytical equations used to describe the process. Prior electrolyte systems used to investigate the properties of Nickel-Iron are covered in section 4.2. A review of anomalous co-deposition is provided in section 4.3. An advantage of this alloy is the ability to tailor the films properties during deposition via magnetic field annealing, a description of this process is provided in section 4.4. Preliminary experiments using a DC waveform deposition are presented and results discussed in section 4.5. The chapter concludes with a discussion of the preliminary data presented, section 4.6.

#### 4.1.1 Basics of Electrodeposition

The electrodeposition of metallic films has been known for a long time and used for manufacturing a variety of products i.e. PCB tracks, mirrors, corrosion resistant surfaces, etc. In its simplest form, the electrodeposition bath consists of an electrolyte containing metal ions, an electrode or substrate on which the deposition is desired, and a counter electrode, referred to as the anode. When a current flows through the electrolyte, the cations and anions move toward the cathode and anode, respectively, and may deposit on the electrodes after undergoing a charge transfer reaction [4.1]. The simple electrodeposition system shown in Fig.4.1 consists of the following components:

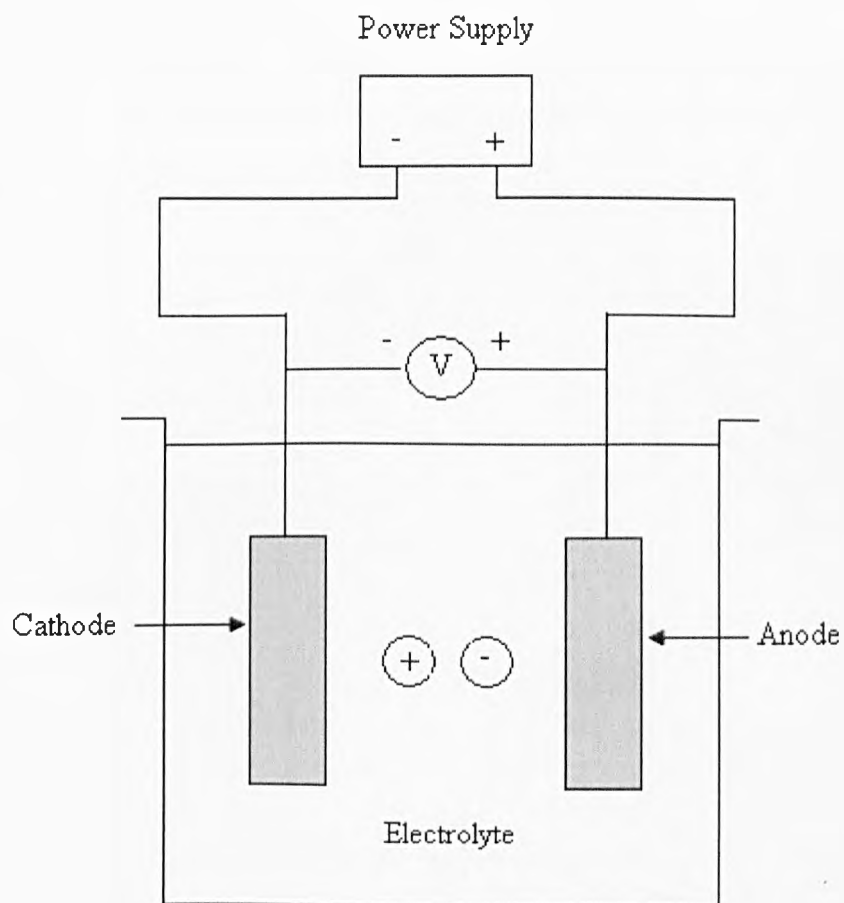


Figure 4.1 Schematic representation of a simple electroplating bath.

*Electrolyte.* The electrolyte or bath provides the ions to be electrodeposited. It has to be electrically conductive; it can be aqueous, non-aqueous, or molten but it must contain suitable metal salts. Additives are sometimes included to improve the quality of the electrodeposit. An ideal additive should not become incorporated in the film but should lead to improvement of its adhesion, surface finish, uniformity etc.

*Electrodes.* At least two electrodes, cathode and anode, are needed. An applied electric field across these provides the main driving force for the ions. The positive (M) and negative (X) ions deposit on the cathode and anode respectively. Cathodic deposition is more popular in the electroplating because (1) most metal ions are positive ions and (2) anodic deposition has been found to give poor stoichiometry and adhesion.

*Power Supply.* The power supply can be (1) direct current at constant voltage which leads to potentiostatic deposition; (2) direct current at constant current which leads to galvanostatic deposition; or (3) a current or voltage waveform or pulse. There is a variety of electrical waveforms that can be used for electroplating but the three considered in this thesis are shown in Fig.4.2.

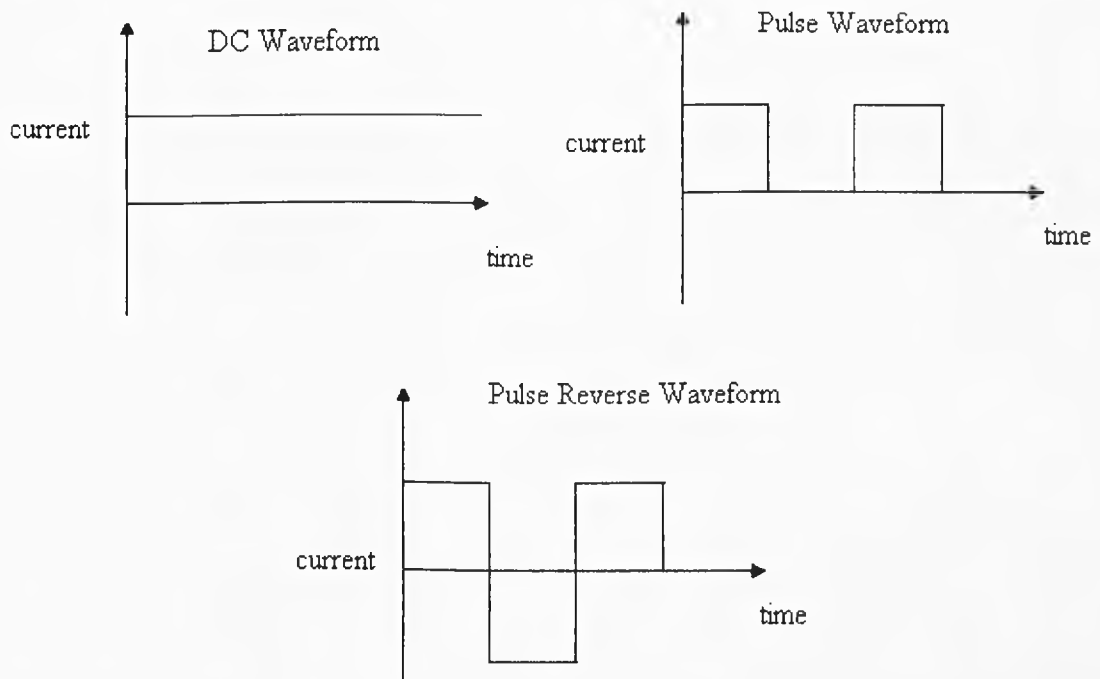


Figure 4.2 Illustration of (a) Direct Current, (b) Pulse and (c) Pulse Reverse waveforms used in electrodeposition.

The mass,  $\Delta_m$ , deposited over a unit area to the current density  $j$  flowing for a time  $t$  are given by the Faraday's laws such that:

$$\Delta_m = \text{const} \times jt = C_e jt \quad (4.1)$$

Where  $C_e$  is the chemical equivalent. The rate growth of electrodeposited material per unit area can be written as

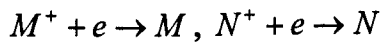
$$\frac{d}{dt} \Delta_m = C_e j \quad (4.2)$$



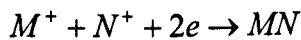
If  $z$  is the ionic charge, then  $j/zF$  gives the growth rate of the electrodeposit in gram molecules of the substance.  $F$  is the Faraday constant or 96500 C. On the application of an electric field, the ions  $M^{z+}$  move to the cathode and the elemental electrodeposition process can be written as



If the electrolyte contains more than one ionic species that can be simultaneously deposited, as in our Ni-Fe deposition system, then the electrodeposition process for two types of ionic species can be written as



or



The expression above provides a simplistic description of electrodeposition and in reality the process is more complex [4.2].

## 4.2 Electrolyte Systems for Nickel-Iron deposition

This section provides an overview of prior work in the field of nickel-iron electrodeposition. The results of various electrolytes are discussed and their primary findings highlighted.

### 4.2.1 Sulphate and chloride electrolytes

Glasstone and Symes investigated the variation of the deposit composition with Fe content of the bath, total metals concentration, current density, agitation, temperature, pH, and type of buffer from buffered solutions of ferrous sulphate and nickel sulphate [4.3, 4.4]. This first extensive and systematic study demonstrated that, with an initially low but increasing current density, a rapid increase in iron content occurs until a peak-maximum in iron content is reached. As the current density increased further, the iron content of the alloy gradually decreased. This decrease in iron content with increasing

current density was attributed to mass transfer limitations on the deposition of Fe. The maximum in Fe content versus current density therefore indicated the value of current density above which mass transfer effects become noticeable. Consistent with this idea is the observation that for more dilute plating baths in this diffusion influenced region, the Fe content of the alloy decreased more rapidly with increasing current density. The maximum in Fe content versus current density was found to be highly dependent on the relative amount of ferrous ions in the solution. The maximum Fe content was independent of pH in the range studied (pH 3.2-5.2), but the pH had an effect on the current density at which the maximum in Fe content occurred.

Dahms and Croll examined how the pH near the cathode surface affected the composition of Ni-Fe alloys using a sulphate solution with no additives [4.5]. Through use of a rotating disk, variation of metal ion concentration and polarization curves, an explanation of anomalous deposition was developed. They concluded that a rise in pH near the cathode surface caused formation of iron hydroxide species which inhibits Ni deposition.

Horkans, using a rotating disc electrode system, with  $0.5M Ni^{2+}$  and  $0.01M Fe^{2+}$  studied the current efficiency and deposit composition of Ni-Fe alloys as a function of plating bath variables and boric acid content for both chloride and sulphate electrolyte systems [4.6, 4.7]. This work led to a direct comparison between chloride and sulphate electrolyte systems under similar conditions. Deposits produced from sulphate electrolytes contained a higher percentage of iron than deposits produced from chloride electrolyte. An explanation of these results was based on Dahm's and Croll's model of Ni-Fe electrodeposition [4.5]. Weak complexation of Fe by chloride ion, hindering the formation of surface iron hydroxides, was postulated as being responsible for the iron content of deposits from chloride baths being less than that from sulphate baths. The addition of boric acid resulted in an increase in the Fe content of the deposit at a pH of 3 for current densities less than  $2 A/dm^2$  for both sulphate and chloride baths. At pH=2, addition of boric acid had only a small effect on composition and no effect at a current density of  $2 A/dm^2$ . Boric acid had little effect on current efficiency, but did result in an improvement in the appearance of the deposit. Today it is common place for boric acid to typically be used in various electrolytes as a brightener to improve the appearance of deposits.

#### 4.2.2 Sulfamate electrolytes

A sulfamate electrolyte can be advantageous due to the high solubility, stability and non-toxic nature of metal sulfamates. Sulfamate baths have also been reported to yield deposits with low internal stress [4.8]. The first use of metal sulfamates for the electrodeposition of Ni-Fe alloys was carried out onto a wire substrate for the purpose of forming memory elements [4.9].

Rama Char studied Ni-Fe deposition from acetate buffered sulfamate baths at pH 3.5 for a wide range of compositions [4.10]. The effects of current density on composition of the alloy followed the same trends as for sulphate baths. Cathode current efficiencies increased with current density. However, a rotating cylindrical cathode resulted in a large decrease in cathode current efficiency.

Sadakov fabricated thick (0.1-0.2mm) Ni-Fe films of various compositions from a boric acid buffered sulfamate electrolyte at 60°C and pH=2.5 with a total metal content of 1.8M [4.11]. Anomalous deposition was observed for alloys which contained less than 90% Fe. An electrolyte containing a low percentage of Fe displayed decreasing Fe content within the deposit with increasing current density. A high Fe deposit composition was relatively independent of density from 3 to 15 A/dm<sup>2</sup>. The variation of the composition versus current density is in accordance with the trends discussed for sulphate baths. An increase in internal stress of the deposits occurred with increasing Fe content. However, the inclusion of saccharine and increased bath temperatures reduced the internal stress of the deposits.

A comparison of electrodeposited Ni-Fe alloys from sulphate, chloride, and sulfamate electrolytes has been reported [4.12-4.14]. For electrolyte systems containing less than 24% Fe of the metals, the sulfamate solutions resulted in deposits with a higher percentage of Fe than the other electrolyte systems. The deposit composition was also less dependent on current density than for other electrolytes.

In addition to the more common chloride, sulphate and sulfamate baths, other plating baths have been examined for the electrodeposition of Ni-Fe alloys, such as pyrophosphate-chloride electrolytes, cyanide containing solutions, acetate, fluoroborate

baths and electroless deposition from a sulphate electrolyte with a large excess of tartrate using sodium hypophosphite as a reducing agent has been reported [4.13].

### 4.2.3 Periodic deposition of Nickel-Iron Alloys

Most research on electrodeposition of Ni-Fe alloys has focused on DC deposition. However, current waveform modifications in the deposition of metals and alloys have been the object of increasing research in recent years. Periodic currents, such as pulse plating (PP) and pulse reverse (PR) plating have been observed to alter deposit characteristics such as hardness, porosity, surface topography, internal stress, and the crystal structure of deposits. A review on the fundamentals and applications of periodic waveforms in electrodeposition was edited by Puipe [4.14, 4.15].

The first systematic attempt at an explanation of periodic current waveforms was performed by Kovac who superimposed an AC current on a cathodic DC current [4.15, 4.16]. Acidic sulphate/tartrate solutions and alkaline citrate solutions (pH=9.25) were used. In the acidic solutions an AC superimposed on DC current waveform ( $i_{avg} = 0.2$  A/dm<sup>2</sup>) resulted in a reduction in anomalous deposition if the waveform frequency was less than 3 kHz. This behaviour was explained in terms of oxidation of absorbed hydrogen atoms. At frequencies less than 3 kHz the anodic pulse was of sufficient duration that oxidation of absorbed surface hydrogen atoms could occur. This allowed the pH and hence the amount of metal hydroxides near the electrode surface to decrease during the anodic pulse to values closer to the bulk pH. With surface pH closer to the bulk pH, the amount of metal hydroxide species formed near the cathode decreased resulting in less anomalous deposition.

Shershadri studied Ni-Fe deposition from a dilute sulphate electrolyte system [4.17]. A sinusoidal alternating current, either square or triangular, waveform was superimposed on a direct current. The effects of pulse magnitude and frequency (10-50 Hz) on alloy composition were studied. If the magnitude of the superimposed alternating waveform was small enough such that no reversing waveform existed, then no effect on composition was observed. When reversing current did exist, a reduction in Fe content was seen. This was explained in terms of preferential dissolution of Fe during the anodic pulse.

Maksimovic described Ni-Fe deposition utilising a pulsed current, a pulse reverse waveform and a superimposed alternating current at various frequencies up to 1 kHz [4.18]. The PP waveform had no effect on composition. The PR waveform and the superimposed alternating current both decreased the Fe content of deposits, with the PR waveform having the most pronounced effect.

### 4.3 Anomalous Deposition

Nickel-Iron (Ni-Fe) alloys have been used in early magnetic recording head equipment due to their magnetic properties and dimensional stability [4.19-4.24]. The main Ni-Fe alloy of interest for microscale magnetic components applications within this thesis is called permalloy and has a typically 80:20 composition.

Ni-Fe exhibits anomalous co-deposition phenomena. When Fe and Ni are deposited individually from separate equivalent electrolyte systems at the same applied potential, Ni deposits more rapidly than Fe due to the electrode potential of  $\text{Fe}^{2+}/\text{Fe}$  (-0.45V vs. Standard Hydrogen Electrode) compared  $\text{Ni}^{2+}/\text{Ni}$  (-0.26V). However when Fe and Ni are deposited from the same solution Fe deposits more rapidly than Ni. This phenomenon of alloy deposits having an unexpectedly high amount of the metal with the more negative reduction potential is called anomalous deposition.

For sulphate electrolytes, Dahms and Croll developed an explanation of anomalous deposition. Using rotating disk electrodes with solutions containing 0.5M ferrous sulphate, 0.5M nickel sulphate, and 0.01M  $\text{H}_2\text{SO}_4$ , Dahms and Croll investigated how the pH at the cathode surface influenced the co-deposition of Ni-Fe alloys [4.5]. By accounting for the net steady state diffusion of species normal to the rotating disk cathode, an equation was derived which allowed the calculation of the pH at the surface of the cathode as a function of the solution conditions and hydrogen evolution. The theoretical pH at the electrode surface agreed well with experimental values determined by the use of microelectrodes. It was assumed that hydrogen evolution at the cathode resulted in an increase in the pH near the cathode. Dahms and Croll concluded that anomalous deposition occurred only when the surface pH increased to values at which metal hydroxide formation could occur (pH=6-7). When surface pH remained close to the value in the bulk of solution, deposition was not anomalous i.e. the partial current for Ni is greater than the partial current for Fe.

The surface metal hydroxides suppress the deposition rate of Ni, but not Fe in solutions that contained both Ni and Fe. According to prior work, when Ni and Fe are deposited individually, this metal hydroxide formation near the cathode had no effect on the rate of deposition.

In summary, electrolyte systems such as sulphates, chlorides, and sulfamates exhibit anomalous deposition [4.25]. A collection of experimental results which illustrates the anomalous nature of Ni-Fe alloy deposition is presented in Fig.4.3. In this figure the percentage of Fe in the deposit is plotted as a function of the percentage Fe in the solution. Under a variety of deposition conditions the Fe content of the deposit is greater than in the solution. This is a universal trend observed in much of the literature of anomalous co-deposition. Another characteristic of anomalous deposition concerns the effect of deposition rate on the deposit composition, shown in Fig.4.4. This data shows that with increasing current density the Fe content rapidly increases within the deposit then levels off with further increases in current density. The levelling off of the Fe content at high current densities is due to mass transfer effects. The current efficiency for metal deposition increased with increasing current density or pH. The increase in current efficiency with increasing deposition rate is illustrated in Fig.4.5 for several electrolyte systems. This trend is attributed to the mass transfer effect on hydrogen evolution due to the fact that the current efficiency for metal deposition is similar for the various electrolyte systems.

A feature of the electrodeposition process of Ni-Fe not covered yet is the plating of anisotropic as opposed to isotropic magnetic films. To fabricate the anisotropic Ni-Fe, electrodeposition takes place in the presence of a magnetic field. With a small DC magnetic field applied in the hard axis direction and equal to the anisotropy field of the magnetic film,  $H_k$  (300 A/m), the easy axis permeability assumes a very large value [4.26]. A description with illustrations and reference to an analytical model is contained in the proceeding section.

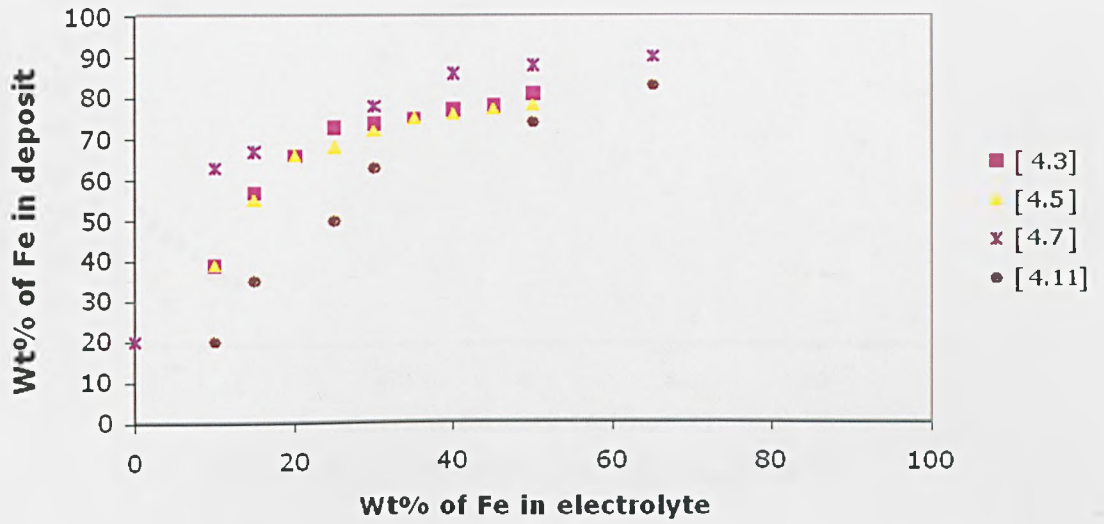


Figure 4.3 Solution composition vs. deposit composition.

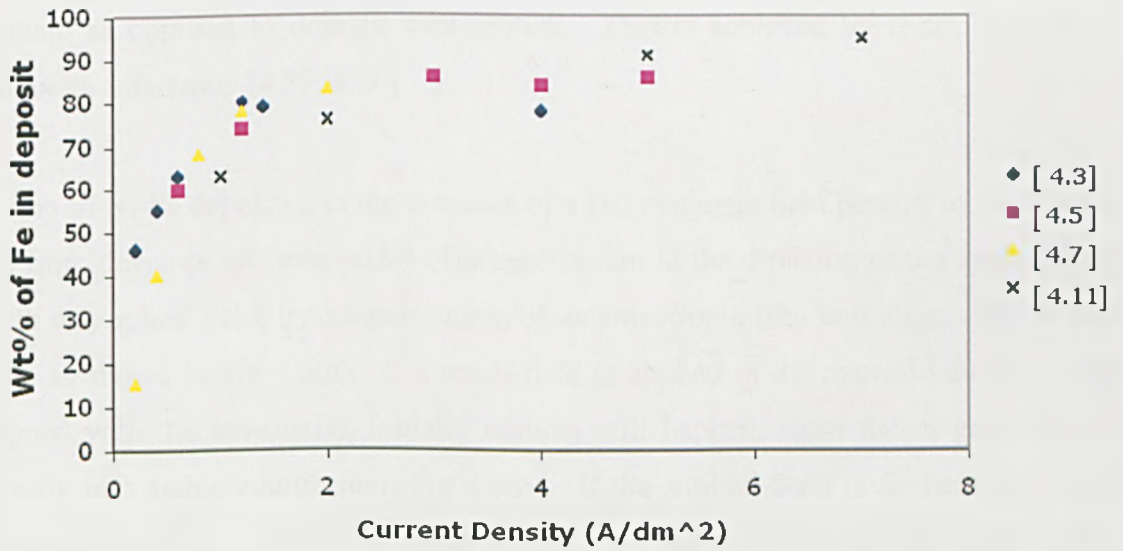


Figure 4.4 Current Density vs. Deposit composition.

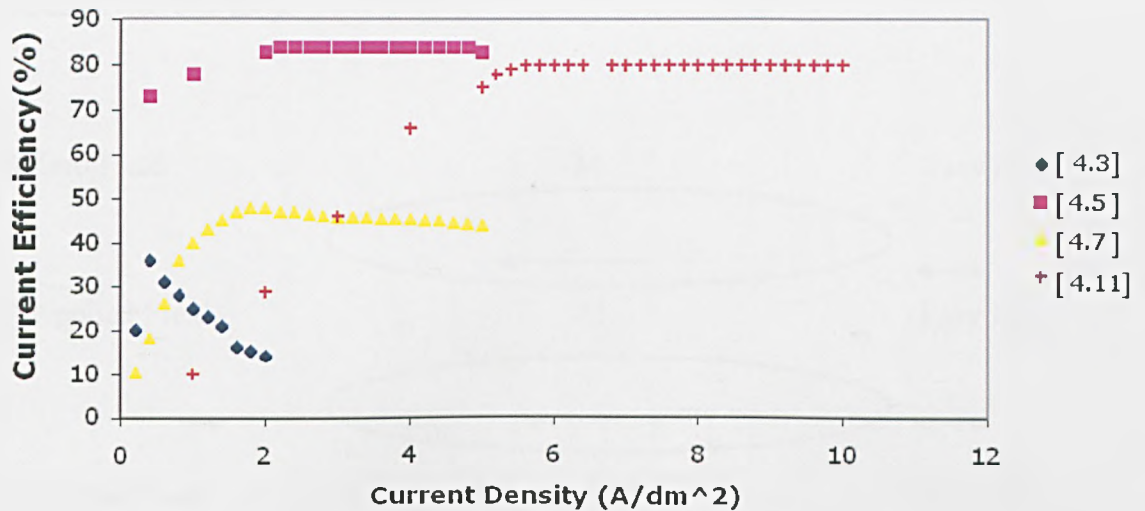


Figure 4.5 Current Density vs. Current Efficiency.

#### 4.4 Magnetic field annealing during electrodeposition

Hysteresis loss in Ni-Fe films can in principle be eliminated if changes in magnetisation proceeded by coherent rotation of the magnetisation in a single domain as opposed to domain wall motion. This is achieved by controlling the magnetic anisotropy [4.23, 4.26].

A film of Ni-Fe deposited in the presence of a DC magnetic field parallel to the plane of the film, develops an "easy-axis" of magnetisation in the direction of the applied field. With no applied field, the magnetisation of an anisotropic film will align with the easy axis, as shown in Fig 4.6(a). If a small field is applied in the opposite direction (still aligned with the easy axis), initially nothing will happen, since the magnetisation is already in a stable equilibrium, Fig 4.6(b). If the applied field is further increased it eventually reaches a threshold at which point the magnetisation suddenly flips to align with the applied field, Fig 4.6(c). This switching behaviour is lossy and leads to a wider hysteresis loop i.e. greater coercivity.

If the magnetic field is applied perpendicular to the easy axis, but still in the plane of the film the behaviour is illustrated in Fig 4.7. Initially with no applied field, the magnetisation still lines up with the easy axis, Fig 4.7(a). If a small field is applied in the hard axis direction, the magnetisation immediately rotates slightly in the direction of the applied field, Fig 4.7(b). As the field is increased the magnetisation rotates further, Fig 4.7(c). This process is reversible; a decrease in the applied field will result in the magnetisation rotating back to the smaller angle. This implies that it has a single value



lossless hysteresis loop.

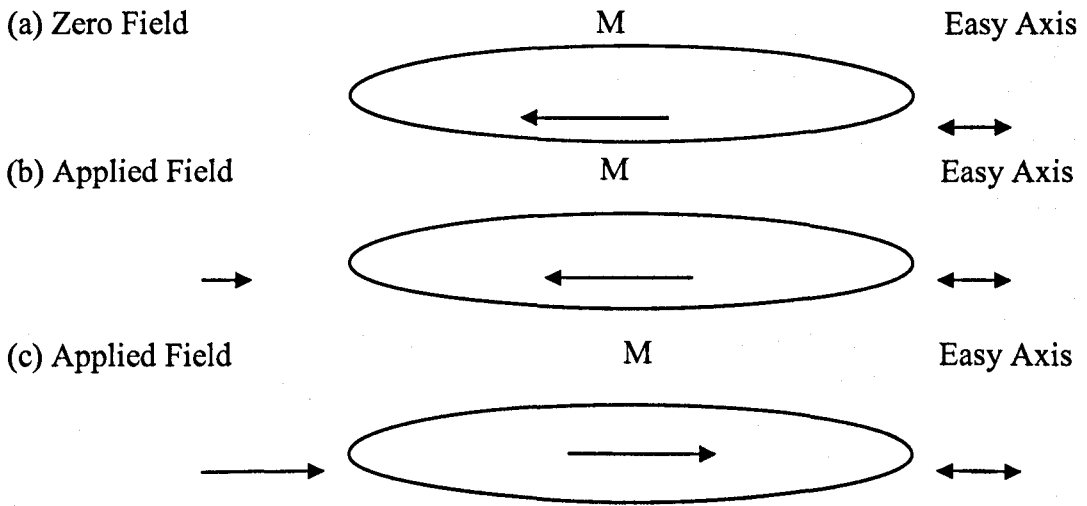


Figure 4.6 Behaviour of magnetisation with field applied in the easy-axis direction.

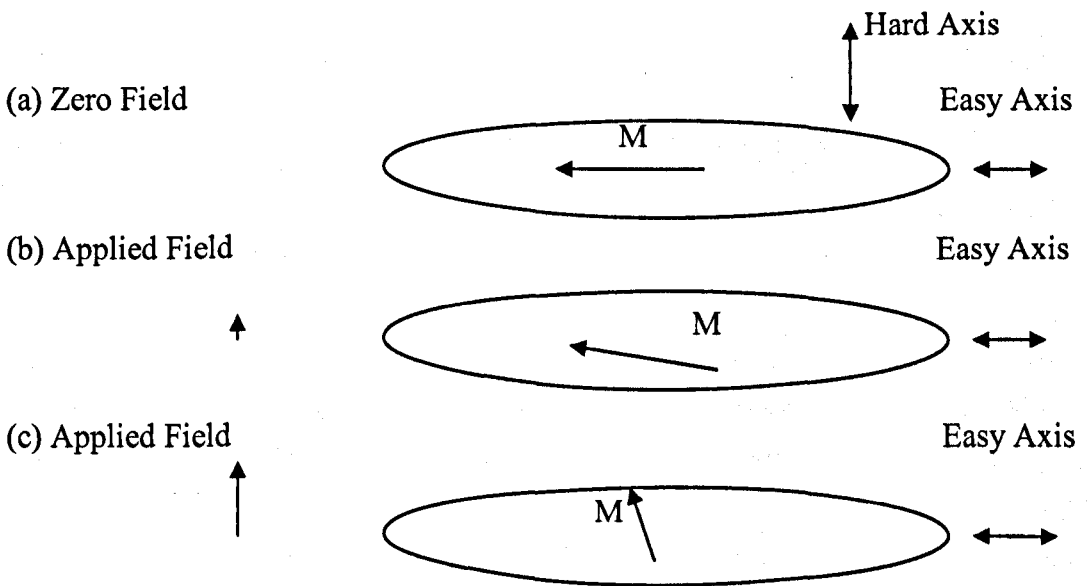


Figure 4.7 Behaviour of magnetisation with field applied in the hard-axis direction.

For MHz applications the hard axis loop is preferred. The performance of Ni-Fe films at low frequency does not degrade with increasing frequency, with frequencies up to 100 MHz predicting similar performance [4.23, 4.27-4.28]. Thus, coherent rotation can be used to almost completely eliminate hysteresis loss.

## 4.5 Experimental results for DC Nickel-Iron electrodeposition

This section outlines the data recorded from the preliminary investigation into Ni-Fe electrodeposition. The experimental set-up, description of analysis procedure and discussion of results for the DC deposition of Ni-Fe are presented.

### 4.5.1 DC Plating Cell

The DC waveform is the simplest waveform with the only variable being the cathodic current density. Ni-Fe samples with varying composition were fabricated with DC deposition with the  $Ni_{80}Fe_{20}$  composition the primary area of interest.  $Ni_{80}Fe_{20}$  is the film of interest due to its high saturation flux density of approximately 1T, good relative permeability, low coercivity and near zero magnetostriction. A sulphate electrolyte was selected due to its well documented properties during the extensive research into Ni-Fe deposition covered in section 4.2. The composition of the electrolyte is provided in Table 4.1.

The experimental set-up was custom made and consisted of two stationary parallel planar electrodes. The plating cell was a 2 litre beaker containing the electrolyte, a high purity sacrificial nickel anode, at a positive potential, and a wafer holder cathode constructed of tough-set plastic, at a negative potential. The anode and cathode are approximately 7cm apart. The cathode is a 3 inch glass wafer with a highly conductive seed layer of titanium and copper. A 10 $\mu$ m thick layer of AZ 9260 photoresist is applied and patterned to the seed layer. The exposed regions of the seed layer outline the profile of the core geometry. The deposition of the seed layer and patterning of the photoresist are covered in Chapter 7. The cathode holder was constructed from tough-set as this material is chemically resistant to the electrolyte, therefore would not erode and contaminate the electrolyte. The plating cell has a lid to limit environmental contamination such as dust from entering the electrolyte. The constructed cell can be viewed in Fig.4.8 (a) & (b). The plating cell of Fig 4.8 is sufficient for preliminary experiments. However reliable and repeatable manufacturing would require monitoring of the depleted iron, e.g. acoustic wave monitoring [4.29], filtration, controlled agitation etc.

The influence of intrinsic thin film properties, discussed in Chapter 2, highlighted the importance of performing the magnetic characterisation in-situ. Therefore the

electrodeposits analysed are of exact dimensions to that incorporated into prototype devices in Chapter 7.

Component: NiFe	Quantity
$NiSO_4 \cdot 6H_2O$	200 (g/l)
$NiCl_2 \cdot 6H_2O$	5 (g/l)
$FeSO_4 \cdot 7H_2O$	8 (g/l)
$H_3BO_3$	25 (g/l)
Saccharin	3 (g/l)
pH	2.5-3
Temperature	25-30°C
Current Density	13 mA/cm <sup>2</sup>

Table 4.1 Electrolyte composition of Nickel-Iron.

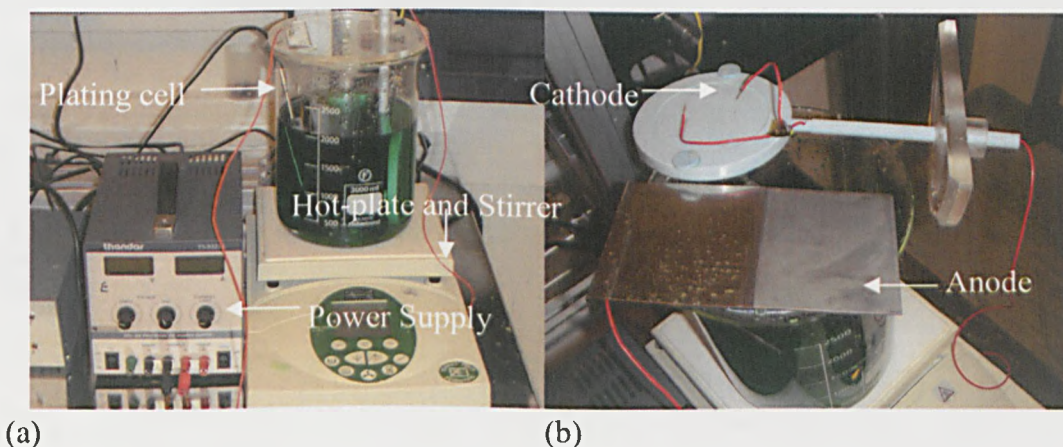


Figure 4.8 Ni-Fe electroplating cell (a) Electroplating cell positioned on top of a hot-plate and stirrer with a DC power supply, (b) Image of the cathode wafer holder, background, and sacrificial nickel anode, foreground.

The nickel sulfate  $NiSO_4 \cdot 6H_2O$  and nickel chloride  $NiCl_2 \cdot 6H_2O$  each provide  $Ni^{2+}$  ions. The ferrous sulfate  $FeSO_4 \cdot 7H_2O$  provides  $Fe^{2+}$  ions. The Ni-Fe bath is prepared by first weighing the various constituents of the electrolyte. The components are then mixed in a glass beaker, and the beaker is filled with DI water to 2000 ml. A magnetic stirrer is used to stir the bath overnight. In addition to the metal salts, the bath also contains boric acid,  $H_3BO_3$ , and saccharin. Boric acid is a buffering agent that is used

to stabilize the pH in the cathode film. The saccharin is added to the solution to reduce the residual stress in the metals deposited.

During deposition the plating cell is removed from the hotplate and stirrer. The hotplate and stirrer contain a magnet. The magnet could create undesired domain alignment during deposition and affect the magnetic response of the alloy. Agitation was not applied during deposition but reapplied when the plating cell was returned to the hotplate and stirrer to help maintain a uniform distribution of Ni and Fe ions.

#### 4.5.2 Experimental analysis of DC Ni-Fe

Firstly, the area of exposed seed layer for the cathode wafer was determined. Values of applied current in accordance with prior work, section 4.2, were selected to produce a current density in the range of 5-50 mA/cm<sup>2</sup>. To apply this current to the cathode the voltage of the power supply must overcome the ohmic resistance of the electrolyte. With the anode and cathode connected to the positive and negative terminals of the power supply, respectively, the voltage value was incremented until the required current was applied. A voltage 10% greater than the minimum was applied to account for any changes in resistance that may occur during deposition due to the depletion of ions.

The rate of deposition, or deposit growth rate, for the range of current density values was estimated:

$$Thk = \frac{J.MW.time}{\delta_{Ni}Faraday.n_{el}} \quad (4.4)$$

Where *Thk* is the thickness of nickel deposited in cm; *J* is current density (A/cm<sup>2</sup>); *MW* is molecular weight of nickel (58.71 g/mol); *Time* is the plating time in second;  $\delta_{Ni}$  is the density of nickel (8.9 g/cm<sup>3</sup>); Faraday is a constant (96488 C/mol);  $n_{el}=2$  is the number of electrons.

The Fe content of the electrolyte is less than 4% of the electrolyte composition compared to Ni sulphate and chloride content, and, due to the anomalous codeposition effect, a Ni rich alloy is anticipated. The molecular weight and density of Ni are therefore used in Eq(4.4). The results of Eq(4.4) are displayed in Fig 4.9 which displays

a trend of increased deposit thickness with time, and increased growth rate with increased current density.

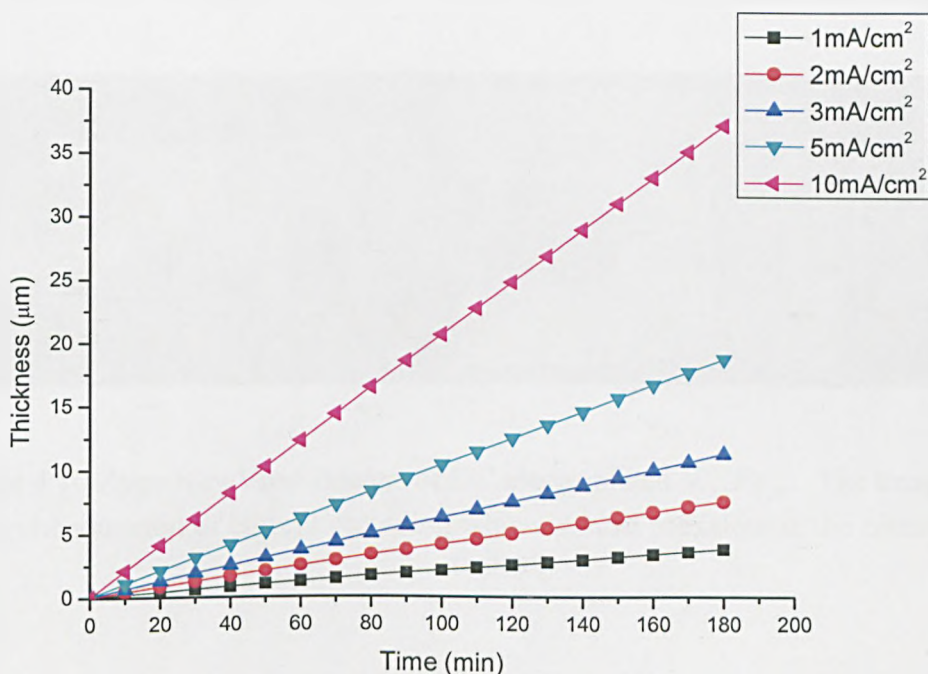


Figure 4.9 Deposition rate of Ni at varying values of current density. The deposition rate of Ni is used as a guide to the deposition rate of Ni-Fe.

#### 4.5.2.1 White light interferometer analysis

The actual deposition rate was recorded using white light phase shifting interferometer Zygo Viewmeter 5200. Firstly, a reference measurement with the patterned cathode wafer prior to any electrodeposition was recorded. The same measurement was then performed at the mid-point of the estimated deposition period followed by a final measurement at the end of the period. The recorded results for 5mA/cm<sup>2</sup> and 10mA/cm<sup>2</sup> exhibit a similar linear growth in deposit thickness with constant current density and increasing time. The analytical error compared to the experimental data was under 10%. This difference is attributed to the non-ideal values for Ni-Fe in Eq(4.4) and chemical side reactions such as hydrogen evolution.

Fig.4.10 displays an image of the 3D plot obtained by the Zygo Viewmeter 5200 for an electroplated  $Ni_{80}Fe_{20}$  deposit. The surface profile of the thin film displays a deposit surface with minimal pitting. The DC electroplated sample exhibits current crowding effects in the corner of the deposit. The photoresist is an insulator and forms a mould



for the electroplated structure, areas of unexposed seed layer results in a non-uniform distribution of current and therefore of deposit. This is illustrated in Fig 4.11.

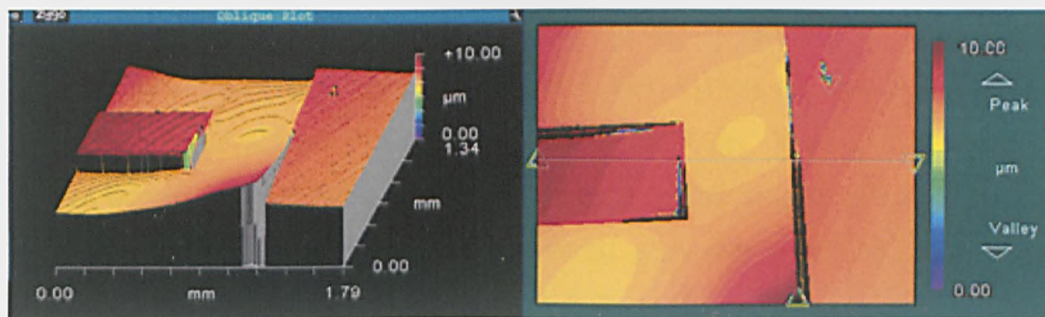


Figure 4.10 Zygo NewView images of DC electroplated  $Ni_{80}Fe_{20}$ . The images display the phenomenon of current crowding which is most prevalent in the corners of the deposit.

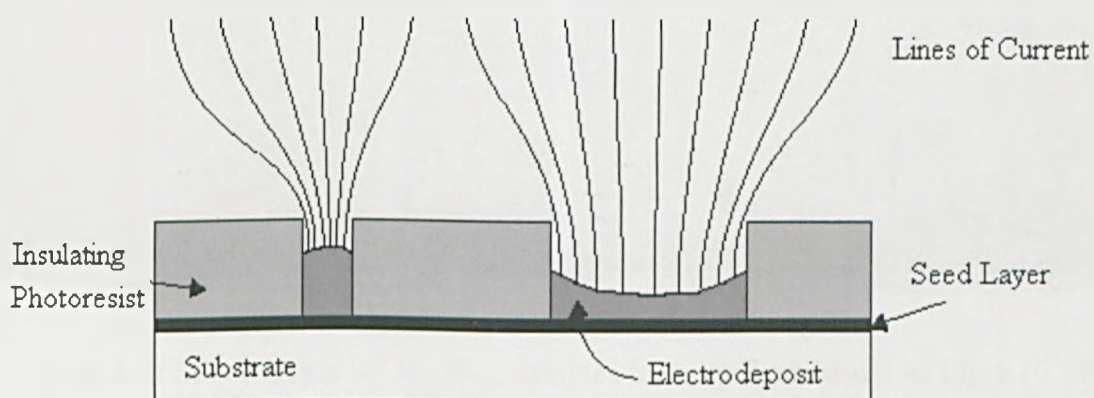


Figure 4.11 Illustration of the current crowding phenomena that occurs due to non-uniform distribution of current density.

Micro-inductor and transformer applications require a core material with uniform cross sectional area (c.s.a). Non-uniformity of the core c.s.a produces a non-uniform distribution of magnetic flux. Areas of the core will become hot-spots due to flux crowding and become prone to thermal failure. In addition, a non-uniform flux density will generate errors in analytical predictions of inductance and core loss that typically assume a uniform flux density.

#### 4.5.2.2 SEM-EDX Analysis

Scanning Electron Microscope with Energy Dispersive X-ray analysis (SEM-EDX) examined the surface profile and composition of the electroplated films. The SEM image of the  $Ni_{80}Fe_{20}$  deposit is displayed Fig 4.12; the image shows the deposit to be smooth and relatively defect free. Without the use of agitation during deposition there was the possibility that hydrogen bubbles that evolve as side reactions within the electrolyte could adhere to the surface of the cathode. In this circumstance the ions cannot deposit on the surface of the cathode resulting in a pit or cavity forming in the deposit. Pitting is undesirable as the overall core area is reduced and the pits act as miniature air gaps increasing the levels of leakage flux.

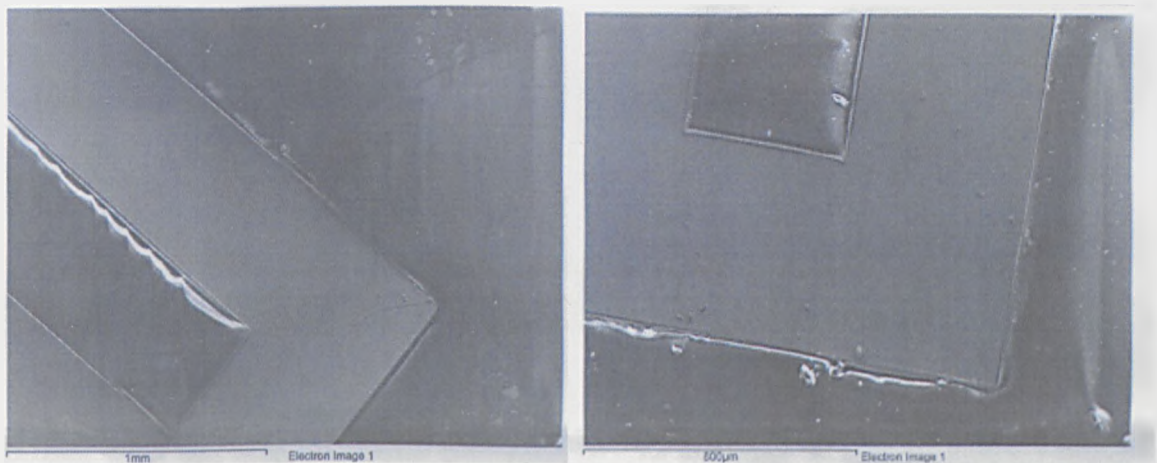


Figure 4.12 SEM images of  $Ni_{80}Fe_{20}$  samples from the same wafer as Fig 4.10. The samples exhibit a smooth morphology, high purity and minimal pitting. Pitting is observable on the right hand side.

The output of an EDX analysis is an EDX spectrum as shown in Fig 4.13. The EDX spectrum displays peaks corresponding to the energy levels of the X-rays released. Each of these peaks is unique to an atom, and therefore corresponds to a single element. The higher a peak in a spectrum, the more concentrated the element is in the specimen. All of the samples fabricated exhibited a high level of purity,  $\geq 99\%$ . Hence the co-deposition of species such as sulphur from the additives or environmental contaminants was minimal. The variation of the current density with the DC waveform results in anomalous co-deposition in Ni-Fe thin films as shown in Fig.4.14. The Fe content for the DC deposition decreases with increasing average current density. Dahms and Croll surmised that iron hydroxides, which form as a result of the rise in pH at the cathode



during co-deposition of hydrogen, inhibit nickel deposition resulting in anomalous co-deposition [4.5].

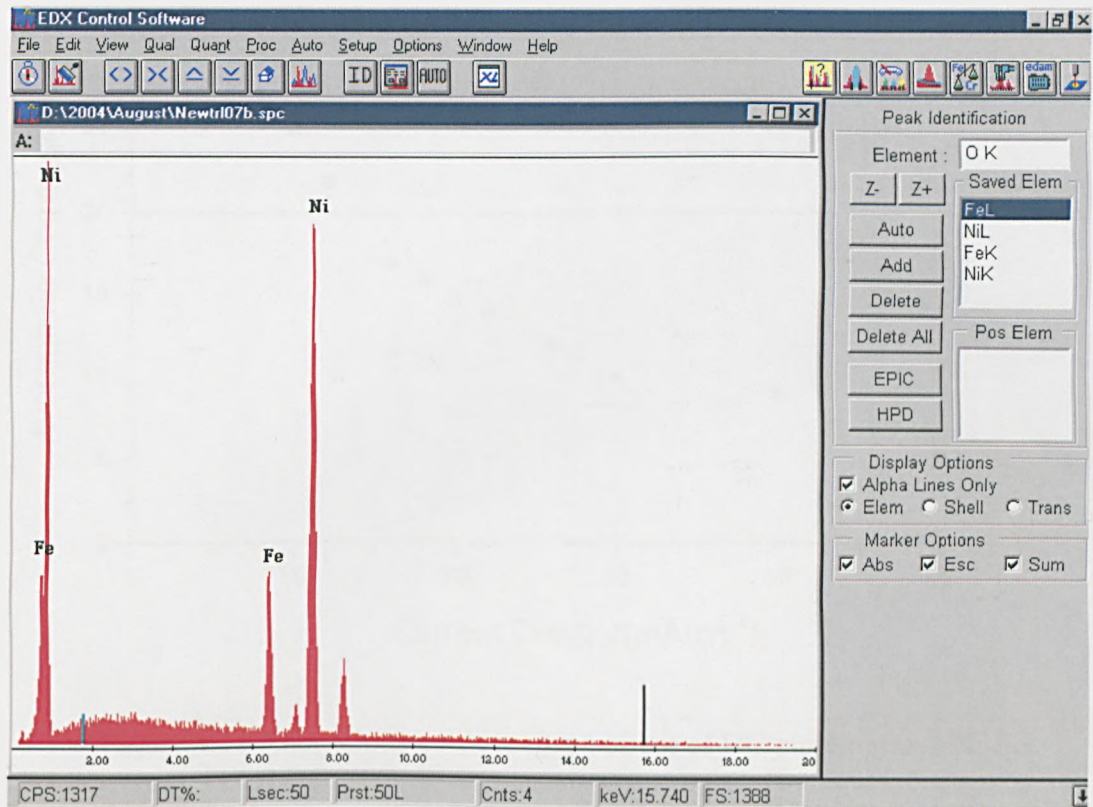


Figure 4.13 EDX spectrum of the  $Ni_{80}Fe_{20}$ . The Ni concentration is greater than that of Fe indicated by the respective peaks of the EDX spectrum. If the film contained contaminants then this would have been indicated on the EDX spectrum.

In view of this a small sample of the electrolyte was withdrawn with a syringe in order to measure the pH. The pH increased from 2.5 in the bulk of the solution to 6 near the cathode. The accuracy of the actual pH value is arguable since disturbing the electrolyte affects the build-up of species at the cathode. As shown in Fig.4.14 a current density of approximately  $13\text{mA}/\text{cm}^2$  achieves the 80:20 composition for the DC waveform. Composition variation of Ni-Fe films has a direct affect on the permeability, coercivity, resistivity and saturation flux density of the Ni-Fe deposit [4.27]. Therefore, it is important to achieve a uniform current distribution to obtain the required film composition and desirable film properties.



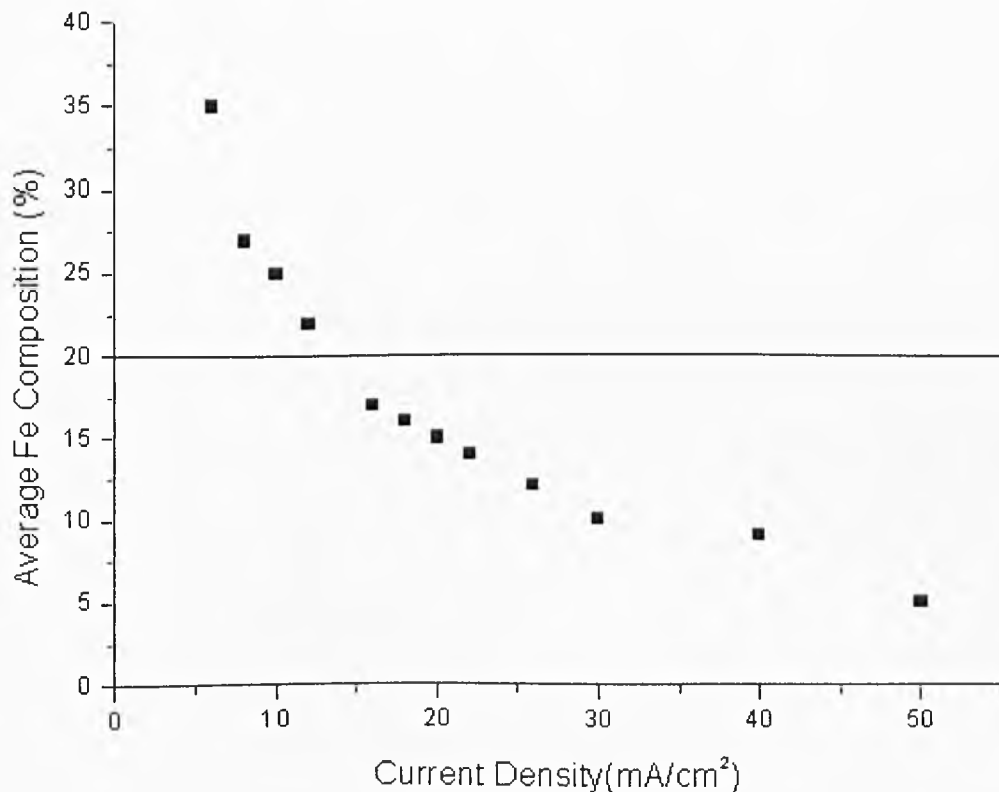


Figure 4.14 Anomalous co-deposition effect of DC electroplated Ni-Fe

#### 4.5.2.3 AFM and XDA Analysis

The grain size and crystal structure influence the magnetic properties of a ferromagnetic material [4.30, 4.31]. Therefore, grain size and crystal structure of the various samples were analysed to assess the influence of varying current density and composition. An Atomic Force Microscope (AFM) and X-ray Dispersion Analysis (XDA) were used to record grain size and crystal structure, respectively. The AFM has two common modes of operation: contact and non-contact mode. In non-contact mode the AFM cantilever is vibrated near the surface of the sample near its resonant frequency with amplitude of a few tens of angstroms. The AFM then detects changes in the resonant frequency or vibrational amplitude as the tip comes near the surface. The non-contact mode was selected as it minimises damage to the measuring tip of the AFM and the sample being analysed.

AFM data for a Ni-Fe sample fabricated at 13mA/cm<sup>2</sup> is shown in Fig 4.15(a)&(b). The AFM data indicates an average grain size of 57nm for a deposition composition of  $Ni_{80}Fe_{20}$ . Initially it was surmised that a grain size reduction might occur with increasing current density, as has been recorded for Ni and Cu grain size with increased

DC waveform current density in prior work [4.8, 4.32]. However the results displayed in Fig 4.16 do not indicate this trend. Fig 4.16 displays the variation in grain size with Fe content of the film. The grain size decreases with increasing Fe content in the electrodeposit, which is a result of reduced current density. The co-deposited Fe produces a grain refining effect which is more profound at increased Fe content. The influence of the Fe on grain size was confirmed by comparing the results of a pure Ni electrodeposited from the same plating bath, without Fe sulphate, and fabricated at 13mA/cm<sup>2</sup>. The Ni sample consisted of grains with an average size of 100 nm, thus, the reduction to an average grain size of 57 nm for the  $Ni_{80}Fe_{20}$  sample is attributed to grain refining of the Fe.

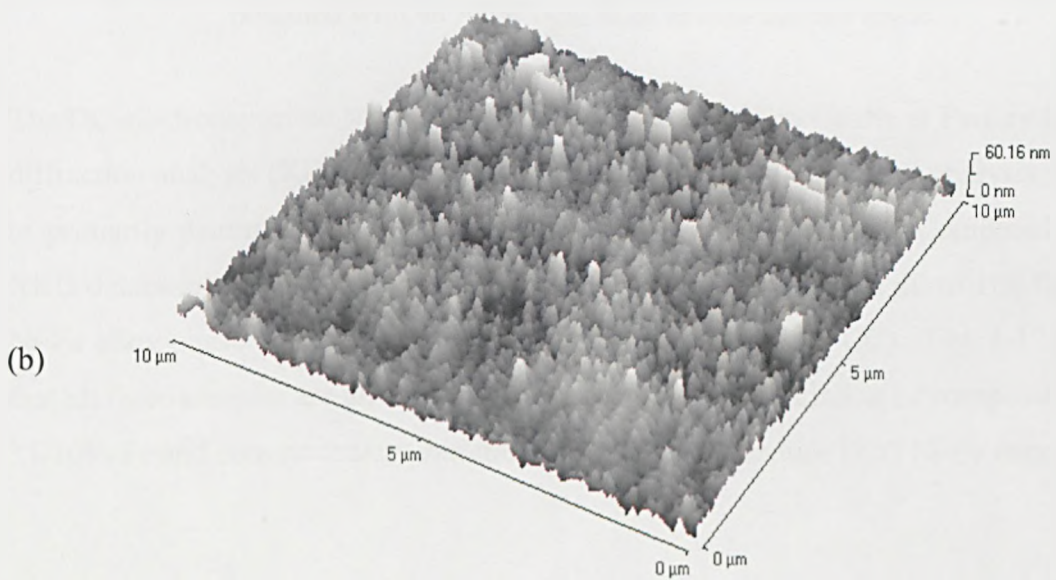
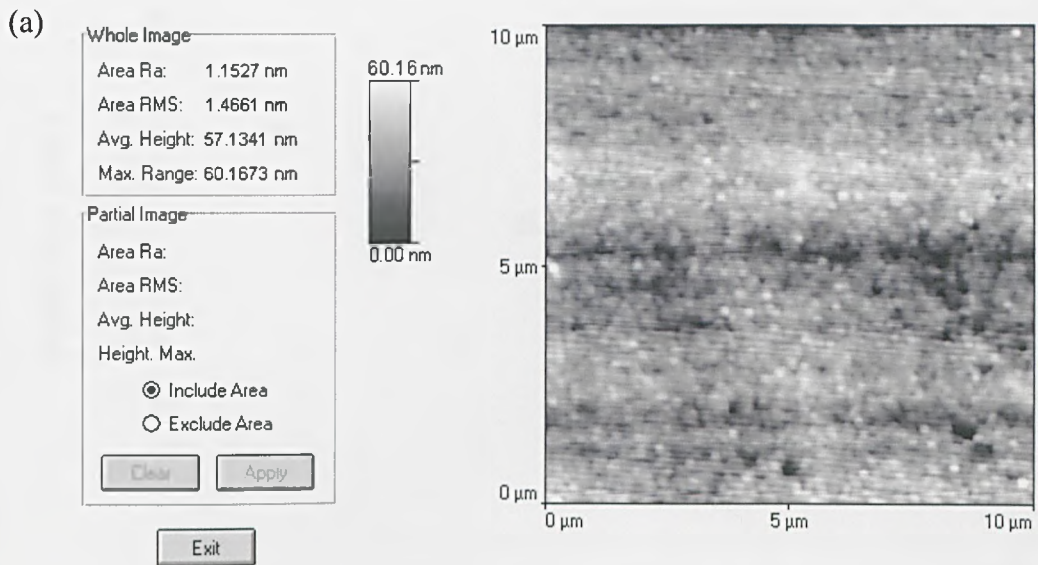


Figure 4.15 (a) AFM data of a Ni-Fe sample fabricated at  $13\text{mA}/\text{cm}^2$ , and (b) a 3D plot of the surface profile of a  $10\mu\text{m} \times 10\mu\text{m}$  area of the same sample.

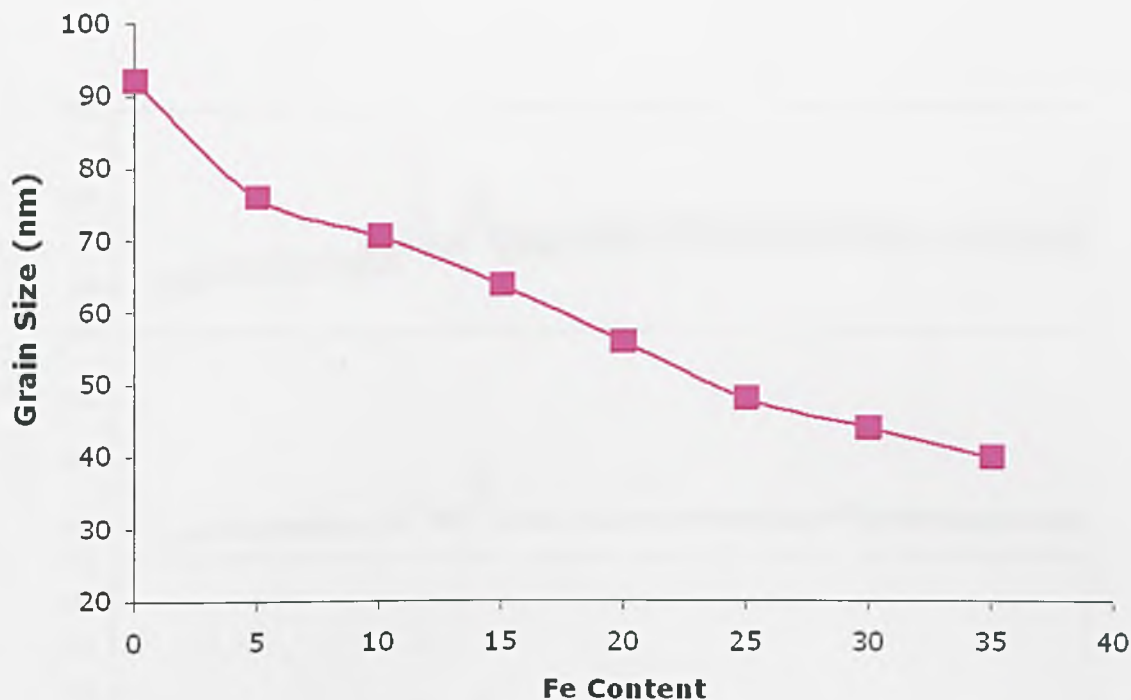


Figure 4.16 Grain Size vs. Fe content of the Ni-Fe samples. The grain size was obtained with an AFM operating in non-contact mode.

The DC electrodeposited samples were sent to the Thin Film Centre at Paisley for X-ray diffraction analysis (XDA), the results are displayed in Fig 4.17. The analysis was used to primarily determine the crystal structure of the Ni-Fe samples. Compared with an XRD database and by refining with software, the two peaks from 40 to 100 match the Ni-Fe alloy phase very well, this phase is face centre cubic (FCC). Fig. 4.17 displays that all three samples are all FCC in structure. Hence the variation of composition from 35-10% Fe and current density variation 6-30 mA/cm<sup>2</sup> produce FCC Ni-Fe deposits.

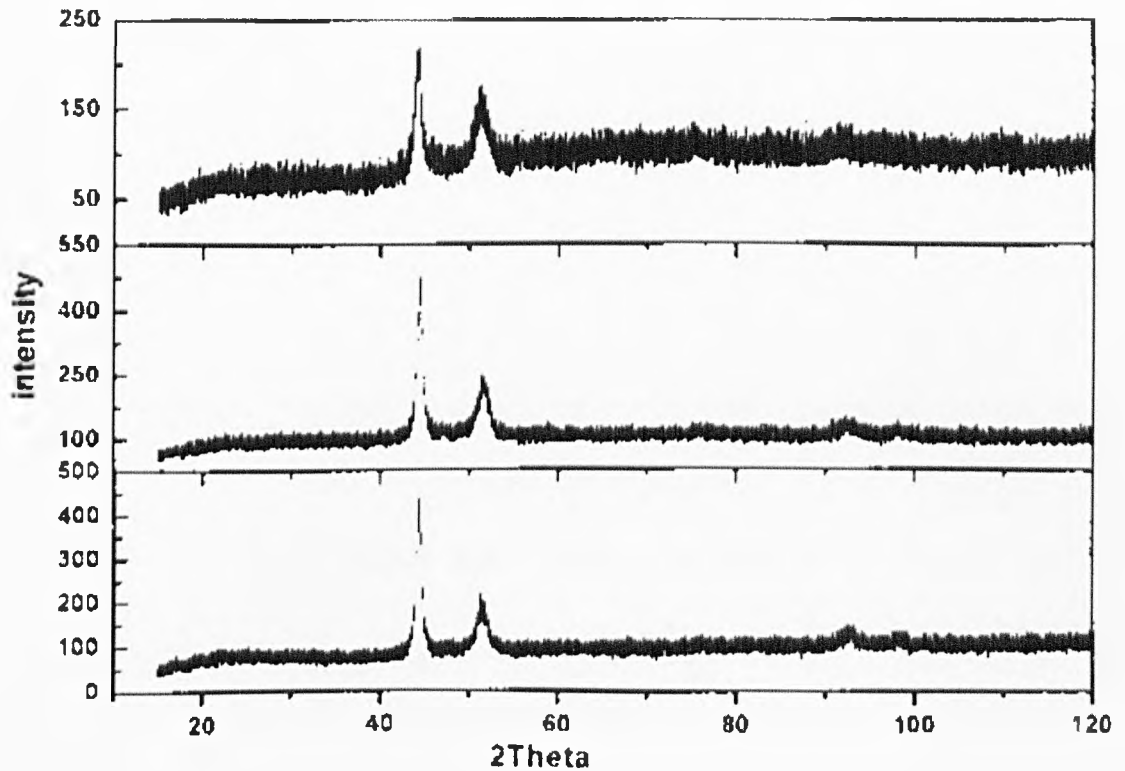


Figure 4.17 XRD analysis of Ni-Fe samples ranging in composition from (1) 65:35, (2) 80:20, and (3) 90:10

#### 4.5.2.4 Electrical and magnetic characterisation

Resistivity measurements were performed by Raytheon Systems Limited (RSL) at Glenrothes, Scotland. The resistivity determines the maximum thickness of each laminate. The laminate is typically no greater than one skin depth in order to reduce losses via eddy currents. Therefore the resistivity is a vital parameter in determining the frequency of operation of a magnetic film and the number of laminate layers required for a given core area. The cost model of a micro-inductor/transformer is likely to be related to the number of laminate layers.

The resistivity was determined using a four-point probe technique [4.33]. Fig.4.18 displays the results of the resistivity measurements for Ni-Fe alloys of varying composition.

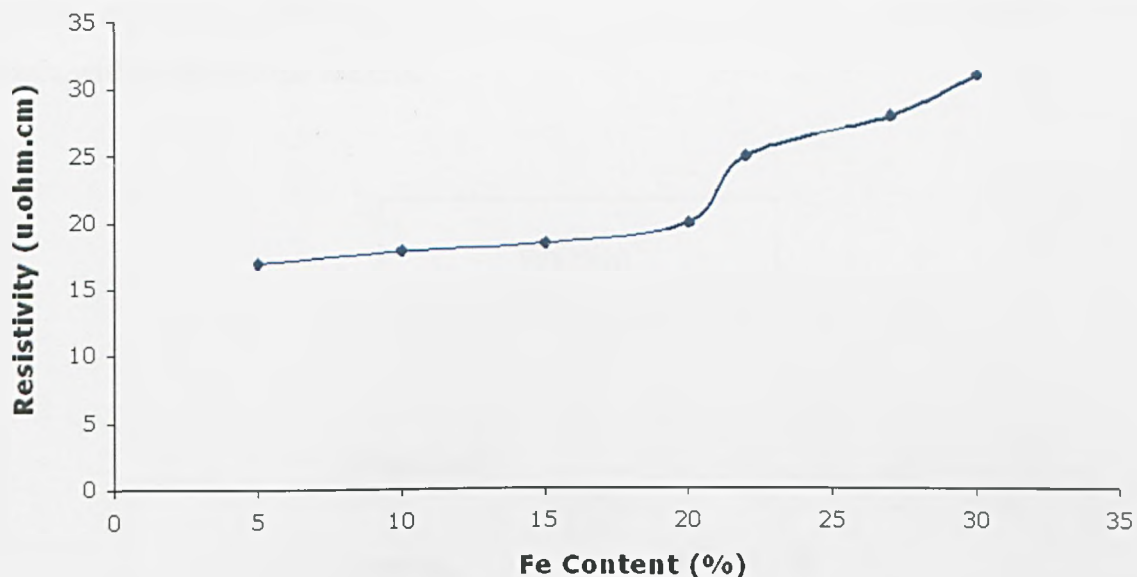


Figure 4.18 Resistivity measurements

The resistivity of Ni is less than Fe,  $7\text{m}\Omega\cdot\text{cm}$  and  $9.7\text{m}\Omega\cdot\text{cm}$  respectively. The reduction in Fe content from 25% to 20% resulted in a drop in resistivity of 23%. The central factor in the variation of the resistivity may be due to the decreased grain size and not necessarily the composition variation. Grain boundary electron scattering effects become increasingly important in materials with very small grain size. In fact, for nanocrystalline materials, considerable increases in the overall electrical resistivity have been observed [4.34, 4.35]. The relationship between grain size and film resistivity is examined in more detail in Chapter 5.

Two techniques were used for the magnetic characterisation of the DC samples; a superconducting quantum interference device (SQUID) and vibrating sample magnetometer (VSM). Any magnetic specimen in a uniform magnetic field produces a distortion to that field, in-turn the flux distribution is affected and can be detected by an inductive coil. This is the basic principle for VSM and SQUID magnetometer. The VSM measurements were performed at the University of Leeds under the guidance of Prof. Cywinski, and the SQUID measurements were performed at the University of Edinburgh by Prof. Harrison.

The VSM method is based on the magnetic flux change in a coil when a magnetic sample is vibrated near it, Fig 4.19. The sample is mounted to the end of a glass rod; the electromagnet produces a uniform field to magnetise the sample and the field can be



swept; the pick up coils are clamped to the magnet in order to avoid vibration of the coils with respect to the magnet.

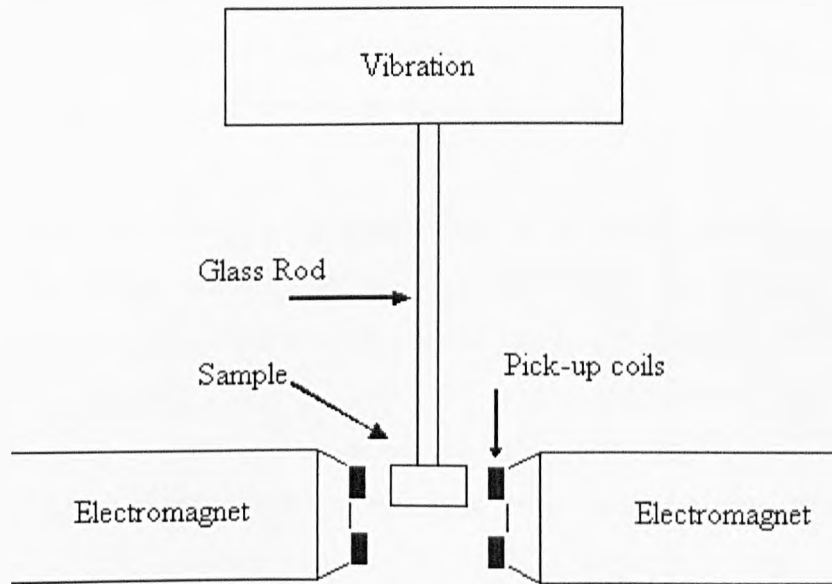


Figure 4.19 Schematic of the VSM. The sample is vibrated near a pick-up coil, and the magnetic flux change is detected, which is proportional to the magnetic moment of the sample.

During the measurement, the sample is vibrated at small amplitude with a frequency of 70 Hz, which produces a field distortion in an AC manner. The field distortion is detected by pick-up coils and then computed with conventional AC processing equipment. The sample's magnetic moment is obtained according to Faraday's Law of induction, namely that a potential drop,  $V$ , is induced across the pick-up coils due to a change of flux:

$$V = N \frac{d\Phi}{dt} \quad (4.5)$$

where  $N$  is the number of turns in the detection coils and  $\Phi$  is the flux in the coils, which is proportional to the magnetic moment of the sample.

The Superconducting quantum interface device (SQUID) is the most sensitive device available for measuring magnetic fields. The basic element of a SQUID is a superconducting loop interrupted in two places by Josephson junctions (a thin layer of insulating material sandwiched between two superconducting layers). When a sufficient electrical current is conducted across the SQUID body, a voltage is generated proportional to the strength of any nearby magnetic fields.

The SQUID in the SQUID magnetometer is the source of the instrument's sensitivity, but it does not detect directly the magnetic field from the sample. During the measurement, the sample moves through a set of superconducting detection coils, which is illustrated in Fig 4.20. This detection coil is set to connect to the SQUID with superconducting wires, and it is located outside the sample chamber and at the centre of the superconducting electromagnet, which generates a uniform field perpendicular to the coil. As the sample moves through the coils, the magnetic moment of the sample induces an electric current in the detection coils. Because the detection coils and the connecting wires form a closed superconducting loop, any change of magnetic flux in the detection coils, which is proportional to the magnetic moment of the sample, produces a change in the persistent current in the detection circuit. The SQUID sensor is inductively coupled with the detection coils, so the SQUID electronics produces an output voltage that is strictly proportional to the flowing current. Therefore, SQUID essentially functions as an extremely sensitive current to voltage converter.



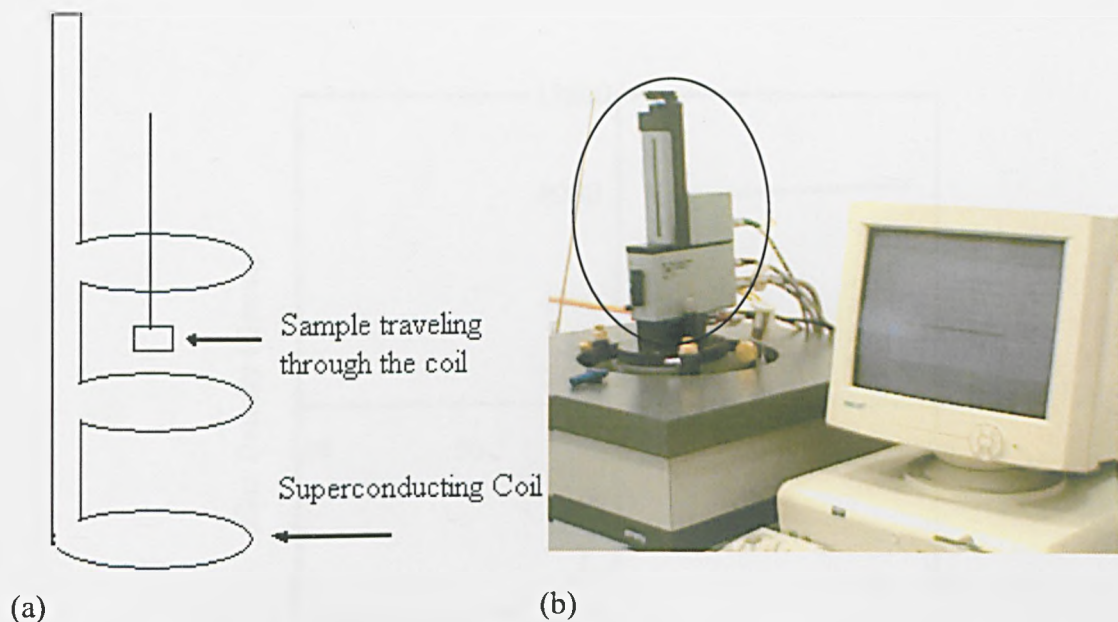


Figure 4.20 (a) A schematic of three coils configured as a second-order gradiometer is used as superconducting detection coils in SQUID magnetometer. (b) Edinburgh University's SQUID with the sample holder and detection coil chamber encircled.

The detection coil is a single piece of superconducting wire wound in a set of three coils configured as a second-order gradiometer. In this configuration, the upper coil is a single turn wound clockwise, the centre coil comprises two turns wound counter-clockwise, and the bottom coil is a single turn wound clockwise. When the magnetic field is changing uniformly through the entire coil, the flux change in the two-turn centre coil will be exactly cancelled by the flux change in the single-turn top and bottom coils. But when the sample is travelling through the coil, the coil set measures the local changes in magnetic flux density produced by the sample, and the magnetic moment of the sample can be obtained according to Faradays law of induction.

Results for the magnetic characterisation of the DC samples were identical for each device. The SQUID measurement requires the sample to travel through the detection coils; this incurs a time delay in the measurement cycle. In comparison, the VSM produced results in under 15mins in comparison to 1 hour for the SQUID; therefore the VSM was the method of choice for the rest of this investigation.

Fig 4.21 displays the hysteresis response of the DC electroplated  $Ni_{80}Fe_{20}$  sample.

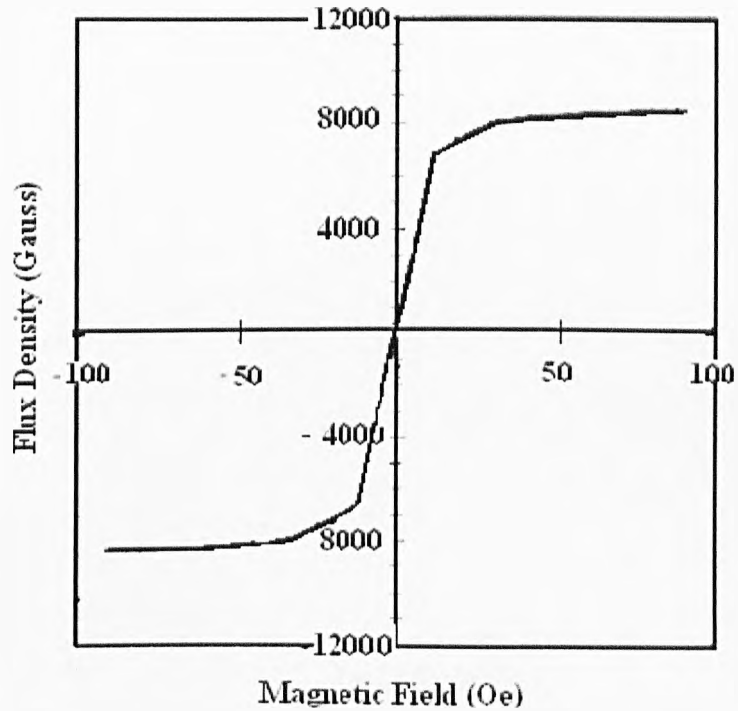


Figure 4.21 Hysteresis response of DC electroplated  $Ni_{80}Fe_{20}$  recorded from the VSM. Image courtesy of Leeds University.

The data obtained from Fig.4.21 and the electrical characterization is contained in Table 4.2. The five parameters: resistivity, flux density, coercivity, relative permeability and film thickness allow an analytical assessment of the film's performance. Details are contained in Chapter 6. The values of saturation flux density, Tesla, and coercivity, Oe, of Ni-Fe alloys with varying Fe content, 5-30%, are displayed in Fig 4.22 & Fig 4.23, respectively.

Material	$\rho_s$ ( $\mu\Omega.cm^2$ )	$B_{sat}$ (T)	$H_c$ (Oe)	$\mu_r$	Film thickness ( $\mu m$ )
NiFe	20	0.8	3	2000	10

Table 4.2 Magnetic and Electrical Properties of DC  $Ni_{80}Fe_{20}$

In Fig. 4.22 the saturation magnetisation increases linearly with increasing Fe content due to the increased contribution of the Fe atoms to the overall magnetic moment observed in each sample. This trend agrees well with prior work [4.27]. Fig 4.23 displays a reduction in coercivity with increasing Fe content, or decreasing grain size. The reduction in coercivity was expected as Ni-Fe alloys in the 20-25% Fe range

exhibit low coercivities as a result of low or zero magnetostriction and low values of anisotropy constants [4.28].

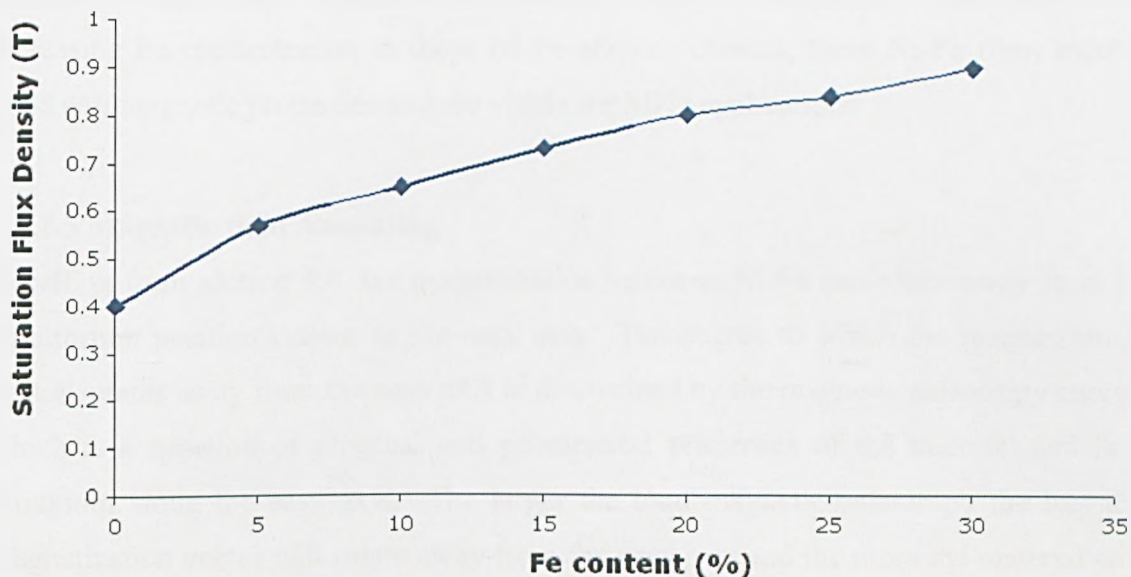


Figure 4.22 Saturation Flux Density (T) vs. Fe content of the Ni-Fe samples. The saturation flux density increases with Fe content of the film.

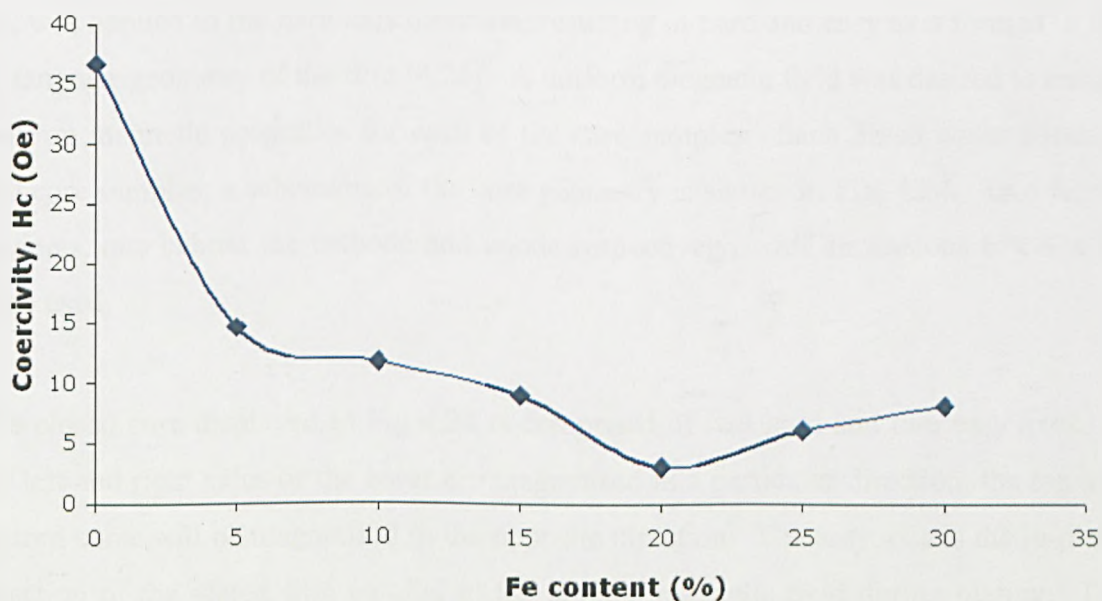


Figure 4.23 Coercivity vs. Fe content of the Ni-Fe samples. The 80:20 composition displays a minimal coercivity value of 3 Oe.

In summary, good soft magnetic material is said to have a coercivity below 6 Oe, or 500A/m, and the nanocrystalline Ni-Fe in the range 15%-30% Fe satisfies this demand. The saturation magnetization of the electrodeposited Ni-Fe increases linearly with increasing Fe content up to 30% Fe. Currently, it is assumed that saturation is a

compositional dependent parameter but the influence of grain size will be assessed in Chapter 5. The coercivity of the Ni-Fe samples decreases with increasing Fe content and decreasing grain size. It is believed that low magnetostriction combined with low values of anisotropy constants, can account for this decrease in coercivity with increasing Fe concentration in these Ni-Fe alloys. Overall, these Ni-Fe films exhibit good soft magnetic properties and are viable for MHz applications.

#### **4.5.2.5 Magnetic field Annealing**

Recalling from section 4.4, the magnetization vector in Ni-Fe can rotate away from its equilibrium position known as the easy axis. The degree to which the magnetization vector rotates away from the easy axis is determined by the magnetic anisotropy energy which is a function of physical and geometrical properties of the material and is a minimum along the easy axis. The larger the total magnetic anisotropy the less the magnetization vector will rotate away from the easy axis and the more the material will act like a permanent-magnetic material. To fabricate magnetically anisotropic Ni-Fe, electrodeposition takes place in the presence of a magnetic field. The magnetic field must be strong enough to overcome the magnetic anisotropy. A DC magnetic field, 800 Oe, was applied in the hard axis direction, resulting in hard and easy axis formed in the rectangular geometry of the film [4.26]. A uniform magnetic field was desired to ensure uniform magnetic properties for each of the core samples. Each 3inch wafer contains 150 core samples; a schematic of the core geometry is shown in Fig. 4.24. Two ferrite magnets, one behind the cathode and anode respectively, with dimensions 6"x 4"x 6" were used.

The closed core displayed in Fig 4.24 is comprised of two hard and two easy axes. If the left and right sides of the cores are magnetised in a particular direction, the top and bottom cores will be magnetised in the opposite direction. The easy axis is the in-plane direction of the plated film parallel to the applied magnetic field during plating. The hard axis is the in-plane direction of the film perpendicular to the applied magnetic field. The annealing field is of sufficient strength to overcome the anisotropy energy, and aligns the magnetic moments along the field direction. With a composition of 80:20 and the addition of stress relieving additives magnetostriction is a minimum. Therefore, the anisotropy energy is the dominant mechanism of magnetisation. This remains for as long as the film operates under the Curie temperature, which would result in thermal energy producing magnetic disorder.

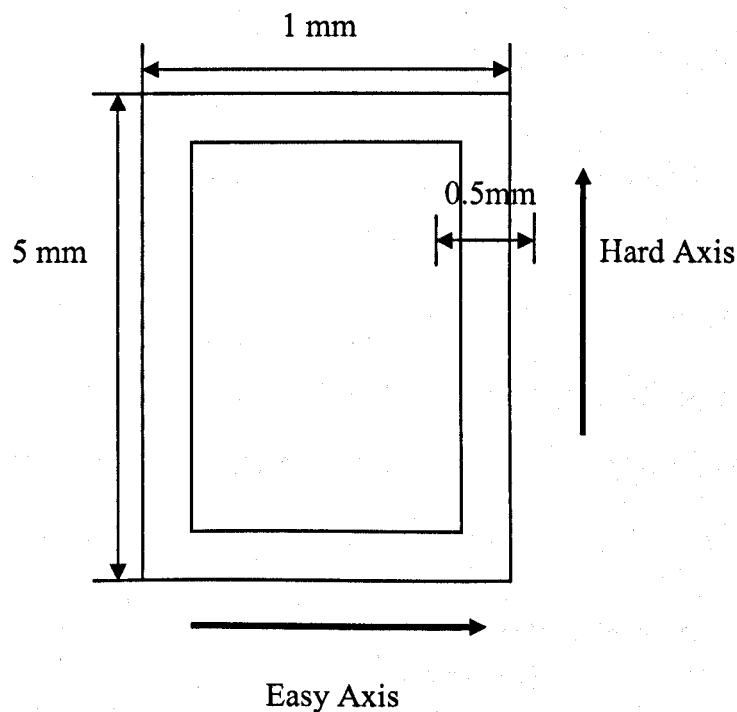


Figure 4.24 Schematic of the Core geometry with magnetic easy and hard axis indicated.

Prior work has indicated that a variation of the magnetic field strength can produce a variation in the relative permeability of the film while maintaining high saturation flux density and minimal coercivity [4.23]. Therefore the fabrication of a *tunable* thin film is possible. Figure 4.25 displays the results of the VSM analysis of a DC anisotropic Ni-Fe sample.

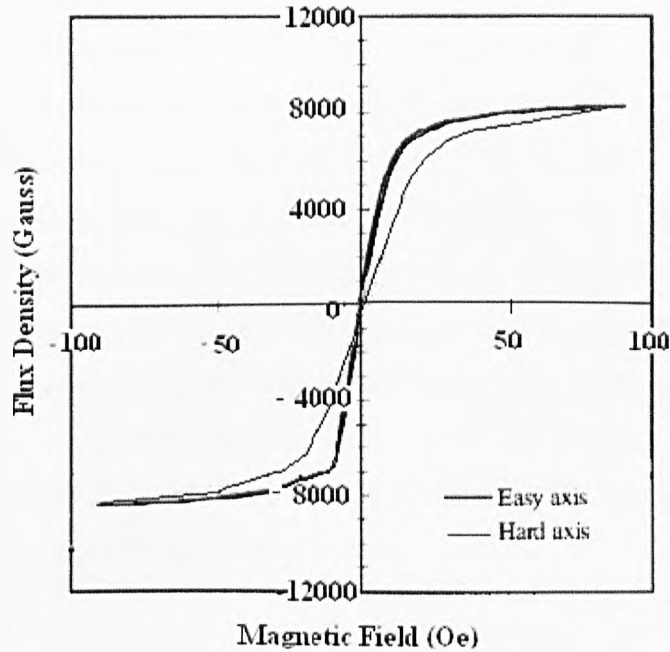


Figure 4.25 Anisotropic Ni-Fe after magnetic field annealing in DC field of 300 A/m. Image courtesy of Leeds University.

The properties of the anisotropic and isotropic  $Ni_{80}Fe_{20}$  are compared in Table 4.3.

Material	$\rho_s$ ( $\mu\Omega.cm^2$ )	$B_{sat}$ (T)	$H_c$ (Oe)	$\mu_r$	Film thickness ( $\mu m$ )
NiFe	20	0.8	3	2000	10
NiFe anisotropic	20	0.8	Easy 0.4 Hard 0.635	Easy 2200 Hard 1300	10

Table 4.3 Anisotropic and Isotropic  $Ni_{80}Fe_{20}$  film properties.

The magnetisation rotation process has not produced the ideal response predicted by the Stoner-Wolfarth (S-W) model i.e.  $H_c = 0$ . The S-W model considers only single domain elements. It is almost impossible to produce a well defined ellipsoid single domain element and as the film is polycrystalline, magnetisation orientation varies from grain to grain due to magnetocrystalline anisotropy, so magnetisation is not uniformly distributed throughout the volume, therefore not a true single domain particle [4.28].

The relative permeability of the easy axis is greater than the isotropic value. The

permeability is determined by the magnetization of the film. The magnetization is determined by two processes: domain wall motion and domain rotation. At low frequencies domain wall motion is the dominant mechanism. An applied field causes domain walls to shift, and the motion results in a change in magnetization and hence flux density. Therefore, highly magnetized thin films will have larger low frequency permeability. However, highly magnetized films (easy axis) will have very small restoring forces and therefore are unable to follow rapidly varying fields. At high frequencies, the domain rotation becomes dominant and is responsible for permeability. The large domains of the easy axis cannot respond rapidly and struggle to rotate, while the small domains of the hard axis can rotate much more easily. As the films will be utilized at high frequency, 1-10 MHz, only films with the hard axis constituting the majority of magnetic path length are considered.

#### **4.6 Summary**

The fundamentals of electrodeposition have been covered. Prior work into electrolytes used to investigate the deposition process and properties of Ni-Fe have been reviewed. The theory behind magnetic field annealing has been presented and applied to the DC deposition of Ni-Fe. The anomalous co-deposition effect has been described and experimentally verified. The DC deposition results have indicated a variation of grain size with Fe content. Magnetic field annealing has been demonstrated to produce magnetically anisotropic films with favourable film properties. A Design of Experiment (DOE) is introduced in the next chapter that investigates more extensively the influence of waveform parameters on deposit structure and properties.



## References

- [4.1] M. J. Madou, "Fundamentals of Microfabrication," 2<sup>nd</sup> Edition, CRC Press, 2002.
- [4.2] R. K. Pandey, S. N Sahu, S. Chandra, "Handbook of semiconductor Electrodeposition," CRC Press, 1996.
- [4.3] S. Glasstone and T.E. Symes, "The electrodeposition of Iron-Nickel Alloys," *Trans. Faraday Soc.*, vol. 23, p.213, 1927.
- [4.4] S. Glasstone and T.E. Symes, "The cathodic behaviour of Alloys," *Trans. Faraday Soc.*, vol. 19, p.574, 1924.
- [4.5] H. Dahms and I. M. Croll, "The Anomalous Codeposition in Nickel-Iron Alloys", *J. Electrochem. Soc.*, vol.112, p.771, 1965.
- [4.6] J. Horkans, "On the Role of Buffers and Anions in NiFe Electrodeposition," *J. Electrochem. Soc.*, vol.26, p.1861, 1979.
- [4.7] J. Horkans, "Effect of Plating Parameters on Electrodeposition of NiFe," *J. Electrochem. Soc.*, vol. 128, Issue 12, pp.2604-2605, Dec. 1981.
- [4.8] M. Schlesinger and M. Paunovie, "Modern Electroplating," 4<sup>th</sup> edition, John Wiley & Sons, 2000.
- [4.9] L. T. Romankiw, "Thirty Years of Thin Film Magnetic Heads for the Hard Disc Drives—The Challenges and Solutions of Problems 30 Years Ago and Today," *J. Magn. Soc. Jpn.* vol.24, no. 1, pp.1–4, 2000.
- [4.10] T. L. Rama Char, "Electroplating and Electrorefining of Metals from the Sulfamate Bath," *Electroplating and Metal Finishing*, vol.11, p.343, 1958.
- [4.11] G. A. Sadakov, A. A. Mazin, V. V. Gordienko, V. V. Kovalev and N. T. Kudryavstev, "Electrodeposition of Ni-Fe Alloys from Sulfamate Electrolytes, and their Structure and Properties," *J. Applied Chem. U.S.S.R.*, vol. 53, pp. 2038-2042, 1980.
- [4.12] D.L. Grimmet, M. Schwartz, and K. Nobe, "Electrodeposition of Iron-Nickel (Invar) Alloys," *Plating Surface Finishing*, vol.75, p.94, Jun. 1988.
- [4.13] P. C. Andricacos and L. T. Romankiw, "Magnetically Soft Materials in Data Storage: Their Properties and Electrochemistry," *Advances in Electrochemical Science and Engineering*, vol. 3, Heinz Gerischer and Charles Tobias, Eds., VCH, New York, pp. 227–321, 1994.
- [4.14] C. K. S. Cheung, "Synthesis and Micro structural Characterisation of Electrodeposited Nanocrystalline Soft Magnets," PhD thesis, Queens University Kingston, Ontario, Canada, Aug. 2001.



- [4.15] J.C.Puippe and F.Leaman, "Theory and Practice of Pulse Plating", AESF, 1986.
- [4.16] S.S. Djokic, M.D. Maksimovic and D.C. Stefanovic, "The effect of a.c. superimposed on d.c. and pulsating potential on the coercivity of electrodeposited Ni-Fe alloy thin films," vol. 19, pp.802-805, Nov. 1989.
- [4.17] B.S. Sheshadri, "Cathodic Inhibition Effects during NiFe and ZnNi Alloy Deposition," Transaction Institution of Metal Finishing, vol. 73, pp. 66-68, 1995.
- [4.18] M.D. Maksimovic and S.S. Djokic, "Modern Aspects of Electrochemistry," Plenum Press, New York, 1992.
- [4.19] L. T. Romankiw and D. A. Thompson, "Thin Film Inductive Transducer," U.S. Patent 4,295,173, Oct. 13, 1981.
- [4.20] O. Kohmoto, Recent Developments of thin film materials for magnetic heads. IEEE Trans. On Magn., vol. 27, pp.3640-3647, July 1991.
- [4.21] A. S. Kao and P. Kasiraj, "Effect of Magnetic Annealing on Plated Permalloy and Domain Configurations in Thin-Film Inductive Head," IEEE Trans. Magn., vol. 27, no. 6, Nov. 1991.
- [4.22] R. F. Soohoo, "Magnetic Thin Films," Harper and Row, 1965.
- [4.23] C. R. Sullivan and S. Sanders, "Design of Microfabricated Transformers and Inductors for High-Frequency Power Conversion," IEEE Trans. Power Electron., vol. 11, no. 2, March 1996.
- [4.24] T. Jagielinski, "Materials for future high performance magnetic recording heads", MRS Bulletin, vol.15, pp.36-44, March, 1990.
- [4.25] E. I. Cooper et al, "Recent developments in high-moment electroplated materials for recording heads," IBM. J. Res. & Dev. vol. 49, no. 1, Jan. 2005.
- [4.26] D. Flynn, A. Toon, M.P.Y. Desmulliez, "Microscale magnetic components for the application of DC-DC converters operating in the 1-10 MHz range," IEEE Proc. of Electronic Materials and Packaging (EMAP) Conference, Tokyo, Japan, pp. 192-198, 2005.
- [4.27] R. M. Bozorth, Ferromagnetism, IEEE Press, New York 1978.
- [4.28] L. Sun, "Tuning the properties of magnetic nanowires", IBM J. Res. & Dev., vol. 49, no. 1, Jan., 2005.
- [4.29] F. R. Williams, "Monitoring and Control of Semiconductor Manufacturing Using Acoustic Techniques," PhD Thesis, Georgia Institute of Technology, Nov. 2003.

- [4.30] J. L. McCrea, "Properties and Applications for Electrodeposited Nanocrystalline Fe-Ni Alloys," *Rev. Adv. Mater. Sci.* 5, pp.252-258, 2003.
- [4.31] A. J. Martin, "Magnetic Properties of Nanocrystalline Transition Metals", PhD thesis, Queen's University, Canada, 1999.
- [4.32] W. C. Grande and J. B. Talbot, "Electrodeposition of Thin Films of Nickel-Iron," *J. Electrochem. Soc.*, vol.140, p.675, 1993.
- [4.33] M. Brown and E. Jakeman, "Theory of the four-point probe technique as applied to the measurement of the conductivity of thin layers on conducting substrates," *J. Appl. Phys.*, vol.17, pp.1143-1148, 1966.
- [4.34] Hitachi Metals, "Nanocrystalline soft magnetic material-FINEMET", Jun. 2004.
- [4.35] G. Herzer, "Amorphous and Nanocrystalline Soft Magnets", NATO ASI Series, vol. 338, 1997.

## Chapter 5

### Design of Experiments for electrodeposition of nickel-iron

#### 5.1 Introduction

This chapter investigates the influence of pulse reverse (PR) deposition on the structural, magnetic and electrical properties of Ni-Fe, by using a Design of Experiments (DOE). Section 5.2 outlines the rationale behind this investigation and introduces the concept behind the development of DOE. The experimental set-up and waveforms used in the investigation are contained in section 5.3. The deposits are examined in terms of pitting, grain size and composition and the resulting experimental data are presented in section 5.4. In section 5.5 the alloys are assessed in terms of their electrical characteristics. The magnetic characteristics of the films are assessed in section 5.6. The chapter concludes with a discussion of the presented data in section 5.7.

#### 5.2 Rationale for using DOE for nickel-iron electrodeposition

The demand for improved magnetic materials to operate efficiently at high frequencies was discussed in Chapter 2. The development of such materials could be achieved in three ways: (1) a combination of different materials forming new alloys, (2) the manufacturing of a novel material or (3) the tailoring of the film properties during deposition. The development of new alloys and materials would require an extensive investigation beyond the scope of this Ph.D. thesis. Hence, the alteration of the properties of known alloys is the approach adopted in this thesis. Magnetic field annealing during deposition as presented in Chapter 4 was one method of optimising film properties during deposition for high frequency operation. However, this method only concerned the alteration of the magnetic properties of the Ni-Fe film. In Chapter 2 the low resistivity of alloys was outlined as the primary loss mechanism in thin film alloys at high frequencies. Therefore, the ability to tailor the electrical as well as the magnetic properties during deposition is desired.

Resistivity can be altered during deposition with the inclusion of more resistive materials to the alloy composition at the expense however of potentially damaging the magnetic response of the alloy. To avoid altering the composition of the film, the influence of grain boundary engineering on the resistivity was explored. A reduction in

grain size is accompanied by an increase in grain boundaries and a consequent increase in resistivity in nanocrystalline materials [5.1,5.2]. The nucleation and growth of electrodeposits is discussed in detail in [5.3-5.5]. In this reference the relation of grain size with overpotential is also discussed. The overpotential is the difference in the electrode potential of an electrode between its equilibrium potential and its operating potential when a current is flowing. It represents the extra energy needed to force the electrode reaction to proceed at a required rate (or its equivalent current density). The overpotential increases with increasing current density, as indicated by the Tafel equation [5.3].

The overpotential also controls whether the deposition is limited by diffusion, activation or both. At low overpotentials a small number of nuclei form and grow independently. It is therefore expected that a large-grained deposit will be obtained under these conditions. As the overpotential is increased, a large number of nuclei may be formed leading to a decrease in the grain size. Fig 4.14 demonstrated that an increase in current density alters the composition of the film and, as a result, its magnetic properties. Pulse Reverse (PR) waveforms were investigated as a solution to this challenge. PR waveforms offer an increased number of variables during deposition, namely, anodic current density, cathodic current density, cathodic pulse duration, anodic pulse duration, and pulse off-time. For example, PR waveforms allow increased cathodic current density, deposition cycle, whilst maintaining the same average current density as its DC equivalent due to the anodic current density, dissolution cycle. Hence, films with identical composition but with altered grain structure can be compared.

The aims of this DOE are to record the influence of the PR variables on deposit composition, electrical and magnetic properties through the implementation of a few critical experiments. The primary objective is the assessment of the influence of grain size on the magnetic and electric properties of the alloy. With the increase in deposition variables it is necessary to use statistical principles in the DOE to ensure that experiments are economical, allow the user to measure the influence of one or several factors on a response and enable the estimation of the magnitude of experimental error.

Experiments designed without adhering to statistical principles usually violate one or more of the aforementioned goals. Without using statistical principles in experimental design economy is often achieved by severely limiting the number of factors whose

effects are to be studied, and the sequence of tests may require that only one of the factors of interest may be varied at a time, thereby preventing the evaluation of any joint effects of the experimental factors. The waveforms developed by the DOE and experimental set-up are described in section 5.3.

### 5.3 Experimental Set-up & Waveforms Generated by the DOE

The plating cell and electrolyte composition are identical to the investigation carried out in Chapter 4 using DC waveforms. The only alteration to the experimental apparatus is the inclusion of a pulse rectifier to generate the PR waveforms, Fig 5.1.



Figure 5.1 The Pulse Rectifier is connected to an oscilloscope displaying a pulse reverse waveform (PR).

During the DOE the background conditions kept constant are: concentration of metal salts, conductive salts & buffering agents, concentration of impurities, electrolyte temperature, electrolyte pH, plating cell geometry, composition and condition of the anode, anode/cathode surface area ratio and the nature and condition of the substrate as well as its conductive seed layer.

In an attempt to minimise the variation in the background conditions over time, all waveforms to be assessed were done in quick succession over a two-day period. All cathodes (samples) were prepared with conductive seed layer and patterned photoresist prior to the start of the DOE.

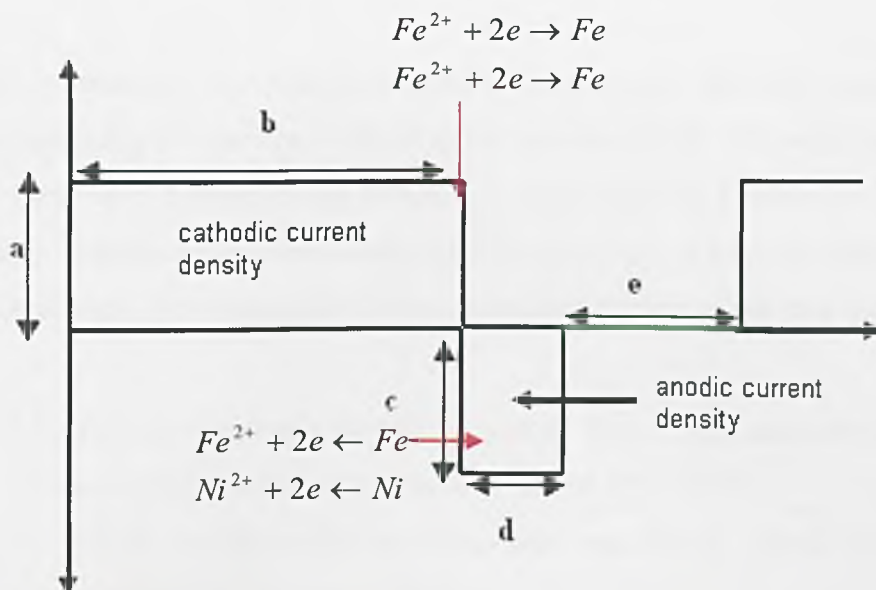


Figure 5.2 Pulse Reverse Waveform with the 5 factors highlighted; (a) cathodic current intensity amplitude, (b) cathodic pulse duration on time, (c) anodic current intensity amplitude, (d) anodic pulse duration on time, and (e) represents the off-time of the pulse. The electrochemical reactions associated with the pulse parameters are also highlighted.

The definitions of the PR parameters of the waveform are outlined in Table 5.1.

Pulse Reverse Waveform Parameter	Equation
Frequency where, $\lambda = b + d + e$	$F = \frac{1}{\lambda}$
Average Current Density where, $x = a * b$ and $y = c * d$	$I = \frac{(x + y)}{\lambda}$
Current Ratio	$R = \frac{c}{a}$
Off-time	$t_{off} = e$
Positive duty cycle	$\partial^+ = \frac{b}{\lambda} \times 100\%$
Negative duty cycle	$\partial^- = \frac{d}{\lambda} \times 100\%$
On duty cycle	$\partial^{on} = \frac{(b + d)}{\lambda} \times 100\% = \partial^+ + \partial^-$

Table 5.1 Pulse Reverse waveform parameters and associated equations

Once the constant and variable parameters are determined, the next stage in the DOE involves assigning the number of levels to the variables [5.6]. The simplest approach is adopted here, with 2 levels being selected, 1 maximum and 1 minimum. This means that, in any combination, a factor would be in its high or low state generating maximum  $2^5=32$  waveforms. The values for the maximum and minimum are now determined:

- $f > 1\text{Hz}$ , the frequency should be greater than 1Hz. Literature states that no benefit is gained over DC plating at or below 1 Hz [5.5].
- $f < 500\text{ Hz}$ , the frequency should be less than 500 Hz which is the maximum operating point of the pulse rectifier
- $I_d > 10\text{ mA/cm}^2$ , the average current density should be more than 10 mA/cm<sup>2</sup>. Preliminary experiments with DC deposition indicated that below a current density of 10 mA/cm<sup>2</sup>, the film composition lead to a film with high magnetostriction if sulfate is used as the electrolyte.
- $I_d < 60\text{ mA/cm}^2$ , the average current density should be less than 60 mA/cm<sup>2</sup>. DC deposition beyond this value leads to poor quality deposits.
- $c/a > 1$ , the anodic to cathodic current ratio should be greater than 1. This parameter is reported to be the most influential in obtaining conformal depositions [5.5].
- $x > y$ , cathodic current density greater than the positive current density. This condition is required for metal deposition on the cathode.

Certain combinations of variables lead to invalid waveforms. An excel spreadsheet utilising a macro was used to generate the valid and invalid waveforms. From the potential 32 waveforms, 25 valid waveforms were generated. The values of each of the parameters were altered until the maximum number of valid waveforms was generated by the macrocode in the spreadsheet. The parameters of the 25 waveforms are contained in Table 5.2. The experiments, Doe01-Doe25, were conducted in a randomised order to reduce the influence of experimental error. In reference to Table 5.2, the anodic amplitudes are greater than the cathodic values. High anodic amplitudes tend to lead to preferential dissolution of deposit in areas that typically over-plate. Thus, an improvement in deposit cross sectional area (c.s.a) is anticipated.

With the anodic amplitude greater than the cathodic amplitude, the maximum and minimum anodic pulse durations have to be less than the cathodic maximum and minimum. Off-time maximum and minimum values were selected as 10ms and 0ms, respectively. With zero and 10ms off-times, it was hoped that this would provide an insight into the distribution of Fe. With no agitation and depletion of Fe ions at the cathode surface, Fe content may become limited due to the lack of mass transfer effects.

	a	b	c	d	e
	Amps	Seconds (mS)	Amps	Seconds (mS)	Seconds (mS)
Exp. No.	a	b	c	d	E
Doe01	0.5	20	-0.6	2	0
Doe02	0.5	20	-0.6	2	10
Doe03	0.5	10	-0.8	10	0
Doe04	0.5	100	-0.6	10	10
Doe05	0.5	100	-0.8	2	10
Doe06	0.5	100	-0.8	10	10
Doe07	0.3	100	-0.6	2	0
Doe08	0.3	100	-0.8	10	0
Doe09	0.5	200	-0.6	10	0
Doe10	0.3	100	-0.6	2	10
Doe11	0.5	100	-0.6	2	0
Doe12	0.3	100	-0.6	10	0
Doe13	0.5	20	-0.8	2	10
Doe14	0.3	100	-0.6	10	10
Doe15	0.3	20	-0.8	2	10
Doe16	0.3	20	-0.6	2	10
Doe17	0.5	20	-0.6	10	10
Doe18	0.3	100	-0.8	10	10
Doe19	0.3	100	-0.8	2	0
Doe20	0.3	100	-0.8	2	10
Doe21	0.5	100	-0.8	2	0
Doe22	0.3	20	-0.8	2	0
Doe23	0.5	100	-0.6	10	0
Doe24	0.5	100	-0.6	2	10
Doe25	0.5	20	-0.8	2	0

Table 5.2 DOE PR waveform parameters.

The following section presents the analysis and discussion of results for the DOE waveforms.



#### 5.4 Structural properties of DOE samples

The composition of the samples produced from the DOE was determined by SEM-EDX. The composition of the DOE deposits is displayed in Table 5.3. The exposed area of patterned seed layer is approximately 9.12cm<sup>2</sup>, which is 20% of the overall wafer area. In Chapter 4, Fig 4.15 displayed a trend of decreasing Fe content with increasing current density for the DC deposition. However, the results of the DOE contained in Table 5.3 displays that Fe content for the PR waveforms is not solely determined by current density. Data for Doe 8, 10, 15, 18 and 22 has been omitted due to the poor quality of deposits. Fig 5.3 displays the data of Table 5.3 in comparison to the DC deposition of Chapter 4.

	Average current density (mA/cm <sup>2</sup> )	Fe %
Doe11	47.84	10
Doe21	47.45	7
Doe24	43.57	6
Doe05	43.21	8
Doe23	40.00	15
Doe01	40.00	27
Doe03	38.18	26.3
Doe25	38.18	25
Doe04	36.66	5.2
Doe06	35.00	3.5
Doe07	28.23	17.5
Doe19	27.84	16
Doe02	27.50	20
Doe13	26.25	5
Doe20	25.35	15
Doe12	21.81	4
Doe14	20.00	2
Doe16	15.00	31
Doe09	13.33	9
Doe17	10.00	6.5

Table 5.3 SEM-EDX analysis results for PR waveform deposits fabricated from the DOE. The results are presented in descending order of average current density.

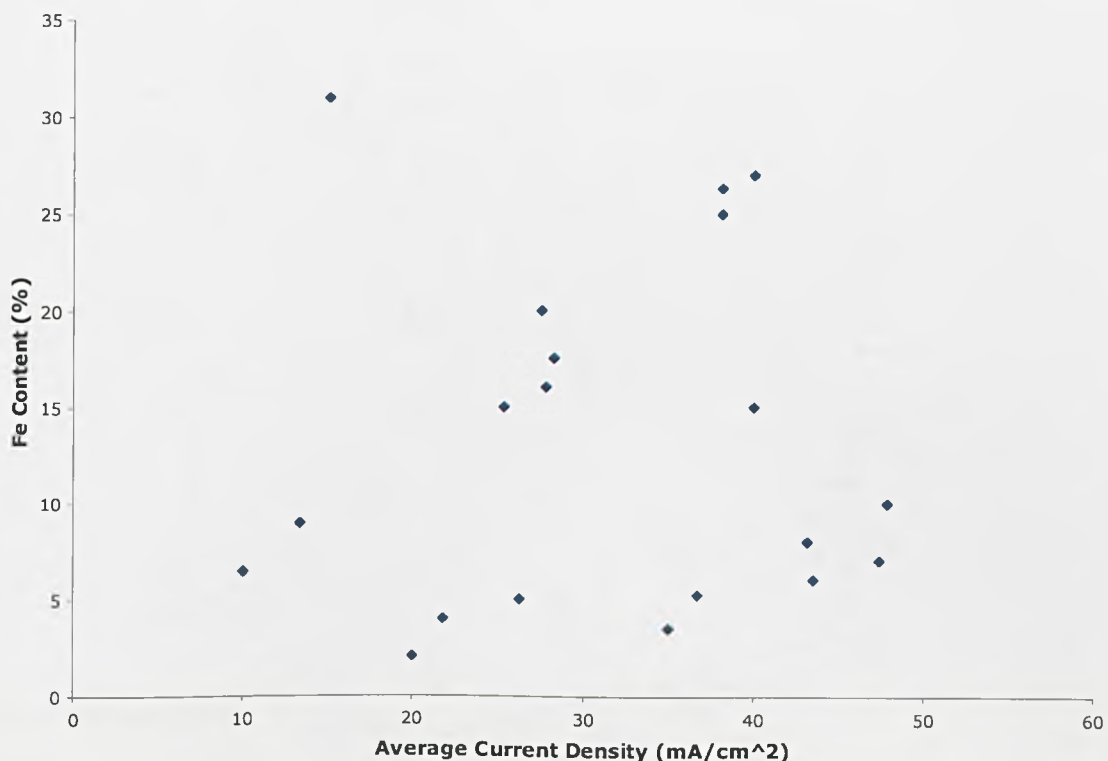


Figure 5.3 Fe content in percentage as a function of average current density.

The composition of interest that provides a low magnetostriction and favourable magnetic properties is for 15 to 22% Fe content. The DOE, according to Fig 5.3, has successfully produced deposits within this range. In Fig 5.3 the anomalous co-deposition effect is not visible as in the case of DC deposition with varying current density. The results indicate that the additional variables of the PR waveform have a definite influence on the iron content of the deposits. Fig 5.4 displays a 3-dimensional representation of the Fe content in percentage as a function of cathodic and anodic pulse densities. The data in Fig 5.4 indicates that a low cathodic and anodic pulse density are both required for a high Fe content, demonstrating thereby that the PR waveforms can monitor the anomalous co-deposition effect.

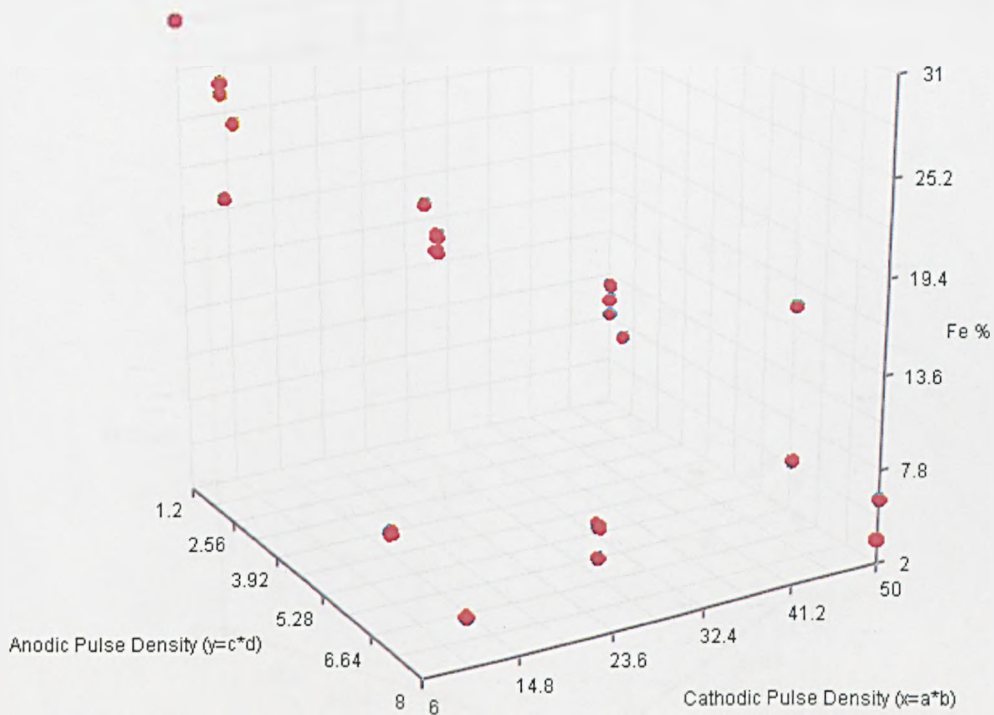


Figure 5.4 Fe Content as a function of cathodic pulse density and anodic pulse densities expressed in mA/cm<sup>2</sup>.

The influence of the off-time on the composition of the deposits appears to be minimal. The influence of the off-time is expected to be more prevalent when the Fe concentration at the cathode becomes minimal. In that regime, the Fe ions are solely dependent on the mass transfer from the bulk of the electrolyte. An adequate off-time permits the replenishment of Fe near the cathode surface. Increases in agitation would be expected to yield an increase in Fe deposition.

No relation between the frequencies of the pulses, ranging from 8-45 Hz, and the composition could be determined. Prior work has found that no difference in PR and DC deposition occurs when the only variable is frequency, when lower than 500 Hz [5.5].

Another important parameter is pitting. As mentioned earlier, pitting reduces the effective core area of the magnetic component increases its leakage inductance,

resulting in unwanted stored magnetic energy in transformer applications etc. Fig 5.5 displays the results of pit count as a function of average current density and off-time.

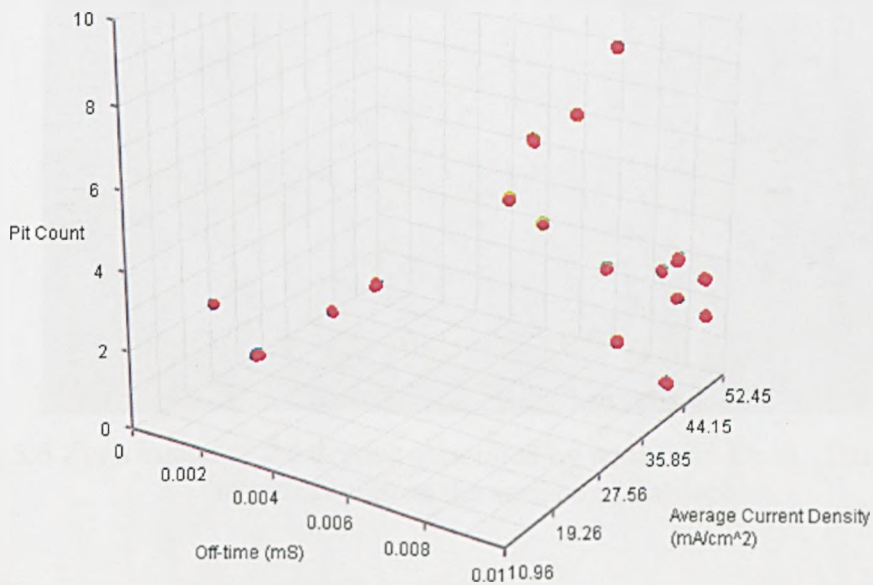


Figure 5.5 Pit count as a function of the off-time and average current density expressed in mA/cm<sup>2</sup>

The pit-count increases when the off-time is 10ms and the average current density is in the 35-47.84 mA/ cm<sup>2</sup> range. This increase in pit count is a result of the mass transfer limited nature of hydrogen evolution [5.3]. At increased current densities, i.e. deposition rates, plating efficiencies tend to increase. The increase in off-time permits the transfer of  $H^+$  reduction from the bulk of the electrolyte to the surface of the cathode. An example of the effects of pitting on the deposit surface of Doe4 is shown in Fig 5.6.



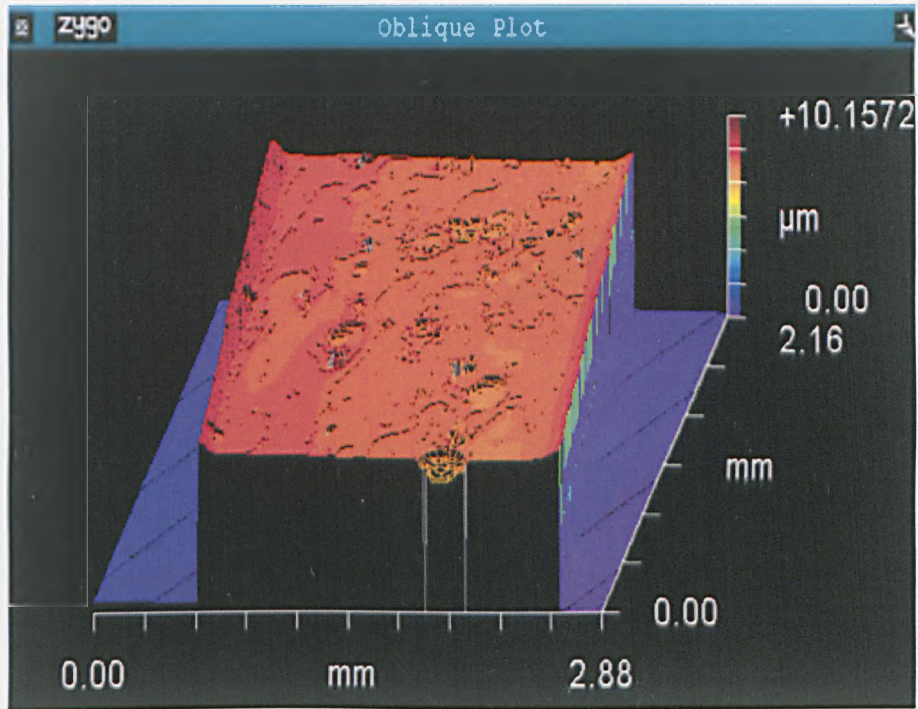


Figure 5.6 Zygo image of the deposit generated by waveform Doe4. Pitting has resulted in pit/cavities on the surface of the deposit.

Uniform core c.s.a is generated by minimal pitting and reduction of current crowding effects. Current crowding typically occurs in the corners of deposits, as shown in Fig 5.7. The deposit in Fig 5.7 was fabricated by DC deposition at an average current density of  $13\text{mA}/\text{cm}^2$ . The amplification of the current crowding effect in comparison to Fig 4.10 is due to a reduction in exposed seed layer. A higher concentration of field lines in the corner of the deposit results; this effect is demonstrated by Fig 4.11.

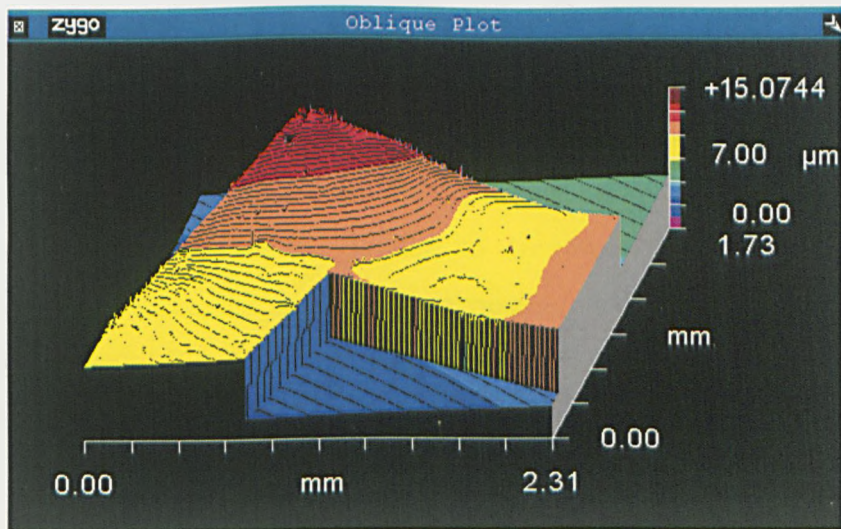


Figure 5.7 Zygo image of current crowding effects on deposit profile. The peak of the deposit is in the corner of the deposit where current crowding is prevalent.

Zygo images of the surface profile of a deposit fabricated by Doe 2 using the same photomask as the DC deposition are shown in Fig 5.8.

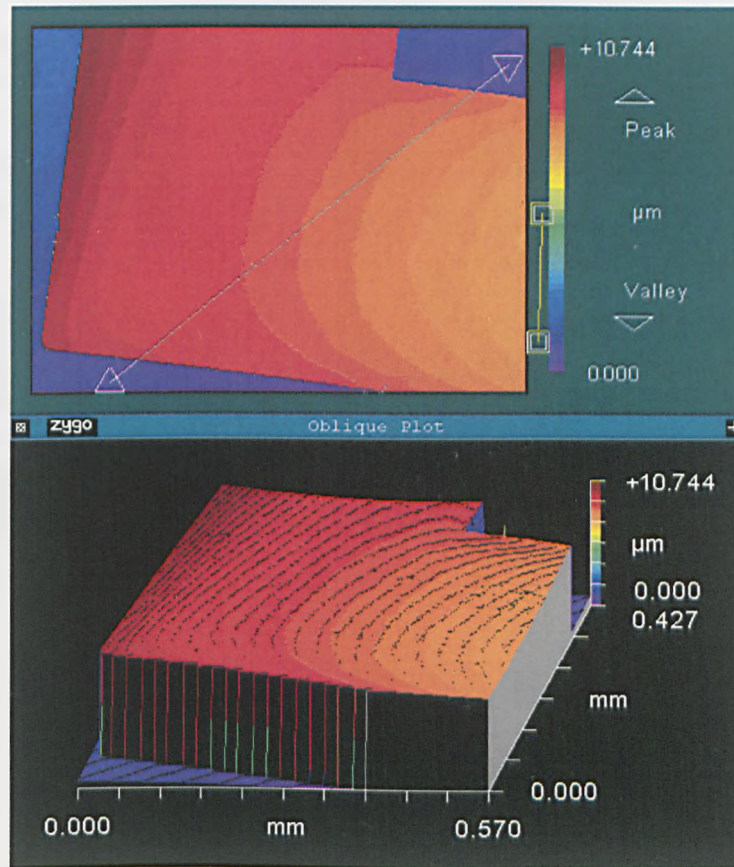


Figure 5.8 Profile of deposit surface generated by PR waveform Doe 2. The deposit shows a reduction in current crowding in the corner of the deposit.

Fig 5.8 displays the improvement in c.s.a with a reduction in current crowding. The variation in film thickness from the corner, prone to current crowding, to the centre of the deposit is less than 3%. The improvement in c.s.a in comparison to Fig 4.10 is due to preferential dissolution of the deposit during the anodic cycle. The improvement in deposit c.s.a compared to Fig 5.7 is due to an improvement in current density distribution, due to increased seed layer exposure, and anodic cycle dissolution. Samples of Doe 6 exhibit a minor variation of only 2% which is attributed to the large anodic pulse density, 8mA.

With the increase in PR control variables it is possible to fabricate a deposit of 80:20 Ni-Fe at a current density of 27.50mA/cm<sup>2</sup>, Doe02 Table 5.3. The DC current density



for a similar composition was  $13.5\text{mA}/\text{cm}^2$ . Fig 5.9 displays the grain size for the PR waveform.

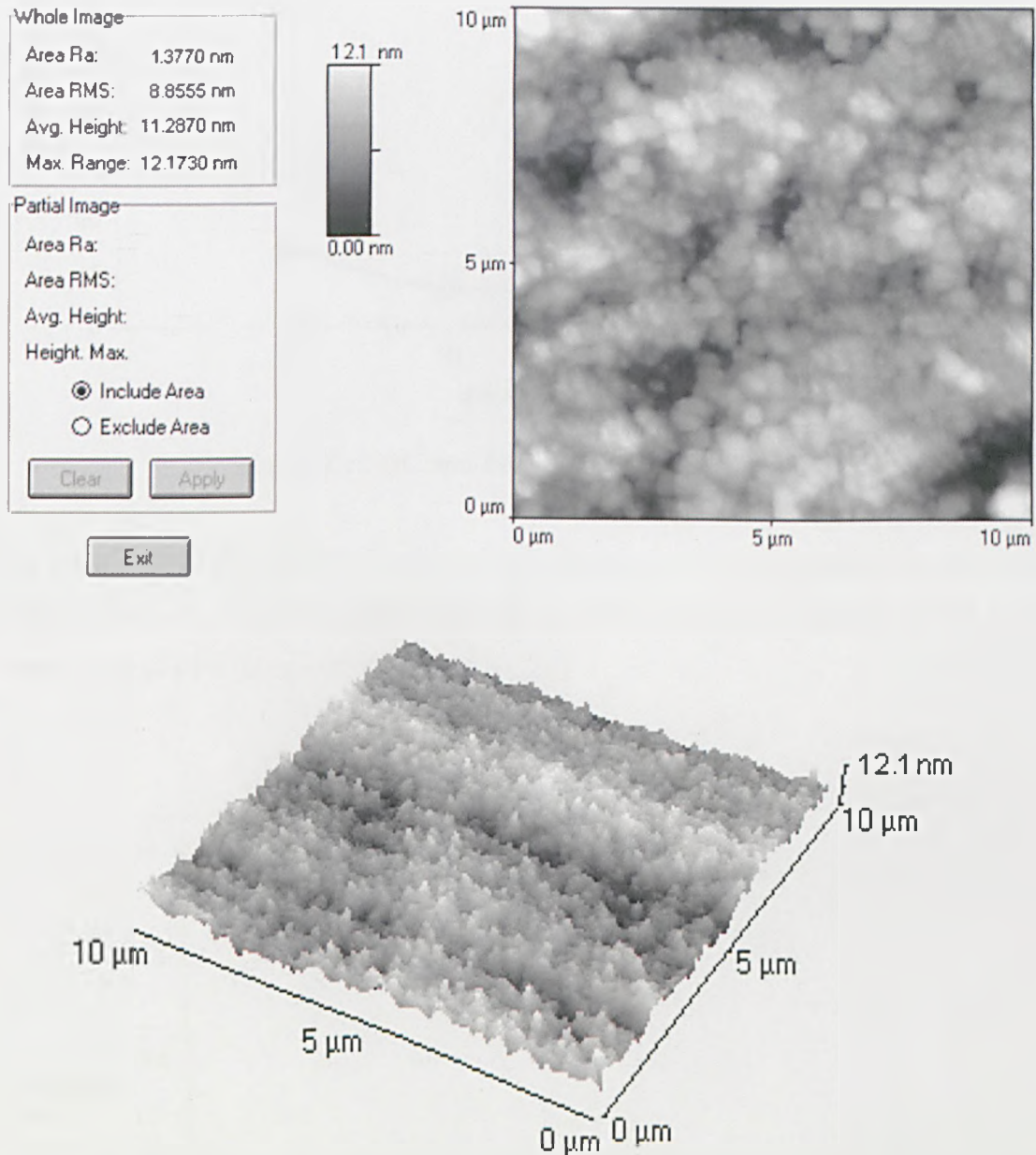


Figure 5.9 (a) AFM data of a Ni-Fe sample fabricated at  $50\text{mA}/\text{cm}^2$ , and (b) A 3D plot of the surface profile of a  $10\mu\text{m} \times 10\mu\text{m}$  area of the same sample.

The average grain size for the PR waveform, of identical composition, is  $11.28\text{nm}$ . Fig 5.10 displays the average grain size of DC and PR deposits as a function of Fe content. As discussed in Chapter 4 the DC grain size reduces with Fe content. Such behaviour is not observed with the PR deposits. The variation in grain size is minimal and considering experimental error, the influence of increasing Fe content on grain size could be regarded as negligible.

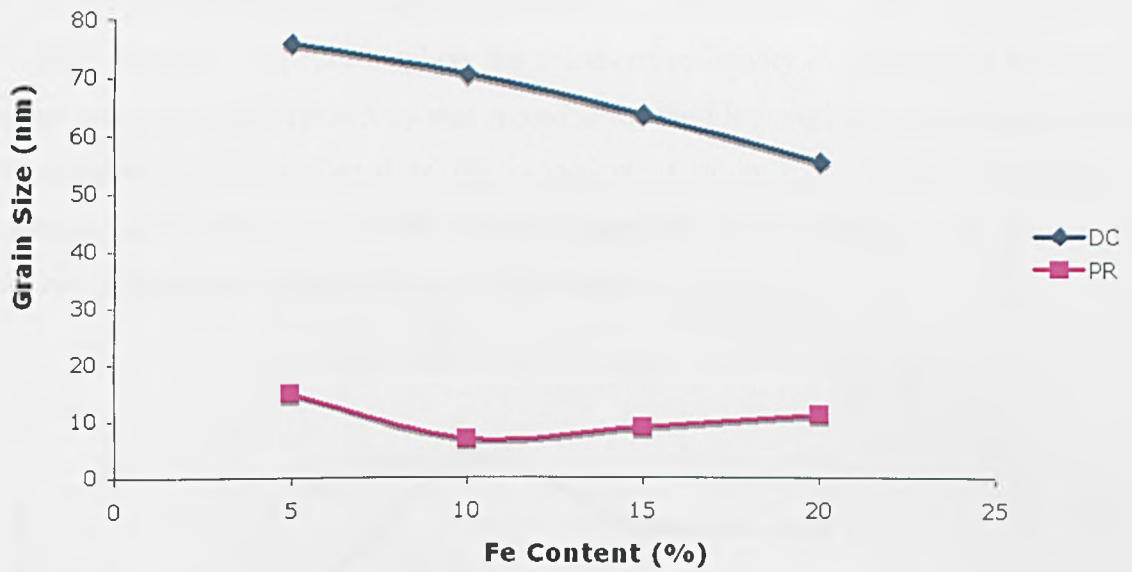


Figure 5.10 DC and PR grain size vs. Fe content.

The grain size of PR deposits is plotted as a function of cathodic pulse density and Fe content, Fig 5.11. The finer grain structure occurs at the highest cathodic pulse density irrespective of film composition.

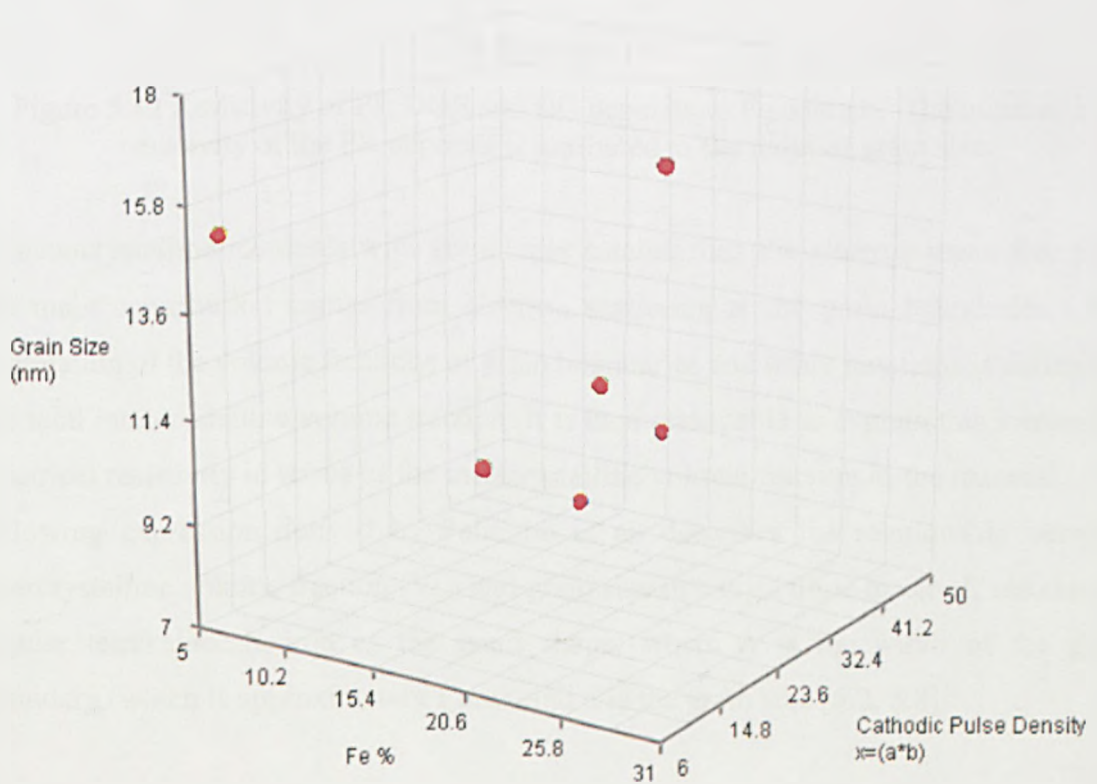


Figure 5.11 Grain size (nm) as a function of Fe content and cathodic pulse density. The finer grains are generated in the upper range of cathodic pulse densities.



## 5.5 Electrical Properties of DOE samples

Using the four point probe technique, resistivity measurements were recorded for the PR DOE samples. Fig 5.12 displays the values of resistivity in comparison to the DC values. An increase in resistivity was recorded for the PR samples in comparison to the DC samples and is attributed to the reduction of grain size. Reduced grain size produces an increase in volume fraction interfaces, such interfaces are known to produce electron scattering at the grain boundaries [5.1, 5.7].

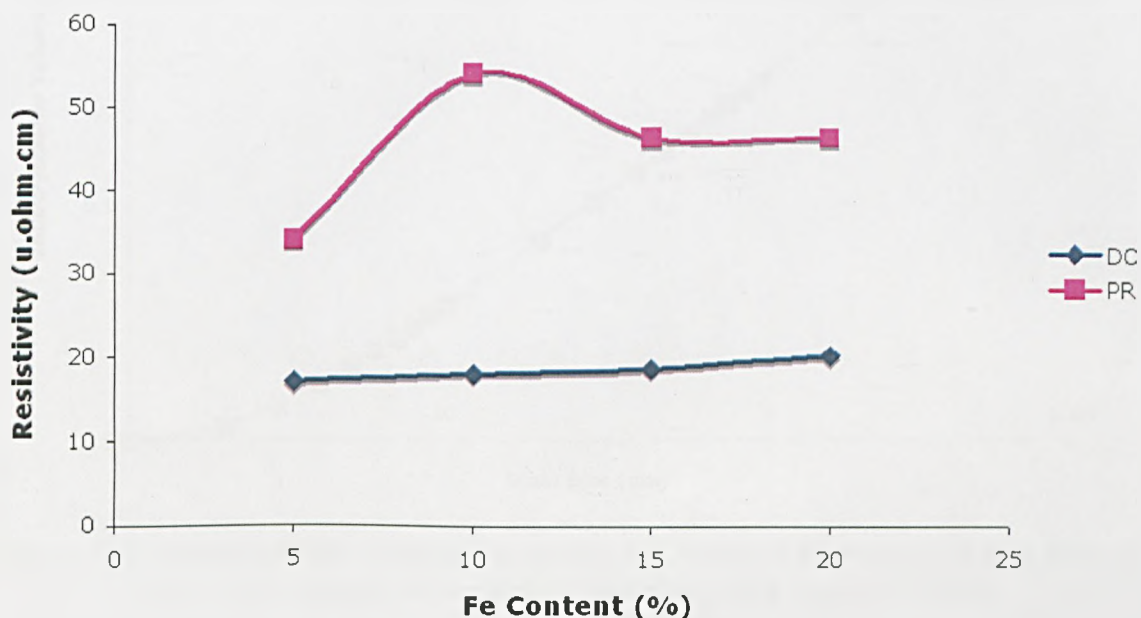


Figure 5.12 Resistivity of PR DOE and DC deposits vs Fe content. The increase in resistivity of the PR deposits is attributed to the reduced grain size.

In nanocrystalline materials with grain sizes smaller than the electron mean free path, the main contribution comes from electron scattering at the grain boundaries. The summation of the volume fractions of grain boundaries and triple junctions is defined as the total intercrystalline volume fraction. It is then reasonable to explain this increase in electrical resistivity in terms of the intercrystalline volume fraction in the material. The following expression derived by Palumbo et al. describes the relationship between intercrystalline volume fraction ( $V_t$ ) and grain size in a crystalline material, assuming a regular tetrakaidecahedron as the grain shape, where  $\Delta$  is the width of the grain boundary (which is approximately 1 nm), and  $d$  is the grain size [5.2, 5.8].

$$V_t = 1 - \left[ \frac{(d - \Delta)}{d} \right]^3 \quad (5.1)$$

The relationship between grain size and intercrystalline volume fraction, according to Eq (5.1), is plotted in Fig 5.13.

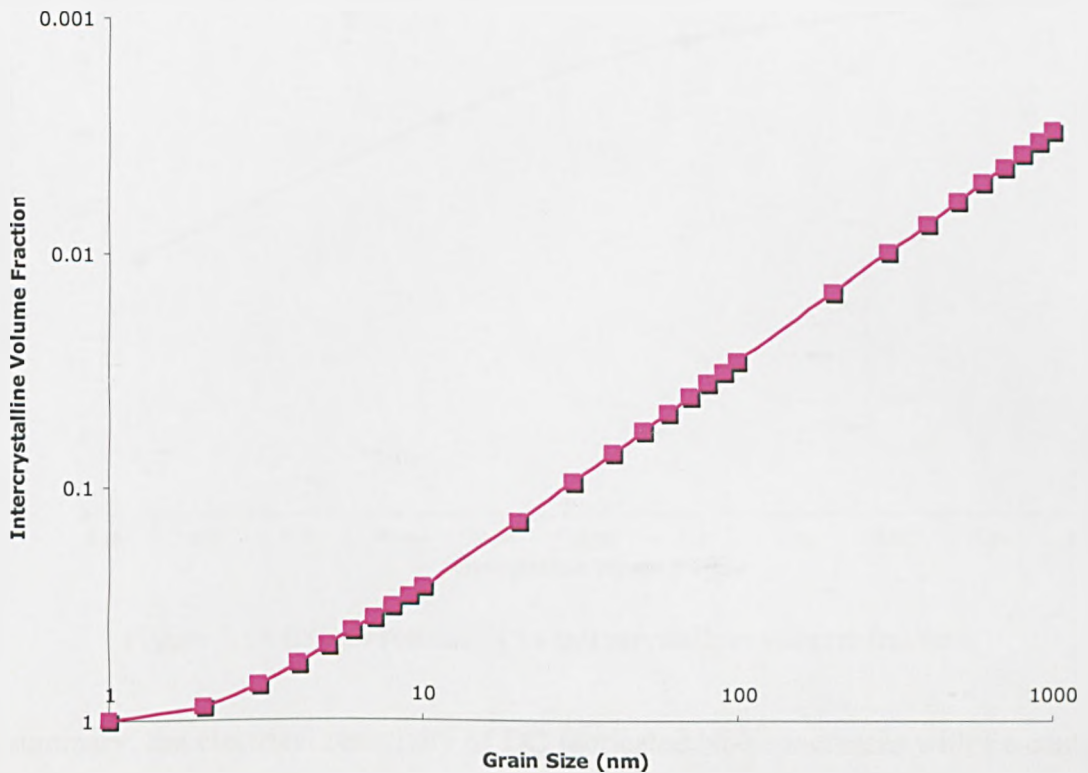


Figure 5.13 Intercrystalline Volume Fraction as a function of Grain size. A reduction in grain size produces an increase in intercrystalline volume fraction.

Figure 5.13 highlights that the overall quantity of grain boundaries (intercrystalline volume fraction) in nanocrystalline materials increases with reducing grain size. Nanocrystalline materials represent a novel class of materials with grain sizes less than 100 nm resulting in significant increases in grain boundary and triple junction volume fractions. As the grain size reduces the material becomes densely packed with fine grains resulting in an increase in the overall number of grain boundaries. Hence, there are many more 1nm grain boundary walls,  $\Delta$ .

In order to determine the relationship between the intercrystalline component and resistivity, Fig 5.14 illustrates the excess resistivity as a function of the intercrystalline volume fraction at room temperature. The excess resistivity is defined here as the total resistivity minus the resistivity of the DC deposits. It can be seen that the excess resistivity increases almost linearly with the intercrystalline volume fraction. This behavior indicates that the observed increase in resistivity is mainly controlled by scattering events on intercrystalline defects.

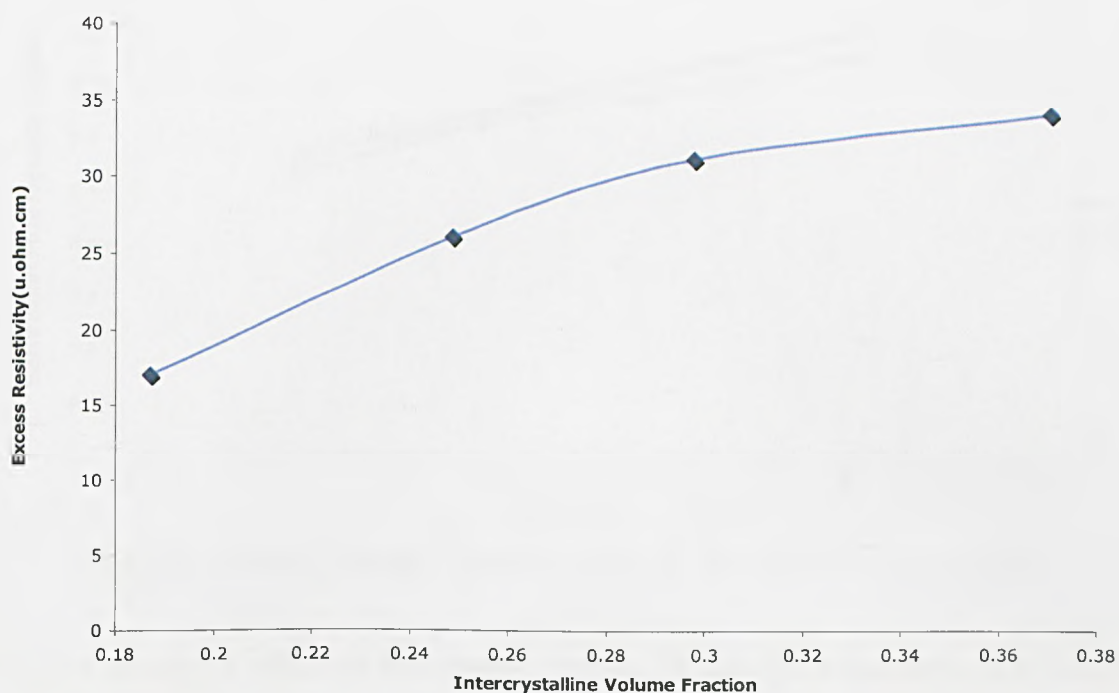


Figure 5.14 Excess resistivity vs intercrystalline volume fraction.

In summary, the electrical resistivity of DC fabricated Ni-Fe increases with Fe content. PR deposits display an increase in resistivity in comparison to the DC equivalents. The difference is attributed to the decreasing grain size of the PR deposits which led to electron scattering at grain boundaries. At room temperature, the resistivity of the 80:20, permalloy composition, with a grain size of 11nm is enhanced by a factor of 2 over the resistivity value observed for a DC deposit that has an average grain size of 56nm.

### 5.6 Magnetic Properties of DOE Samples

The DOE samples were magnetically characterised with the VSM. The magnetic saturation flux density and coercivity of the PR DOE samples are shown in Fig 5.15 & 5.16, respectively. The saturation flux density of the PR deposits follows the same increase in flux density with Fe content as in the DC deposit. The flux density of the PR deposits is typically 2 to 5% lower than their DC equivalents. This result demonstrates that the influence of the grain size on the flux density is minimal and that the composition of the film determines primarily the flux density.



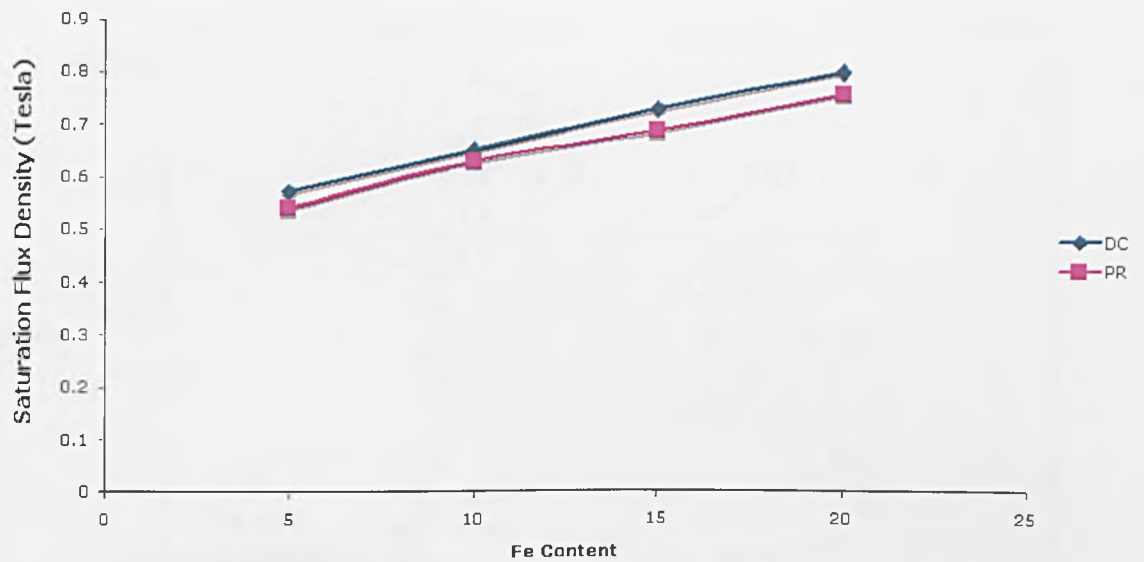


Figure 5.15 Saturation flux density of DC and PR deposits vs. Fe content.

Fig 5.16 displays a reduction in coercivity for the PR deposits in comparison to the DC deposits. The reduction in coercivity is attributed to the reduction in grain size of the PR films. It is well known that the microstructure, noticeably the grain size, essentially determines the hysteresis loop of a ferromagnetic material. Fig 5.17 summarises the present understanding of coercivity in relation to grain sizes,  $D$  [5.8].

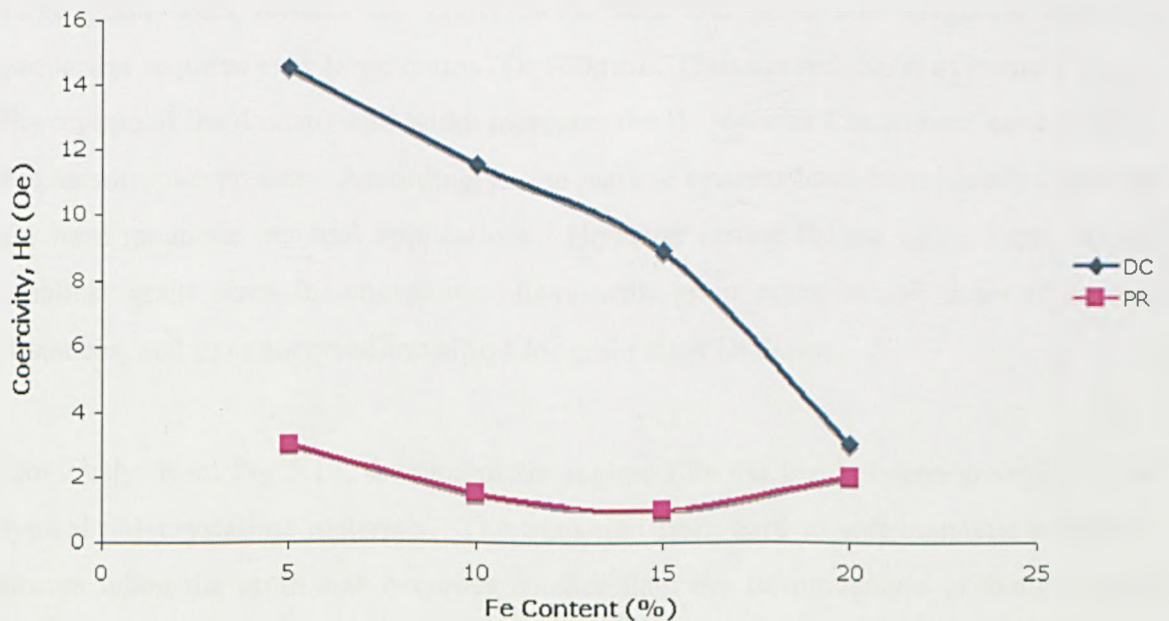


Figure 5.16 Coercivity of DC and PR deposits vs Fe content.

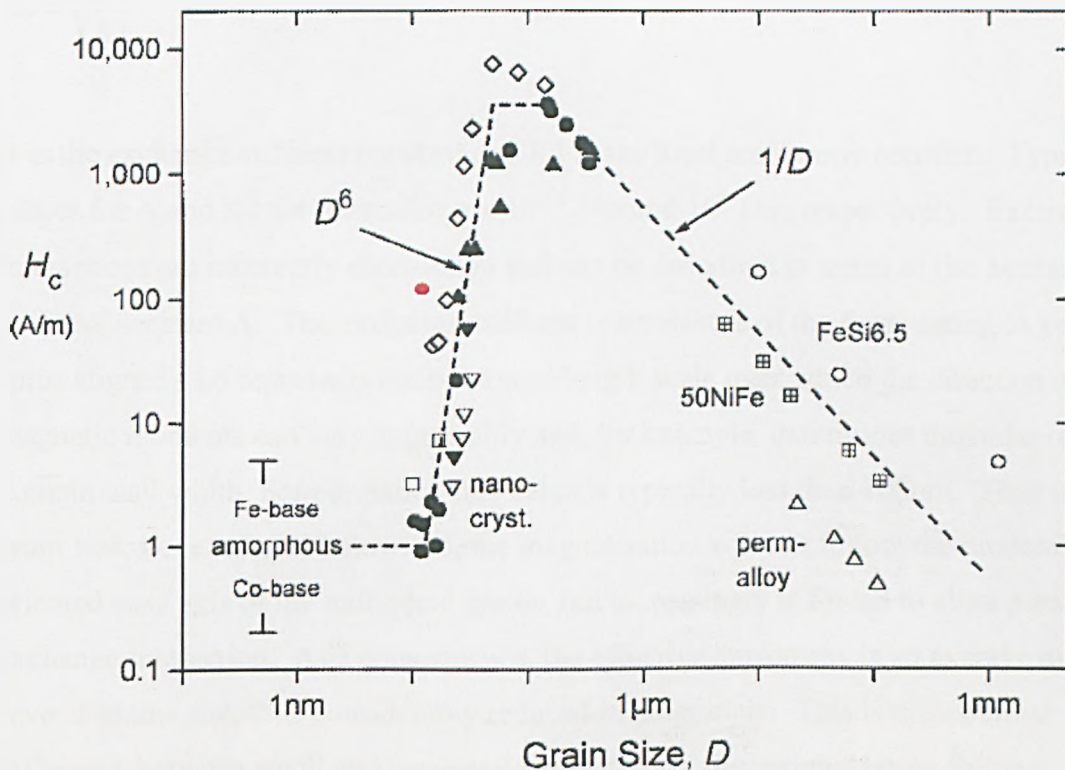


Figure 5.17 Coercivity,  $H_c$ , vs. grain size,  $D$ , for various soft magnetic alloys [5.8]. The grain size and coercivity of the PR permalloy, Doe2, is indicated by the red circle.

In reference to Fig 5.17, from nanometer regime up to macroscopic grain sizes, the permeability is essentially inversely proportional to  $H_c$ . The  $1/D$  dependence of  $H_c$  for large grain sizes reflects the conventional rule that good soft magnetic materials properties requires very large grains ( $D > 100 \mu\text{m}$ ). Thus the reduction of particle size to the regime of the domain wall width increases the  $H_c$  towards a maximum controlled by the anisotropies present. Accordingly, fine particle systems have been mainly discussed for hard magnetic material applications. However lowest  $H_c$  are again found for the smallest grain sizes in amorphous alloys with grain sizes in the order of atomic distances, and in nanocrystalline alloys for grain sizes  $D < 20 \text{nm}$ .

Obviously, from Fig 5.17, the nanometer regime fills the gap between amorphous and typical polycrystalline materials. The transition from hard to soft magnetic properties occurs when the grain size becomes smaller than the ferromagnetic exchange length [5.9]. In this case the local anisotropies are randomly averaged out by exchange interaction so that there is no anisotropy net effect on the magnetisation process.

The ferromagnetic exchange length,  $L_0$ , the determinant of magnetic softening, is calculated as follows [5.8]:

$$L_0 = \sqrt{\frac{A}{K_1}} \quad (5.3)$$

A is the exchange stiffness constant and  $K_1$  is the local anisotropy constant. Typical values for A and  $K_1$  for permalloy are  $10^{-11}$  J/m and  $10^3$  J/m, respectively. Exchange interactions are inherently short-range and can be described in terms of the exchange stiffness constant A. The exchange stiffness is a measure of the force acting to keep the spins aligned.  $L_0$  represents the minimum length scale over which the direction of the magnetic moments can vary appreciably and, for example, determines the order of the domain wall width. For permalloy this value is typically less than 100nm. Thus if the grain size, D, is reduced below,  $L_0$ , the magnetisation will not follow the randomly oriented easy axis of the individual grains, but increasingly is forced to align parallel by exchange interaction. As a consequence, the effective anisotropy is an average over several grains and, thus considerably reduced in magnitude. This is the essential difference between small and large grained materials, the magnetization follows randomly oriented easy axes of the individual grains and, accordingly, the magnetisation process is controlled by the full magnetocrystalline anisotropy of the grains i.e. if there FCC, BCC preferential axis.

The reduction in grain size has been advantageous in terms of reduced coercivity and increased resistivity, however the superparamagnetic regime when reducing the grain size of materials must be avoided [5.10]. Coercivity disappears but large magnetic fields are required due to the low permeability of the films. In the present case the small ferromagnetic crystallites are assumed to be well coupled by exchange interaction as indicated by the low coercivity, Fig 5.16, and simultaneously by the high permeability of the films as shown in Fig 5.18. Verification of this assumption requires an assessment of the magnetic response as a function of temperature. Equipment was not available to perform this analysis.

The relative permeability increases with Fe content, shown in Fig. 5.19. Further increases in Fe content produce however a reduction in permeability [5.11]. The increase in permeability is due to the reduction of magnetostriction and anisotropy constants in the permalloy composition. It is assumed that the increase in the PR DOE relative permeability is a result of reduced anisotropy constants due to the reduction of grain size.

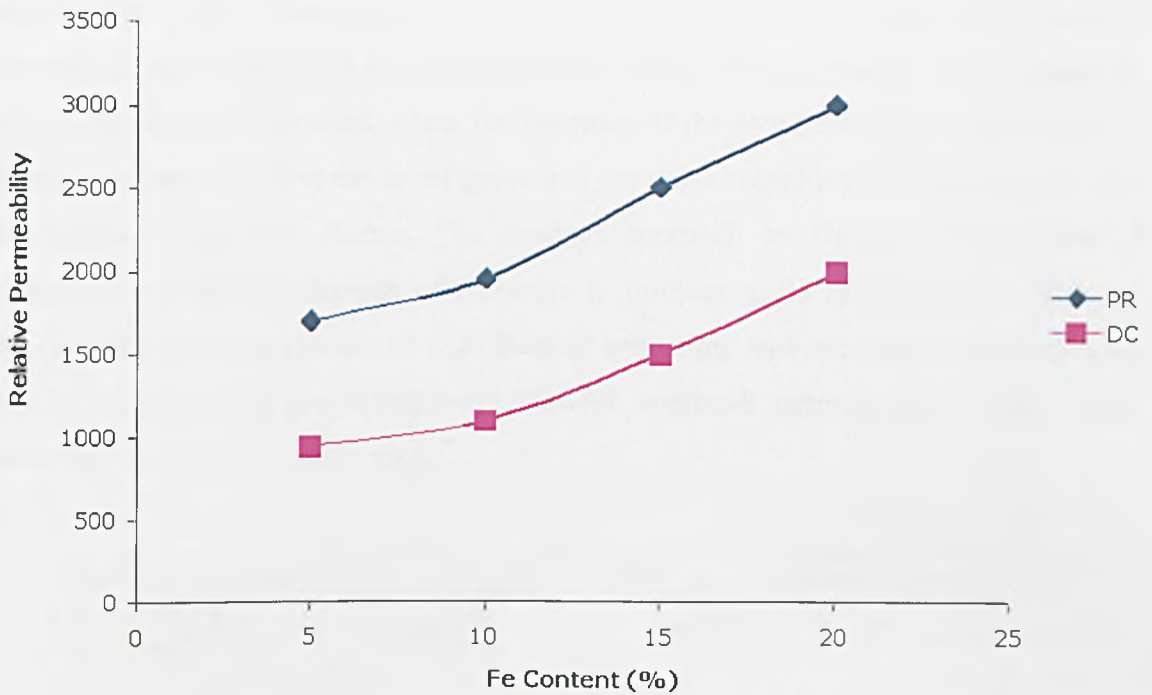


Figure 5.18 Relative permeability vs. Fe content. The relative permeability is maximised at 20% Fe as this region has minimal magnetostriction and anisotropy constants.

Amorphous alloys, such as Vitrovac and FINEMET, with grains smaller than the nanometer regime, typically fabricated via cold rolling, can exhibit relative permeability on the order of a 100,000 [5.12, 5.13].

In Chapter 4 the influence of magnetic field annealing on the hysteresis loop was explained in terms of the magnetic anisotropies. Understanding the influence of microstructure on film properties requires a similar explanation. Coercivity,  $H_c$ , increases with anisotropy energy density,  $K$ , and the permeability, shows the inverse behaviour. Thus the basic conditions for good soft magnetic properties are in low or vanishing magnetic anisotropies. The angular distribution of the anisotropy axis finally controls the shape of the hysteresis loop.

### 5.7 Summary

The impact of microstructural features on the anisotropy contributions and the associated magnetic properties have been discussed. The properties of Ni(80)Fe(20) fabricated via DC and PR are summarised in Table 5.4. The prerequisite for soft magnetic behaviour is that the effective magneto-crystalline anisotropy is low. Superior properties additionally require a low magnetostriction which reduces magneto-elastic

anisotropies. Once these contributions are sufficiently suppressed, the magnetic properties are determined by uniaxial anisotropies induced during field annealing, which, if properly controlled, allow the tailoring of the hysteresis loop to the demands of the application. The variation of grain size via pulse waveform is advantageous over the process utilised by Herzer. The analysis approach by Herzer involved thermal annealing and the introduction of elements to produce grain refining [5.8]. With the increase in grain size, associated with thermal annealing, and composition alteration the effects of grain size are ambiguous. The PR approach permits more clarity when assessing the effects of grain size.

Material	$\rho_s$ ( $\mu\Omega.cm^2$ )	$B_{sat}$ (T)	$H_c$ (Oe)	$\mu_r$	Film thickness ( $\mu m$ )
NiFe (DC)	20	0.8	3	2000	10
NiFe (PR)	46	0.76	1.9	3130	10

Table 5.4 Comparison of DC and PR Ni(80)Fe(20) properties.



## References

- [5.1] J. L. McCrea, "Properties and Applications for Electrodeposited Nanocrystalline Fe-Ni Alloys," *Rev. Adv. Mater. Sci.* pp. 252-258, 2003.
- [5.2] J. A. Martin, "Magnetic Properties of Nanocrystalline Transition Metals," PhD thesis, Queen's University, Kingston, Ontario, Canada, 1999.
- [5.3] M. Schlesinger and M. Paunovic, "Modern Electroplating," 4<sup>th</sup> edition, John Wiley & Sons, 2000.
- [5.4] R. K. Pandey, S. N Sahu, S. Chandra, "Handbook of semiconductor Electrodeposition," CRC Press, 1996.
- [5.5] J.C.Puippe and F.Leaman, "Theory and Practice of Pulse Plating," AESF, 1986.
- [5.6] R. O. Kuehl, "Design of Experiments: Statistical Principles of Research Design and Analysis," 2<sup>nd</sup> Edition, Brookes/Cole, 2000.
- [5.7] B. S. Murty, M. K. Datta and S. K. Pabi, "Structure and thermal stability of nanocrystalline materials," *Sadhana*, vol.28, parts 1&2, pp. 23-45, 2003.
- [5.8] G. Herzer, "Nanocrystalline Soft Magnetic Alloys", *Handbook of Magnetic Materials*, vol. 10, Elsevier Science, 1997.
- [5.9] D. Jiles, "Introduction to magnetism and magnetic materials," Chapman and Hall, 1991.
- [5.10] L. Sun, "Tuning the properties of magnetic nanowires," *IBM J. Res. & Dev.*, vol. 49, no. 1, Jan., 2005.
- [5.11] R. M. Bozorth, *Ferromagnetism*, IEEE Press, New York 1978.
- [5.12] Hitachi Metals, "Nanocrystalline soft magnetic material-FINEMET," Jun. 2004.
- [5.13] O. Dezuari, S. E. Gilbert, E. Belloy, M. A. M. Gijs, "High Inductance Planar Transformers," *Sensors and Actuators*, vol.81, pp. 355-358, 2000.

## Chapter 6

### Design of Microscale Magnetic Components

#### 6.1 Introduction

This chapter describes in detail the design process used for the microscale magnetic components manufactured within this thesis. Basic geometry considerations and manufacturability issues are discussed in section 6.2. The layout of the windings is reviewed in section 6.3. Parameters affecting the performance of the magnetic core are covered in section 6.4. The sequence of analytical equations used to predict the performance of the prototype components is contained in section 6.5. Thermal and electromigration issues are discussed in section 6.6. The impact of converter operation on the design of the magnetic component is demonstrated in section 6.7. The importance of efficient magnetic components is emphasised with a review of the component parasitics and losses and their influence on the converter performance in section 6.8. Lastly, this chapter concludes with a summary of the main design considerations.

#### 6.2 Microfabricated component design

The design of microscale magnetic components has typically involved either research into material development or component design and fabrication. This thesis focuses on all these aspects. A preliminary requirement is that the devices to be manufactured must provide a clear evaluation of the magnetic core material. Hence, irrespective of component geometry, an enclosed magnetic path is required to assess the suitability of the magnetic material. A closed magnetic path confines the majority of the flux to the magnetic core fully utilizing thereby the relative permeability of the material. As a result, the leakage flux is minimized and the inductance is maximized. The winding loss occurring as a result of induced eddy currents by leakage flux is also reduced and the electromagnetic Interference is minimized. The importance of a closed magnetic path for determining the suitability of a given material can be demonstrated by considering the solenoid geometry in Fig 6.1. The flux path passes partly through the magnetic core and partly through the air.

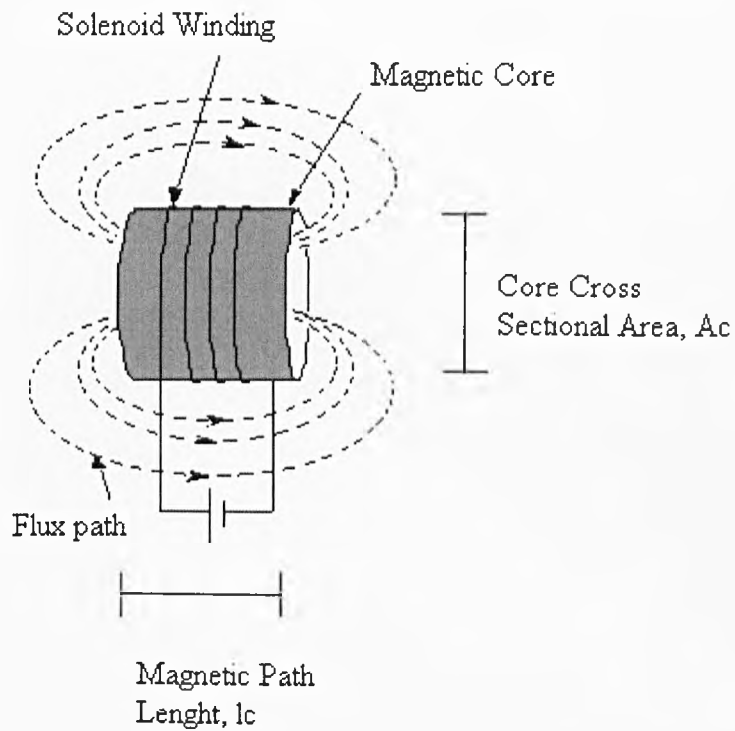


Figure 6.1 Solenoid inductor with a magnetic core. The solenoid component design parameters and flux path are indicated.

The reluctance of the flux through the core is defined as:

$$R = \frac{l_c}{\mu_o \mu_r A_c} \quad (6.1)$$

The reluctance of the return flux path through air is defined as:

$$R = \frac{l_c}{\mu_o A_{air}} \quad (6.2)$$

$\mu_o$  is the permeability of free space (approx  $1.256 \times 10^{-6}$  Hm),  $\mu_r$  is the permeability of the core material (e.g. for permalloy 2000),  $A_c = A_{air}$  is the cross-sectional area, and  $l_c$  is the magnetic path length.

The reluctances are in series therefore the total reluctance is:

$$\frac{l_c}{\mu_o \mu_r A_c} + \frac{l_c}{\mu_o A_{air}} = \frac{l_c + l_c \mu_r}{\mu_o \mu_r A_{ce}} \quad (6.3)$$

This can be approximated to  $\frac{l_c}{\mu_o A_{ce}}$  for  $\mu_r \gg 1$

$$\text{The flux produced by } NI \text{ Amp turns is } \frac{\mu_o A_c NI}{l_c} = \frac{NI}{R} \quad (6.4)$$

With flux density:

$$B = \frac{\mu_o NI}{l_c} = \mu_o H \quad (6.5)$$

$$\text{where } H = \frac{NI}{l_c} \quad (6.6)$$

The inductance of the component is then calculated as follows;

$$\text{Inductance } L = \frac{\mu_o A_c N^2}{l_c} \quad (6.7)$$

Eq (6.7) demonstrates that the relative permeability of the core becomes insignificant and the structure behaves similar to an air cored winding. The suitability of the core material cannot be evaluated when its relative permeability is made redundant. Therefore, the core should contain a closed magnetic path in order for the relative permeability to be effective.

Another consideration is the influence of the core geometry on the properties of the core material, and, as a result, the impact on component performance. Consider a core material for a one-turn micro-inductor. The saturation flux density,  $B$ ,

$$B = \frac{\mu_o \mu_r NI}{l_c}$$

is a predetermined constant for a given material. In the same way, the current applied to the component would be known for a given application. Therefore, the only free parameter left will be either the relative permeability or the flux path length, since

$$\frac{l_c}{\mu_r} = \frac{I\mu_o}{B}$$

The core, typically a rectangle, triangle or a circle, has a certain perimeter. A simple rectangular component is shown in Fig 6.2. With increasing frequency the skin depths of the magnetic material and winding decrease. Therefore, to minimise skin depth losses and maintain the inductance value i.e. overall magnetic core area, the device becomes thinner and wider. The resulting increase in flux path length requires an increase in relative permeability for the inductance value to be maintained. An increase in relative permeability for the same resistivity value will make the material susceptible to skin depth losses at reduced frequency.

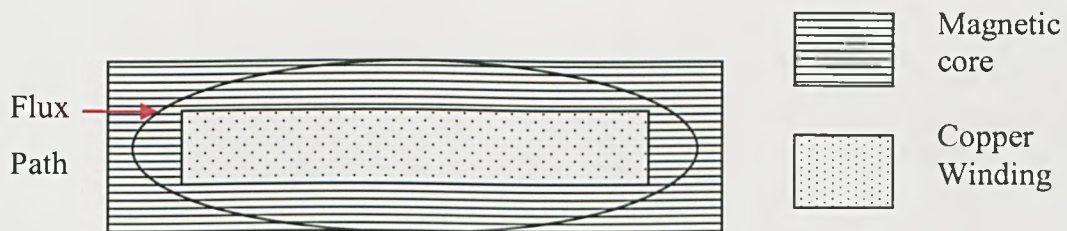


Figure 6.2 Simple rectangular one-turn micro-inductor.

If, for the same area and core material, the rectangular geometry was changed to a triangular geometry, the perimeter is reduced by one third, see Fig 6.3. The required permeability is then reduced by 1/3 and greater skin depth is achieved for the same resistivity.

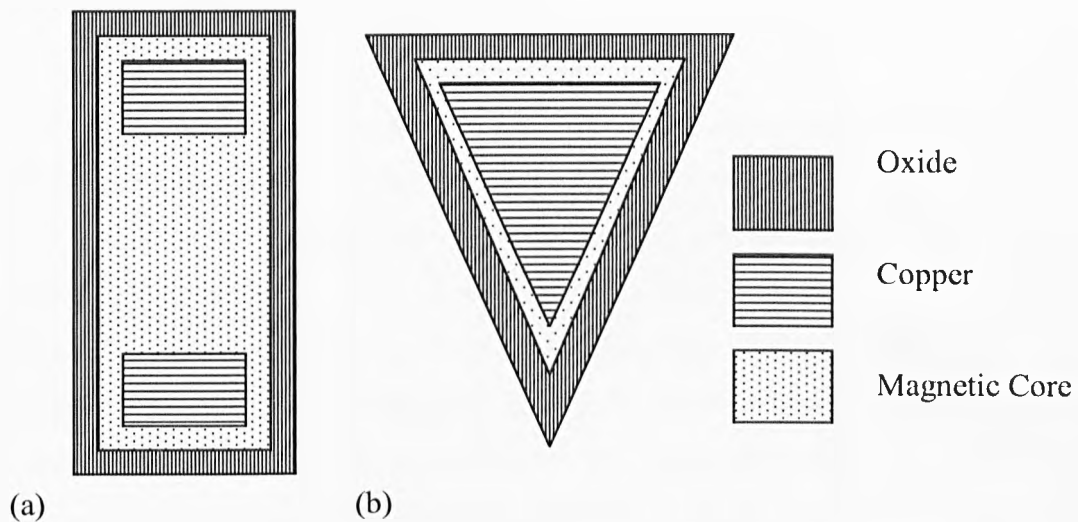


Figure 6.3 (a) Top view displaying the exposed copper contacts & (b) Side view showing the enclosed magnetic path. The illustration of a V-groove micro-inductor is similar to the component fabricated by Sullivan et al [6.1].

A one turn micro-inductor with a triangular trench structure was fabricated by Sullivan et al [6.1]. The fabrication of this V-groove micro-inductor required sputter deposition. As discussed in Chapter 3, sputtering is a slow and costly process, and due to delamination can only be used for small core areas. Chapter 9 will demonstrate that limited laminate layers can have an adverse effect on component performance.

A circular component would suffer from the same technical disadvantages as the triangular component. Moreover, a circular component fabricated by micromaching methods would require non-planar construction. Minimal footprint and low profile are prerequisites for present and future magnetic components. Therefore, a circular component was not investigated. Due to the aforementioned complications of triangular and circular geometries, the investigated components herein are of rectangular planar form. Disadvantages of this geometry will be overcome via tailored core properties and optimal component design. The following section highlights the design and fabrication issues encountered in the selection of micro-inductor and transformer geometries.

### 6.2.1 Basic geometry

Any closed core micro-inductor or micro-transformer made by a process of alternately depositing conductor or magnetic material must have at least two steps of conductor deposition or two steps of core deposition in order to interlink the core and winding.

Designs in either category may be considered as variations or combinations of the basic constructions termed pot-core or solenoid [6.2].

A decision on which design approach is optimal requires a comparison across a variety of factors such as power handling, efficiency, practicality of fabrication, inductance requirement etc. Sullivan et al demonstrated that analytically the pot-core design can handle more power for the same area as the solenoid geometry [6.3] by using a simplified model as shown in Fig 6.4. Winding and core layers were interchanged to represent the two different configurations. Each component was modeled with the same layer thicknesses. At low power density the two designs have the same efficiency, given that the ratio of flux density and current density in each is set to maximize efficiency. However with the same power density, the solenoid has a higher flux density. This concept can be simply demonstrated by Eq (6.8).

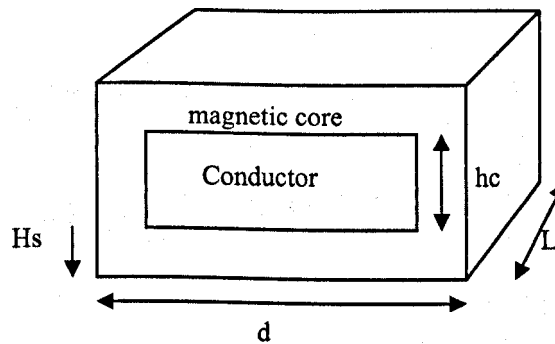


Figure 6.4 Simplified pot-core component. When adapted to solenoid component the magnetic layer and conductor layer are interchanged [6.3].

$$B_{pk} = \frac{V}{KNA_c f} \quad (6.8)$$

The constants  $K$ ,  $N$ ,  $f$  and  $V$  represent the waveform parameter, number of turns, frequency and voltage, respectively. The pot-core structure has a greater  $A_c$ , therefore, a reduced peak flux density.

Sometimes an important issue in choosing a core shape is the magnitude and distribution of external magnetic fields generated by the transformer or inductor. The conventional pot-core is regarded as performing more favorably in minimizing external



magnetic fields, as the core encloses and so shields the windings. The result is low external fields regardless of the distribution of primary and secondary windings inside the core. Solenoid components also have low external fields due to the winding distribution. In transformer applications the primary and secondary windings are customarily distributed evenly around the core, lying on top of each other with little space between. Thus the currents cancel each other, so little external field results. In micro-fabrication the ability to finely pattern windings makes it relatively easy to arrange the windings so that primary and secondary currents locally cancel. Hence, external fields are not a primary concern in component development within this thesis.

Perhaps the most important factor in comparing the pot-core and solenoid designs is the ease of manufacture. This parameter is the most difficult to quantify and obviously dependent on fabrication capability. In the solenoid case, a difficulty often encountered is the interconnection of the top and bottom winding layers to encircle the core. This requires accurate alignment between the layers to insure proper connections, requires low-resistance contacts and connection over a vertical distance greater than the thickness of the core. A novel flip-chip bonding procedure introduced in Chapter 7 developed by the author overcomes the aforementioned difficulties.

In the pot core design, the inter-layer connection requirements are less severe because the windings are planar and manufactured in a single deposition process. A complication arises if the inductor winding is spiral as access to the output pad is required. This typically requires a fourth deposition step, or the use of external connections such as bond wires. The thickness of the conductor layers is also typically larger than the thickness of the core layers, therefore, the vertical distance over which connections must be made is larger in the pot-core design. Furthermore, to form a closed magnetic core the upper and lower sections of the core have to be joined, as shown in Fig 6.5. The points where the two layers join is within the main flux path and can generate an unfavorable leakage flux.

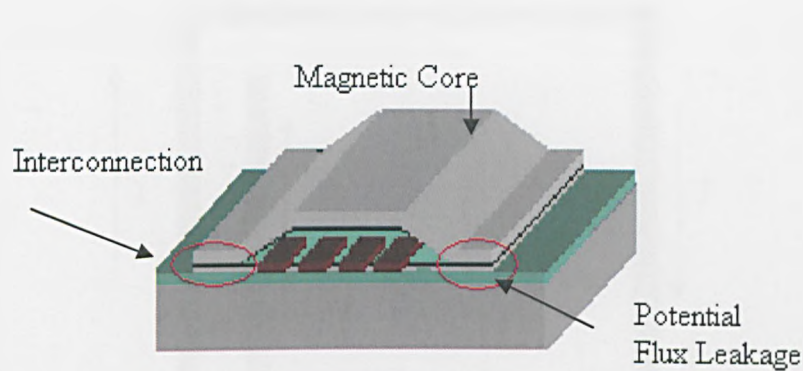


Figure 6.5 Pot-core with magnetic core enclosing the windings. The points of potential leakage flux due to core assembly are circled.

Another consideration is the tailoring of magnetic film properties with magnetic field annealing. Both geometries can be used with magnetic field annealing; therefore, this is not a design restriction. As mentioned in Chapter 4 the solenoid core can have the majority of the length oriented in the favorable hard axis. In the pot-core design, the easy axis orientation is not difficult if, again, the shape is long and rectangular.

There are advantages and disadvantages to both fundamental configurations. A decision on which is optimal cannot be made without consideration of the winding geometry. The following section outlines the attributes of various windings and their influence on both configurations.

### 6.3 Winding design

Micromachined magnetic components have different fabrication approaches and characteristic properties depending on their winding geometries: (1) Spiral, (2) Solenoid, and (3) meander [6.4].

#### (1) Spiral Geometry

The spiral inductor is typically considered as a set of connected microstrips [6.5]. Fig 6.6 displays a basic spiral winding made of 5 connected microstrips. The spiral winding belongs to the pot-core configuration.

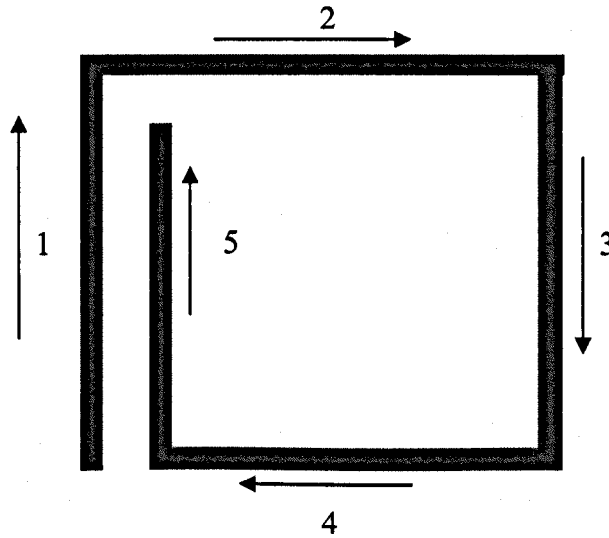


Figure 6.6 Layout of a spiral winding. The arrows indicate the path of the applied current.

Based on Grover's formulas Greenhouse developed an algorithm for computing the inductance of planar rectangular spirals. The Greenhouse method states that the overall inductance of a spiral can be computed by summing the self-inductance of each winding segment and the positive and negative mutual inductance between all possible winding segment pairs. The mutual inductance between two sections depends on their angle of intersection, length, and separation. Two sections orthogonal to each other have no mutual coupling since their magnetic flux is not linked together. The direction of current flow in the respective sections determines the sign of coupling. The coupling is positive if the currents in the two sections are in same direction and negative for opposite currents [6.5].

For an individual section with a rectangular cross section area, the DC self inductance can be expressed as follows:

$$L_{self} = 2l \left( \ln \frac{2l}{w+t} + 0.5 + \frac{w+t}{3l} \right) \quad (6.9)$$

where  $L_{self}$  is the self inductance in nH; and  $l$ ,  $w$  and  $t$  are the length, width and thickness of the section in centimetres.

Since the inductance is primarily determined by the magnetic flux external to the winding, the variation in the wire cross-section dimensions has little effect on the

inductance. In general, the windings with a smaller cross-section area have a slightly larger inductance because they generate more magnetic flux external to the wire. Eq (6.9) is not valid for windings with cross-section dimensions greater than approximately twice their length.

The mutual inductance between two parallel sections can be calculated using

$$M(i, m) = 2lQ \tag{6.10}$$

where  $M$  is the inductance in nH between sections  $i$  and  $m$ , the multiple of two is simply used to indicate the equivalent  $M(m, i)$  is the same,  $l$  is the wire length in cm, and  $Q$  is the mutual inductance parameter, which is calculated as follows

$$Q = \ln \left[ \frac{l}{GMD} + \sqrt{1 + \left( \frac{l}{GMD} \right)^2} \right] - \sqrt{1 + \left( \frac{GMD}{l} \right)^2} + \frac{GMD}{l} \tag{6.11}$$

In Eq(6.11), GMD denotes the geometric mean distance between sections, which is approximately equal to the pitch of the sections. In most cases, indicated by Fig 6.6 & 6.7, the mutual inductance calculation is performed for two segments of different lengths ( $i$  and  $m$ , where  $i > m$ ).

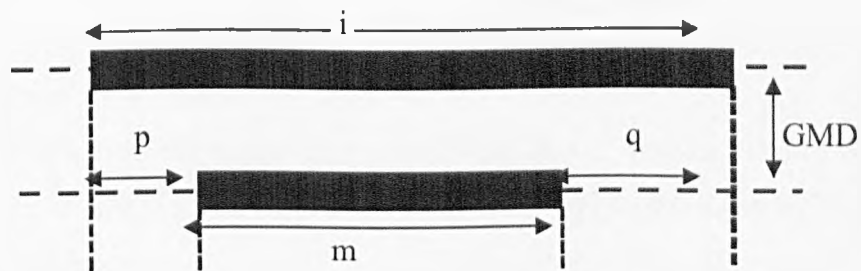


Figure 6.7 The parameters for the calculation of mutual inductance between two sections of windings.

In this situation, the mutual inductance is calculated as follows

$$2M(i, m) = (M_{m+p} + M_{m+q}) - (M_p + M_q) \quad (6.12)$$

and the individual  $M$  terms are calculated using Eq (6.10) and the lengths corresponding to the subscripts

$$M_{m+p} = 2l_{m+p}Q_{m+p} - 2(m+p)Q_{m+p} \quad (6.13)$$

Where  $Q_{m+p}$  is the mutual inductance parameter  $Q$  for  $GMD/(m+p)$ . The overall inductance of the spiral windings, as depicted in Fig 6.8, is determined as follows;

$$L_{total} = L_1 + L_2 + L_3 + L_4 + L_5 - 2(M_{1,3} + M_{2,4} + M_{3,5}) + 2M_{1,5} \quad (6.14)$$

The total inductance of the device with a magnetic core in the pot-core configuration becomes the summation of the inductance of the windings and the core contribution,

$$L_{total} = L_{winding} + L_{core} \quad (6.15)$$

Where

$$L_{core} = \frac{\mu_o \mu_r N^2 A_c}{l_c} \quad (6.16)$$

## (2) Solenoid Geometry

Fig 6.8 illustrates a typical solenoid component [6.4]. Conventional macro-inductors usually have a solenoid shape as they can be simply fabricated by wrapping coils around magnetic cores. However, the three-dimensional winding structure presents a significant fabrication challenge in micromachining.

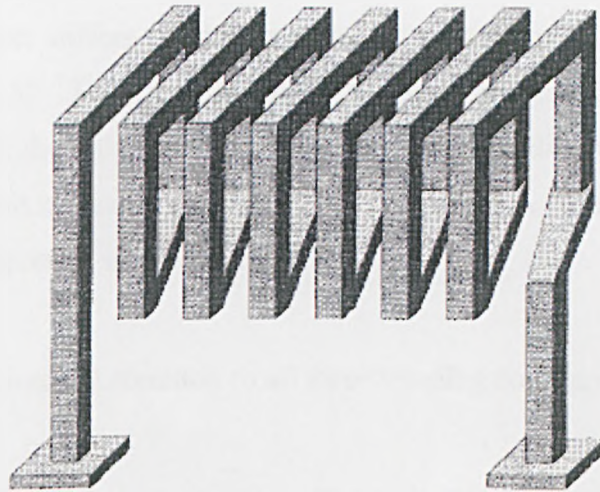


Figure 6.8 Solenoid winding. The winding turns enclose a magnetic that would pass through the centre of the windings [6.4].

Due to the 3D nature of the solenoid geometry and for a given footprint area, a higher number of turns can be fabricated in comparison to a planar winding. However, with increased turns the parasitic capacitances between windings increase and the SRF reduces. As with the spiral windings, the total device inductance is the sum of the inductances of the windings and the core. Eq (6.16) is used to determine the inductance.

### (3) Meander Geometry

A schematic diagram of meander windings with the magnetic core is shown in Fig 6.9 [6.4]. In this device a magnetic core is wrapped around a planar conductor. As with the spiral windings, the meander geometry has an advantage over the solenoid geometry in that the windings are planar, requiring no interconnection vias that may increase the overall resistance.

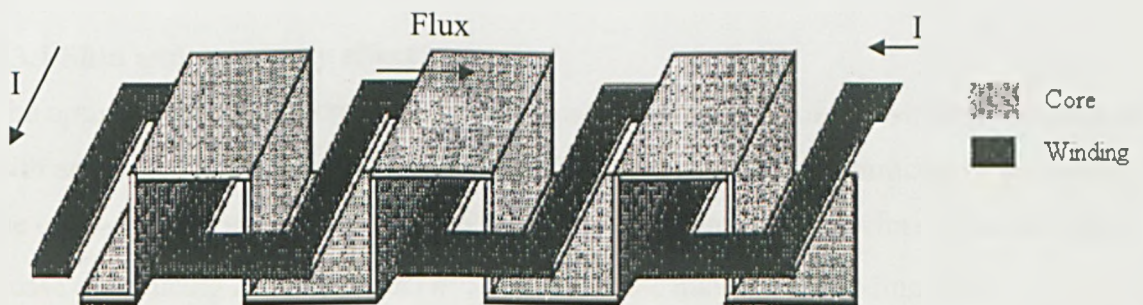


Figure 6.9 Meander windings. The arrows indicate the path of the current through the winding [6.4].

The meander windings are simple to fabricate but because of the negative turn-to-turn mutual inductance, suffers from lower overall inductance in comparison to the spiral approach [6.4, 6.5]. Therefore, to obtain the same inductance as an equivalent spiral component, when the only variable is the number of winding turns, more winding turns are required which increases the component footprint. A reduction in power density of the meander component would then follow.

The following points are common to all three winding configurations:

- (1) When assessing potential core materials within a component, the individual windings must be able to carry the saturation current in order to fully utilise the core material and maximise the power density.
- (2) Winding inductance is a minor contributor to the overall inductance value. This is due to the high relative permeability of the alloys as explained in Chapter 2.
- (3) Common to all of the winding geometries discussed is the model shown in Fig 3.2. This model displays the universal parasitic losses that must be minimised if efficient operation is to occur. The total winding resistance of the component, which produces joule losses, is in series with the inherent winding inductance, with total parasitic capacitance in parallel.
- (4) All of the windings fabricated within this thesis will be single layer, not multi-layer.

The spiral and solenoid winding geometries are studied in the next chapter. The meander geometry was not investigated due to the potential reduction in power density in comparison to the spiral configuration. The following section describes the losses incurred in the windings of transformers and inductors.

### **6.3.1 Skin and proximity effect**

The optimization of a micro-inductor or transformer in terms of the winding loss begins with an assessment of the DC resistance. The DC resistance is minimized by increasing the cross-section of the windings and reducing their number. Therefore, it is not simply a case of reducing  $R$  but rather  $R/n^2$ , where  $n$  is the number of winding turns.

Simple DC,  $R/n^2$  minimization would dictate that the conductor should be as wide as



possible and the spacing between the conductors as narrow as possible. The DC resistance is calculated as follows

$$R_{dc} = \rho \frac{l}{A_w} \quad (6.17)$$

where  $\rho$  is the resistivity of the winding,  $l$  is the length of the winding and  $A_w$  is the total cross-sectional area of the windings. For high frequency currents skin effect becomes important and when the conductor is large compared to its skin depth, it is not effectively utilized [6.6]. At low frequencies all conductor dimensions are small compared with skin depth i.e. the current density is homogeneous over all conductor cross-sections. At high frequencies, the opposing fields created by eddy currents are strongest in the centre of the conductor, causing the current density in this region to decrease sharply. Most of the current flows much more strongly near the surface of the conductor, causing the apparent cross-sectional area of the current-carrying conductor to decrease, and consequently causing the AC resistance to increase. The skin depth can be calculated using the magnetic permeability,  $\mu$ , and the electrical conductivity,  $\sigma$ , of the material, as well as the frequency of operation,  $\omega$ , using the following equation [6.7-6.9]:

$$\delta = \sqrt{\frac{2}{\omega \mu_o \mu_r \sigma}} \quad (6.18)$$

The proximity effect is another manifestation of eddy currents, in which nearby conductive material experiences induced eddy currents due to the magnetic field of a separate conductor. Due to the close proximity between windings, the current in each winding can induce eddy currents in other segments and cause the resistance to increase [6.10].

As a rule of thumb, the thickness of the windings, must be twice the skin depth [6.6]. There is also an optimal width for the windings: narrow windings waste inter-winding space, and large widths encounter large skin effect and proximity effect losses. Fig 6.10 illustrates this trade-off.

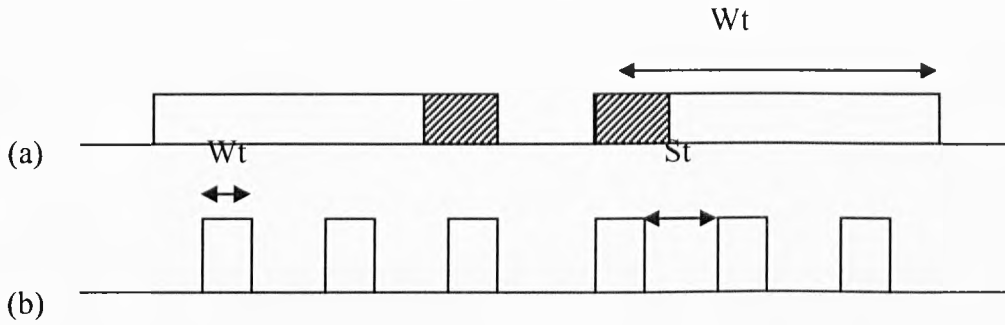


Figure 6.10 Optimum width of windings (a) the width of the winding is far greater than the skin depth. The current flows in the shaded region of the winding wasting the majority of the area. (b) When the width of the winding is too small a lot of the component footprint is lost on insulation between the turns.

The skin effect and proximity effect losses can be described by an AC resistance, determined by multiplying the DC resistance by a factor  $F_r$ ,

$$F_r = 1 + \frac{5p^2 - 1}{45} \phi^4 \quad (6.19)$$

where  $p$  is the number of winding layers and  $\phi$  is the ratio of conductor thickness to skin depth [6.6]. To minimize AC resistance for transformer and inductor applications the width of the individual turns,  $W_t$ , is adjusted to minimize the resistance factor,  $F_r'$ , that takes into account the reduction in conductor area due to spacing between windings;

$$F_r' = F_r \frac{W_t + S_t}{W_t} \quad (6.20)$$

where  $S_t$  is the spacing between turns.

Eq (6.19) is based on two important approximations. Firstly, (6.19) represents the first terms of a series of expansion of the hyperbolic trigonometric terms in the exact one dimensional solution,

$$F_r = \text{Real} \left[ \alpha \coth(\alpha) + \frac{2}{3} (p^2 - 1) \alpha \tanh(\alpha/2) \right] \quad (6.21)$$

where

$$\alpha = (1 + j)\varphi \quad (6.22)$$

A comparison between the total resistance factor  $F_r'$  based on the exact one-dimension solution (6.21) with the approximation (6.19) at 1MHz, with 90  $\mu\text{m}$  thick copper windings and 20  $\mu\text{m}$  spacing between turns, an optimal width of approximately 200  $\mu\text{m}$  was determined by both sets of equations. The variation in  $F_r$  is negligible, and the choice of  $W_t$  is not significantly affected by the approximation.

The second important approximation is that the field is one-dimensional. Experimental and simulated results in Chapters 8 and 9 demonstrate that the one-dimension field approximation is adequate for the pot-core and solenoid geometries investigated. The purpose of the optimization is primarily to insure that possible means of implementing large performance improvements can be achieved quickly by adjusting the design parameters. In that context, complex 3D analysis based on finite element methods is not necessary at this stage.

#### **6.4 Core loss in micro-inductors and transformers**

Core losses, as discussed in Chapter 2, consists of hysteresis and eddy current power losses. The shape of the hysteresis loop is shown in Fig 6.11.

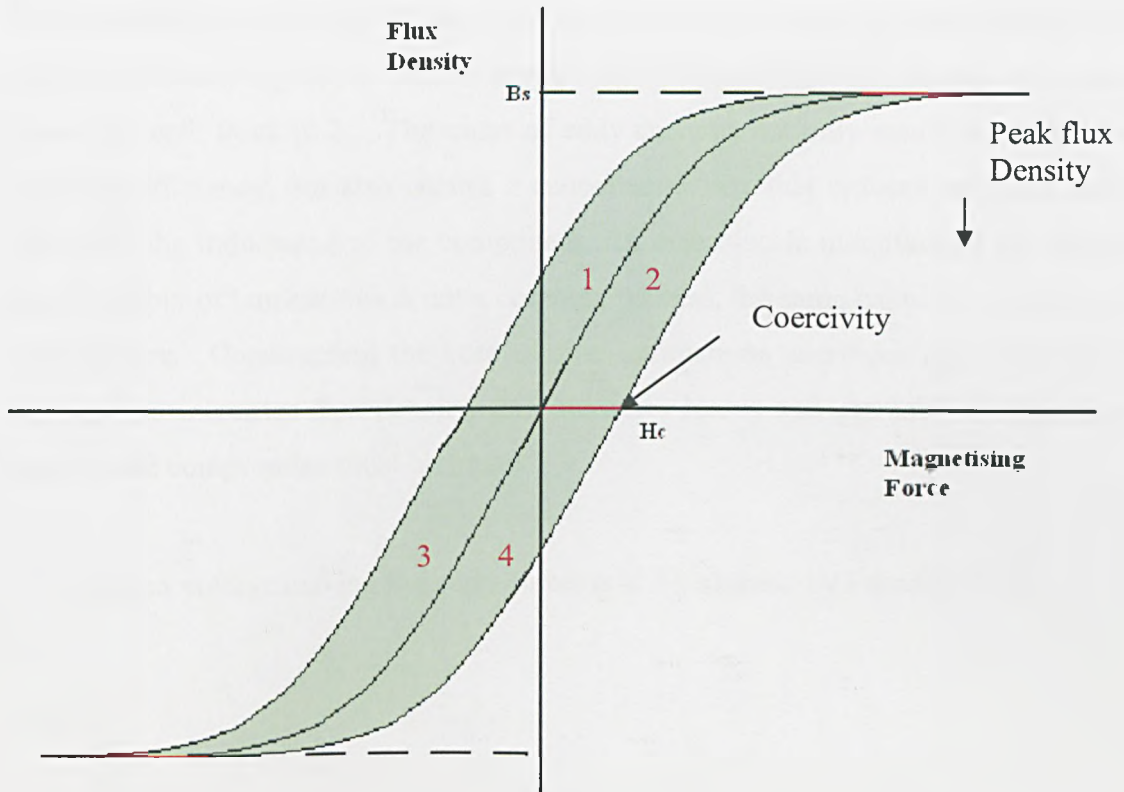


Figure 6.11 Hysteresis loop of a magnetically soft material. The peak flux density and coercivity are highlighted as they are used in the power loss approximation.

The area within the hysteresis loop is representative of the power loss of the hysteresis curve. A quarter of the overall area of the loop is found by multiplying the peak flux density and the coercivity. The volume of the core (*length x width x height*),  $V$ , is then multiplied by the number of times the loop is cycled,  $f$ , i.e. frequency. Eq (6.23) represents the power loss incurred by hysteresis;

$$P_{hys} = \frac{3}{4} fV(4B_{pk}H_c) \quad (6.23)$$

The correction factor  $3/4$  is used to approximate the actual area of the hysteresis loop [6.2, 6.11].

Eq (6.23) highlights that reducing coercivity reduces the hysteresis loss. A reduction in flux density also reduces the hysteresis loss; however, this is undesirable from a power density perspective.

Eddy current losses in the core can be minimized by consideration of skin depth. Instead of one solid core layer, the core is constructed of numerous laminations approximately one skin depth thick [6.2]. The onset of eddy currents not only results in Joule heating, reducing efficiency, but also creates a cancellation flux that reduces the main flux and, therefore, the inductance of the component. In macro-scale manufacture the fabrication and assembly of laminations is not a complex process, the same cannot be said for micro-manufacture. Constructing the core of fine laminations sacrifices core cross-sectional area and so increases flux density, this increases losses and can lead to saturation. An appropriate compromise must be found.

The induced voltage driving the eddy currents is determined by Faraday's law:

$$V = \frac{d\phi}{dt}$$

for a winding with N turns this becomes;  $V = N \frac{d\phi}{dt}$

Then;  $\frac{V}{N} = \frac{d\phi}{dt}$

And using the power loss relationship

$$P_{eddy} = \frac{V^2}{R} = \frac{\left(\frac{V_{rms}}{N}\right)^2}{R_{eddy-core}} \tag{6.24}$$

The eddy current core resistance is obtained through a one-dimensional analysis of the electromagnetic diffusion in a stack of laminations for sinusoidal excitation [6.12]. In order to find an analytical solution for the resistance and inductance of a laminated core as a function of frequency, assume that a winding is uniformly wound around a laminated magnetic core of length  $l$  as shown in Fig 6.12. The magnetic core material is assumed to be linear, isotropic, and homogeneous. Therefore it has a constant conductivity,  $\sigma$ , and a constant permeability  $\mu$ . In this model, it is assumed that (1) the length of the magnetic lamination stack is much larger than either of its cross-sectional

dimensions (2) the cross-sectional thickness is much smaller than the cross-sectional width. Under these assumptions, the edge effects of the film can be neglected. In other words, the field is penetrating only from the top and bottom sides (i.e. one-dimensional analysis), and the fringing field effects of the front end and the back end are neglected, as shown in Fig 6.12.

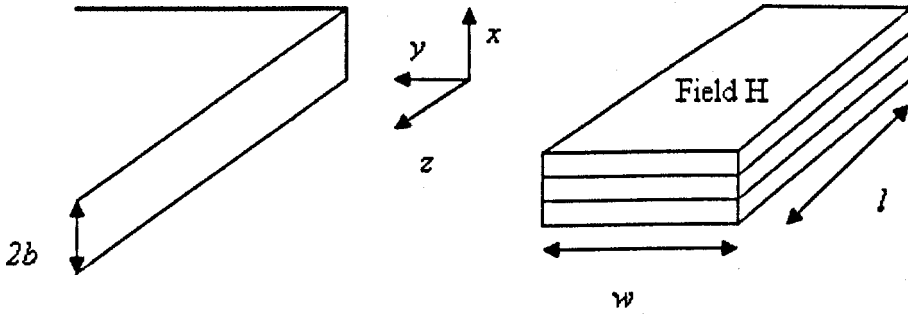


Fig 6.12 An illustration for a core model ( $l \gg w$  and  $w \gg 2b$ ) and: (a) a sheet and its thickness, and (b) stack of laminations and its dimensions.

Finally, resolving this expression into its real and imaginary parts, the inductance,  $L_{ac}$ , is

$$L_{ac} = L_o \frac{1}{\frac{2b}{\delta}} \times \frac{\sinh \frac{2b}{\delta} + \sin \frac{2b}{\delta}}{\cosh \frac{2b}{\delta} + \cos \frac{2b}{\delta}} \quad (6.25)$$

And the resistance,  $R_{ac}$ , representing the eddy current loss is

$$R_{ac} = \omega L_o \frac{1}{\frac{2b}{\delta}} \times \frac{\sinh \frac{2b}{\delta} - \sin \frac{2b}{\delta}}{\cosh \frac{2b}{\delta} + \cos \frac{2b}{\delta}} \quad (6.26)$$

Appendix A details the derivation of Eq (6.25) & (6.26).

The cost and ease of fabrication will depend on the number of laminates. The results of the one manufactured core layer will be assessed and compared against improvements in performance via multiple layers at one skin depth thick. This optimisation is performed in Chapter 9.

Irrespective of the number of laminates it is important that the maximum flux density is utilised. For example, in a design thought to be optimal with the flux below the maximum allowable, the voltage and current are scaled up by a factor  $s = B_s/B_p$  where  $B_s$  is the saturation flux density or other maximum allowable flux and  $B_p$  is the maximum flux density in the original design. The  $I^2R$  loss increases by a factor of  $s^2$ . The eddy current loss in the core also increases by  $s^2$ . Thus, assuming minimal hysteresis loss, the total loss scales by  $s^2$ . The power handled, approximately VI, also increases by  $s^2$  and so the efficiency remains constant. Thus, the power handling has been increased without affecting efficiency proving that the original design was not optimal.

Section 6.4 applies the aforementioned winding and core theory to the design of the prototype.

### **6.5 Component design: the solenoid approach**

Inductors and transformers are designed for a specific application. The application typically specifies parameters such as inductance, frequency of operation, current etc. However, the only design constraints at this stage of prototype development are manufacturability and capability of assessing various core materials. Due to the complications of multi-layer alloy deposition, the initial objective is to attain high operating efficiency of a single layer magnetic core component.

As discussed, the geometries encountered can be spiral, meander or solenoid. The solenoid approach is favored because of the higher number of turns that can be obtained for a given area [6.13]. The solenoid also permits the inclusion of the core prior to interconnecting the lower and upper layers of the winding. The electrodeposited magnetic core can then be characterized magnetically and electrically prior to inclusion within the component. A novel fabrication process is explained in detail in Chapter 7. Fig 6.13 displays an illustration of the prototype. The overall width, length and height of the component are 2mm, 5mm and 250 $\mu$ m, respectively. The windings surround the magnetic core made, in the first instance, of the permalloy Ni<sub>80</sub>Fe<sub>20</sub>, 10 $\mu$ m thick. The core is positioned between an upper and lower insulation layer of 5 $\mu$ m thick AZ 9260.



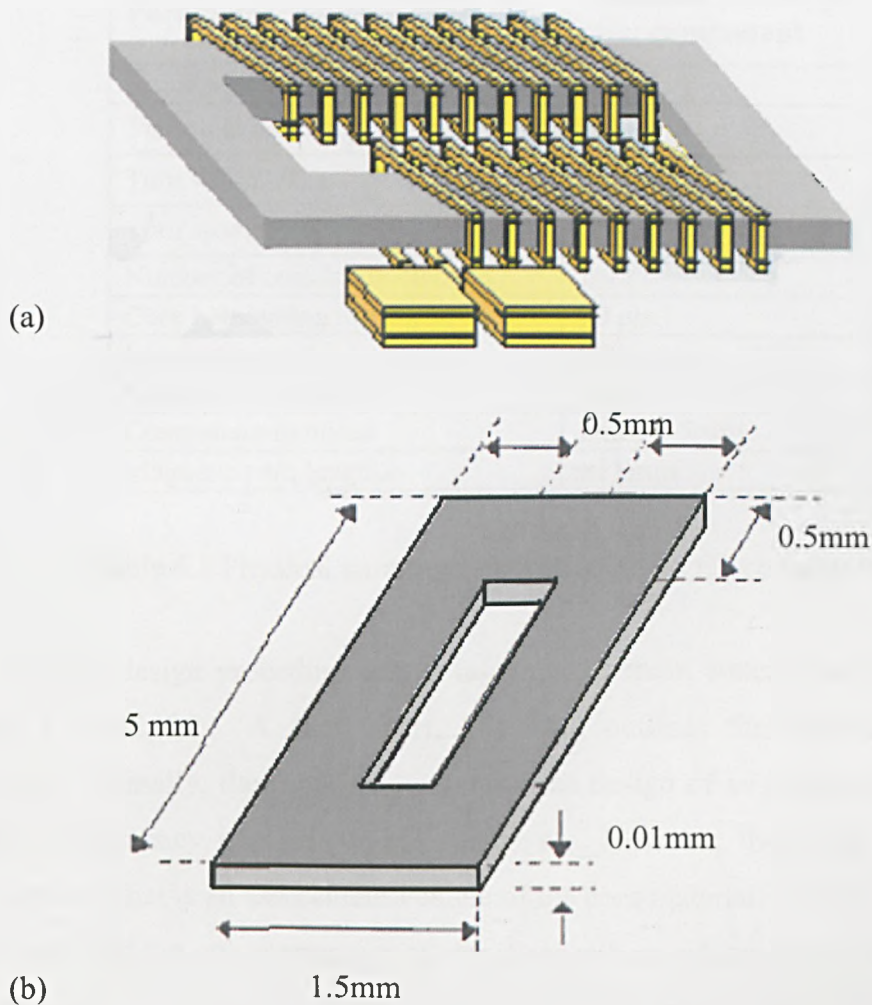


Figure 6.13(a) Illustration of the solenoid micro-inductor of size  $2\text{mm} \times 5\text{mm} \times 250\mu\text{m}$  ( $W \times L \times T$ ). 33 windings wrap around the core, (b) The closed magnetic core dimensions.

The windings are optimised for operation at 1 MHz; the physical parameters of the solenoid micro-inductor are contained in Table 6.1.

Parameter	Solenoid prototype component
Number of turns, $N$	33
Turn thickness, $H_t$	90 $\mu\text{m}$
Turn width, $W_t$	200 $\mu\text{m}$
Turn spacing, $S_t$	20 $\mu\text{m}$
Number of core laminations, $n$	1
Core Lamination thickness, $h$	10 $\mu\text{m}$
Lamination width	500 $\mu\text{m}$
Lamination insulation	5 $\mu\text{m}$
Component footprint	2mm x 5mm
Magnetic path length, $l_c$	$\approx 1$ mm

Table 6.1 Physical parameters of the solenoid micro-inductor.

The following design procedure brings together the main conclusions and formula of sections 6.3 and 6.2. A flow chart, Fig 6.14, outlines the analytical assessment procedure. Normally, the input parameters to the design of an inductor would include inductance, frequency, applied current, voltage etc. However, the design in this thesis is for an inductor that is an assessment vehicle of the core material. Hence, the component is fabricated and the only parameter of significance here relates to the properties of the magnetic core.

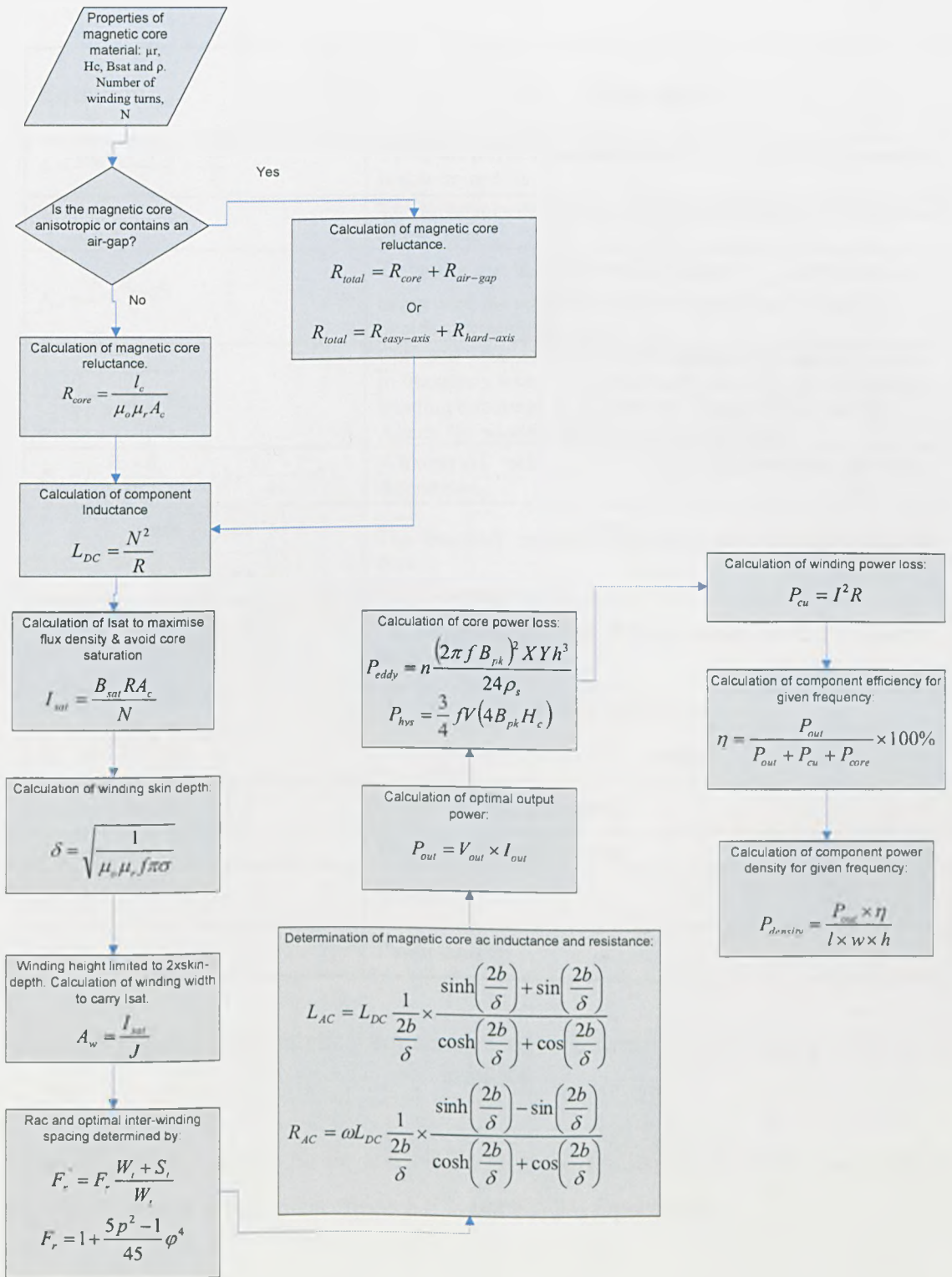


Figure 6.14 flowchart of analytical equations used to determine component efficiency and power density. The flowchart indicates that anisotropic and cores with an air-gap require their respective reluctances values to be calculated.

Table 6.2 summarises and describes the analytical equations used in defining component performance.

Equation	Description
$L = \frac{(\mu_0 \mu_r A_c N^2)}{l_c} = \frac{N^2}{R}$	Using the physical parameters of the core the DC inductance is determined.
$R = \frac{l_c}{\mu_0 \mu_r A_c}$	The reluctance of the core is determined using the dimensions of the core.
$I_{sat} = \frac{B_{sat} R_{total} A_c}{N}$	To ensure that the highest flux density, $B_{sat}$ , of the core is being used the saturation current is calculated. This also avoids saturating the core.
$\delta = \sqrt{\frac{1}{\mu_r \mu_0 f \pi \sigma}}$	Core and winding skin depth is calculated to assess the point in frequency when ac losses occur. $2x\delta$ is the typical optimal winding thickness. With a typical current density of 10 A/mm <sup>2</sup> the winding width can be determined.
$F_r' = F_r \frac{W_l + S_l}{W_l} \quad F_r = 1 + \frac{5\rho^2 - 1}{45} \varphi^4$	Winding AC resistance and optimal inter-winding space is determined.
$L_{ac} = L_{DC} \frac{1}{\delta} \frac{\sinh\left(\frac{2b}{\delta}\right) + \sin\left(\frac{2b}{\delta}\right)}{\cosh\left(\frac{2b}{\delta}\right) + \cos\left(\frac{2b}{\delta}\right)}$	The frequency response of the inductance due to the magnetic core.
$R_{eddy} = \omega L_{DC} \frac{1}{\delta} \frac{\sinh\left(\frac{2b}{\delta}\right) - \sin\left(\frac{2b}{\delta}\right)}{\cosh\left(\frac{2b}{\delta}\right) + \cos\left(\frac{2b}{\delta}\right)}$	The frequency response of the resistance due to the magnetic core.
$P_{out} = V_{out} \times I_{out}$	Optimal output power is determined.
$P_{eddy} = n \frac{(2\pi f B_{pk})^2 XYh^3}{24\rho_c}$	Power loss due to core eddy currents
$P_{hyst} = \frac{3}{4} fV(4B_{pk}H_c)$	Power loss due to hysteresis
$P_{Cu} = I^2 R_{ac}$	Power loss due to windings
$\eta = \frac{P_{out}}{(P_{out} + P_{core} + P_{Cu})}$	Efficiency
$P_{density} = \frac{P_{out} \times \eta}{l \times b \times h}$	Power density

Table 6.2 Summary of analytical equations used to define the performance of the micro-inductor.

Magnetically anisotropic Ni-Fe and Ni-Fe with the inclusion of a finely patterned air-gap are discussed briefly in sections 6.5.1 and 6.5.2, respectively.

### 6.5.1 Solenoid anisotropic core

The value of the DC inductance of the fabricated micro-inductor utilizing an anisotropic Ni-Fe core is provided by equation (6.27), where N is the total number of coil turns and  $R_{total}$  is the total reluctance of the magnetic film. As indicated in Chapter 5, the relative permeability of the electroplated alloy is derived from the linear portion of the magnetization curve of the plated materials. However, the reluctance value of the anisotropic permalloy film requires the summation of the reluctance values along the

easy and hard axes according to equations (6.29) & (6.30) [6.14].

$$L_{DC} = \frac{N^2}{R_{total}} \quad (6.27)$$

$$R_{total} = R_{easy-axis} + R_{hard-axis} \quad (6.28)$$

$$R_{easy-axis} = \frac{2L_{e-axis}}{\mu_0 \mu_{r,e-axis} A_c} \quad (6.29)$$

$$R_{hard-axis} = \frac{2L_{h-axis}}{\mu_0 \mu_{r,h-axis} A_c} \quad (6.30)$$

In Eq(6.29) & (6.30)  $L_{h-axis}$  and  $L_{e-axis}$  are the lengths of the closed magnetic path along the hard and easy axes. The two easy axes and hard axes are 1.5mm and 5mm respectively, see Fig 6.13(b). The constants  $\mu_0$  and  $\mu_r$  are the permeability of free space and the relative permeability of the magnetic core. The same evaluation procedure of section 6.3 then follows.

### 6.5.2 Solenoid air-gap

The inclusion of an air-gap in the core or the flux path increases the reluctance of the core. The effective relative permeability decreases and, as a result, the inductance is decreased. The increase in reluctance leads to an increase in saturation current, as indicated in Fig 6.14.

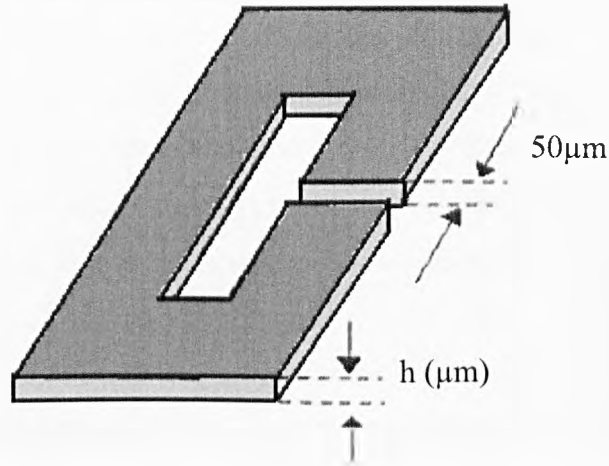


Figure 6.15 The inclusion of an air-gap in the flux path of the core.

An illustration of the air-gap within the electrodeposited and commercial alloy is shown in Fig 6.15. The inclusion of an air gap, either one single air-gap or a series of finer gaps, provides a method of tailoring the relative permeability of the film. This is useful if the film has not been tailored during deposition or if post thermal annealing was not possible. The calculation of inductor performance follows the same procedure as before with the relative permeability being replaced by the effective permeability. The effective permeability is calculated as follows [6.4]

$$\mu_e = \frac{\mu_r}{1 + \frac{l_g \mu_r}{l_c}} \quad (6.31)$$

With  $l_g$  and  $l_c$  the gap length and magnetic path length respectively. The air-gap length fabricated in electrodeposited and commercial alloys is  $50\mu\text{m}$ . A disadvantage of the air-gap is that large fringing effects may induce additional winding loss and unacceptable EMI to neighbouring components. Therefore, it is advantageous to tailor the film properties during deposition. However, if fringing is minimal and the reduction in inductance acceptable, there will be an increase in power density due to greater  $I_{sat}$ . With an increasing power density requirement, knowledge of thermal and electromigration issues is required.

## 6.6 Thermal dissipation & electromigration

An important parameter in the design of magnetic passive power component is the allowable temperature rise that is determined by the power dissipated and heat removal capability of the component. Typical power semiconductors are rated to dissipate about 500 W/cm<sup>2</sup> [6.3]. In practice this data-sheet value is typically reduced 50% or more depending on the type of heat sinking used. 500 W/cm<sup>2</sup> represents an upper bound for aggressive heat sinking such as liquid cooling. With similar mounting and heat-sinking techniques to those used for semiconductors similar power dissipation should be possible for microfabricated magnetic components. The upper bound of 500 W/cm<sup>2</sup> is far above the typical dissipation of our designs of approximately 5-150 W/cm<sup>2</sup>. Only very low efficiency, high power density many layered core designs would exceed this limit.

Another concern when trying to maximise the power handling of metallic conductors is electromigration effects. Electromigration is the transport of material caused by the gradual movement of the ions in a conductor due to the momentum transfer between conducting electrons and diffusing metal atoms. Fortunately electromigration will not be a problem for our devices, copper is less susceptible to electromigration than aluminium, current densities are within typical PCB limitations, and the conductor line widths are relatively large.

Section 6.7 presents a description of the pot-core components fabricated and tested within this thesis.

## 6.7 Pot core micro-inductors and transformers

A 4-turn spiral micro-inductor, a pot-core “race-track” 3 turn micro-inductor and a 1:1 pot-core transformer, were also designed and manufactured. The three components are planar and have a Ni-Fe permalloy magnetic core of 10µm thickness. The only variable being the winding layout. The details of the pot-core components are displayed in Table 6.3.



Type	Description
4 turn spiral micro-inductor	Number of turn: 4 Winding width: 300μm Winding Thickness: 30μm Component footprint: 5mmx15mm Core layer Thickness: 10μm
1:1 “race-track” micro-transformer	Number of Primary & Secondary Turns: 3 Winding width: 300μm Winding Thickness: 30μm Component footprint: 15mmx10mm Core layer Thickness: 10μm
3 turn “race-track” micro-inductor	Number of Turns: 3 Winding width: 300μm Winding Thickness: 30μm Component footprint: 15mmx15mm Core layer Thickness: 10μm

Table 6.3 Details of the pot core microscale magnetic components.

The assessment of efficiency and power density of the pot-core magnetic components follows the same procedure outlined in section 6.3. The micro-transformer, as mentioned in Chapter 3, is simply two inductors that are coupled through a shared magnetic circuit, that is, two or more windings that link some common flux. The important parameter that defines this relationship, the coupling factor,  $K$ , can be calculated by:

$$K = \frac{L_{ps}}{\sqrt{L_{sp}L_{ss}}} \quad (6.32)$$

Where  $L_{ps}$  is the mutual inductance,  $L_{sp}$  is the primary self-inductance and  $L_{ss}$  is the secondary self-inductance. The coupling coefficient is equal to 1, if  $L_{ps} = \sqrt{L_{sp}L_{ss}}$ ; this would only occur if there were no leakage inductance. As with the solenoid component, analytical and experimental results will be compared in Chapter 8.

## 6.8 Review of circuit parameters on component design

One of the main parameters to specify is the switching frequency of the converter. The higher the frequency the smaller the flux carrying demand is, therefore the components can be made smaller. Once the circuit topology is known and the operating frequency is selected, in this case 1 MHz, the next influence on component size is the mode of operation. For example, a buck converter in Continuous Current Mode of operation (CCM), with the same specification, will then be altered into a Buck converter with zero-voltage switching (ZVS), to demonstrated this fact.

The circuit specifications are contained in Table 6.4 and the CCM Buck is shown in Fig 6.16. These specifications were provided to us by the company sponsoring the project.

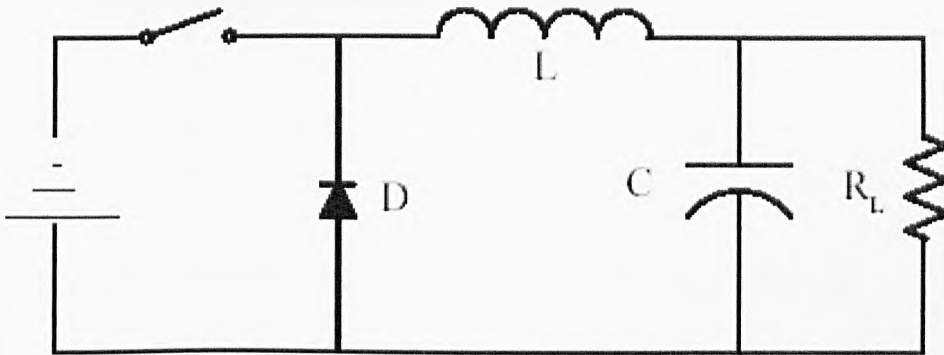


Figure 6.16 Buck (CCM) converter.

$V_{in}$	28 Volts
$V_{out}$	5 Volts
Switching frequency	1 MHz
$I_{out}$	5 Amp
Average ripple current	0.5 Amps

Table 6.4 Buck specifications

The procedure for calculating the value of inductance,  $L$ , is as follows. The ripple current is calculated as a typical rule of thumb to be around 5 to 10% of the applied current. With a switching frequency of 1 MHz, the period,  $T$ , is calculated as  $1\mu s$ .

The Duty cycle at 28V is:

$$D = \frac{V_{in}}{V_{out}} = 0.17 \quad (6.33)$$

The off  $I_{max}$  is then 0.83 Amps

The on and off duty cycle times,  $D_{on}$  and  $D_{off}$  respectively, are as follows:

$$D_{on} = 0.3\mu s \text{ \& } D_{off} = 1.7\mu s$$

But

$$L = \frac{VT}{I} \quad (6.34)$$

With the current taken as  $1/5^{\text{th}}$  of the applied current:

$$L = \frac{5VT}{I_{max}} = \frac{5 \times 5 \times 1.7}{5} = 8.5\mu H$$

Now, the circuit is altered to its ZVS equivalent, as shown by Fig 6.17

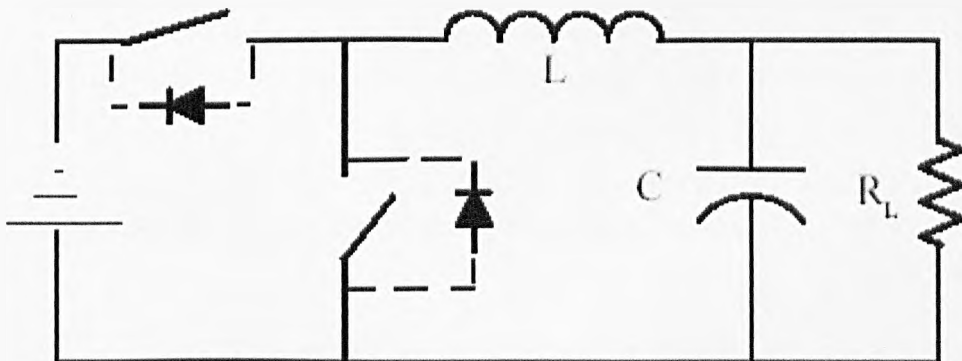


Figure 6.17 Buck (ZVS) converter

In approximately  $1\mu s$  the current through the inductor will fall to zero, plus some value as it draws current from the capacitor and load. Using equation (6.6) the inductance is calculated as:

$$L = \frac{VT}{I} = \frac{5 \times 1}{10} = 0.5 \mu H$$

This configuration requires an inductance that is only 6% of the previous one.

Consider a component fabricated with  $Ni_{80}Fe_{20}$ , the permalloy characteristics are contained in Table 6.5.

Property	Value
Resistivity	$20 \mu\Omega \cdot \text{cm}$
Bsat	0.8 Tesla
$\mu_r$	2000

Table 6.5 Permalloy characteristics

$$V = N \frac{d\Phi}{dt} \quad (6.35)$$

or

$$VT = NA_e B \quad (6.36)$$

And from equation (6.6.5)

$$LI = NA_e B \quad (6.37)$$

Therefore the core area of the component can be computed via:

$$A_e = \frac{LI}{BN}$$

The inductance of the two applications has been calculated, the current is known and saturation value of 0.6T, which is less than  $B_{\text{sat}}$  in order to avoid saturation, is selected.

Therefore:

$$A_e N = \frac{LI}{B} = 53.12 \text{mm}^2 \text{ (CCM)} \quad \& \quad A_e N = \frac{LI}{B} = 6.25 \text{mm}^2 \text{ (ZVS)}$$

Note the dramatically reduced area of the core for the inductor with the ZVS operation.

Now that the area of the inductor is set a design trade off between the numbers of turns begins. The skin depth at 1 MHz is  $5\mu\text{m}$ , the core laminate will be restricted to one skin depth and the number of laminations is restricted to 10 (an expenditure factor). Table 6.6 and Table 6.7 display the values for the CCM and ZVS mode buck converter, respectively.

N (turns)	$A_e (53.12/N) \text{ mm}^2$	Core width (mm)	Core height (mm)
1	53.12	1062.4	0.05
2	26.56	530.6	0.05
3	17.70	354	0.05
4	13.28	265.6	0.05
5	10.62	212.4	0.05
6	8.85	177	0.05
7	7.58	151.6	0.05

Table 6.6 Buck (CCM) converter

N (turns)	$A_e (0.83/N) \text{ mm}^2$	Core width (mm)	Core height (mm)
1	0.83	16.6	0.05
2	0.42	8.4	0.05
3	0.27	5.4	0.05
4	0.20	4	0.05
5	0.16	3.2	0.05
6	0.13	2.6	0.05
7	0.11	2.2	0.05

Table 6.7 Buck (ZVS) converter

With the effects of increased turns on dimensions it is then possible to consider possible inductor structures. The advantage of the ZVS mode of operation is apparent with the

reduction in core area displayed in Table 6.7. Table 6.7 provides an indication of the influence of digital control schemes on the development of high power density microscale magnetic components.

### 6.8 Influence of magnetic component on circuit operation

This thesis is primarily concerned with the design of microscale inductors and transformers. However, it is important to mention that to achieve an efficient DC-DC converter utilising microscale magnetic components, the magnetic design engineer should not design such components as stand alone components. In other words he/she must be aware of the effects of component parasitics on overall converter performance.

There are numerous aspects of the inductor that should be considered in conjunction with the converter such as footprint, heat sinking etc. The following effects will be discussed:

- (1) inductor DC resistance on converter performance
- (2) inductor AC resistance on converter performance
- (3) effect of stray inductance on efficiency and performance.

#### (1) Effect of inductor dc resistance on converter performance

One important source of loss in a converter is the DC winding resistance,  $R_{dc}$ , of the output inductor. This parameter defines the minimal loss condition of the inductor. For example, if  $R_{dc} = 1 \text{ m}\Omega$ , and DC output current of  $I=100$  Amps the inductor DC power loss is

$$P_{dc} = I^2 R_{dc} = 10 \text{ (W)}$$

If the converter is to provide 100 Amps at 0.75 Volts, the loss in efficiency due to the inductor  $R_{dc}$  would be 11.76 %. This result demonstrates that the converter would be less than 89% efficient due to  $R_{dc}$  alone. As can be seen from Fig 6.18, the impact of just  $1\text{m}\Omega$  of  $R_{dc}$  becomes unacceptable in a 100 Amp or greater converter. A winding construction technique that minimizes  $R_{dc}$  is a crucial requirement in output inductors operating at microprocessor current handling levels.

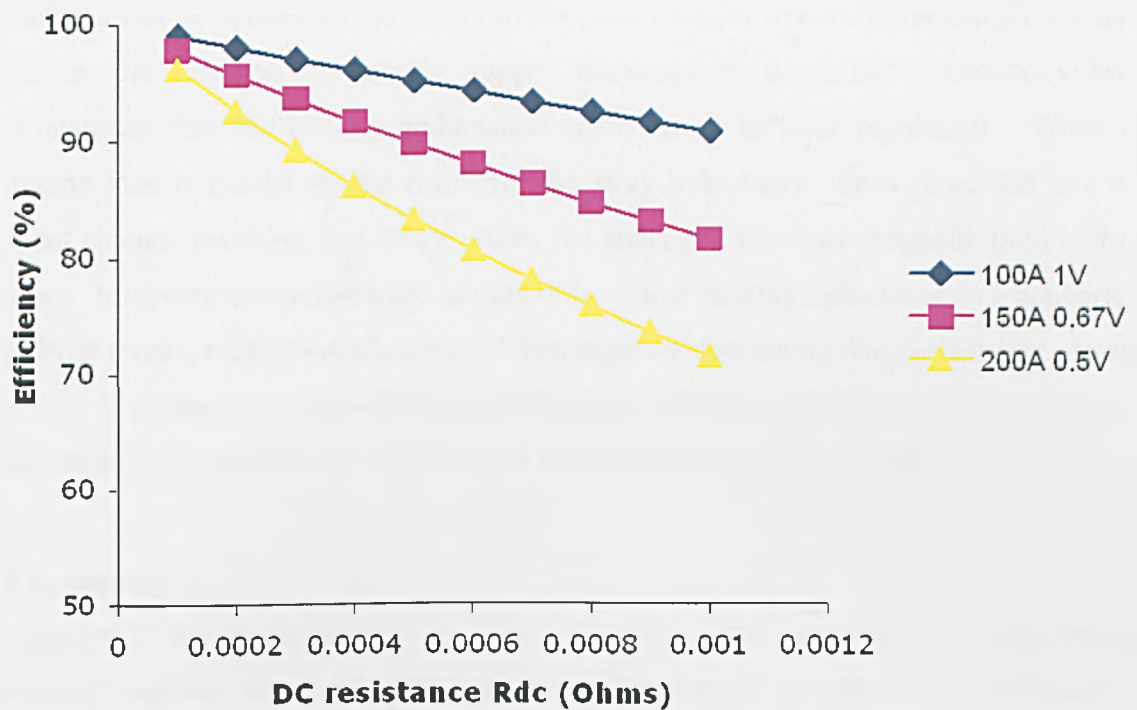


Figure 6.18 Efficiency drop in converter performance as a result of DC winding resistance,  $R_{dc}$ .

### (2) Inductor $R_{ac}$ loss and its effect on converter performance

The AC winding resistance,  $R_{ac}$ , is a function of the voltage, current, and frequency imposed on the inductor. The higher the inductor voltage, current and frequency are in the application, the more important the winding AC loss and core loss become. For example, the core loss increases with the square of the volts per turn. In a 48 Volt input bus the core loss would be 4 times greater than in the comparable 24 Volt input bus.

Although core loss is relatively independent of frequency, AC winding loss is totally dependent on frequency. This fact is demonstrated by the skin effect and proximity effect. Therefore there is a limit in the gains made by increasing operating frequency, for the higher the frequency of operation the greater the  $R_{ac}$  is compared to the  $R_{dc}$ . The greater the ripple current magnitude and frequency are in the application the greater the winding loss.

### (3) Effect of stray inductance on efficiency and performance

There is an increasing demand for Point Of Load (POL) converters that maintain good regulation in the presence of fast transient loads i.e.  $(di/dt)$ . For example, Arysten recently introduced POL converter capable of handling transients up to 300 A/ $\mu$ s. Load



regulation can be defined as the ability of the power supply to control the output voltage level as the load on the power supply increases or decreases. Faraday's law demonstrates that the leakage inductance could result in poor regulation. When a dynamic load is placed on the converter the stray inductance slows down the rate of current change, resulting in a delay. Also, the energy in the stray magnetic field is lost energy. Magnetic components are not the only source of stray inductance in a converter e.g. PCB tracks, mosfet switches etc. Advantages of decreasing component size via an increase in frequency, only achieve an efficient and effective result when the magnetic component is designed with consideration to the aforementioned factors.

## **6.9 Summary**

In summary, the importance of a closed magnetic path irrespective of component geometry has been explained. The influence of core shape on component performance and material characteristics was presented. Manufacturing issues of the pot-core and solenoid have been discussed. The solenoid component has been selected due to its small footprint, high number of windings and due to its flip-chip 3D winding assembly capability permitting the inclusion of various core materials. The analytical equations used to estimate component performance have been outlined. The issues of thermal dissipation and electromigration have been covered. The impact of converter operation on the design of the magnetic component was demonstrated. The importance of efficient magnetic component design was emphasised through the discussion of converter performance in the presence of stray inductance, AC loss and DC loss.

## References

- [6.1] C. R. Sullivan and S. R. Sanders. "Measured Performance of a High-Power-Density Microfabricated Transformer in a DC-DC Converter." IEEE Power Electronics Specialists Conference, pp. 287-294, June 1996.
- [6.2] E.C. Snelling, "Soft Ferrites, Properties and Applications," Butterworths, 2<sup>nd</sup> edition, 1988.
- [6.3] L. Daniel, C. R. Sullivan, and S. R. Sanders, "Design of microfabricated inductors", 27<sup>th</sup> Annual Power Electronics Specialists Conf., vol. 2, pp. 1447–1455, June 1996.
- [6.4] C. H. Ahn, and M. G. Allen, "Micromachined Planar Inductors on Silicon Wafers for MEMS Applications," IEEE Trans., Industrial Electronics, vol. 45, no. 6, pp. 886-876, Dec. 1998
- [6.5] H. Greenhouse., "Design of Planar Rectangular Microelectronic Inductors," Parts, Hybrids, and Packaging, IEEE Trans., vol.10, pp.101-109, Jun 1974.
- [6.6] W. G. Hurley, E. Gath, J. G. Breslin, "Optimizing the AC Resistance of Multilayer Transformer Windings with Arbitrary Current Waveforms," IEEE Trans. Power Electron., vol. 15, no.2, pp. 369-376, March 2000.
- [6.7] H. Lu, D. Flynn, C. Bailey and M. Desmulliez, "Computer Modelling of a Micro-manufactured One-turn Inductor," IEEE Proc. of High Density Packaging Conference, Shanghai, June, 2006.
- [6.8] S. J. Kim, Y. G. Lee, S. K. Yun, H. Y. Lee, "Novel high-Q bondwire inductors for RF and microwave monolithic integrated circuits" Microwave Symposium Digest, IEEE, vol. 4, pp.1621 – 162, June 1999.
- [6.9] Y. G. Lee, S. K. Yun, H. Y. Lee, "Novel high-Q bondwire inductor for MMIC," Electron Devices Meeting, pp.548 – 551, 6-9<sup>th</sup> Dec. 1998.
- [6.10] H. A. Wheeler, "Formulas for the skin effect," in Proc. I. R. E., vol. 30, pp. 412–424, Sept. 1942.
- [6.11] M. Brunet, T. O'Donnell, J. O'Brien, P. McCloskey, C. O'Mathuna, "Design Study and Fabrication Techniques for High Power Density Micro-Transformers," IEEE Trans., Magn., pp. 1189-1195, 2001.
- [6.12] M. K. Kazimierczuk, G. Sancineto, G. Grandi, U. Reggiani, A. Massarini, "High frequency Small-Signal Model of Ferrite Core Inductors," IEEE Trans. Magn., vol. 35, no.5, pp. 4185-4189, Sept 1999.
- [6.13] M. Seitz et al, "Squeeze More Performance Out of Toroidal Inductors," Power Electronics Technology August 2005.

[6.14] D. Flynn, R.S. Dhariwal, M.P.Y. Desmulliez, "Study of a solenoid microinductor operating in the MHz frequency range," *IoP Journal of Microengineering and Micromechanics*, vol 16, pp. 1811-1818, 2006.

## Chapter 7

### Microfabrication of Power Inductors and Transformers

#### 7.1 Introduction

This chapter presents the fabrication process of the microinductors and transformers investigated within this thesis. All components fabricated within this thesis require a photomask. The importance of the photomask is discussed in Section 7.2. Section 7.3 presents a detailed fabrication process of the solenoid microinductor. Within this section the novel flip-chip bonding process of the microinductor winding is described. The manufacturing processes of the solenoid microinductor are transferable to the fabrication of the pot-core inductor and transformer. The assembly of the pot-core inductor and transformer is documented in section 7.4. Section 7.5 summaries the properties of the electrodeposited and commercial alloys investigated. Section 7.6 concludes the chapter summarising the main aspects of the fabrication process.

#### 7.2 Mask Design

Design of photo-masks has been carried out using the L-Edit mask designing software from Tanner Research, Inc. Conversion of L-Edit data format to other data format (such as GDSII or Gerber) is carried using LINKCAD software from BAY Technology. The solenoid component requires 6 masks each designed to the dimensions of the 3-inch wafers used in the fabrication (1:1 exposure magnification). Fig 7.1 displays the mask used in the fabrication of the core for the solenoid component. The photomask was designed for use with a positive photoresist, AZ 9260. The masks are fabricated on an acetate sheet approximately A4 in size, with one sheet containing six masks. Since the fabrication process is an additive procedure, each mask has alignment marks on its perimeter to allow accurate alignment with subsequent layers. The solenoid component is fabricated on three separate wafers for the lower winding layer, upper winding layer and core, respectively. The magnetic core is etched free from the wafer, magnetically and electrically characterised, and then positioned onto the lower winding insulation layer prior to assembly. Appendix B outlines a summarised fabrication procedure.

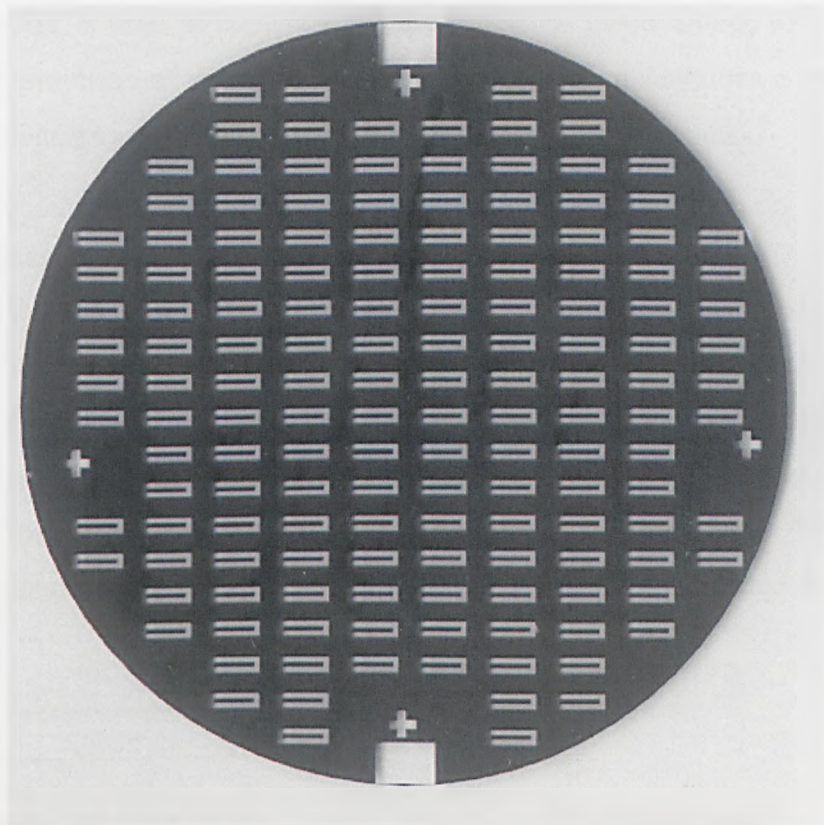


Figure 7.1 Acetate mask for the fabrication of the core of the solenoid micro-inductor. The four cross-hairs on the perimeter of the mask are the alignment.

There are approximately 150 samples per wafer. The number of devices was determined based on simply achieving a well distributed pattern to promote uniform current density during electroplating. The high number of components increases the probability of an operational sample after production. Also, with a reasonable yield, the characterisation of more than one core material within a device can be performed after a single production run.

The photo-masks of the pot-core inductors and transformers are also produced on acetate. There was no alignment marks on these photo-masks as each layer is selectively etched and then assembled. Section 7.3 explains this fabrication process of the pot-core components in details.

The acetate photo-mask is relatively cheap, approximately £85 for 6 3-inch masks i.e. 1 A4 acetate sheet. The 20 $\mu$ m wide spacing between windings is the smallest feature size on the mask. Such a feature size could be lost during the exposure due to diffraction caused by the non-perfect transparency of the acetate mask or a minor air-gap between

the photomask and photoresist during exposure. To minimise these diffraction effects, the acetate mask is used in contact exposure mode. A disadvantage of that method is the rapid deterioration of the mask. The following section describes a solution to this problem by transferring the acetate pattern onto a titanium glass mask.

### 7.2.1 Transferring acetate mask to titanium on glass

This section describes a process that was originally developed to alter the polarity of the mask. The masks were designed with the intention of using a positive photoresist. However if thick film structures were required, negative photoresists such as SU-8 are more suitable. However, the mask is the wrong polarity for negative photo-resists. The polarity can be reversed by transferring the photomask onto glass. The fabrication process for transferring the acetate mask onto Ti/glass mask is presented in Fig 7.2.

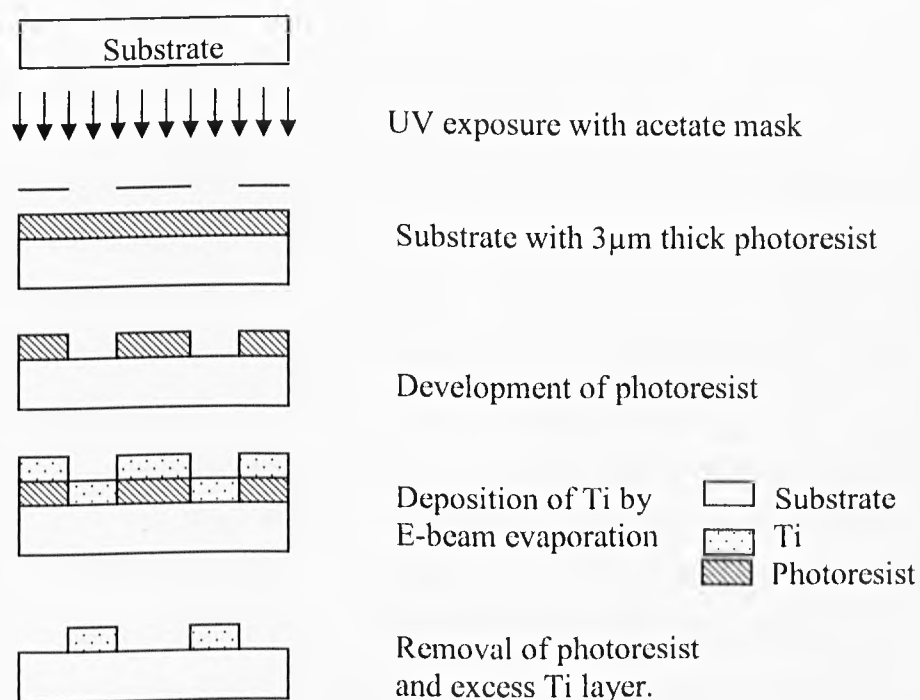


Figure 7.2 Fabrication process of transferring acetate mask on to Ti/glass mask.

The suitability of the acetate mask can only be determined when the wafer surface is analysed after photoresist development. The transfer process provides an alternative mask if the acetate mask fails.

### **7.3 Micro-fabrication & assembly of solenoid microinductor**

The solenoid microinductor requires the manufacturing of three separate wafers that correspond to the upper, lower winding layers and the magnetic core of the component. The following sub-sections detail each stage of the fabrication process.

#### **7.3.1 Preparation of the substrate**

3-inch soda lime glass wafers are used for the substrate as glass is cheaper than silicon, therefore is more cost effective when generating prototypes. Moreover the substrate is used mainly as a support and is sacrificed at the end of the process. When developing the fabrication processes, the need to transfer production onto silicon for assembly into integrated circuits is not neglected. The processes developed on the glass wafers are transferable to silicon. The size of the wafer was selected due to its compatibility with the majority of the equipment within the MISEC cleanroom.

The first stage of the fabrication is substrate preparation and wafer cleaning. Wafer cleaning and surface preparation have always been very important in achieving high yields in semiconductor and MEMS fabrication [7.1]. First, the wafers are inspected to ensure that the surface is defect free e.g. scratches. Subsequent processes such as electroplating will not conceal pre-existing surface blemishes. It is likely that surface defects will result in the conductive path of a seed layer being impeded or electroformed structure being fractured. After inspection the glass wafers are placed in a wafer holder; a biodegradable decontamination liquid (Decon 90) together with deionised water are added to a glass container and the wafer holder is placed in the ultrasonic bath, as shown in Fig 7.3. The purpose of the cleaning process is to remove micro-particles and contaminants present on the surface of the wafer. After approximately 45 minutes in the ultrasonic bath, the diluted decon cleaning solution is replaced with 100% deionised water and returned to the ultrasonic bath for a further 45 minutes. The purpose of this stage of the cleaning cycle is to remove traces of the cleaning agent from the surface of the wafer. Any trace of contamination or grease from the cleaning solution will result in poor adhesion of the subsequent deposited layers. In the final stage of the cleaning process the wafers are removed from the ultrasonic bath. A final inspection for visible defects is performed; the wafers are then dried with pressurised nitrogen. Once dried the wafers are ready for fabrication.



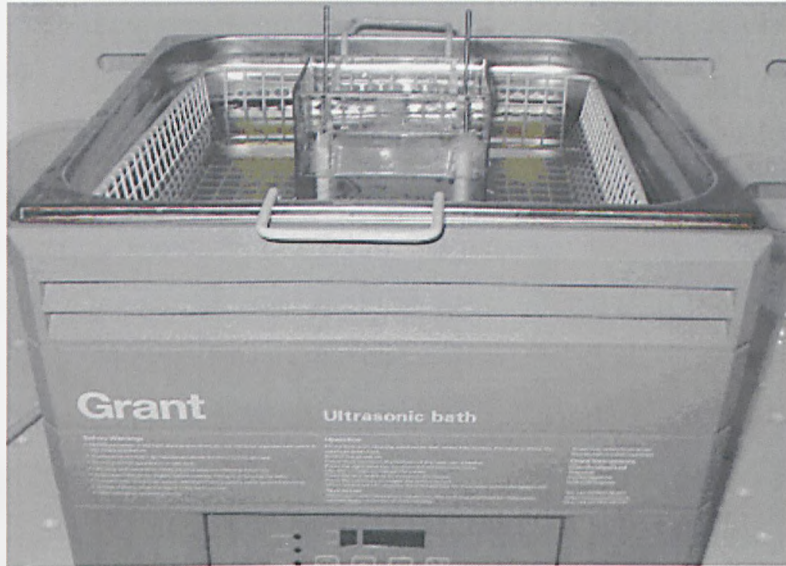


Figure 7.3 A wafer holder containing 5 3-inch glass wafers is placed within a beaker of Decon 90 cleaning solution diluted with deionised water. The wafer holder is then placed within an ultrasonic bath.

### 7.3.2 Deposition of sacrificial layer

The completion of the solenoid micro-inductor structure requires the flip-chip bonding of the windings. To access the pads of the lower winding layer the glass substrate of the chip must be removed. Therefore, a sacrificial layer is applied to assist in the release of the component from the substrate after bonding.

Initially a photoresist sacrificial layer approach was contemplated. The photoresist would be a thin layer of less than  $10\mu\text{m}$  thickness, of AZ 9260, [7.2], applied prior to the conductive seed layer. After the wafer is dried, deposition of the sacrificial layer is done by means of spin coating. The thickness of the photoresist coating layer is primarily determined by the viscosity of the resist, the rotational speed, the ramping rate and the duration of the spin. For the thickness of photoresist considered, the amount of resist has little effect on the thickness of the final deposition layer. The rule of thumb for the amount of photoresist to be deposited is 1 ml per wafer inch, thus 3 ml were deposited onto the centre of the 3" wafer. While depositing the photoresist, care is taken to avoid the creation of air bubbles that would create surface defects. Fortunately air-bubbles can be removed from AZ with a pipette before the spinning cycle commences. The photoresist process is covered in more detail in section 7.3.4.

At the end of the whole manufacturing process, the under-side of the wafer, the side of the wafer with no deposited layers, would be exposed to UV light and subsequent development would remove the AZ, freeing thereby the completed device. The original AZ layer suffered however from cracking during deposition of the Ti and Ni seed layers within the E-beam as shown in Fig 7.4. This phenomenon was attributed to thermo-mechanical stress due to the mismatch of thermal coefficients of expansion between the glass and the resist.



Figure 7.4 Isotropic thermal cracking of a wafer with 10 $\mu$ m thick AZ 9260 layer after the deposition of Ti within the E-beam.

The thickness of the AZ layer was reduced to 5 $\mu$ m and the baking cycle was increased. The baking cycle reduces the solvent content of the resist. A high solvent content within the resist makes the resist soft [7.3]. A thinner layer, baked for longer was anticipated to be harder and thermally more resistant. The 5 $\mu$ m AZ layer did not crack during the deposition of the metal seed layer within the E-beam. The second AZ layer was deposited on top of the seed layer; this layer is patterned to form the winding layer. During the baking cycle of the second layer, thermal isotropic cracking occurred. This was attributed to the three different thermal expansion coefficients of the respective layers. Fig 7.5 displays the thermal cracking and the effect on the structure to be fabricated.



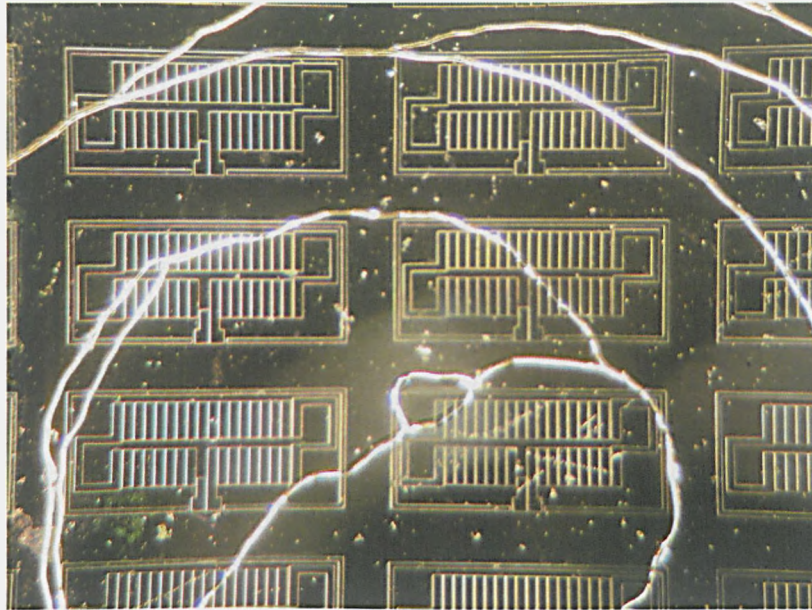


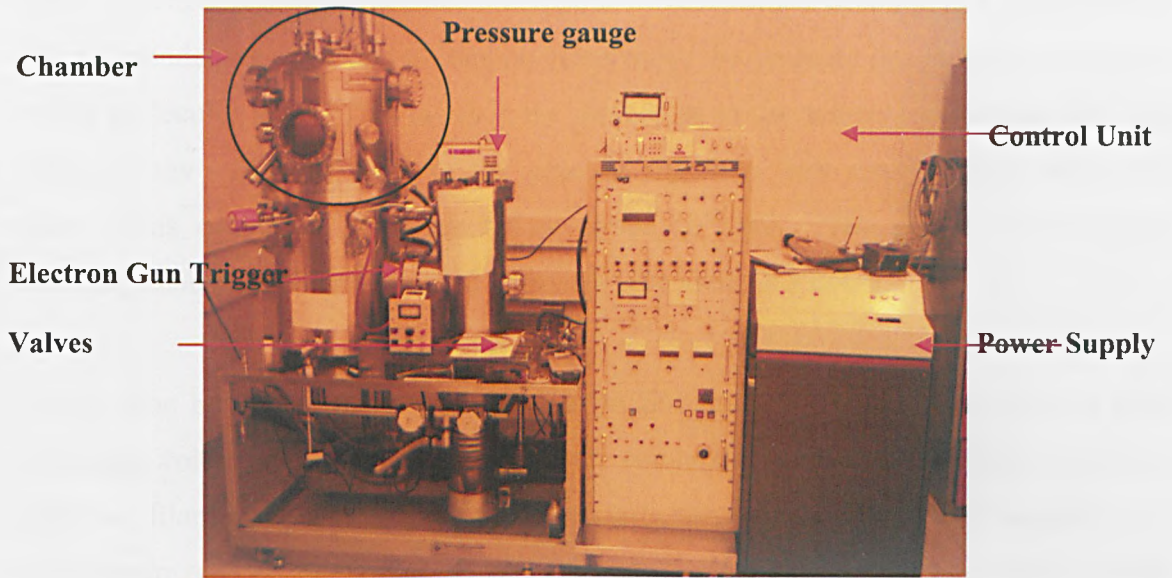
Figure 7.5 Isotropic thermal cracking of a wafer consisting of a sacrificial AZ layer, Ti seed layer and patterned photoresist layer.

The photoresist sacrificial layer would have required a DOE of baking times and temperatures to resolve the thermal cracking problem, not only at the first manufacturing steps but also at all stages of the process. This was not possible due to time constraints. To resolve this issue, a metal sacrificial layer was instead selected. The following section describes the deposition of the metal layer.

### 7.3.3 Deposition of a titanium seed layer

The seed layer is a conductive layer, which, in this design, is the first layer to be deposited onto the glass surface. The seed layer also acts as an adhesion layer. Metals such as copper and nickel, that are less resistive than Ti, do not adhere well onto glass or silicon and require an adhesion layer prior to deposition. The final purpose of the adhesion layer in this fabrication process is to be used as a sacrificial layer.

The deposition of the seed layer is done in a high vacuum chamber using electron beam evaporation [7.4]. Fig 7.6(a) and (b) display the E-beam and auxiliary equipment, and a schematic of the E-beam chamber, respectively.



(a)

(b)

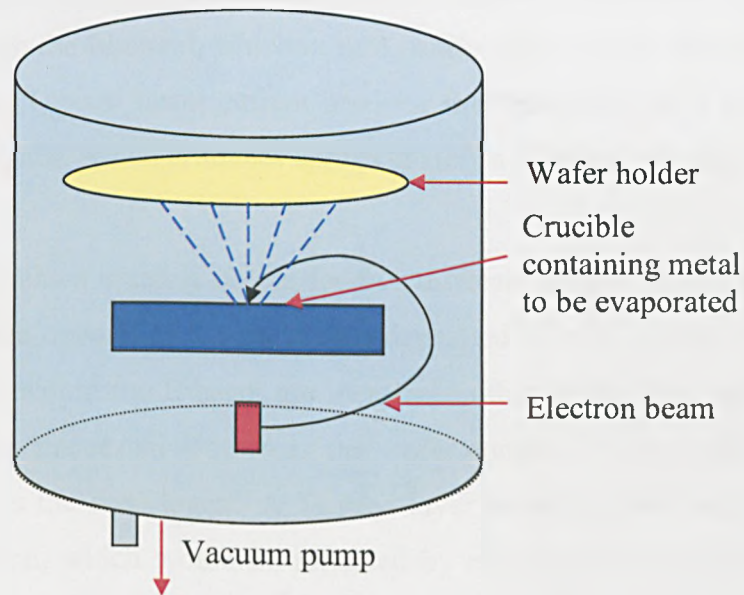


Figure 7.6(a) E-Beam Evaporation with control unit and power supply, (b) Schematic of E-beam evaporation chamber

The glass wafers are loaded, five at a time, into the wafer holder of the E-beam evaporation chamber. The wafer holder is approximately 100mm above a Ti slug of material that is contained in a crucible. The Ti slug is the target of the electron beam, as shown in Fig 7.6(b).

In the vacuum chamber pressure must be low prior to deposition to prevent the Ti metal oxidising when heated to melting point. Also, if a metal is heated to melting point in air, not much happens due to the heavy bombardment of air molecules. If the same

metal is melted in a high vacuum, the vapour travels until it encounters a cold surface, where it condenses. For this to happen effectively, the pressure has to be in the region of free molecular flow. This is when the molecules in the residual gas are so few that although they strike the walls of the vacuum chamber, they rarely collide with each other. This occurs at pressures below about  $10^{-6}$  bar. The process of pumping down/degassing the chamber would normally take about 2-3 hours.

The electron beam is created from a tungsten filament, which is heated up by a high alternating voltage of about 10kV through the anode and cathode. Electrons are emitted from the filament and are directed by an arrangement of permanent magnets and electromagnets onto the target metal to be evaporated. The target material is then heated to the point of evaporation and the vapour condenses on the wafer placed above it, line of sight deposition. The power of the electron beam is effectively controlled by the AC power through the filament, which in turn controls the amount of energy directed to the target metal. Typical beam current used for the deposition of Ti was 60mA for a duration of 3 minutes, which produces approximately a 300nm thick deposition.

The E-beam contains a crucible holder for five different metals. Once each glass wafer has a 300nm thick deposit of Ti, Ni is then deposited on each wafer. The deposition parameters of Ni within the E-beam are identical to that of Ti. The purpose of the Ni layer is to reduce the resistivity across the wafer surface. Ti is highly resistive and cannot be used as the seed layer. A Ti seed layer would produce an uneven current density distribution, which would be reflected by electroplated structures that exhibit non-uniform thickness. Therefore, the Ni layer, approximately 200nm in thickness, is the seed layer for subsequent electrodeposition.

#### **7.3.4 Photoresist deposition and UV photolithography**

The glass wafers with adhesion/sacrificial layer of Ti and seed layer of Ni, now require a deposition of photoresist. Three wafers are coated with AZ 9260, one for the lower winding layer, upper winding layer and core layer, respectively. Fig 7.7 displays an overview of the photoresist deposition and UV photolithography processes.

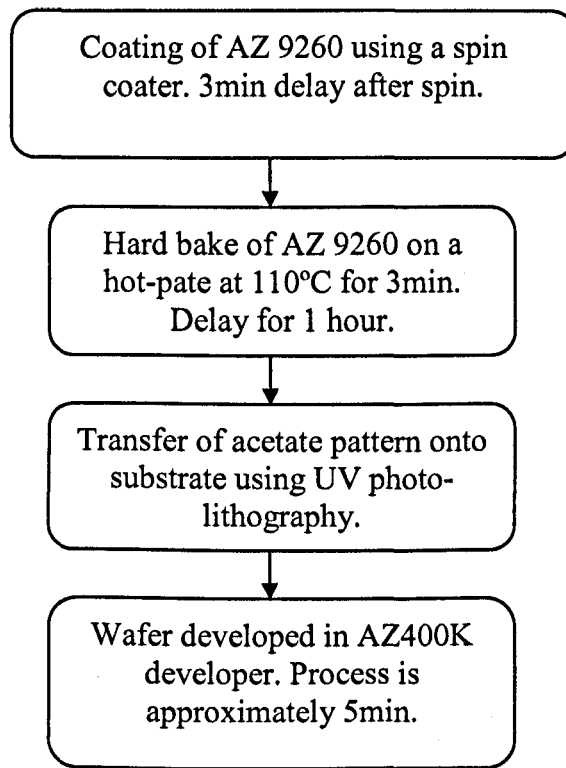


Figure 7.7 Overview of AZ 9260 deposition and UV photolithography

The photoresists available were SU-8 and AZ9260. With the manufacture of the solenoid component requiring the deposition and removal of several photoresist layers, SU-8 was immediately ruled out, as its removal is well known to be extremely difficult to achieve. In comparison, AZ9260 is easier to apply and remove than SU-8. Also, AZ is a very transparent photoresist, resulting in reduced processing times and capability of producing thick, as well as thin, layers with good alignment to prior layers. The suppliers of the AZ, Clariant, advise that optimum conditions may vary with the substrate type, equipment and environmental conditions. Therefore the AZ process required fine tuning based on initial tests. The sequences that were programmed into the spinner to achieve a variety of thicknesses are displayed in Table 7.1.

	30 $\mu\text{m}$	20 $\mu\text{m}$	5 $\mu\text{m}$
Distribution of the AZ	70 rpm	70 rpm	70 rpm
	30 Rev/s	30 Rev/s	30 Rev/s
	20sec	20sec	20sec
Spread cycle for uniform wafer coverage	400 rpm	400 rpm	400 rpm
	100 Rev/s	100 Rev/s	100 Rev/s
	20 sec	20 sec	5 sec
Cycle for final photoresist thickness	1000 rpm	1000 rpm	5000 rpm
	200 Rev/s	200 Rev/s	200 Rev/s
	10 sec	20 sec	30 sec

Table 7.1 Spin cycle parameters for various AZ9260 thicknesses.

Once the spin cycle is complete there is a delay prior to baking the AZ to allow the layer to settle on the wafer. The 5 $\mu\text{m}$ , 20 $\mu\text{m}$  and 30 $\mu\text{m}$  layers are delayed for 90sec, 180sec and 300sec respectively. Depending on the thickness of the AZ layer the baking cycle varies, as indicated in Table 7.2.

30 $\mu\text{m}$	20 $\mu\text{m}$	5 $\mu\text{m}$
Temp: 110 $^{\circ}\text{C}$	Temp: 110 $^{\circ}\text{C}$	Temp: 110 $^{\circ}\text{C}$
300 Sec baking duration	180 Sec baking duration	90 Sec baking duration
1 hour delay	1 hour delay	1 hour delay

Table 7.2 Baking procedures for various AZ thicknesses.

After coating, the photoresist contains a thickness that depends on the concentration of solvent, mostly PGMEA. The baking process serves to reduce by 75-80% the concentration of solvent through evaporation and diffusion in order to avoid several effects [7.3]: mask contamination through the sticking to the mask, popping, bubbling or foaming of the resist by nitrogen created during exposure. The baking also improves resist adhesion to the substrate, minimises dark erosion during development and prevents dissolving one resist layer by the following during multiple coat processing.

Prior to baking the wafers at  $110^{\circ}\text{C}$ , each wafer is baked on an additional hot-plate for 30sec at  $65^{\circ}\text{C}$  to minimise the degree of thermal shock. Thermal shock effects include the resist contracting, retreating from the wafer perimeter due to the sudden elevation of temperature, creating an uneven distribution of photoresist. During the baking cycle the resist must not be over-baked as this will lead to problems during the development of the photoresist. The baking process facilitates the cross linking of the photoresist, making it less soluble to the developer. An increase in development time would result, with the potential for some sensitive structures to be lost during the over-development time period.

After the baking process there is a delay before exposing the wafers to permit rehydration. Re-hydration is important for resist films thicker than  $5\mu\text{m}$  as after baking they are almost  $\text{H}_2\text{O}$  free. During the photoreaction when exposed to UV light a certain amount of water is required for the creation of carboxylic acids. The thicker the film the longer the re-hydration period required. A period of 1hour was sufficient for the thicknesses used within the thesis. AZ layers greater than  $100\mu\text{m}$  can require several hours. Besides an improvement in development rates due to sufficient re-hydration, re-hydration also improves the resist profile by attaining a homogeneous development rate through the resist film.

When producing the  $90\mu\text{m}$  thick windings, two layers of AZ are applied. After the  $30\mu\text{m}$  thick spin and bake cycle, the  $30\mu\text{m}$  spin cycle is repeated. The second AZ layer adheres to the AZ surface better than the original AZ layer did to the glass surface resulting in less AZ being removed during the spin cycle. The baking time is doubled to 600 sec and the resist is left for one hour to re-hydrate. After the delay period contact UV exposure is carried out with the acetate photomask. The wafer is positioned on the chuck of the Tamarack UV aligner. Fig 7.8 shows the Tamarack UV aligner. The hard contact between the wafer and photomask is maintained by vacuum.



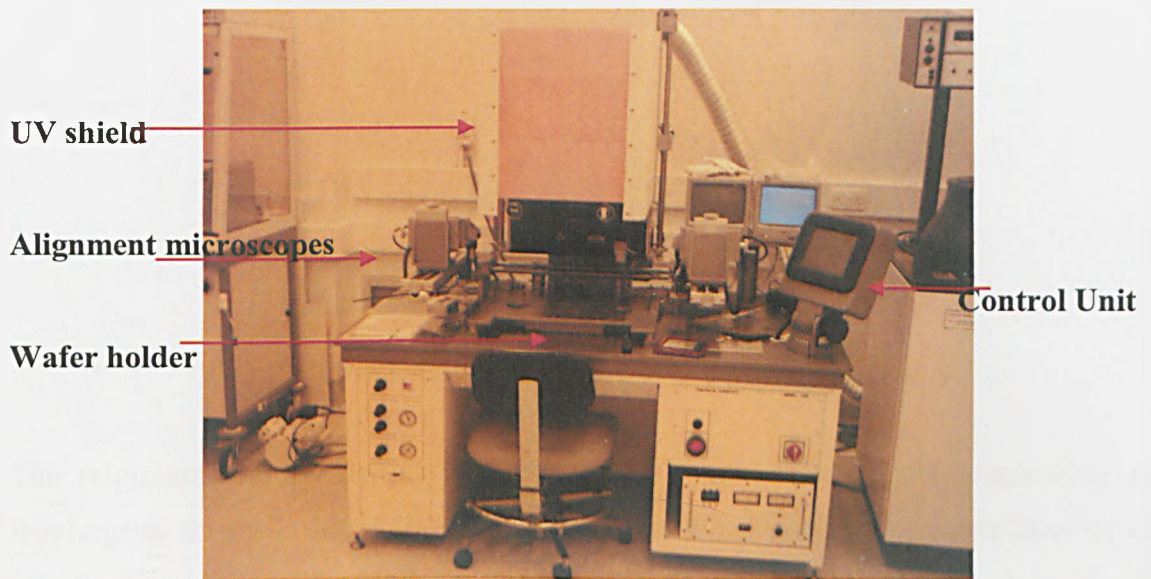


Figure 7.8 Tamarack UV aligner.

AZ9260 is photosensitive to the i and h line (419-329nm). The UV light is filtered so that the resist is exposed to the i-line (365nm). The lateral light intensity distribution is measured prior to exposure; a 5-6% reduction in intensity from central to edge regions is measured over the 3" illumination area.

The energy dose is set via the control unit. For approximately 2000mJ for 90 $\mu$ m thick AZ, the exposure is complete in 40 secs. The energy dosage is reduced to 1200, 1000, and 800mJ respectively for the 30 $\mu$ m, 20 $\mu$ m and 5 $\mu$ m thick AZ layers.

After exposure, the wafer is developed using AZ developer for approximately 3-5 minutes and rinsed with deionised water. The ratio of AZ developer, AZ400K, to deionised water is 1:3. During development the carboxylic acid formed during UV exposure switches from the hydrophobic to the hydrophilic part of the cresolresin and promotes the degradation or deprotonation, of the OH-group defining the resist solubility in aqueous alkaline developers [7.5]. Compared to the unexposed DNQ, the carboxylic acid yields a development rate of the resist several orders of magnitude higher. The wafer surface is cleaned with deionised water and dried with pressurised nitrogen; the surface of the wafer is examined with white light interferometry. Fig 7.9 displays the surface profile of a developed AZ9260 90 $\mu$ m thick.

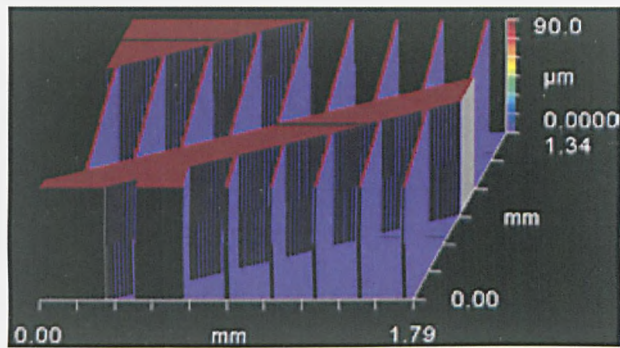


Figure 7.9 AZ9260 patterned with UV photolithography.

The minimum feature size of this component is the 20µm spacer separating the windings as shown in Fig 7.10. This feature size is well within the capabilities of AZ where aspect ratios of 6:1 have been achieved [7.6]. Hence, the 90µm thick resist with 20 µm spacers, an aspect ratio of 4:1, is a practical and repeatable process.

### 7.3.5 Electrodeposition of copper and nickel

After UV photolithography, DC electrodeposition of the winding layers and core follows. The electrodeposition of the Ni-Fe core is covered in detail in Chapter 5. The windings are fabricated with either nickel or copper. Copper is preferred due to its higher conductivity minimising winding resistance. However, due to contamination and component failure issues the dedicated copper plating bath, was not operational for prolonged periods and Ni was used a suitable alternative. The compositions of the Ni and Cu bath cells are shown in Tables 7.3 & 7.4.

<u>Composition</u>	<u>Concentration</u>	<u>Total amount</u>
Nickel sulphamate solution	320 ml/l	6.4 litres
Boric acid	40 g/l	800 gram
Lectro-nic Anode activator	65 ml/l	1.3 litres
Lectro-nic addition agent	12 ml/l	240 ml
Non pitter 62 A	2 ml/l	40 ml

Table 7.3 Nickel plating solution composition

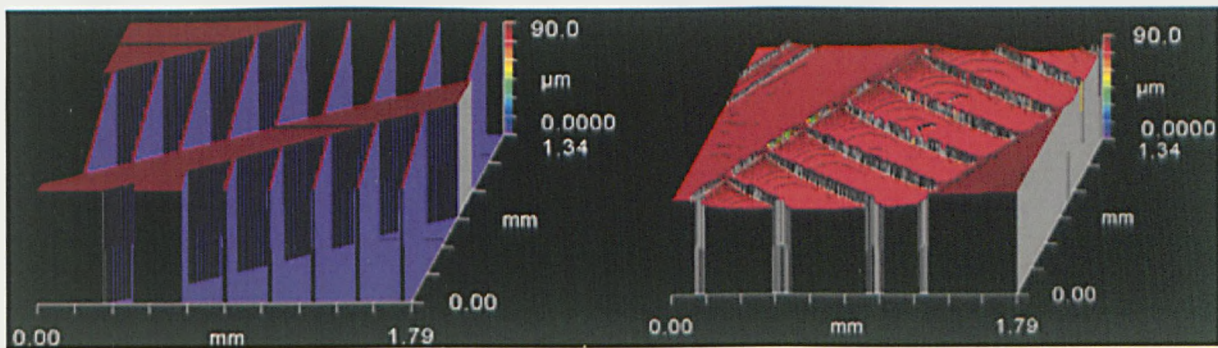


<u>Composition</u>	<u>Concentration</u>	<u>Total amount</u>
Sulfuric acid, H <sub>2</sub> SO <sub>4</sub>	100 ml/l	2.5 litres
Copper Sulfate, CuSO <sub>4</sub> .5H <sub>2</sub> O	40 g/l	1 kilogram
Electrodeposit 1200M	40 ml/l	1 litres
Electrodeposit 1300S	1 ml/l	25 ml
Hydrochloric acid, HCl (S.G. 1.18, 37%)		5 ml
Cupronal BP Carrier		5 ml

Table 7.4 Copper plating solution composition

The current density during the deposition of Ni and Cu is 0.6A/dm<sup>2</sup> initially for approximately 10% of the deposition time; this is ramped to 1.7 A/dm<sup>2</sup> for the remaining 90% of the plating period. The reduced plating density produces an increase in grain size. It was hoped that this would assist with the release of the glass substrate during etching of the sacrificial layer. The electrodeposition of the 90µm thick windings was approximately 5 hours. Fig 7.10 displays the patterned AZ after the electrodeposition.

AZ 9260 is then deposited onto the electroplated Ni or Cu windings. The AZ is processed as before and spun to a thickness of approximately 30µm. The AZ is patterned and developed to produce cavities, 150µm in diameter, at opposite ends of the winding section. Fig 7.11 displays a Zygo 3D plot and intensity image of the component with the patterned cavities.



(a)

(b)

Figure 7.10(a) The patterned AZ 9260 prior to electroplating, and (b) after DC electrodeposition of 90µm thick Ni.

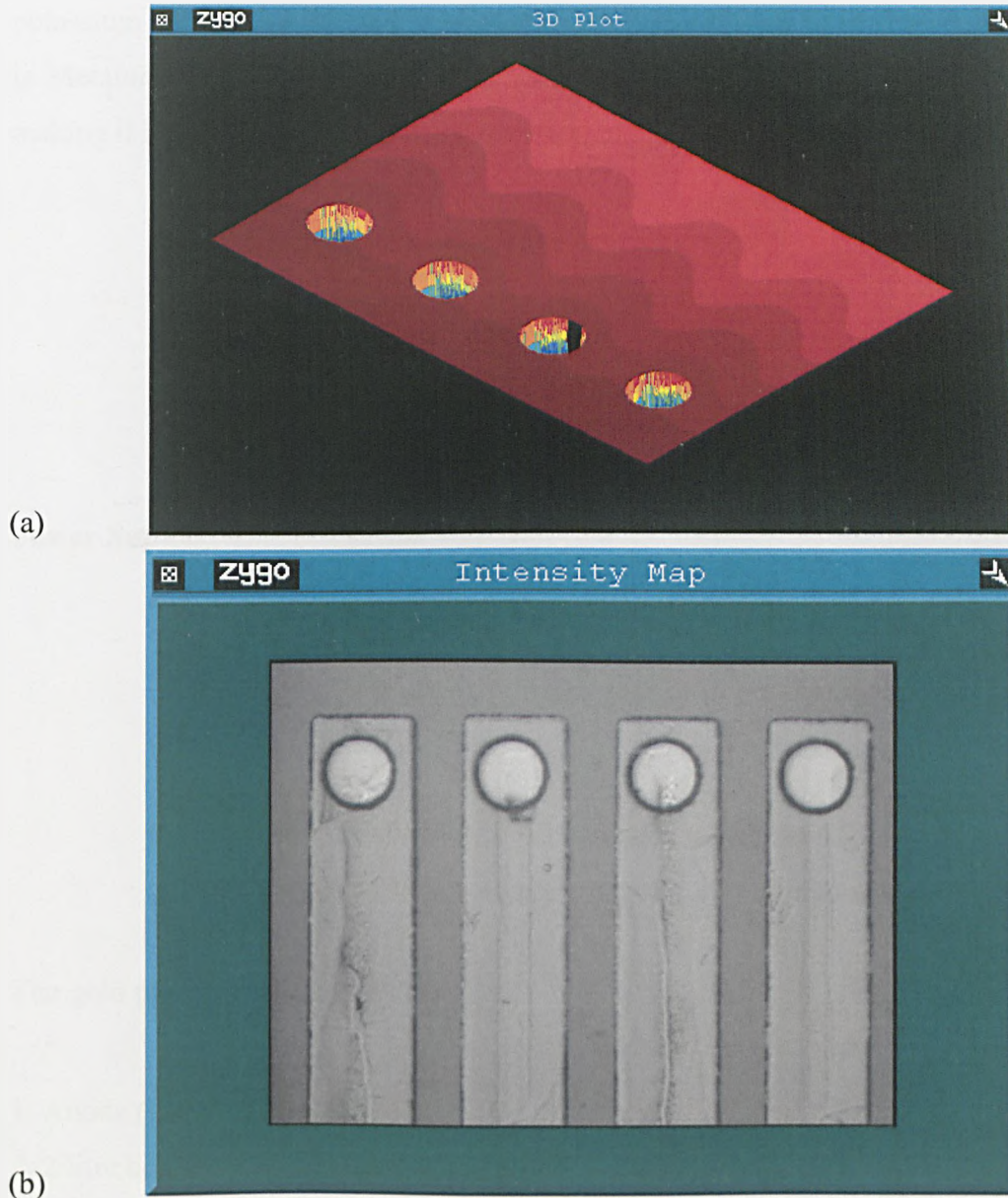


Figure 7.11(a) 3D plot of AZ 9260 patterned to form electroplating cavities for electrodeposition of Cu: Au interconnection bumps, and (b) intensity image of the winding layer.

The cavities are filled with electroplated Cu, or Ni, and capped with 5 $\mu$ m of gold. The electroplated winding layers form the seed layer for the electrodeposition of the interconnection bumps. The following section describes the electrodeposition of Au.

### 7.3.6 Electrodeposition of gold

5 $\mu$ m of Au is plated onto the Cu or Ni posts of the lower and upper winding layers to connect the layers during flip-chip bonding. After Ni or Cu plating of the posts the wafer is rinsed with deionised water to remove any residue of Ni or Cu plating solution.



The Au plating cell is custom made as shown in Fig 7.12. The electrolyte is a potassium sulphite based gold plating solution. The supplier of the gold plating solution is Metalor<sup>R</sup> Technologies (UK) Limited. The electrolyte is a cyanide free solution making it less hazardous and easier to maintain.

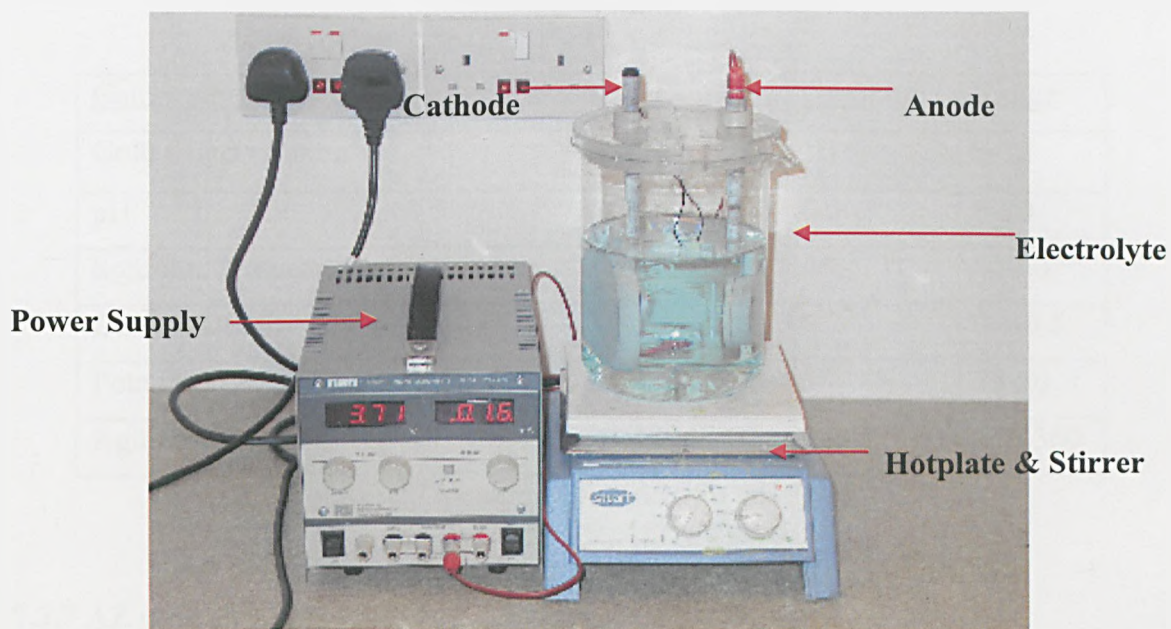


Figure 7.12 Potassium sulphite based gold plating bath set-up.

The gold plating bath consists of:

1. Anode (Platinised Titanium)
2. 2 litre beaker as the plating bath
3. Hot plate with magnetic stirrer, temperature probe with close loop control
4. DC power supplier with resolution up to 1 mA
5. Wafer holder as cathode.

The gold plating system set-up is simple and inexpensive. On the other hand the filtration system is poor and maintenance of the gold solution e.g. replenishment of gold and brighteners is frequently needed. Agitation is achieved through the magnetic stirring at 260 rpm with a 60mm magnetic stirrer. Since potassium sulphite is readily oxidised air agitation could not be used. Optimum speed of rotation has to be used to transport the ions whilst avoiding a turbulent flow that generates bubbles, causing undesired pitting in the sample. Other factors that cause pitting are the use of excessive current density or temperature during electrodeposition. The optimum operating

conditions for gold plating are presented in Table 7.5. Usually the system is turned on 2-3 hours before plating commences to allow the electrolyte to condition itself prior to use. With operation at 46°C deionised water is added to replenish loss of solution through evaporation. The deposition rate for current density of 0.2 A/dm<sup>2</sup> is 1 µm in 8 minutes.

<u>Composition</u>	<u>Unit</u>	<u>Optimum</u>	<u>Range</u>
Gold Concentration	g/l	10	8-12
pH	-	9.5	8-10
Solution Temperature	°C	46	40-60
Current Density	A/dm <sup>2</sup>	0.2	0.1-0.5
Potassium Sulphite	g/l	35	25-50
Agitation	rpm	280	200-360

Table 7.5 Operation condition for gold plating

### 7.3.7 AZ stripping and seed layer etching

After the deposition of 5µm of gold, all of the AZ layers are removed with acetone. Another stripping agent is AZ 400T photoresist stripper, a product of Clariant. Both are effective for AZ removal, however, acetone operates quicker. The wafer is cleaned in deionised water to remove any residue of acetone and dissolved AZ.

Part of the seed layer and adhesion layer is etched with a Ti etchant to remove the electrical connection that forms an effective short across the windings. The composition of the Ti etchant is displayed in Table 7.6. The etching process is completed in 5minutes, no agitation is applied during the etch process. Agitation and prolonged etch periods result in under-etching which is undesirable at this stage of fabrication as the windings are required to remain on the glass substrate. The Ti etchant preferentially etches the Ti layer and removes the thin Ni seed layer effectively. A Ti/Cu seed layer was tested but proven not to be effective. The etchant does not erode the thin Cu layer and begins eroding the permanent structures e.g. the windings. Therefore, only a Ti/Ni layer was used.

<u>Composition</u>	<u>Amount/Unit</u>
Sodium Fluoride powder	20g
Deionised Water	380 ml
Hydrochloric Acid	100 ml

Table 7.6 Composition of Ti etchant

A 5 $\mu$ m thick layer of AZ9260 is applied and patterned to form an insulation layer across the upper and lower windings. The Ni-Fe core is conductive and would form an electric short across the windings. AZ9260 is a good insulator with a dielectric constant of 1.4 and dielectric strength of 1.8kV/mil [7.7]. Fig 7.13 displays fabricated lower windings and a 3D image of the lower windings. Fig 7.14 displays the upper winding layer.

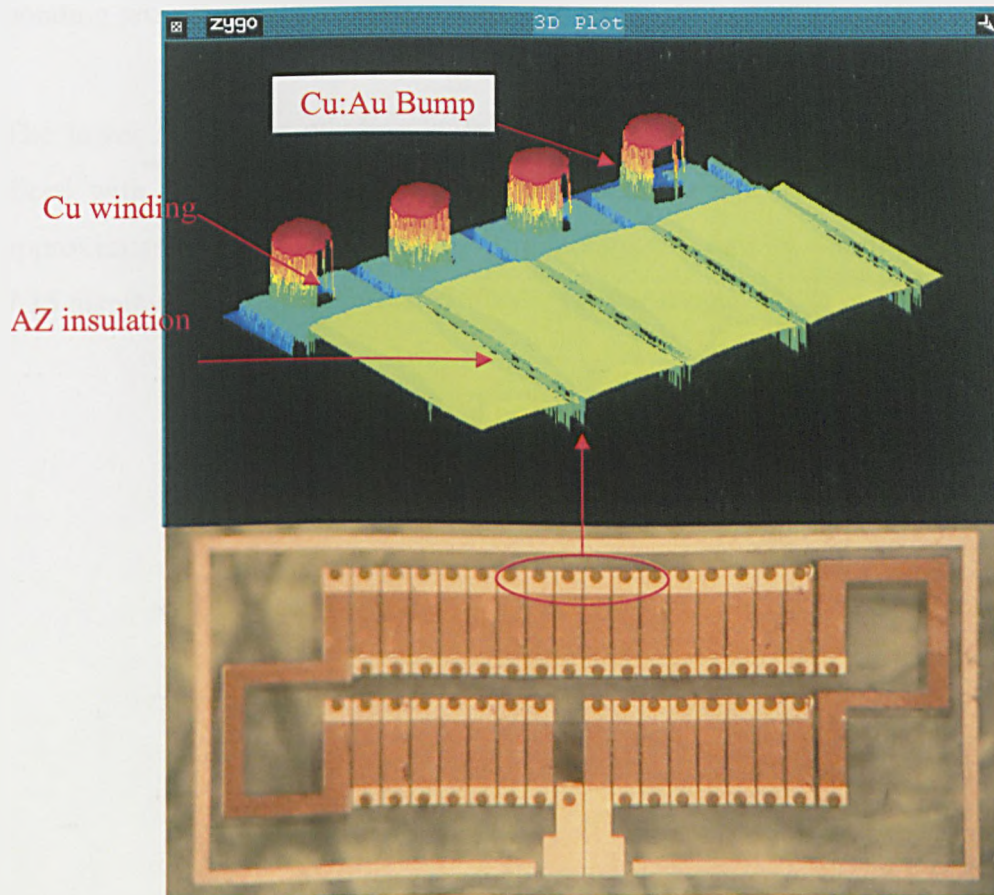


Figure 7.13(a) A 3D plot of the lower winding layer, (b) The lower winding layer with 90 $\mu$ m Cu windings, Cu: Au bumps 25 $\mu$ m and 5 $\mu$ m respectively, etched Ti/Ni layer, and 10 $\mu$ m AZ insulation layer.



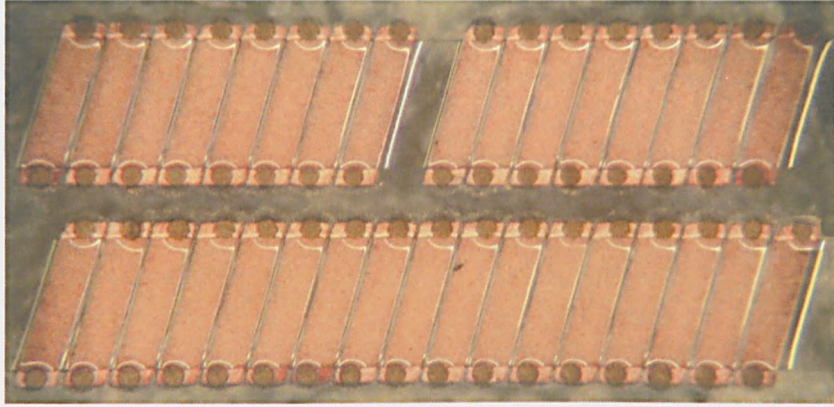
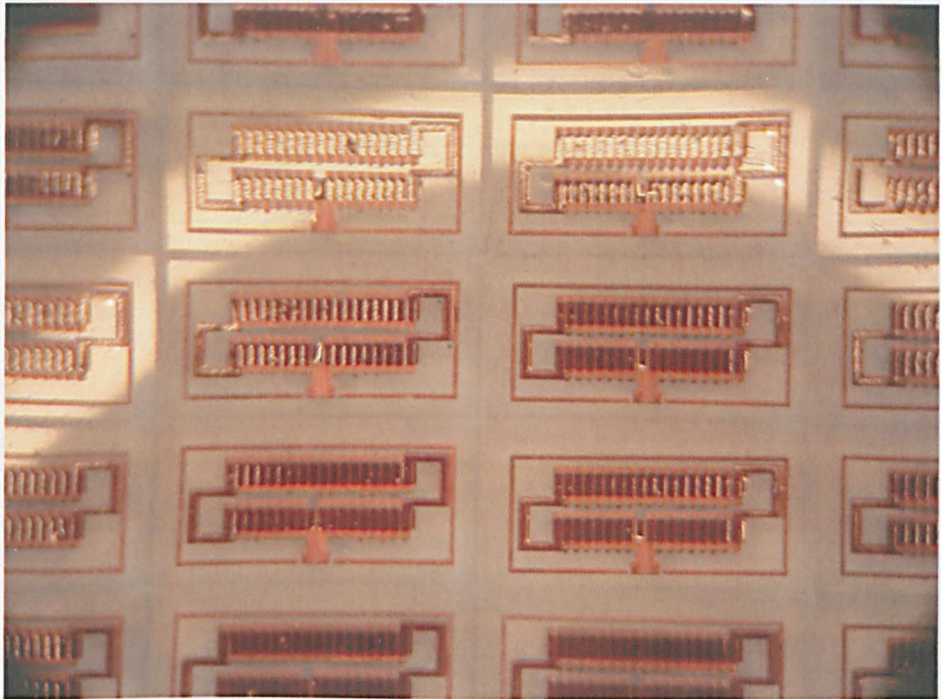


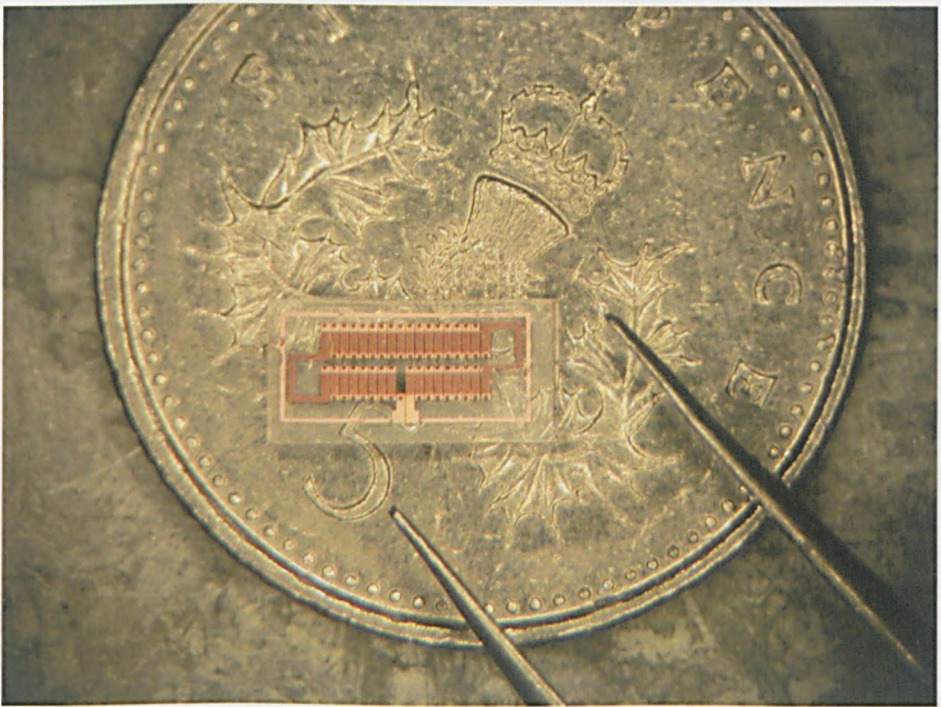
Figure 7.14 The upper winding layer with 90 $\mu$ m Cu windings, Cu:Au bumps 25 $\mu$ m and 5 $\mu$ m respectively, etched Ti/Ni layer, and 10 $\mu$ m AZ insulation layer.

Fig 7.13 shows that the DC deposition of the gold has produced uniform deposit thickness and surface area. If the gold bumps varied in height or in surface area the bonding process would be affected, and the conductive winding path impeded.

The lower and upper winding wafers are mounted onto a UV sensitive film and are diced with a diamond saw. The yield of the upper and lower winding layers was approximately 80%. This provided 120 operational samples out of a potential 150. Fig 7.15 displays a wafer of fabricated windings after dicing.



(a)



(b)

Figure 7.15(a) Glass wafer with 120 functional lower winding layers. The winding layers are now chips that can be flip-chip bonded together with alternative core samples, and (b) a released chip positioned on a 5 pence coin.

A summary of the fabrication process of the electrodeposited core samples is displayed in Fig 7.16.

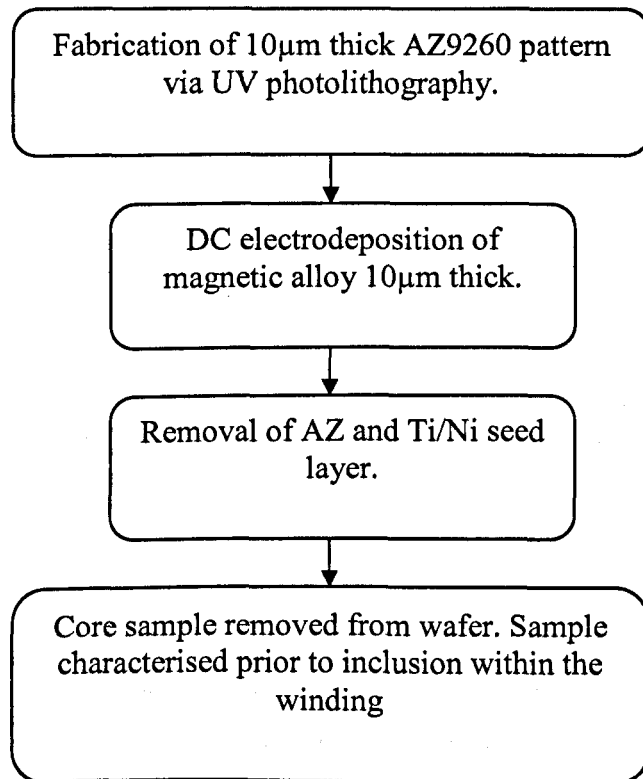


Figure 7.16 Summarised fabrication process of the electrodeposited core samples.

Once the core samples are released from the glass wafer, they are positioned on the insulation layer of the lower windings. The core samples are fabricated under conditions to promote low stress. Stress can influence the magnetic properties of the alloys, as discussed in Chapters 4 & 5, and can also complicate the manual positioning of the alloy. Under stress the alloy will twist and contort. The insulation layer is coated with a light spray of non-conductive adhesive. The insulation layer becomes tacky and the 5µm approx adhesive layer provides a level of control when positioning the alloy. After a period of 10 minutes the adhesive sets and the alloy is held in a permanent position.

Commercial alloys, fabricated via a cold rolling process, were purchased as a roll of film. The alloys were degreased with acetone and secured to a glass wafer. The wafer was patterned with AZ9260 and wet etched to the desired dimensions. As etching is a subtractive process, the patterning of the AZ used a glass titanium mask with the reversed polarity of the core acetate mask. The etchant consisted of  $\text{HNO}_3:\text{HCl}:\text{H}_2\text{O}$ , 2:1:3. The etchant was very aggressive and the etching was completed in less than 60s.

After 60s under-etching would occur and the AZ photoresist also became susceptible to the etchant. The glass wafer was then cleaned in deionised water, the AZ stripped and the core samples released. Dimensions of the sample were verified with Zygo and then placed within an identical solenoid component.

Dry etching of the commercial samples was also investigated. The commercial alloys were secured to the wafer as before, and a CO<sub>2</sub> laser was used to ablate the alloy to the required dimensions. However, this was a slow process and produced a poor quality finish. The ablation process created a ripple type edge effect, which would have generated flux density crowding.

### **7.3.8 Flip-chip assembly of the micro-inductor**

Flip-chip bonding of the inductor windings shown in Fig 7.13 & 7.14 was carried out using the flip chip bonder, Karl SUSS, FC6, shown in Fig 7.17.

The FC 6 system comprises of the following components:

- (1) Chuck XY stage – This is at fixed height but is capable of being manipulated in the X-Y plane with a resolution of 1 micron. The substrate holder, lower winding layer, can be heated (up to 500°C) and holds the substrate in place by vacuum.
- (2) Bonding arm – This is fixed in the XY plane but can move in the Z plane to bring the two components together once aligned. The chip, upper winding layer, is loaded onto the stage. This stage is also independently heated (up to 500°C) and can be manipulated with a resolution of 1 micron. The applied force range is 0-5000g. The chip is held in position by vacuum.
- (3) Microscope – The optics are situated between chuck and bonding arm during the alignment step and are moved out of the way just prior to the bonding step. The image of the substrate and chip are superimposed on the same screen, but are differentiated by image colour: blue for chip and red for substrate. The microscope can move in XY plane with a resolution of 1 micron and focus in the Z plane. The microscope has a fixed magnification and provides a 375 × 280 μm field of view.



- (4) User controls – These consist of two joysticks to control substrate, chip and microscope movement, a keyboard for menu selection and programming and a screen to display parameters.

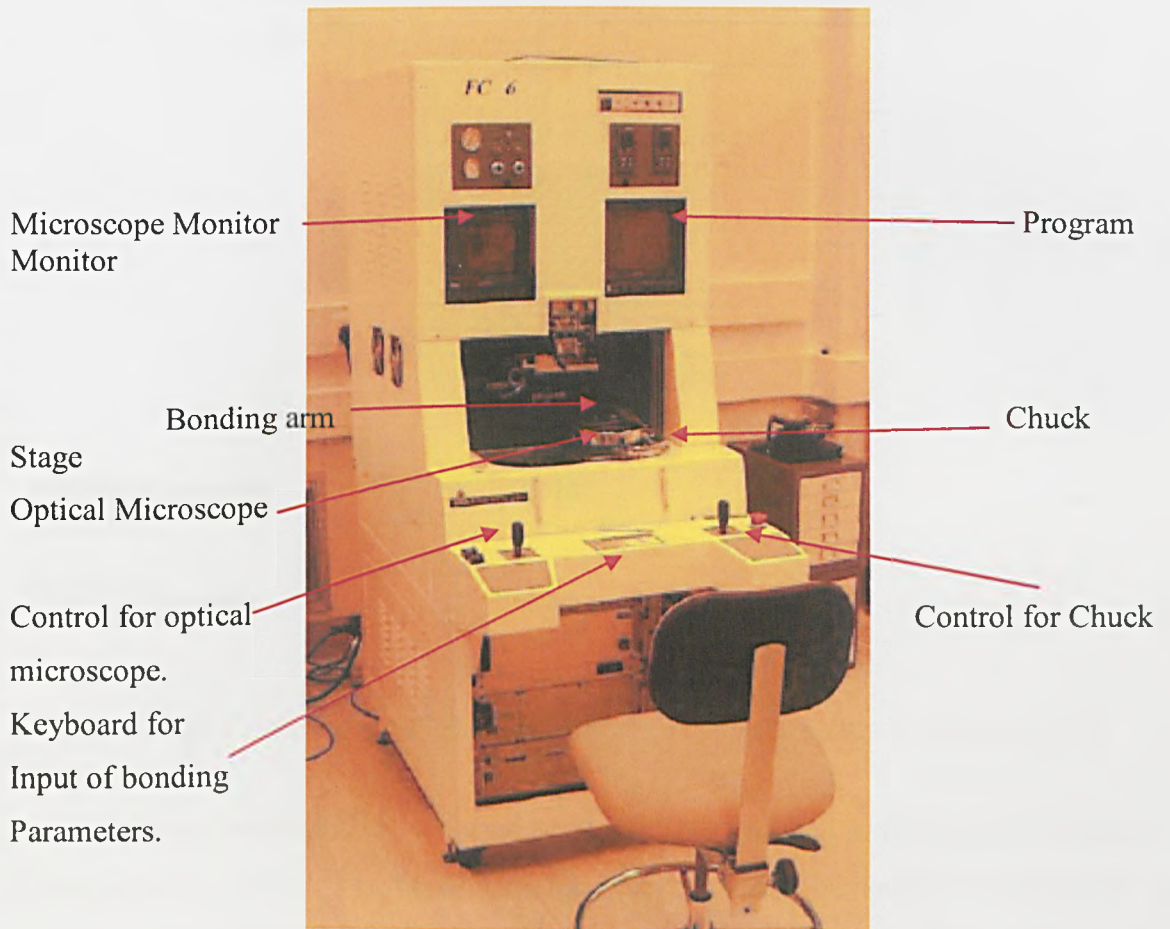


Figure 7.17 Flip-chip bonding machine Karl SUSS FC6

Bonding of the gold capped interconnection bumps of the upper and lower winding layers was achieved using thermo-compression bonding. The process of thermo-compression flip-chip bonding of the gold capped bumps is illustrated in Fig 7.18.

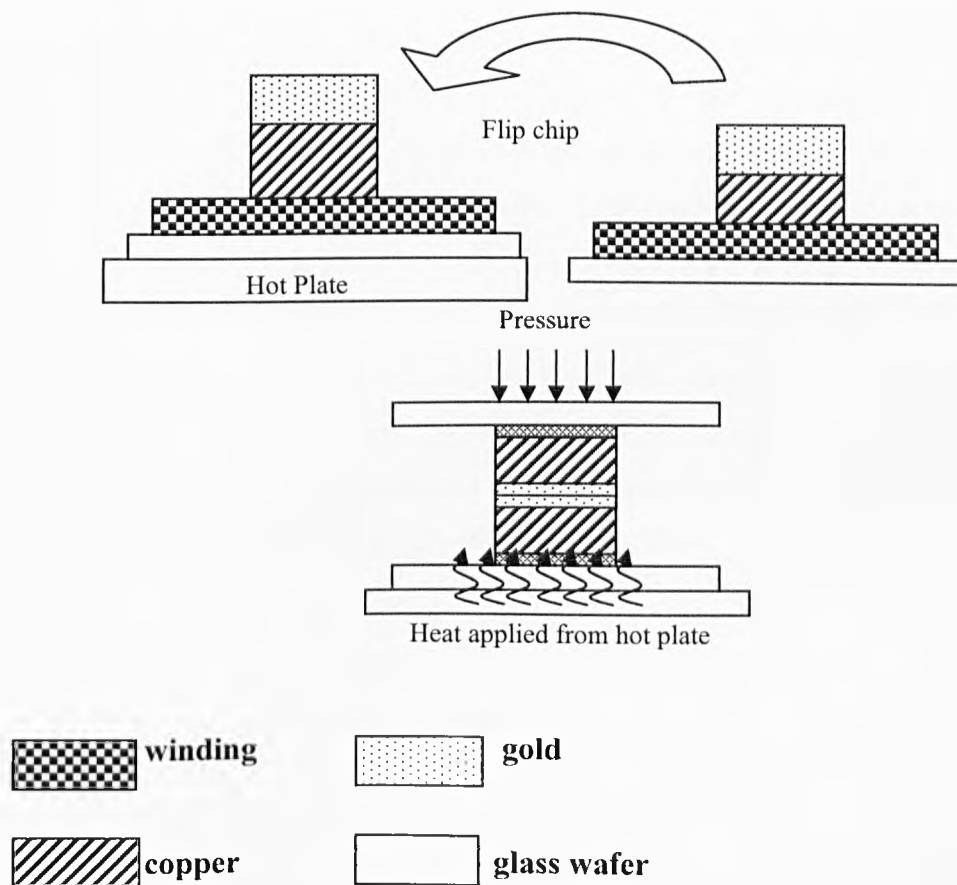


Figure 7.18 Cross-section of the thermo-compression flip-chip bonding process.

First, the lower winding layer with the magnetic core attached to the insulation layer is loaded onto the chuck. The upper winding layer, the chip, is placed onto the bonding arm and held in place by a vacuum. The chip is then flipped over facing downwards, towards the substrate, and the optical microscope is moved in-between the chuck and the bonding arm. The alignment of the bumps to its counterpart is then carried out.

The next stage of the bonding process is the pre-heating of the substrate. As the bonding temperature for Au bumping is around 250°C, both the arm and the chuck are pre-heated to a temperature of 120°C before bonding commences. This is to shorten the ramping time taken to reach the bonding temperature. If the temperature increases from 25°C to 250°C undesirable thermal shock is likely to occur due to rapid expansion of both chip and substrate, especially the carrier chip, because the mass of the holder on arm is much smaller as compared to the chuck substrate.

The bonding profile is then entered covering the parameters of temperature, timing and force shown in Fig 7.19. During bonding the optical microscope is moved aside, and the bonding arm holding the carrier chip, aligns and approaches the chuck and the bonding profile is activated. Both arm and chuck temperature start to rise from 120°C to bonding temperature as illustrated in Fig 7.19, at temperature of 240°C, bonding force of 80g per bump is applied to the chuck for a 20 second period. While the temperature rises to 250°C and remains there for 10s, cooling is then applied for 10s. After 30s, the force in the bond arm drops to zero and the chip is released from the bonding arm. The bonding is completed. At this moment the temperature on the chuck is still at around 120°C, compressed air is then used to force cool the bonded device to around room temperature. Fig 7.20 displays the bonded component.

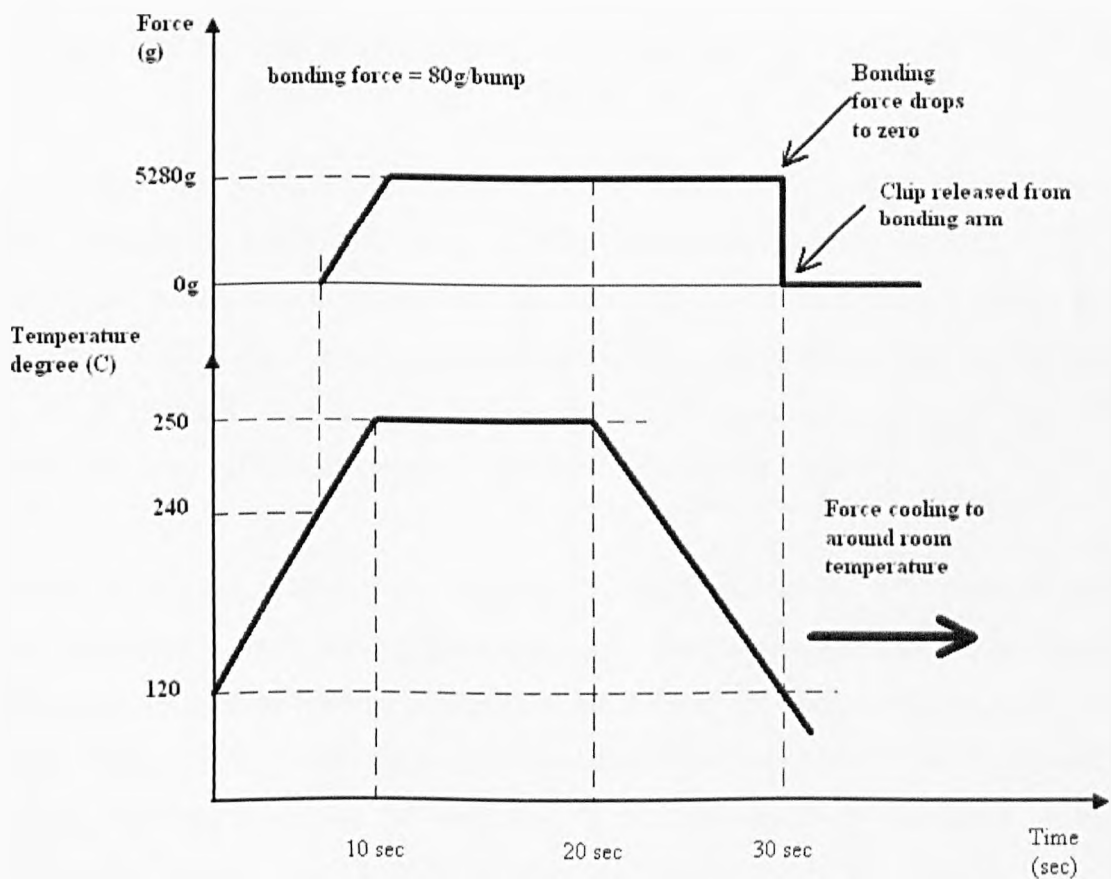


Figure 7.19 Pre-set bonding profile for temperature and force as a function of time.



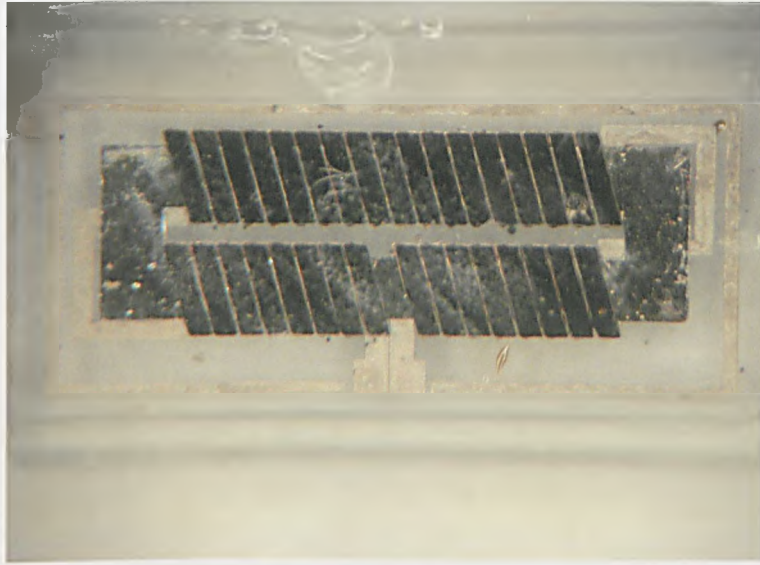


Figure 7.20 Flip-chip bonded solenoid microinductor. The view is through the upper glass substrate displaying the dark Ti adhesion layer.

The parameters displayed in Fig 7.19 are the result of initial flip-chip bonding tests. The temperature for bonding gold, 250°C, was sourced from prior work [7.8]. The minimum force was determined to be 40g/bump, any lower than this and a bond was not formed. The timing was also important; if the force was released while the Au was still soft, at 250°C, then a bond would not be made. Hence, the gradual reduction of temperature to 120°C was followed by the force being removed.

After the bonding profile is complete, the bonding arm returns to its original position and the chuck vacuum releases the component. The glass substrate of the winding layer must be removed to access the input/output pads of the completed inductor winding. This was achieved by immersing the assembled inductor devices in Ti etchant with strong agitation to remove the remaining Ti adhesion layer and seed layer. It takes 5 minutes to ensure a good quality of under-etch, tweezers are then used to remove the glass substrate. When nickel windings are used the windings are not affected by the etchant as they are 450 times thicker than the Ni seed layer.

Fig 7.21 shows a released solenoid microinductor and Fig 7.22 shows a dissected sample displaying the interconnection between windings.

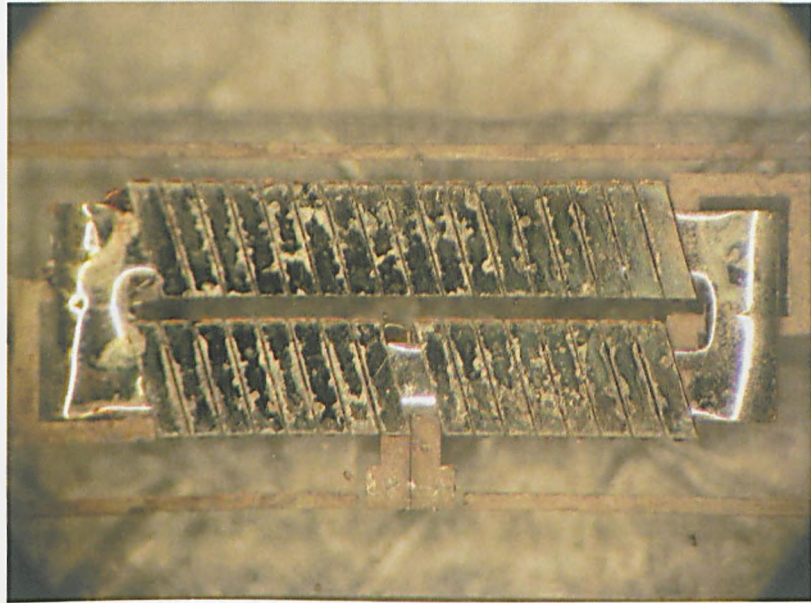


Figure 7.21 Released solenoid micro-inductor of size 2mmx5mmx 250 $\mu$ m (WxLxT). The diagonal nickel windings are clearly visible. The Ni(80)Fe(20) core of O-shape is assembled between the windings by flip-chip bonding.



Figure 7.22 Solenoid micro-inductor showing the interconnection between the upper and lower winding layers. The dark material on the nickel is the residual Ti from the adhesion.

#### 7.4 Fabrication of other microscale magnetic components

Three other microscale magnetic components were fabricated on glass using the fabrication method described in section 7.2. The components were a spiral microinductor, pot-core “race-track” wound micro-inductor and a pot-core transformer. The three components are planar and pot-core in structure with the only variable being the winding layout. The fabrication process is presented in Fig 7.23. The winding structures are fabricated on a 25 $\mu$ m thick aromatic polyamide film, Kapton. Kapton is a strong, tough, transparent and adhesive tape. Kapton exhibits excellent physical and

chemical properties over a wide range of temperatures. The electrical dielectric constant is 3.1 and the bulk resistivity at 23<sup>0</sup>C is about 2x10<sup>17</sup> ohm/cm. The windings are fabricated on Kapton for two reasons: (1) to release the winding structure from the glass substrate and (2) insulate the windings from the lower core layer. The pot core geometry requires magnetic layers surrounding the windings. Successive deposition of the core layers built on the winding layer is not practically realistic with the electrodeposition process. Therefore, manual assembly of winding and core layers is required. The windings are fabricated on a 10mm x15mm footprint.

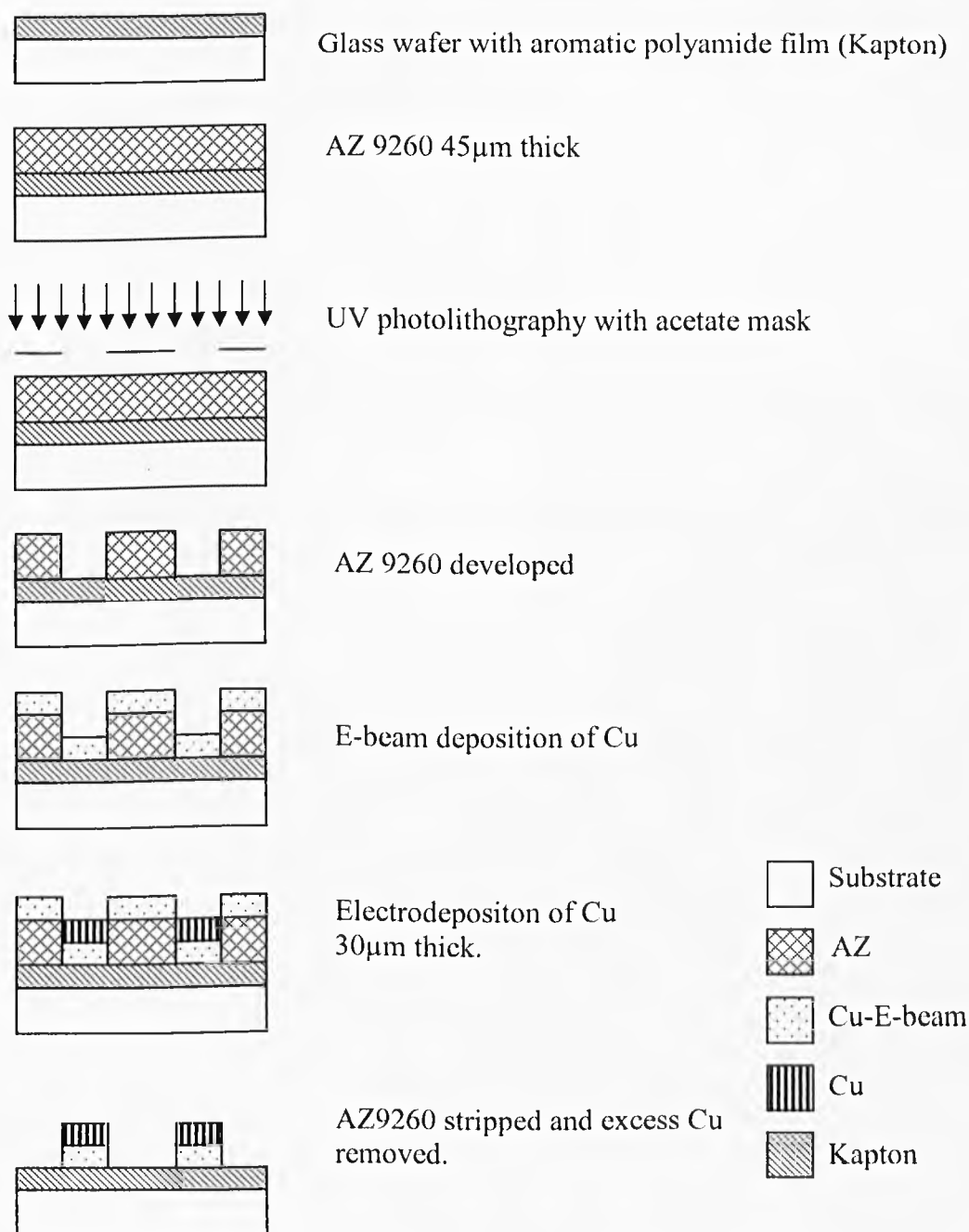


Figure 7.23 Fabrication process of the pot-core planar windings.

The assembly process of the pot-core components is shown in Fig 7.24. Electrodeposited and commercial core layers are fabricated using the same fabrication procedure described in section 7.2. Table 7.7 displays the dimensions of the pot-core planar windings and component.

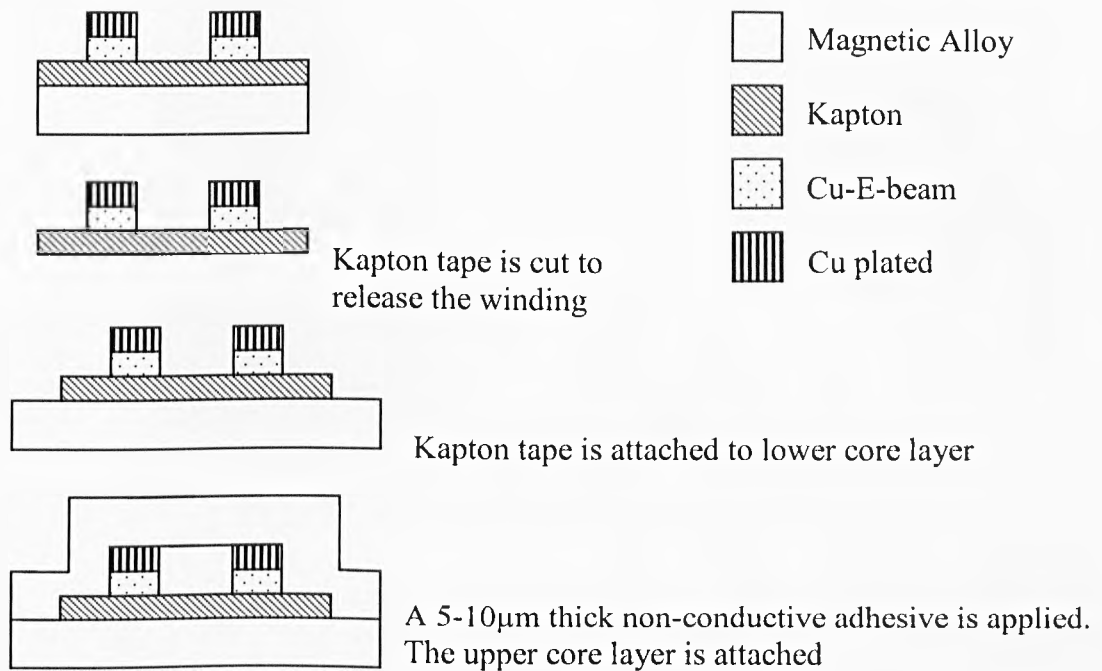


Figure 7.24 Assembly process of the pot-core spiral inductor. The pot-core “race-track” microinductor and transformer follow the same assembly process.

The magnetic path is closed when the upper and lower core layers are attached. The adhesive used in the assembly of the core layers acts as an air-gap. The magnetic path crosses the laminate and accurate alignment of the laminate is therefore required to minimise leakage flux. Due to the manual assembly this method provides a potential source of error between analytical and experimental results.






Type	Pictorial View	Description
4 Turn Spiral Micro-inductor		Number of turn: 4 Winding width: 300 $\mu$ m Winding Thickness: 30 $\mu$ m Component footprint: 10mmx15mm Laminate core layer thickness: 10 $\mu$ m
1:1 "race-track" Micro-transformer		Number of Primary & Secondary Turns: 3 Winding width: 300 $\mu$ m Winding Thickness: 30 $\mu$ m Component footprint: 15mmx10mm Laminate core layer thickness: 10 $\mu$ m
3 Turn "race-track" Micro-inductor		Number of Turns: 3 Winding width: 300 $\mu$ m Winding Thickness: 30 $\mu$ m Component footprint: 15mmx10mm Laminate core layer thickness: 10 $\mu$ m

Table 7.7 Pot-core components and dimensions.

A consideration when fabricating the "race-track" component is that the magnetic core is not continuous over two sets of windings. The two core halves are shown in Fig 7.25. If the core was one continuous layer it could form an effective shorted turn with the onset of eddy currents.

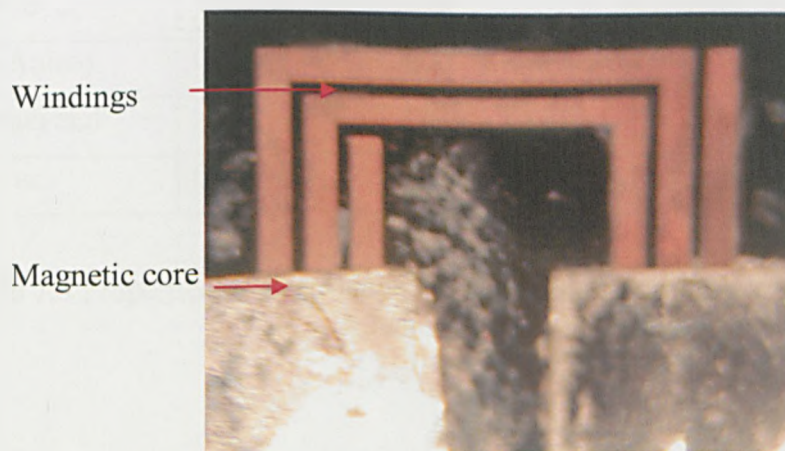


Figure 7.25 Pot-Core 3T "race-track" micro-inductor. The core area is comprised of two sections. If the core was constructed of one segment, induced currents within the core could form a short across the windings.

The pot-core components are labour intensive to construct in comparison to the solenoid component. Direct electroplating of horizontal laminations offers the possibility of fabricating structures of sufficient overall thickness, but the repeated switching of substrates between plating baths, vacuum system and photoresist development becomes unmanageable as the number of layers increases. A mechanical lamination process of fabrication could overcome many of the aforementioned difficulties. A potential mechanical lamination fabrication process is described in Chapter 10.

The following section introduces other magnetic alloys that were investigated for the solenoid micro-inductor.

### 7.5 Other magnetic alloys investigated

The structure of the solenoid component permits the comparison of various magnetic alloys. The properties of the tailored Ni-Fe, Vitrovac, and CoFeCu magnetic alloys are detailed in Table 7.8. The electrolyte composition and deposition parameters of the CoFeCu alloy are outlined in Table 7.9 [7.9, 7.10].

	<b>B<sub>sat</sub>(T)</b>	<b>μΩ.cm</b>	<b>H<sub>c</sub></b>	<b>μr</b>
<b>Electrodeposited</b>				
NiFe	0.8	20	3	2000
NiFe(PR)	0.78	46	1.3	3130
CoFeCu	1.4	18	1	300
NiFe(Aniso)	0.8	20	0.4, 0.63	2200, 1300
<b>Commercial</b>				
Vitrovac	0.5	130	.3	100000

Table 7.8 Properties of electrodeposited and commercial alloys incorporated into the solenoid micro-inductor.

Component: CoFeCu	Quantity
$CH_3COONa.3H_2O$	11.05(g/l)
$CoSO_4.7H_2O$	57(g/l)
$FeSO_4.7H_2O$	5.5-8(g/l)
$CuSO_4.5H_2O$	0.1-0.7(g/l)
Saccharin	4(g/l)
pH	2.5-4
Temperature	25-30°C
Current Density	8 mA/cm <sup>2</sup>

Table 7.9 Electroplating solution and conditions of CoFeCu

CoFeCu is another alloy of interest from the magnetic recording head industry. Low resistivity and poor corrosion resistance which have held back CoFeCu in the magnetic recording field are not as debilitating in power magnetic applications. The CoFeCu alloy exhibits high saturation flux density, low magnetostriction, low coercivity and low internal stress. Therefore, CoFeCu was investigated within the solenoid component.

### 7.6 Summary

A solenoid micro-inductor fabricated with techniques borrowed from the UV-LIGA process has been presented. The novel flip-chip bonding of the upper and lower windings provides a simple method to fabricate a traditional difficult 3D geometry. The details of the manufacturing process of pot-core components was also introduced. Different magnetic cores have been fabricated on glass using electrodeposition and wet etching techniques. The assessment of the various core materials and component geometries is presented in Chapter 8.



## References

- [7.1] H. Mishima, T. Yasui, T. Mizuniwa, M. Abe, T. Ohmi, "Particle-free wafer cleaning and drying technology," IEEE Trans., on Semiconductor Manufacturing, vol. 2, pp. 69-75, Aug. 1989.
- [7.2] [www.microchemicals.com](http://www.microchemicals.com)
- [7.3] "Baking & Delays...chemical/physical reactions in AZ® and TI photo resists," revised 2003-09-25, [www.microchemicals.com](http://www.microchemicals.com).
- [7.4] M. J. Madou, "Fundamentals of Microfabrication, the science of miniaturization," 2<sup>nd</sup> edition, CRC press, pp. 134-136, 2002.
- [7.5] "Exposure & Development...chemical/physical reactions in AZ® and TI photoresists," revised 2003-09-25, [www.microchemicals.com](http://www.microchemicals.com).
- [7.6] M. Brunet, T. O'Donnell, J. O'Brien, P. McCloskey, C. O'Mathuna, "Design Study and Fabrication Techniques for High Power Density Micro-Transformers," IEEE Trans., Magn., pp. 1189-1195, 2001
- [7.7] D. J. Elliott, "Integrated Circuit Fabrication Technology," McGraw-Hill Book Company, page 72, 1982.
- [7.8] J. Zhang, C. H. Wang, A. J. Pang and J. Zeng, "A low cost bumping method for flip chip assembly and MEMs integration," Proc. HDP'04, pp.171-176, 2004.

## Chapter 8

### Characterisation of Micro-Inductors and Transformers

#### 8.1 Introduction

This chapter presents the measurement procedure used to characterize the components manufactured. Comparisons of the experimental and analytical results of the prototype micro-inductors and micro-transformers are also provided within this chapter. An introduction to the measurement method and procedure is contained in section 8.2. The results of the solenoid micro-inductor are presented and discussed in section 8.3. Analysis of the pot-core micro-inductor characterization results is carried out in section 8.4. The assessment of the micro-transformer is detailed in section 8.5. Conclusions based on the theoretical and recorded data are summarized in section 8.6.

#### 8.2 Low frequency impedance measurement

A Hewlett Packard 4192A LF-impedance analyser was used to record the inductance, resistance, Q-factor and impedance over a frequency range of 1 kHz-10MHz. The 4192A LF impedance analyser measures the real and the imaginary parts of the impedance vector and then converts the value to the desired parameters such as  $|Z|$ ,  $\theta$ ,  $|Y|$ , R, etc. The analyser is calibrated through the measurement of “etalons” with known values. The 4192A has a zero offset adjustment function to eliminate the residual impedance and stray admittance of the test fixture and test leads.

Factors to control during measurement include test signal level, DC bias and environmental conditions such as temperature, humidity, etc. Magnetic core inductors depend on the current of the test signal due to the hysteresis of the core material. The inductance of magnetic core inductors varies according to the DC bias current due to the magnetic flux saturation characteristics of the core material. For example, DC bias current remains constant during the measurement of inductance as a function of frequency. All measurements are performed at room temperature and under standard atmospheric conditions.

### **8.3 Measurement results of the microinductors**

The analytical and experimental results of the solenoid microinductor are presented and discussed in section 8.3.1. The solenoid component is characterised with the following magnetic alloys: electrodeposited Ni-Fe(DC), Ni-Fe(PR), Ni-Fe(anisotropic), CoFeCu and the commercial alloy Vitrovac. The effect of increasing the laminate layers is assessed for Ni-Fe(DC) and Vitrovac. In addition, single core layers of Ni-Fe(DC) and Vitrovac are characterised with a 50 $\mu$ m air-gap included in the flux path.

#### **8.3.1 Solenoid micro-inductor: winding & dielectric assessment**

The solenoid micro-inductor was initially flip-chip bonded as an air-core component. The purpose of omitting the magnetic core was to characterize the winding resistance as a function of frequency. Omitting the magnetic core removes any resistance due to induced eddy currents in the core. Hence, when the resistance of the winding becomes greater than the low frequency DC value, the increase in resistance is representative of the skin depth and proximity effect of the winding structure.

The AC resistance value for copper windings of varying thickness, 60 $\mu$ m, 90 $\mu$ m and 200 $\mu$ m, is shown in Fig 8.1. The 200 $\mu$ m thick winding was fabricated with SU-8 due to the limitations of AZ9260 film thickness. The spacing between windings was maintained with a 4:1 aspect ratio resulting in spacings of 15 $\mu$ m, 20 $\mu$ m and 50 $\mu$ m, respectively. The windings have a low resistance,  $R_{DC}$ , at low frequency. However, when the operating frequency increases, the skin and proximity effects induce a greater resistance. The analytical predications obtained in Chapter 6 agree well with the experimental results plotted in Fig 8.1. An analytical error of 10% in the upper frequency range occurs for the 200 $\mu$ m thick winding. This result is an indication of a potential limitation of the analytical model.

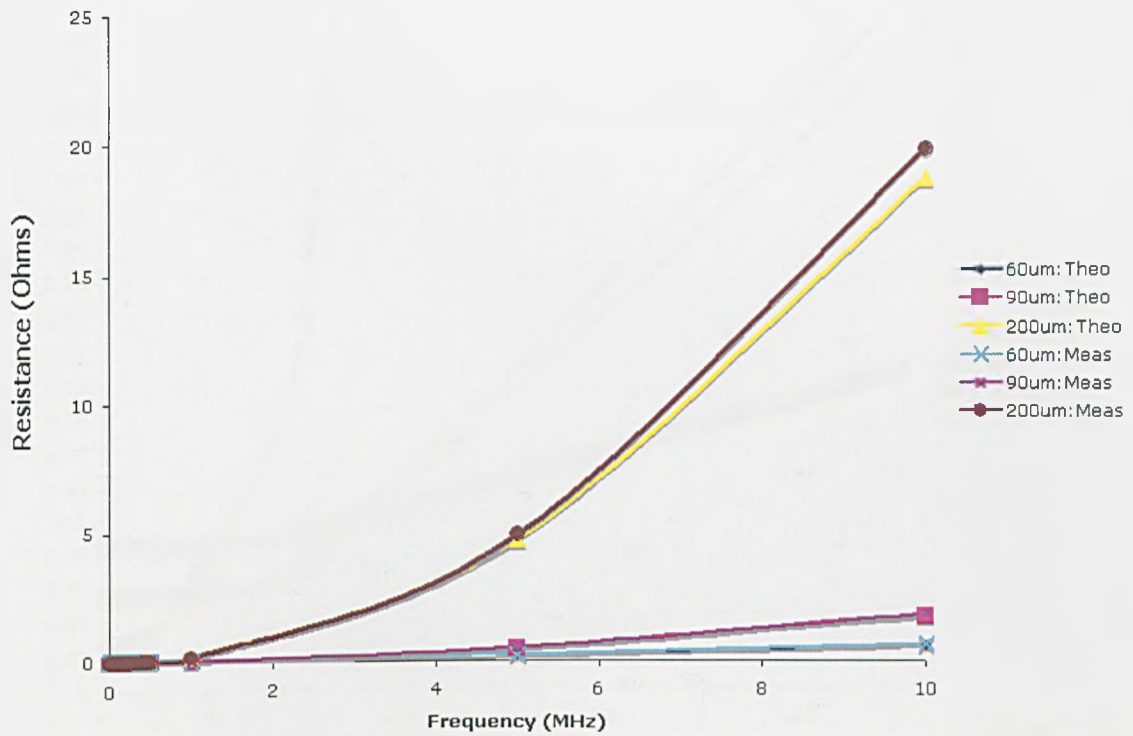


Figure 8.1 Winding Resistance versus Frequency. Analytical and experimental results for winding resistance of 60µm, 90µm and 200µm thick copper windings.

Fig 8.2 displays the increase in winding resistance with frequency in more detail. The 90µm and 60µm thick windings exhibit improved resistance-frequency response in the upper frequency range. With the inter-winding distance determined by the 4:1 aspect ratio for each winding, it is assumed that the skin effect, and not the proximity effect, of the 200µm thick winding is the primary cause of the resistance difference. The skin effect of the 200µm is evident at 1 kHz, in comparison to 750 kHz, approximately, for the 60µm and 90µm thick windings. The advantage of the low DC resistance of the 200µm windings, due to greater cross-sectional area, is superseded with increased resistance,  $R_{AC}$ , at about 505 kHz. When calculating  $R_{DC}$  and resultant  $R_{AC}$  values of the winding resistance, no attempt was made to model the via interconnections. Direct measurement of the vias after bonding was not possible. However, due to the good agreement between experimental and analytical values, the via resistance has been proven to be minimal justifying the use of electroplating and flip-chip bonding as a viable assembly process.

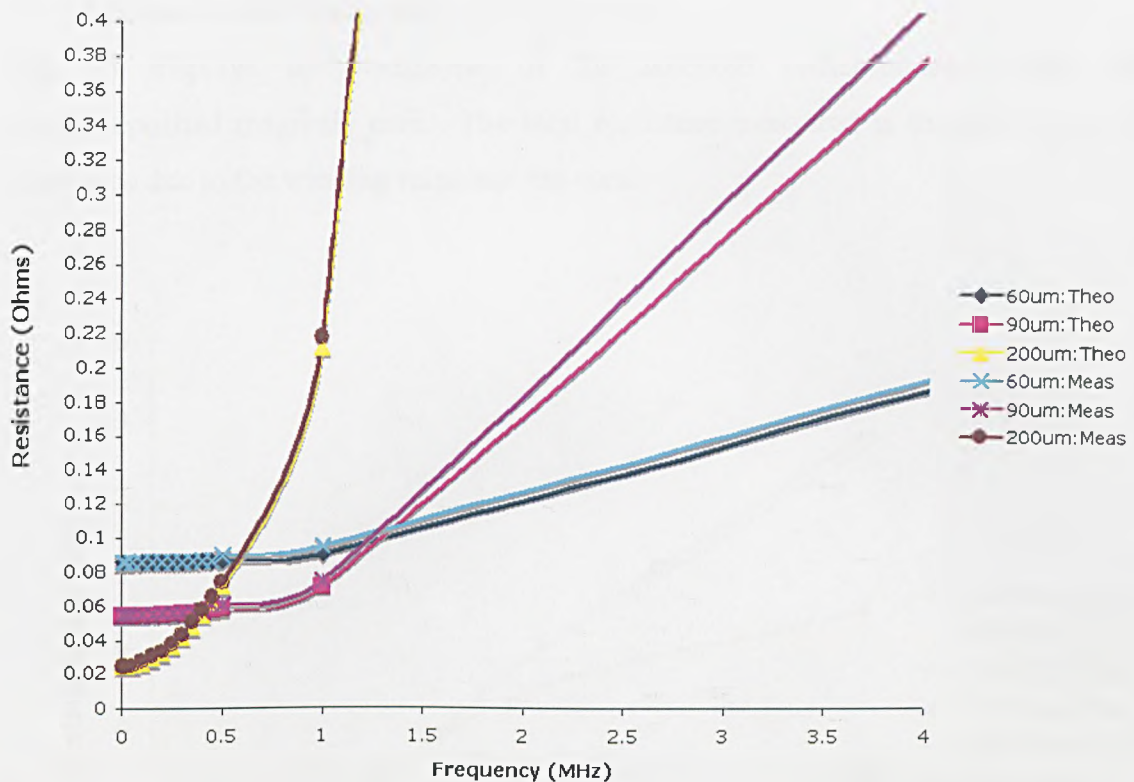


Figure 8.2 Winding resistance versus frequency. Analytical and experimental results for winding resistance of 60µm, 90µm and 200µm thick copper windings.

With the increasing demand for high power density and reduced voltage operation the applied current obviously has to increase. Due to the higher current handling capability of the 90µm windings in comparison to the 60µm windings, and the low winding resistance in the 500 kHz-1,250 kHz range, the 90µm windings have been used in the assessment of the core materials.

AZ9260 serves as an insulation layer and a photosensitive resin for the electrodeposition of structures. The electric field strength of a material represents the value of voltage at which the material breaks-down. The breakdown of the material is indicated by the sudden increase of detected current. The inrush current creates a pit/cavity on the insulator surface. The electric field strength can be determined using a holiday probe [8.1]. The electric field strength of AZ is approximately 1.8kV/mil or 70.86 V/µm [8.2]. The voltages applied to the investigated components will not exceed 1-2 V; therefore, AZ9260 serves as a good insulator for this application.



### 8.3.1.1 Solenoid microinductor: resistance test

Fig 8.3 displays the resistance, of the solenoid micro-inductors with their electrodeposited magnetic core. The total resistance measured is the sum of the AC resistance due to the winding turns and the core.

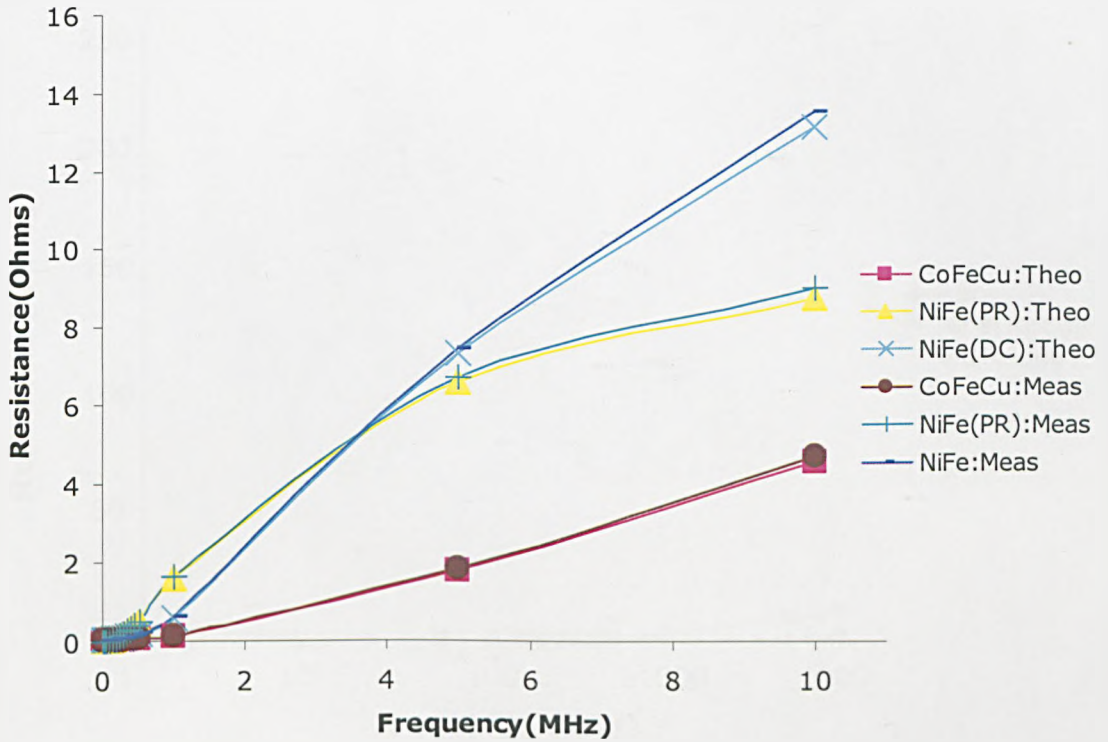


Figure 8.3 Micro-inductor resistances as a function of frequency.

The profile and values of the resistance curve within Fig 8.3 is different to that of Fig 8.1 due to the contribution of AC core resistance. The core resistance is the result of the hysteresis and eddy current effects within the core. Although the analytical model omits the contribution of the hysteresis resistance, the results of the analytical model are in good agreement with the experimental values. The results of Fig 8.3 demonstrate that eddy currents within the core increase rapidly with frequency. For example, the air-core resistance of the 90 $\mu$ m winding at 2MHz is 0.16 $\Omega$ , inclusion of the NiFe(DC) core increases this value to over 2 $\Omega$ . The increase in resistance results in increased power loss via Joule heating.

Fig 8.4 displays the resistance contribution of the 90 $\mu$ m winding and eddy current resistance of the Ni-Fe and Vitrovac core, as a function of frequency. The Vitrovac alloy with high relative permeability,  $\mu_r \approx 100,000$ , is highly susceptible to the skin

effect and as a result the effective resistance of the core increases more rapidly with frequency. In comparison, the eddy current resistance of Ni-Fe, with a relative permeability of  $\mu_r \approx 2,000$ , is 23 times smaller at 1 MHz. The dependence of the eddy current resistance on skin depth and core thickness is indicated by Eq (6.26).

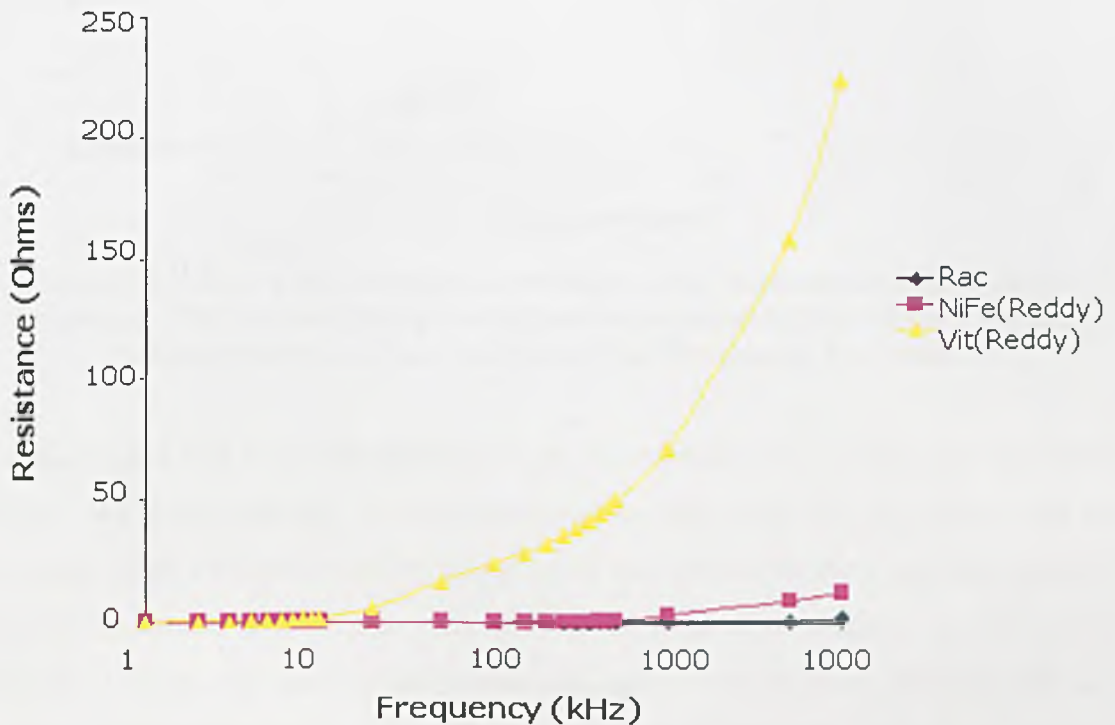


Figure 8.4 Comparison of core and winding resistances as a function of frequency. Vitrovac and Ni-Fe core resistance are compared with 90 $\mu$ m thick copper windings.

At 1 MHz the skin depth of the copper winding is 66 $\mu$ m. The 90 $\mu$ m thick winding, being under twice the skin depth, appears not to be affected by the onset of skin effects. Fig 8.5 displays the recorded resistance of the 90 $\mu$ m windings and analytical value of the eddy current resistance within the Ni-Fe core material in more detail. The winding resistance maintains its DC value at low frequency due to low skin and proximity effects. However, the eddy current core resistance increases linearly with frequency. Fig 8.5 highlights two fundamental facts: the eddy current loss is always present and increases rapidly with frequency. Therefore, it is important to minimize eddy current loss at high frequencies.



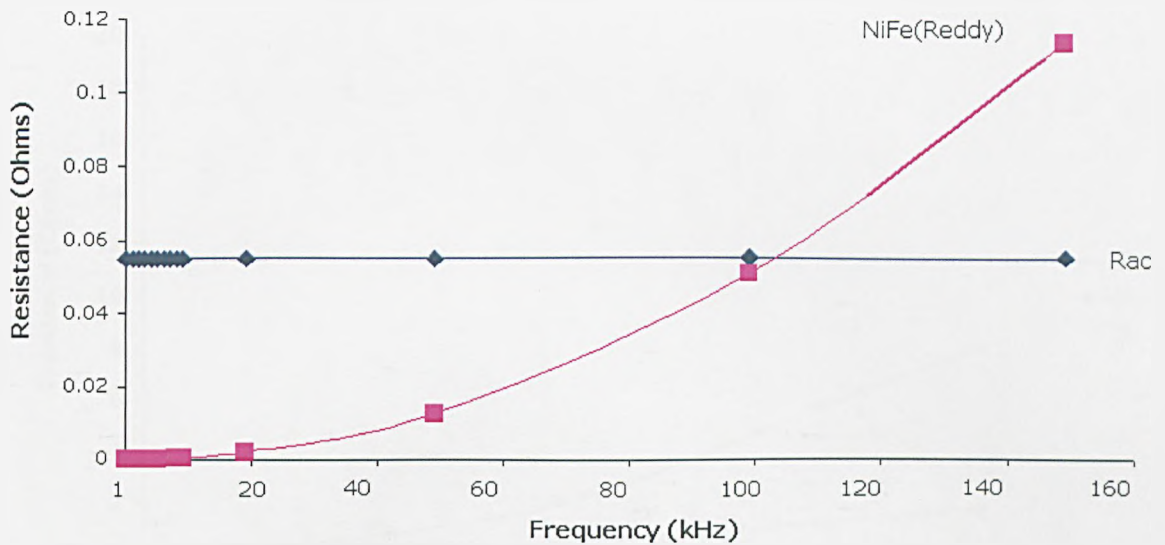


Figure 8.5 Winding resistance and core eddy current resistance as a function of frequency. The increasing eddy current resistance is due to skin effects. The AC winding resistance,  $R_{AC}$ , maintains its DC resistance,  $R_{DC}$ , value.

The  $R_{AC}$  value has been optimized through the consideration of skin and proximity effects. Winding thickness was restricted to less than twice the skin depth and the proximity effect was minimized by selection of the optimal winding spacing. Another factor in the reduction of the proximity effect is the single layer winding structure of the solenoid. Design engineers typically use multi-layer windings when trying to maintain a certain inductance level with reduced component footprint. However, the AC resistance of the multi-layer winding structure increases at high frequencies. Fig 8.6 displays the values of  $R_{AC}$  generated by the analytical model for 1, 2 and 3 winding layers. The difference in  $R_{AC}$  between the 1, 2 and 3 layer winding is attributed to the proximity affect. The increase of winding layers would also reduce the SRF of the inductor due to the increase in parasitic capacitance. An increase in the number of winding layers would also render the fabrication more complex and more expensive.

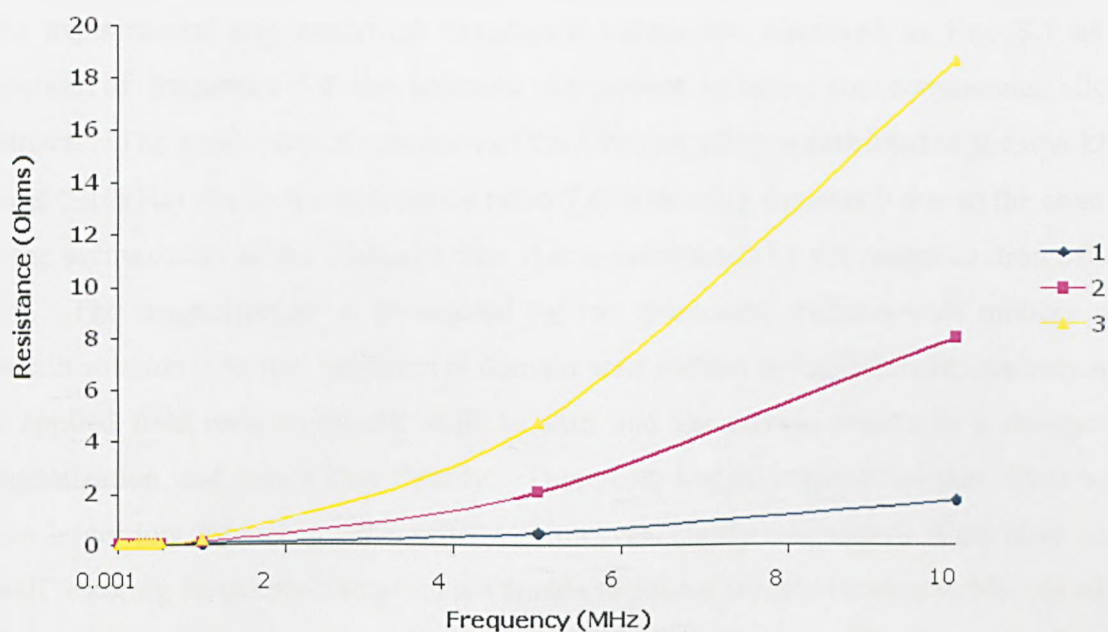


Figure 8.6 Analytical winding resistance as a function of frequency and number of winding layers.

Single-layer solenoids provide near optimal performance, as demonstrated in Fig 8.6. However, the number of turns per single layer of traditionally wound solenoid inductors is limited by the core's inner diameter and how tightly you can pack the turns together. Thus, to increase the inductance a larger core or multiple layers of windings would normally be needed. However, the ability to finely pattern inter-winding spacing e.g. 20 $\mu$ m for the fabricated solenoid permits a higher density of winding turns for a given area, which demonstrates the advantage of the UV photo-lithography process over conventional manufacture.

It is understood that the resistance due to hysteresis is normally greater in the low frequency range but as frequency increases eddy current resistance is more predominant. This transition typically occurs at a few kHz for thin film alloys [8.4]. The largest deviation between experimental and analytical results, 6% underestimation, occurred in the low frequency range e.g.  $\leq 10$ kHz. The increase in the experimental resistance value could be an indication of the hysteresis resistance that is not included within the model.

### 8.3.1.2 Solenoid micro-inductor: inductance & Q-factor test

The experimental and analytical inductance values are displayed in Fig. 8.7 as a function of frequency for the solenoid component utilizing the commercial alloy, Vitrovac. The bandwidth of operation of the Vitrovac alloy is restricted to the low kHz range ( $\leq 10\text{kHz}$ ) due to the inductance tail-off at increasing frequency due to the change of the permeability of the magnetic film that is determined by the magnetization of the film. The magnetization is dominated by two processes: domain wall motion and domain rotation. At low frequencies domain wall motion is the dominant mechanism; an applied field causes domain walls to shift and the motion results in a change in magnetization and hence flux density. Therefore, highly magnetized thin films will have larger low frequency permeability. However, highly magnetized films have very small restoring forces and therefore are unable to follow rapidly varying fields. At high frequencies, the domain rotation becomes dominant and is responsible for permeability. It is hard for the large domains to rotate therefore the relative permeability and therefore the inductance is reduced.

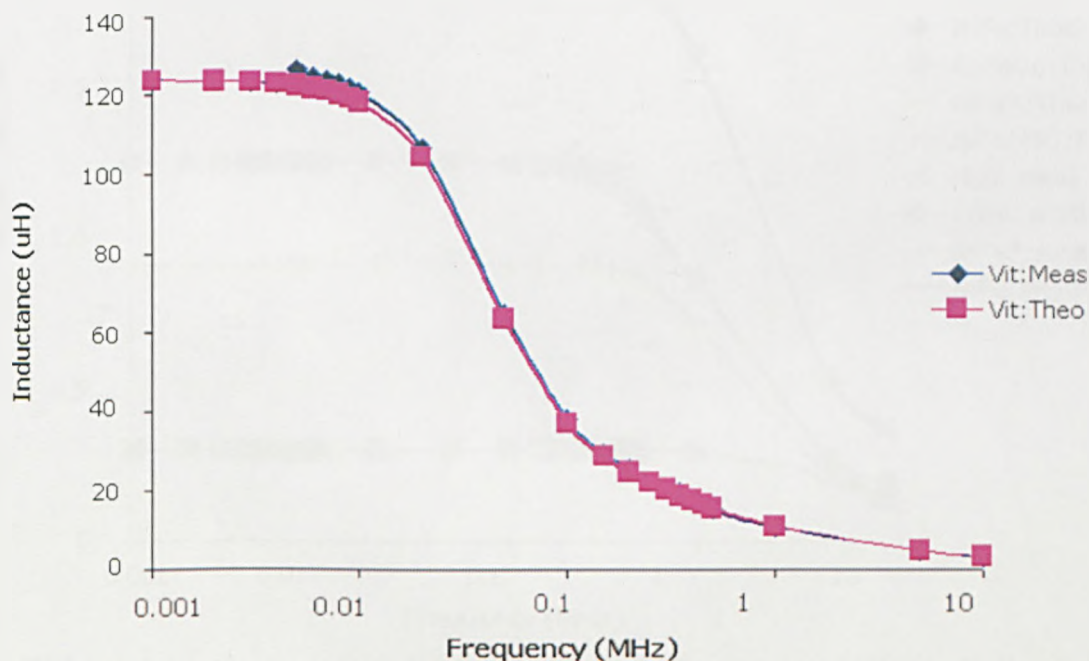


Figure 8.7 Analytical and commercial values of the inductance of the commercial alloy Vitrovac.

Although the commercial alloy has a resistivity 6.5 times greater than the electrodeposited alloys, the thickness of the film,  $20\mu\text{m}$ , and its high relative permeability of around 100,000, make it sensitive to skin depth effects. The skin effect arises due to the presence of eddy currents flowing in the magnetic core. Eddy currents



form because a voltage is induced around the core periphery equal to the volts/turn applied to the windings. The core material has a finite resistivity, which translates into a resistance value around the core periphery. The voltage induced around the core forces a current, the eddy current, to flow through this resistance. By Lenz's law, the swirling eddy current moves in such a way as to create a magnetic field opposing the change; this generates a cancellation flux. Therefore, the overall flux becomes reduced and since inductance is a function of flux linkage, the inductance decreases accordingly.

The inductance versus frequency response of the electrodeposited alloys is shown in Fig 8.8. Whereas the inductance of the commercial alloy tails off at 10 kHz the electrodeposited alloys maintain a constant inductance value beyond 500 kHz.

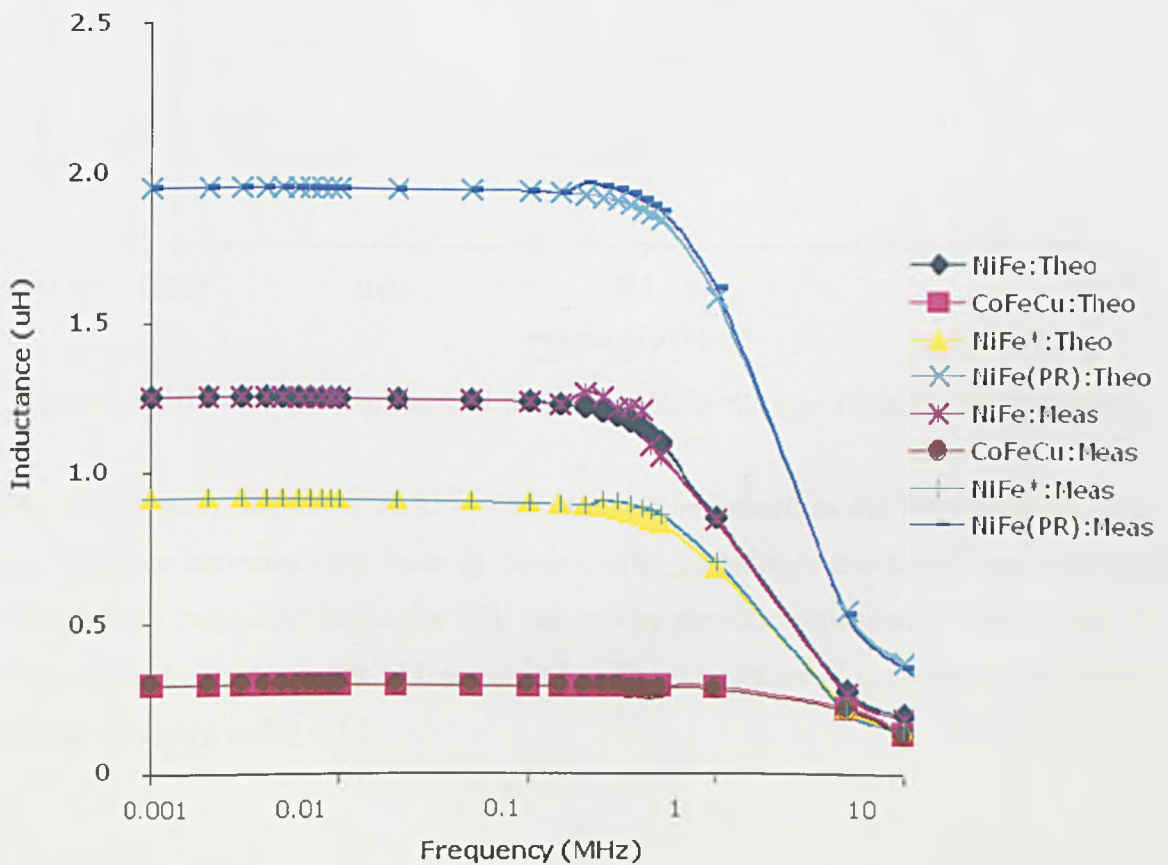


Figure 8.8 Electrodeposited alloys inductance vs. Frequency. NiFe\* indicates the anisotropic Ni-Fe.

The results of Fig 8.8 indicate that the relative permeability and resistivity values of the electrodeposited alloys are better suited to the increased frequency range of the application. The high relative permeability concentrates the flux density inside the core and enhances the inductance. Moreover the film thickness and reasonable electrical resistivity reduces the formation of undesirable eddy currents. As with the commercial

alloy the reduction in inductance with frequency is due to skin effects and the magnetic domains not rotating as readily at higher frequencies. The combination of these two factors results in a reduction of effective relative permeability of the core material. Fig 8.9 displays the effective relative permeability of the Ni-Fe alloy as a function of frequency.

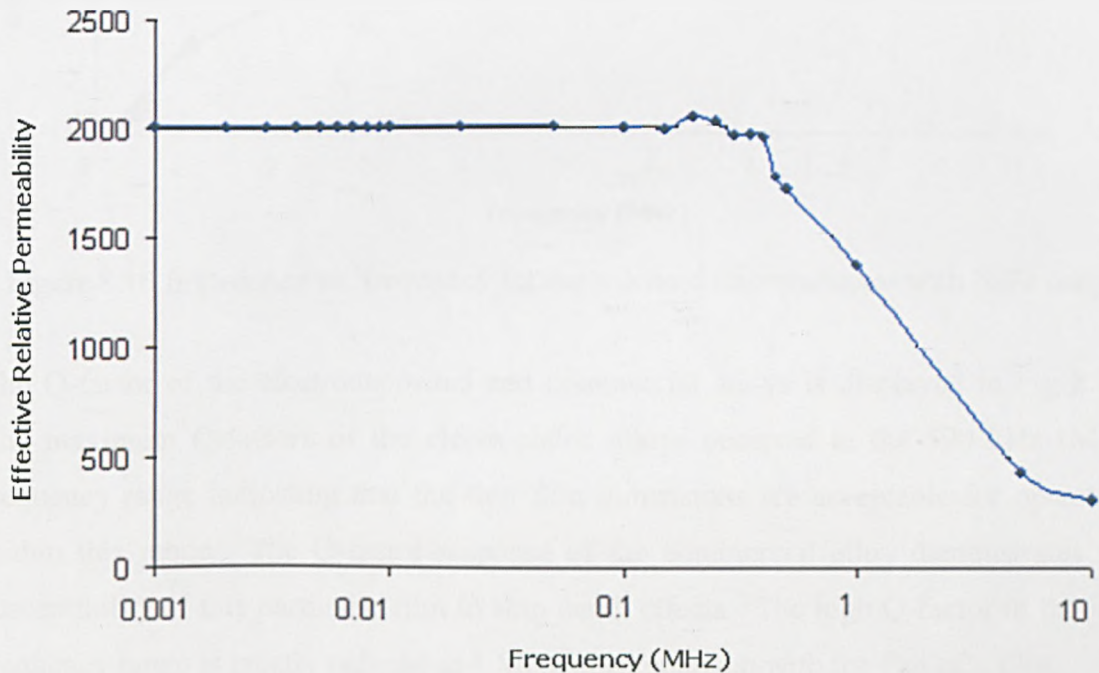


Figure 8.9 Effective relative permeability of the NiFe alloy as a function of frequency.

The self resonant frequency (SRF) of an inductor is defined as the frequency at which the reactance becomes zero (zero Q-factor). The impedance measured here increases linearly with frequency; hence the SRF induced by parasitic capacitance effects does not occur in the frequency range of interest [8.5]. The impedance of the solenoid with a Ni-Fe core is shown in Fig 8.10.

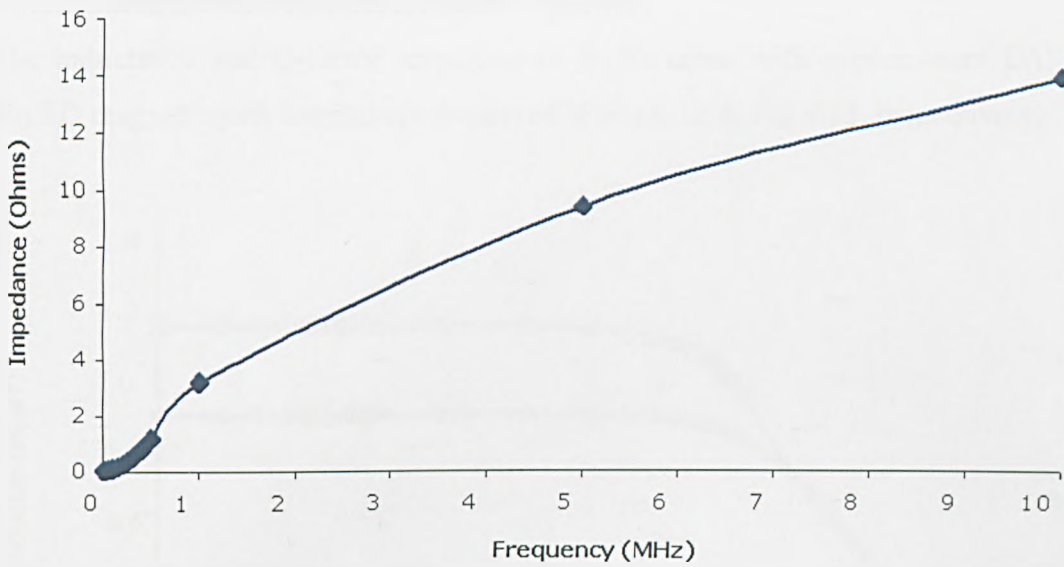


Figure 8.10 Impedance vs. frequency for the solenoid microinductor with NiFe core.

The Q-factor of the electrodeposited and commercial alloys is displayed in Fig 8.11. The maximum Q-factors of the electrodeposited alloys occurred in the 500 kHz-1MHz frequency range indicating that the thin film dimensions are acceptable for operation within this range. The Q-factor response of the commercial alloy demonstrates the susceptibility of this particular film to skin depth effects. The high Q-factor in the low frequency range is greatly reduced at 1 MHz in comparison with the CoFeCu film.

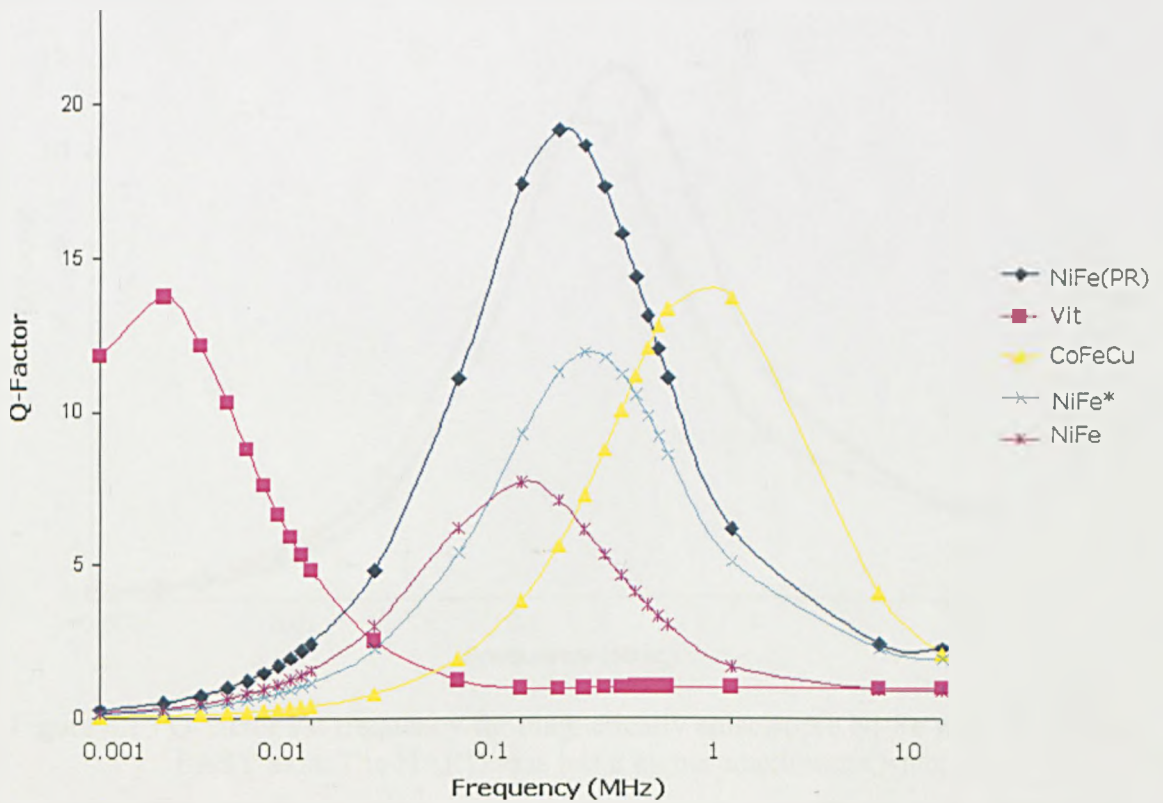


Figure 8.11 Q-Factor vs. frequency for commercial and electrodeposit alloys.



### 8.3.1.3 Solenoid microinductor: anisotropic test

The inductance and Q-factor responses of Ni-Fe cores with predominant EASY and HARD magnetic path lengths are displayed in Fig 8.12 & Fig 8.13, respectively.

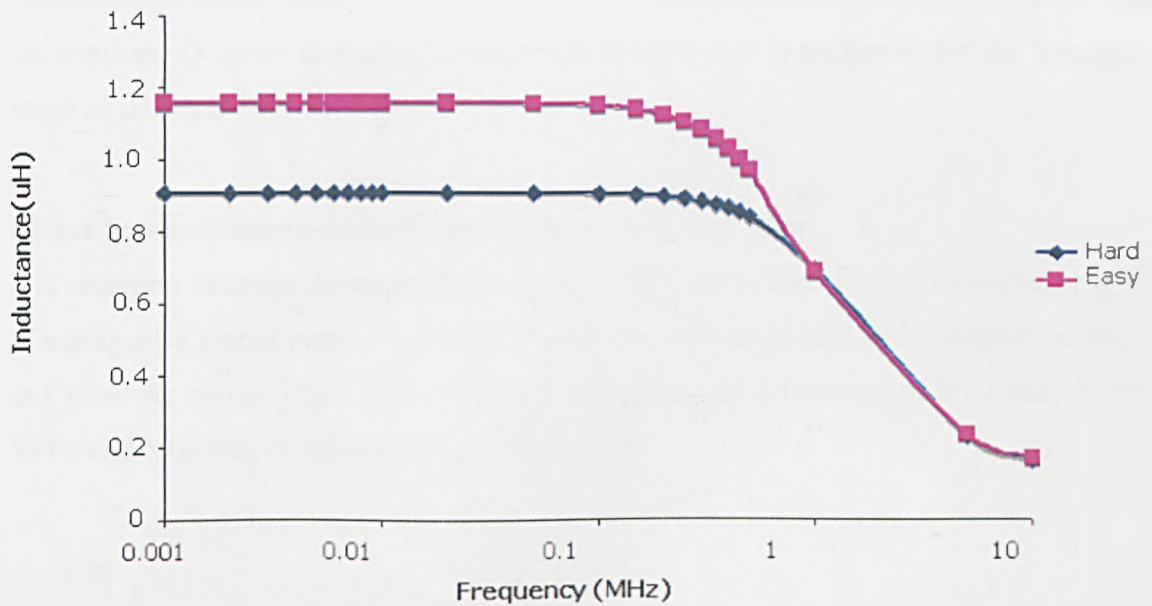


Figure 8.12 Inductance vs. frequency for magnetically anisotropic Ni-Fe with HARD and EASY axes. The reduction of  $L_{DC}$  at 1MHz for the HARD axis is 23%, whereas the EASY axis has a 40% reduction.

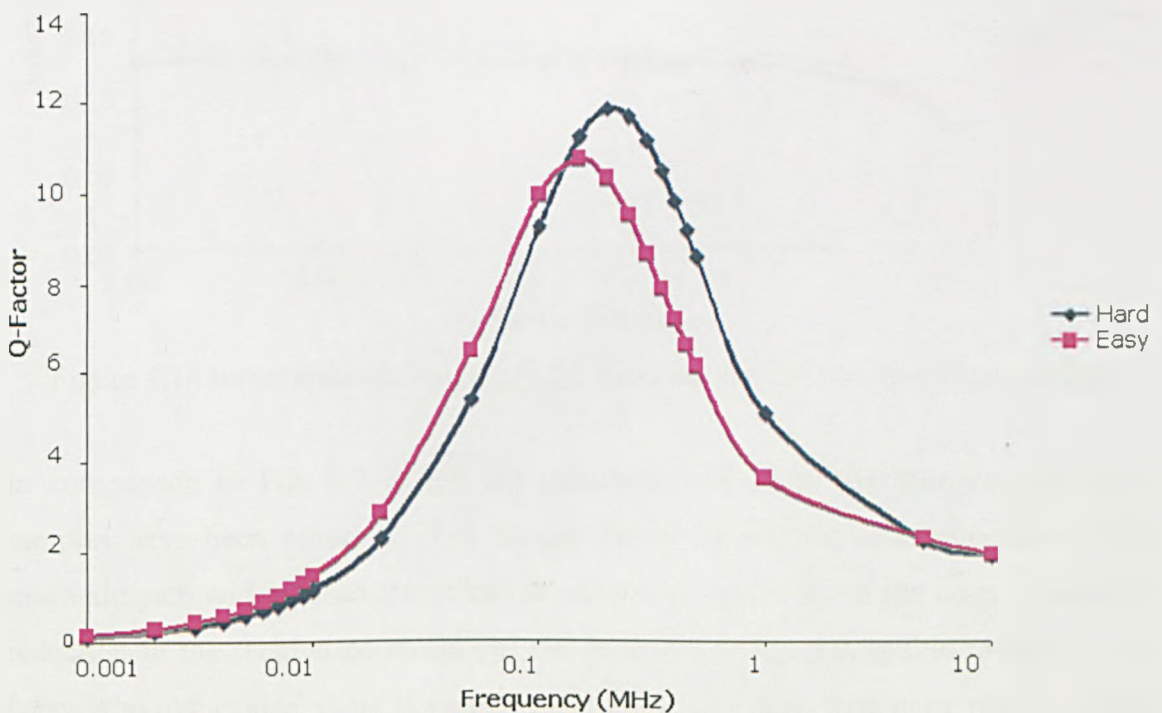


Figure 8.13 Q-factor vs. frequency for magnetically anisotropic Ni-Fe with HARD and EASY axis. The HARD axis has a higher maximum Q-factor.



Components fabricated with the easy axis induced in the predominant length of the alloy exhibit increased inductance at lower frequency. However, the inductance tail-off occurs also at reduced frequency. It is hard for the large domains of the highly magnetised easy axis to rotate, while the small domains of the hard axis can rotate more easily at high frequencies. Thus, the inductance reduction at high frequency is less and the resultant Q-factor is higher. Hence, the HARD axis is preferred for the frequency range of interest.

### 8.3.1.4 Solenoid micro-inductor: air-gap & core area tests

It is common to integrate an air-gap into the flux path to increase the saturation current of a magnetic component. A 50 $\mu\text{m}$  air-gap was fabricated into core samples of Ni-Fe and Vitrovac cores. Fig 8.14 displays the inductance as a function of frequency for the Ni-Fe and Vitrovac components with an air-gap.

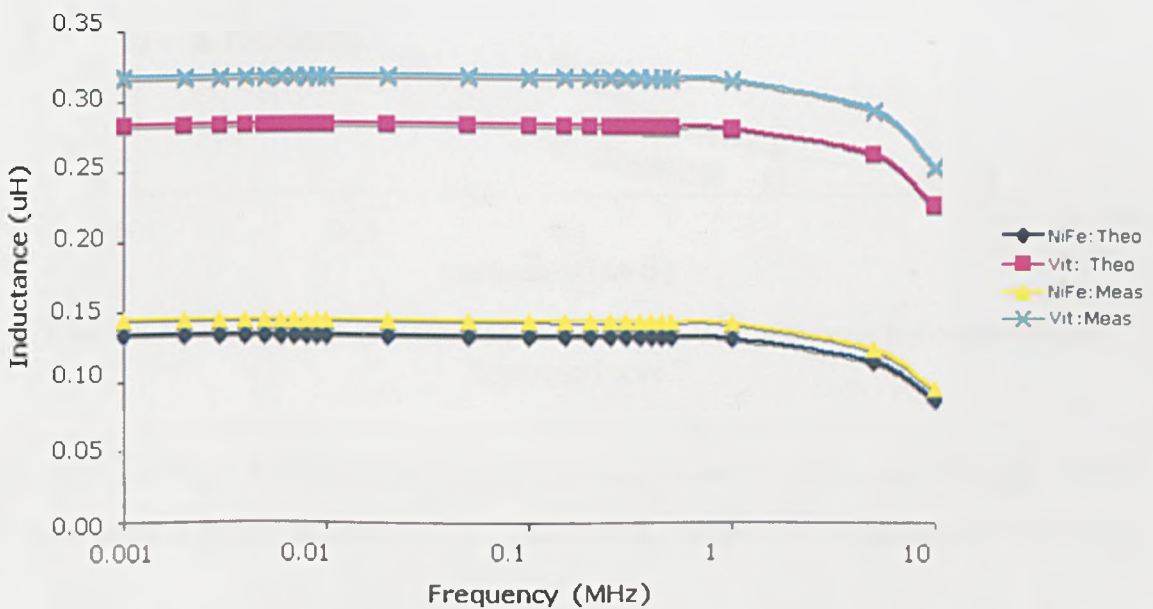


Figure 8.14 Inductance vs. frequency for Vitrovac and NiFe with a 50 $\mu\text{m}$  air-gap.

In comparison to Fig. 8.7 & 8.8 the inductance values of the Vitrovac and Ni-Fe samples have been reduced. The air-gap has increased the total reluctance of the magnetic path and reduced the effective relative permeability of the core. Due to the reduction in the relative permeability, the films are not as susceptible to skin effects, hence, the inductance value is maintained across a broader frequency range. This is clearly evident for the Vitrovac alloy. The difference between the experimental values and analytical values is attributed to fringing field effects. Fringing flux at the air-gap reduces the effective length of the air-gap, thereby, increasing the overall inductance.

The effects of fringing flux are examined in detail in Chapter 9 with models developed in ANSYS.

The influence of the core area was assessed with Ni-Fe and Vitrovac components assembled with 3 laminate layers. A similar analysis is performed with ANSYS in Chapter 9. Fig 8.15 and Fig 8.16 show the inductance versus frequency values for the Vitrovac and Ni-Fe laminated core layers, respectively.

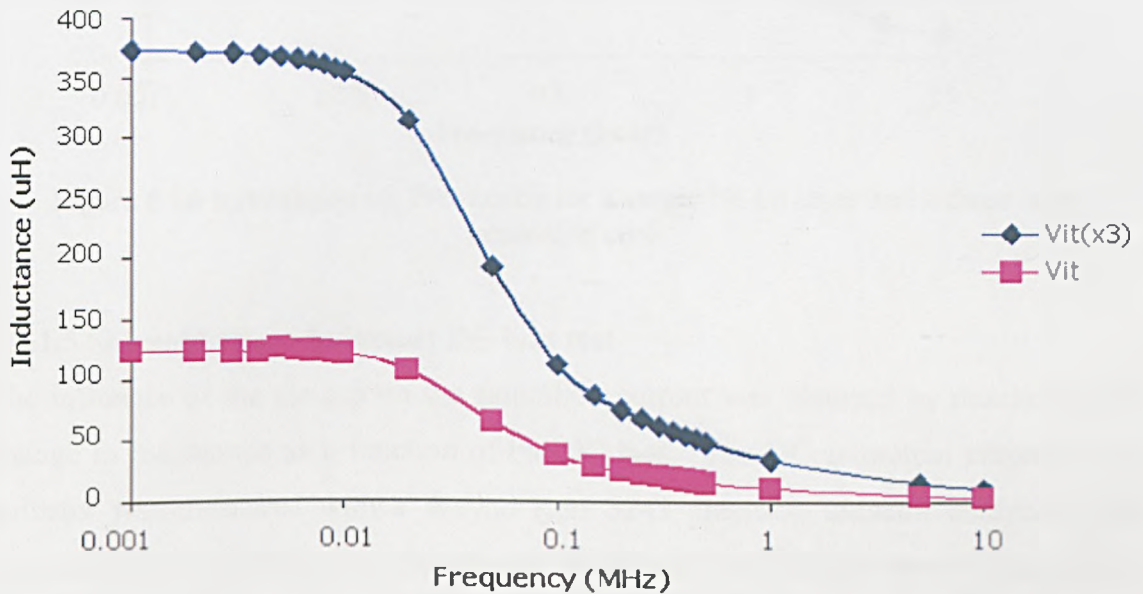


Figure 8.15 Inductance vs. frequency for a single Vitrovac layer and a three-layer laminated core.

Fig 8.15 and Fig 8.16 display an increase in inductance for both core materials. This is in agreement with the fundamental DC inductance equation as presented in Chapter 6.

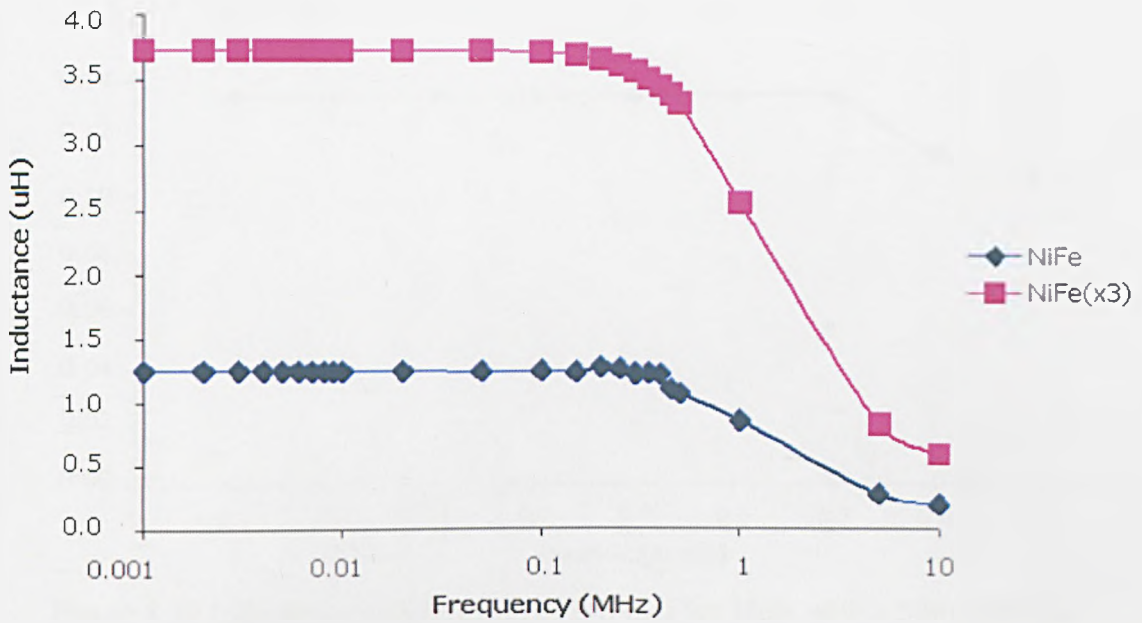


Figure 8.16 Inductance vs. Frequency for a single Ni-Fe layer and a three layer laminated core.

### 8.3.1.5 Solenoid micro-inductor: DC bias test

The influence of the air-gap on the saturation current was assessed by monitoring the change in inductance as a function of the DC bias. The DC saturation current of the inductor was measured with a Wayne Kerr 3245 precision inductor analyzer. The saturation current is defined as the current that results in a 20% reduction of  $L_{DC}$  prior to the applied current. Fig 8.17 and Fig 8.18 display the results of the DC bias test on the Ni-Fe core with and without an air-gap, respectively. Both cores exhibit a similar trend in inductance tail-off, however, the saturation current of the inductor with an air-gap is 9 times greater than the closed magnetic core. To obtain the saturation current for the air-gap component conventional wire wound windings were used. The maximum current to be applied to the 90 $\mu$ m thick windings, in accordance with a current density of 10A/mm<sup>2</sup>, is 180mA.



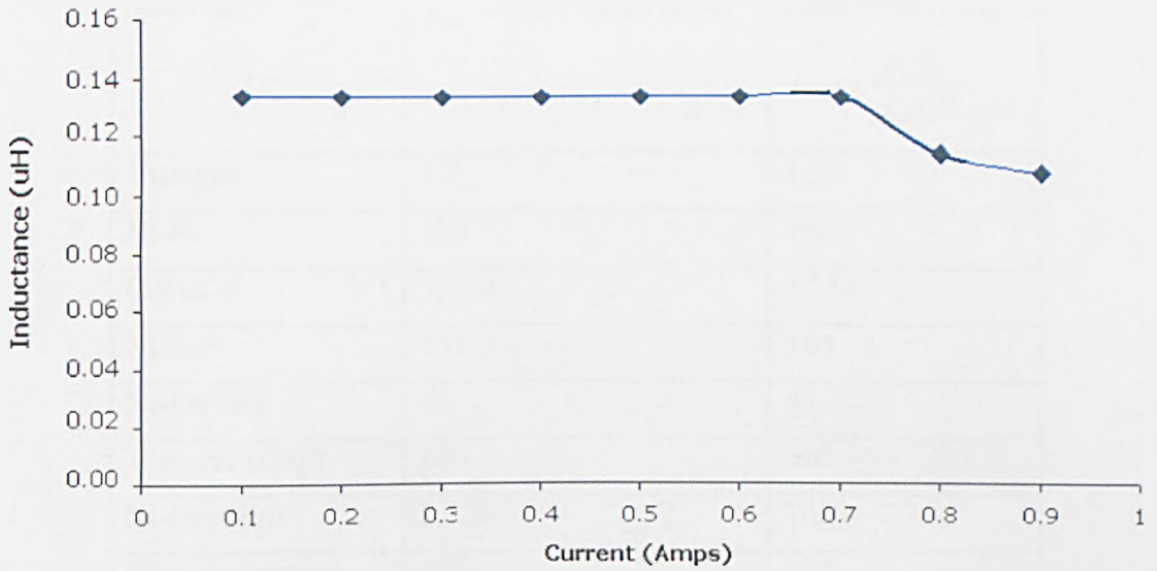


Figure 8.17 Inductance as a function of DC bias for NiFe with a 50μm air-gap.

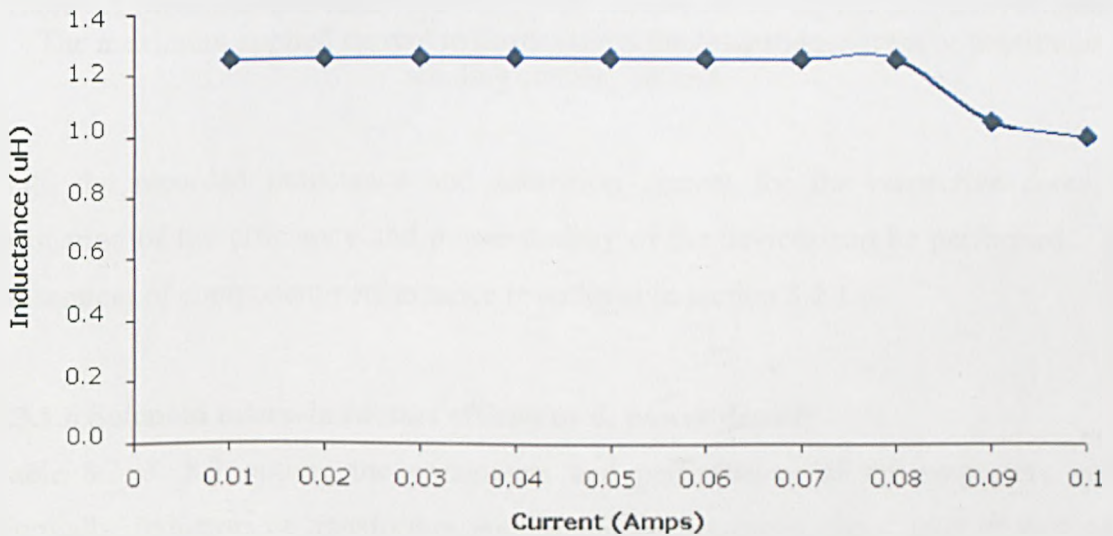


Figure 8.18 Inductance as a function of DC bias for NiFe with a closed magnetic path.

The results of the air-gap component indicate three general trends: the larger the air-gap (1) the greater the saturation current, (2) the lower the inductance and (3) the greater the frequency ranges of constant inductance. Table 8.1 displays the theoretical and measured values of saturation current for the various core materials.

Material	$I_{sat}$ Experimental (mA)	Analytical (mA) $I_{sat} = \frac{B_{sat} l_c}{\mu_o \mu_r N}$
Vitrovac	1.3	1.3
Ni-Fe	100	106
CoFeCu	1,110	1,230
Ni-Fe*	137	140
Ni-Fe(PR)	66	67
Vitrovac (Gap)	600	602
Ni-Fe (Gap)	1,000	1069
Ni-Fe(laminated)	100	106
Vitrovac(laminated)	1.32	1.32

Table 8.1 Measured and analytical saturation current values for the alloys investigated. The maximum applied current to the device is the saturation current or maximum winding current, 180mA.

With the recorded inductance and saturation current for the respective cores, an estimation of the efficiency and power density of the devices can be performed. The assessment of component performance is outlined in section 8.2.1.6.

### 8.3.1.6 Solenoid micro-inductor: efficiency & power density

Table 8.2 & 8.3 outline the parameters and performance of the respective cores. Normally, inductors or transformer are designed to support a given level of voltage in power conversion. However, in this thesis, it is the material that is being assessed so after selecting a frequency the only unknown parameter of Eq(8.2) is the voltage,  $V$ :

$$V = KfNB_{sat}A_c \quad (8.2)$$

Where  $f$  is the operating frequency, which is set at 250 kHz and 500 kHz,  $B_{sat}$  is the saturation flux density,  $K$  is the waveform factor which is equal to 4.44 for sinusoidal waveform and  $A_c$  is the core cross-sectional area. With the applied voltage and current selected for maximum flux density the component is assessed from a material, as opposed to application, perspective for maximum power density at both frequencies.

In reference to Tables 8.1 & 8.2, the single layer and laminate layer of the Vitrovac core is not suitable at the assessed frequencies. The low saturation current as a result of the low flux density and very high relative permeability, results in a low output power that is less than the dissipated eddy current power loss. Therefore, the material cannot be used within the solenoid micro-inductor for operation in the selected frequency range.

The Vitrovac sample with the inclusion of a 50 $\mu$ m air gap, which is less than 0.5% of the overall magnetic path length, increases the permissible applied current. The air-gap also produces a minor reduction in eddy current power loss by interrupting the path of the eddy currents. The hysteresis loss remains very small due to the low coercivity of the film. The overall result is an increase in output power far greater than the increase in winding power loss due to the increase in applied current. The component now exhibits the highest efficiency and the second highest power density at both frequencies.

The Ni-Fe(DC) sample has a reduced efficiency of 85% at 250KHz and 78% at 500 kHz, but witnesses an increase in power density of 4 and 7.8W/cc, respectively. The anisotropic alloy with a reduced effective relative permeability has an increase in applied current. The reduction in coercivity also reduces the hysteresis power loss. In comparison the performance of the Ni-Fe\* alloy is 88% (6W/cc) and 82% (11.3W/cc). Magnetic field annealing of Ni-Fe has therefore produced an increase in component efficiency and power density.



Parameter	NiFe	NiFe*	Vit	NiFe (PR)	CoFeCu	NiFe (x3)	Vit (x3)	NiFe (Gap)	Vit (Gap)
Isat(mA)	100	137	1.32	66	180	100	1.32	180	180
L( $\mu$ H)	1.25	0.9	22	1.96	0.3	3.26	66.91	0.14	0.31
$V_{IN}$	0.146	0.146	0.183	0.142	0.256	0.43	0.54	0.146	0.183
Pout (mW)	14	20	0.24	9.37	46	43	0.7	26	32.9
Peddy (mW)	1.80	1.80	0.8	0.7	6.5	5.42	2.6	1.80	0.8
Phys (mW)	0.09	0.01	0.01	0.04	0.05	.297	0.03	0.09	0.01
Pcu (mW)	0.5	0.93	0.00008	0.21	1.62	0.5	0.00008	1.62	1.62
Efficiency (%)	85	88	X	90	85	87	X	88	93
Power density (W/cm <sup>3</sup> )	4	6	X	3	13	13	X	8	10

Table 8.2 Power density and efficiency of electrodeposited and commercial alloys at 250 kHz. The applied current of the CoFeCu is limited by the winding current density.

Parameter	NiFe	NiFe*	Vit	NiFe (PR)	CoFeCu	NiFe (x3)	Vit (x3)	NiFe (Gap)	Vit (Gap)
Isat(mA)	100	137	1.32	66	180	100	1.32	180	180
L( $\mu$ H)	1.07	0.86	15.5	1.87	0.28	3.32	47.8	0.14	0.31
$V_{IN}$	0.29	0.29	0.36	0.28	0.51	0.879	1.09	0.29	0.36
Pout (mW)	29	40	0.47	18.48	91.8	87.9	1.43	52	64.8
Peddy (mW)	7.23	7.23	3.47	2.86	24.6	21.69	10.41	7.20	3.46
Phys (mW)	0.198	0.03	0.02	0.08	0.11	0.59	0.07	0.197	0.02
Pcu (mW)	0.5	0.9	0.00008	0.21	1.62	0.5	0.00008	1.62	1.62
Efficiency (%)	78	82	X	85	77	79	X	85	92
Power Density (W/cm <sup>3</sup> )	7.8	11.3	X	5.46	24.7	24.17	X	15.3	20.8

Table 8.3 Power density and efficiency of electrodeposited and commercial alloys at 500 kHz. The applied current of the CoFeCu is limited by the winding current density.

The increase in resistivity of the Ni-Fe(PR) to  $48\mu\Omega\cdot\text{cm}$  reduces the eddy current power loss in comparison to the Ni-Fe(DC) sample with  $\rho=20\mu\Omega\cdot\text{cm}$ . The reduced coercivity results in a reduction of hysteresis power loss. However the increase in relative permeability and minor reduction in  $B_{sat}$  reduces the saturation current. As a result the winding power loss also decreases. The Ni-Fe(PR) is more efficient, 90-85%, but has smaller power density, 3-5.46W/cc.

The CoFeCu alloy with  $B_{sat}$  of 1.4T has the highest saturation current. This cannot be fully exploited due to the dimensions of the winding. The increase in applied voltage results in the highest power density at both frequencies. The component has acceptable hysteresis and winding loss in comparison to the other components. However, with the lowest resistivity,  $18\mu\Omega\cdot\text{cm}$ , a high eddy current power loss is incurred. For similar efficiencies and power densities, 3 layers of Ni-Fe are the equivalent to 1 CoFeCu layer.

With increasing frequency the components with the higher efficiency but smaller power density would overcome their competitors with higher power density but reduced efficiency. Lower efficiency may be tolerated in specific applications when gains in weight, size reduction, power density are highly beneficial. A profile of the power loss contributions at 250 kHz and 500 kHz are displayed in Fig 8.19 and Fig 8.20.

Fig 8.19 & 8.20 indicate that eddy current power loss is the main loss mechanism at both of the frequencies. The eddy current power loss contribution increases in all of the tested alloys. A reduction in efficiency for all of the components follows the increase in frequency. Hence, eddy current power loss is the main loss mechanism to control in order to realise a highly efficient high power density device at frequencies greater than 500 kHz.

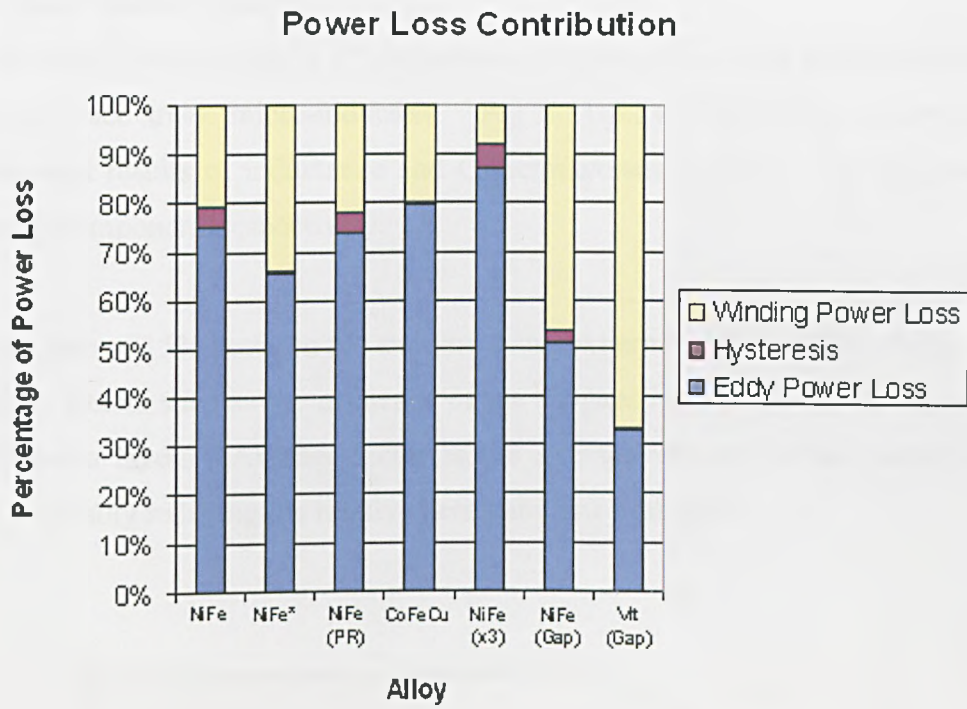


Figure 8.19 Contribution of power loss mechanisms at 250 kHz.

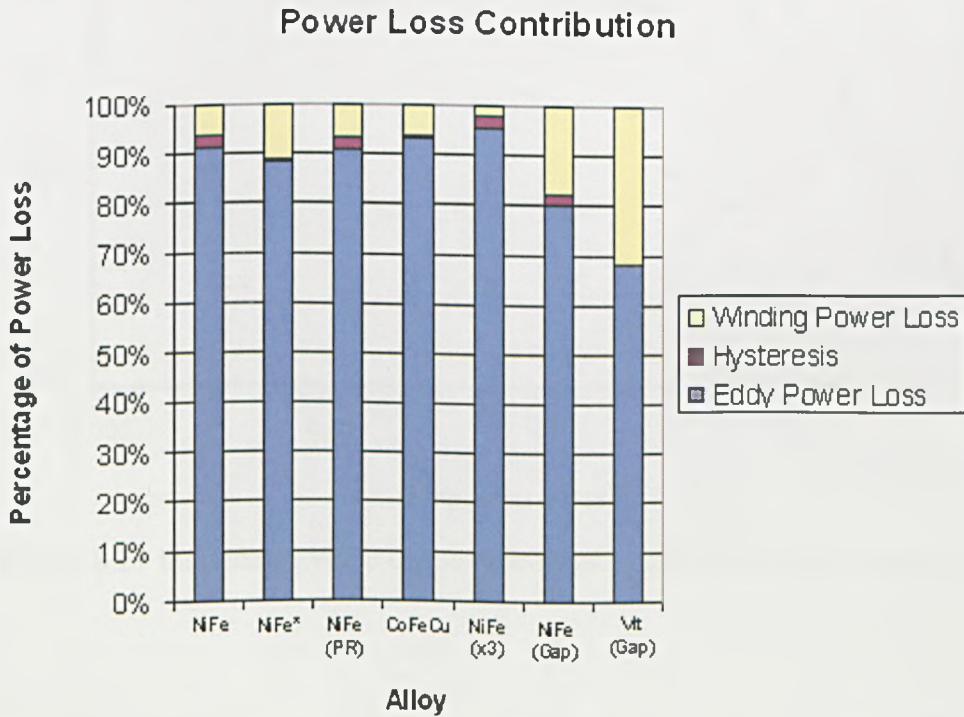


Figure 8.20 Contribution of power loss mechanisms at 500 kHz.

#### 8.4 Pot-core micro-inductor

The Hewlett Packard 4192A LF-impedance analyser was used to characterise the spiral and race track micro-inductors. Fig 8.21-8.24 displays the analytical and experimental results of inductance and Q-factor versus frequency for the race-track and spiral component, respectively.

The variation of 15% between the analytical and experimental results is attributed to a variety of factors such as the influence of the air-gaps introduced by the Kapton film and adhesive layers. Another factor is the stresses induced in the magnetic film during assembly reducing the relative permeability of the film.

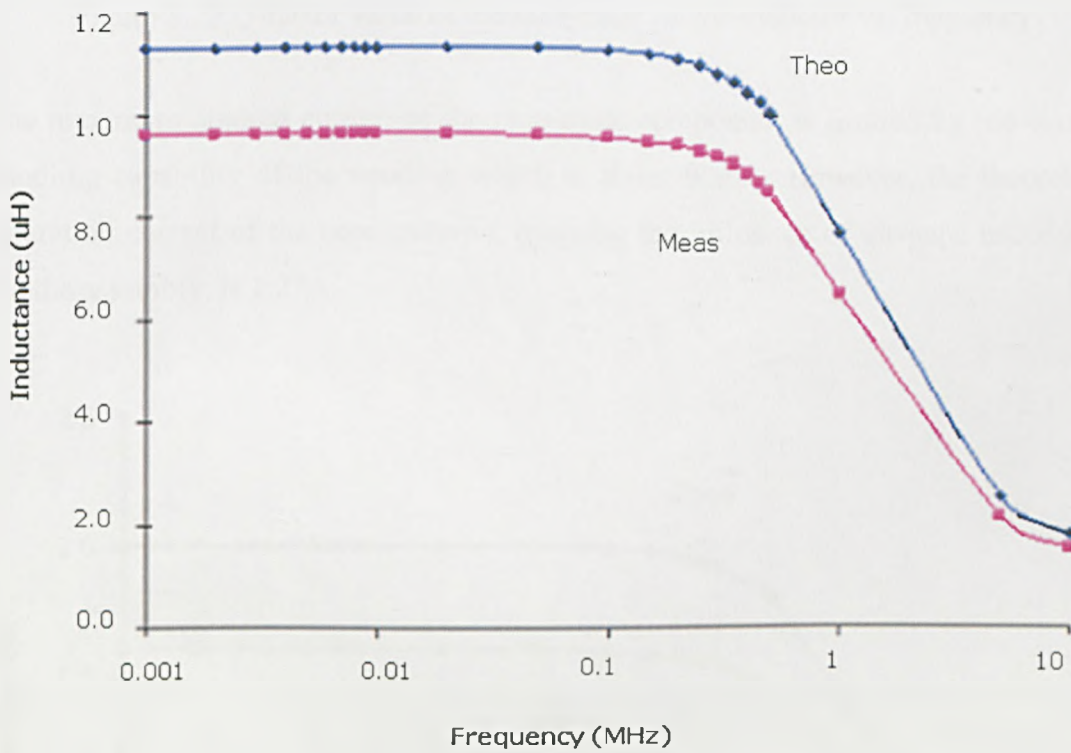


Figure 8.21 Inductance value of the race-track micro-inductor vs. frequency

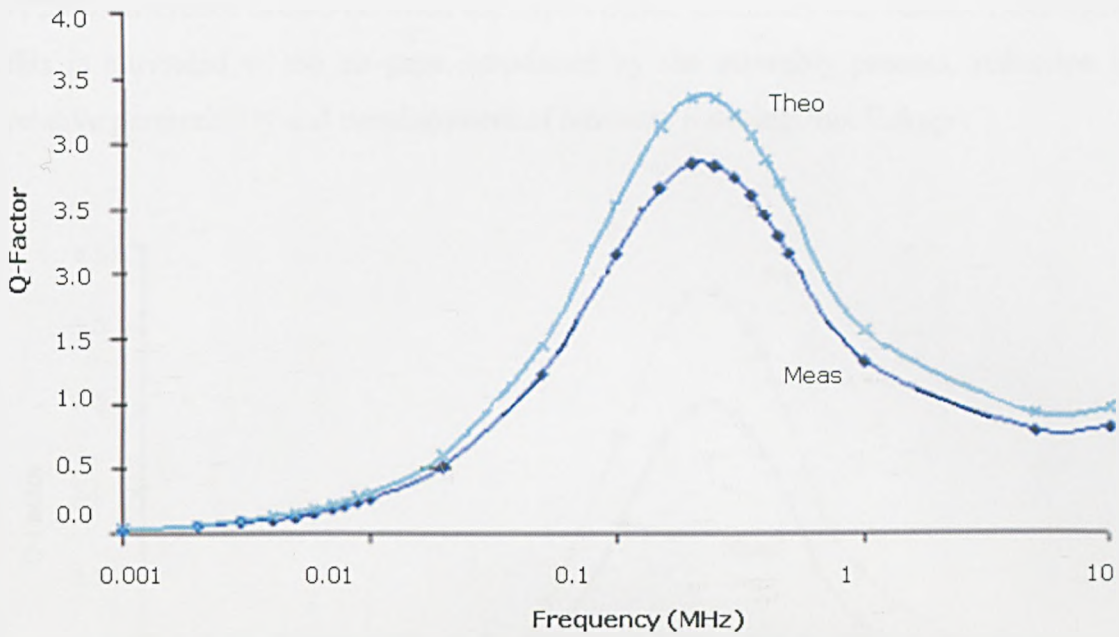


Figure 8.22 Q-factor value of the race-track micro-inductor vs. frequency

The maximum applied current of the race-track component is limited by the current handling capability of the winding which is about 90mA. However, the theoretical saturation current of the core material, omitting the influence of air-gaps introduced via the assembly, is 1.27A.

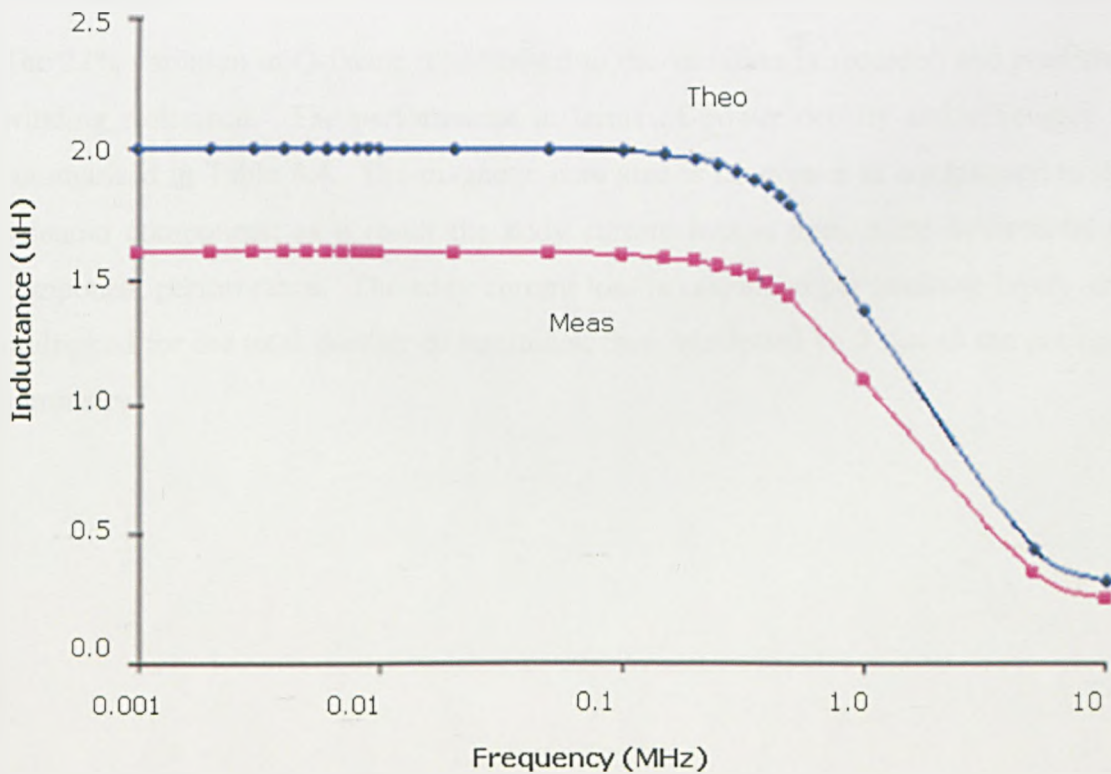


Figure 8.23 Value of the inductance for the spiral micro-inductor vs. frequency



A 20% difference occurs between the experimental and analytical results. Once again this is attributed to the air-gaps introduced by the assembly process, reduction in relative permeability and misalignment of laminate reducing flux linkage.

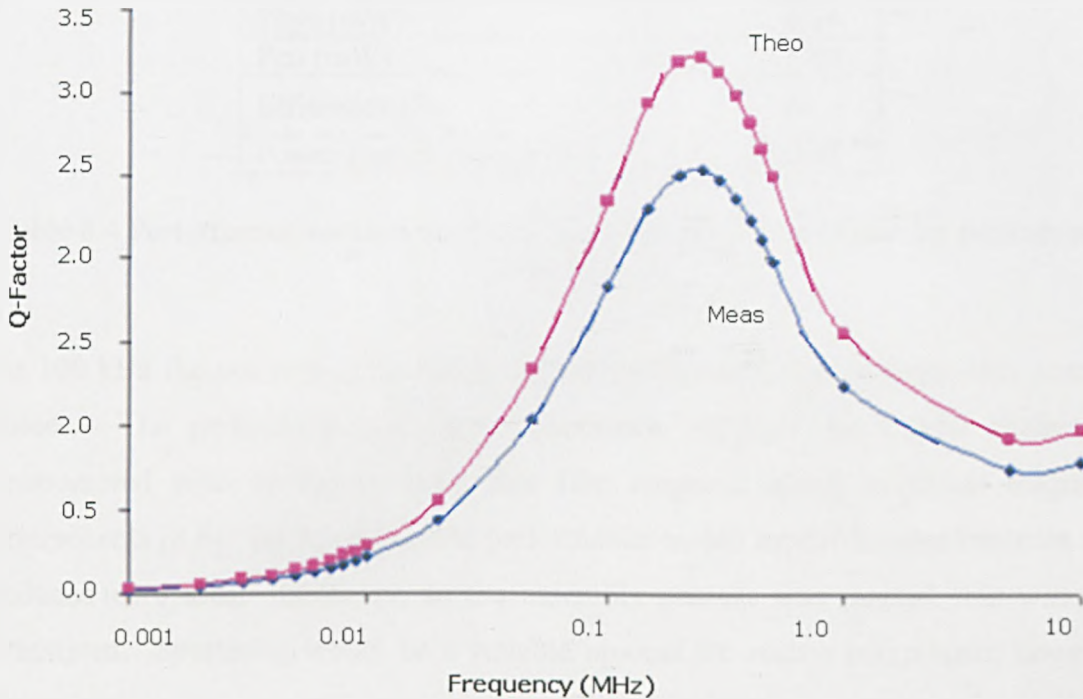


Figure 8.24 Values of the Q-factor of a spiral micro-inductor vs. Frequency.

The 22% variation in Q-factor is attributed to the variation in recorded and predicted winding resistance. The performance in terms of power density and efficiency is summarised in Table 8.4. The magnetic core area is far greater in comparison to the solenoid component; as a result the eddy current loss is even more detrimental to component performance. The eddy current loss is calculated per laminate layer, then multiplied for the total number of laminates, then multiplied by 2 due to the pot-core symmetry.



Parameter	RaceTrack	Spiral
Isat(mA)	90	90
L( $\mu$ H)	0.96	1.59
$V_{IN}$	0.31	0.59
Pout (mW)	27.9	53.1
Peddy (mW)	15.79	22.1
Phys (mW)	4.32	6.04
Pcu (mW)	1.88	1.88
Efficiency (%)	55	63
Power Density (W/cm <sup>3</sup> )	1.1	0.96

Table 8.4 Performance values of the race-track and spiral micro-inductor performance at 50 KHz.

At 100 kHz the pot-core components operate inefficiently due to large eddy current losses. The performance of these components highlight the typical challenges encountered when trying to apply thin film magnetic alloys to power magnetic components [8.6]. Improvements in performance would require thinner laminate and reduced core area. However, as the assembly process was manual this was not attempted. Sputtering would be a suitable process for such a component; however delamination and sidewall coverage would be a problem. Sullivan et al partially melted photoresist posts to create a slant to allow closure of lower and upper core layers [8.7]. Repeatability and temperature effects on the alloy could be recurrent problems. These components were consequently not developed further.

### 8.5 Pot-core micro-transformer

The micro-transformer was characterised with a short circuit and open circuit test [8.8]. The open circuit test gives the core resistance,  $R_c$ , and reactance,  $X_c$ . This test is performed by applying rated voltage to the primary side and leaving the secondary side open. Either winding side may be used. This test assumes that shunt impedances ( $R_c$  and  $X_c$ ) are much larger than the series impedances of the windings. Fig 8.25 and 8.26 display the measured and analytical open circuit inductance and core resistance.

In Fig 8.25 the analytical model of the inductance includes air-gaps. However due to the manual assembly there is a variance between predicted and actual adhesive/dielectric layer thickness in the magnetic path. Another factor could be the reduction of permeability due to stresses incurred in the assembly. The inductance

begins to decrease at 0.5 MHz, which is mainly due to the frequency characteristics of electroplated permalloy.

Fig 8.26 displays the core resistance values. The difference between the measured and analytical values is minimal. This difference could be attributed to hysteresis resistance which is omitted in the model, or leakage flux inducing eddy currents within the windings.

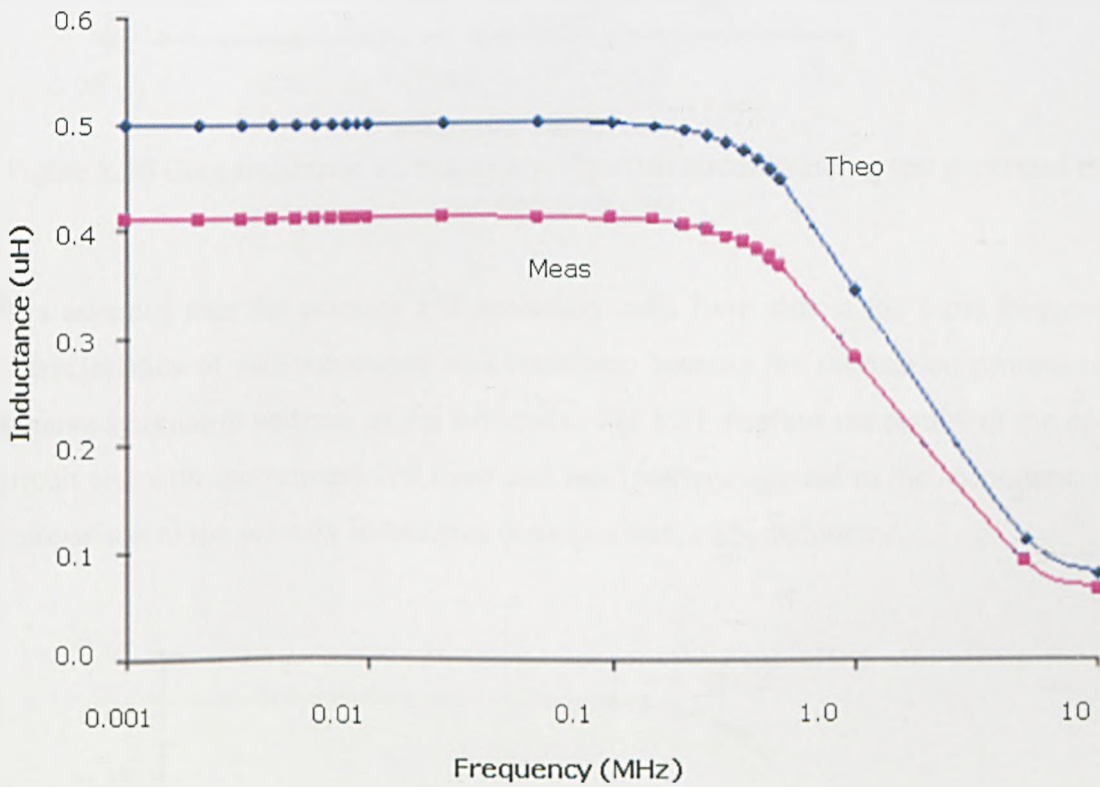


Figure 8.25 Inductance vs. frequency of primary windings. An open circuit winding test generated the measured results.

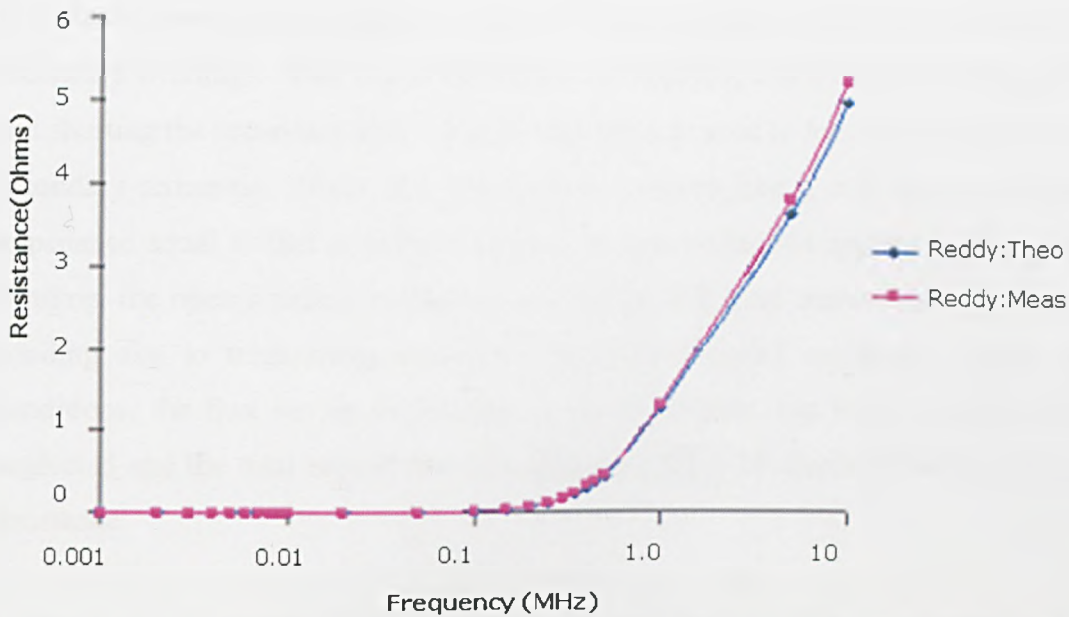


Figure 8.26 Core resistance vs. frequency. An open circuit winding test generated the measured results.

It is assumed that the primary and secondary coils have almost the same frequency characteristics of self-inductance and resistance because the fabrication process can achieve symmetric patterns of the two coils. Fig 8.27 displays the results of the open circuit test with the primary left open and rated voltage applied to the secondary. In comparison to the primary inductance there is a minor 6% difference.

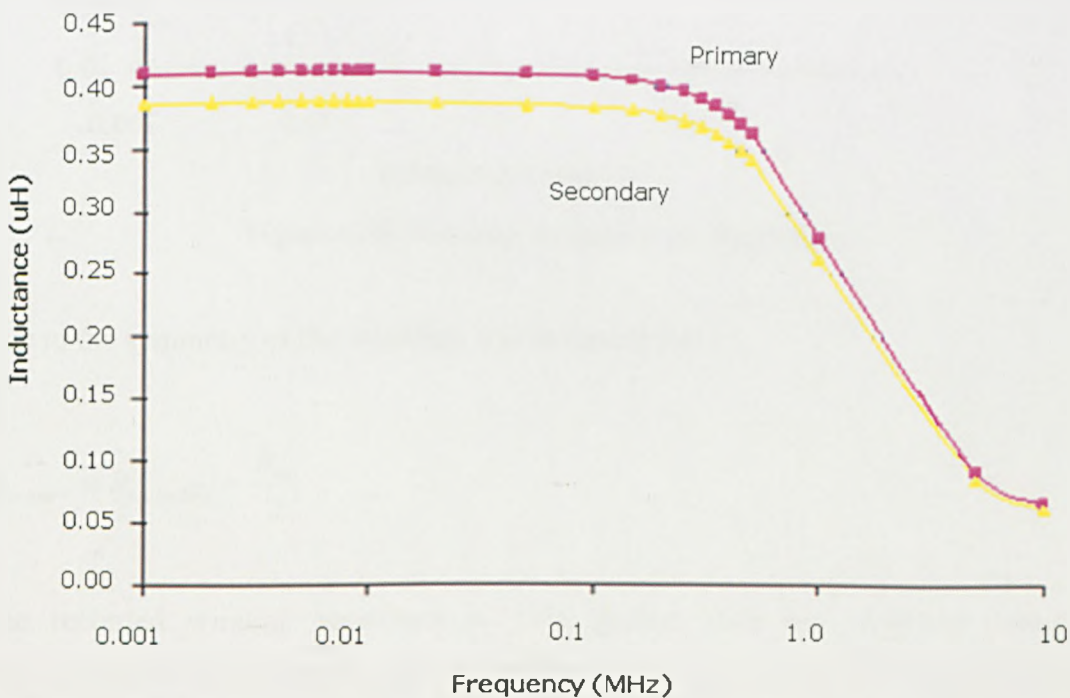


Figure 8.27 Inductance vs. frequency of secondary windings. An open circuit winding test generated the measured results.

The short circuit test provides the resistance and reactance value of the primary and secondary windings. This test is performed by applying rated current to the primary and shorting the secondary side. A gold wire bond is used to form the short across the secondary terminals. Thus, the transformer behaves like a coil having a leakage impedance equal to that of both windings. A low voltage is applied to the primary winding, the open winding, sufficient to circulate full load current through the open winding due to transformer action in the short-circuited winding. Under these conditions, the flux set up in the core is so small that iron losses can usually be neglected and the total copper loss is measured. Fig 8.28 displays the total winding resistance.

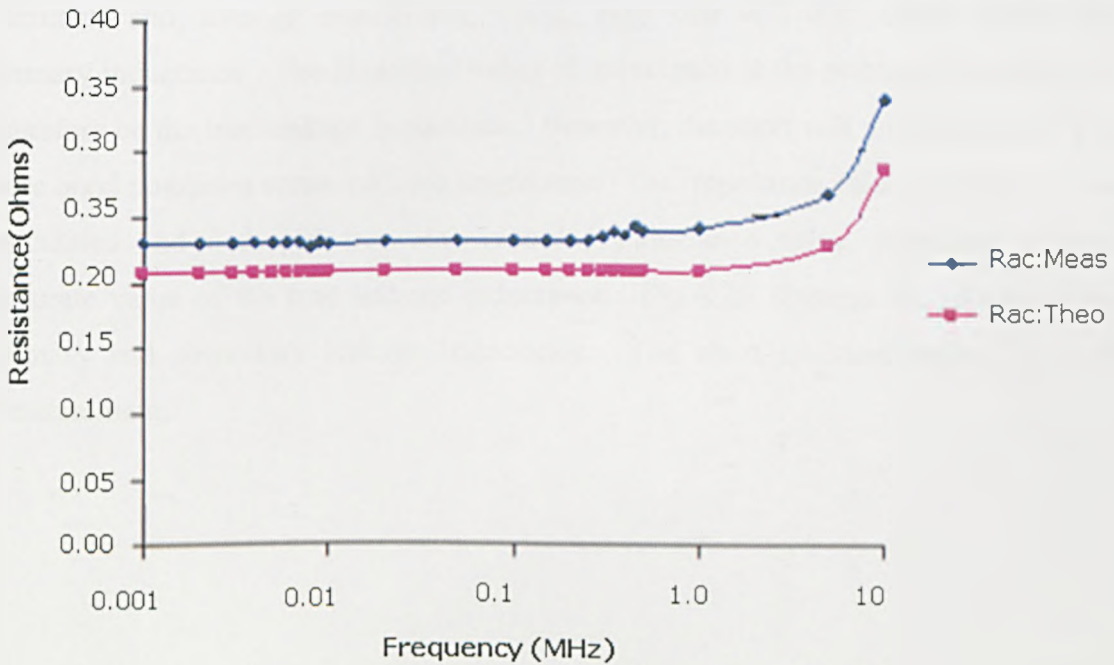


Figure 8.28 Winding resistance vs. frequency.

Due to the symmetry of the windings it is assumed that:

$$R_{primary} = R_{secondary} = \frac{R_{ac}}{2}$$

The recorded winding resistance is 11% greater than the analytical value at frequencies less than 30kHz and this difference increases up to 18% above 30kHz. The dimensions of the windings are precisely controlled and measured prior to

component testing. Therefore, the difference between analytical and measured values is attributed to stray flux inducing eddy currents within the windings. The magnetic core flux path is perpendicular to the windings when the flux gets from the top magnetic layer to the bottom magnetic layer. Therefore, it is assumed that naturally occurring leakage flux and leakage flux due to the misalignment of the laminate layers in this perpendicular direction produce an increase in eddy current resistance within the windings.

The inductance recorded in Fig 8.27 contains the primary inductance and leakage inductance. Leakage inductance cannot be measured directly. By applying a perfect short circuit across the secondary terminals there will be zero volt across the output terminals and, through transformer action, zero volt will also appear across the primary inductance. The measured value of inductance at the primary terminals will therefore be the true leakage inductance. However, the short will not be perfect. The wire bond possesses some intrinsic impedance. The impedance value of the short was calculated and deducted from the recorded inductance value, providing a more accurate value of the true leakage inductance. Fig 8.29 displays the results of the primary and secondary leakage inductance. The short is interchanged for each measurement.



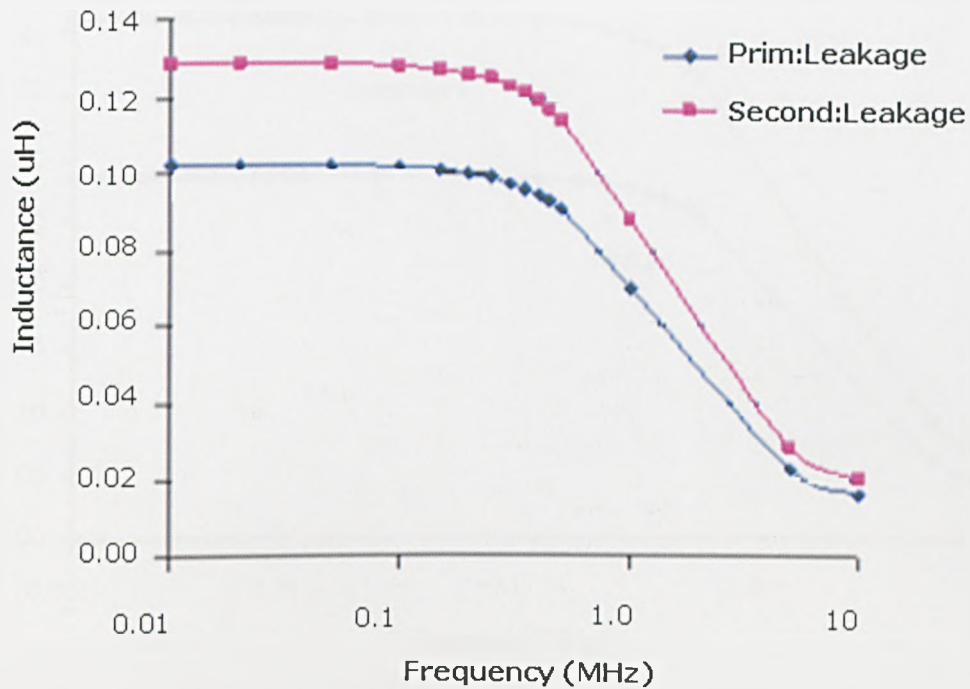


Figure 8.29 Primary and secondary winding leakage inductance vs. frequency.

Another approach to record the leakage inductance uses the open circuit test to record the mutual inductance of the transformer. A primary and secondary terminal with the same polarity is connected and inductance measured, and a primary and secondary terminal with opposite polarity is connected and inductance measured. Fig 8.30 displays the values recorded for mutual inductance.



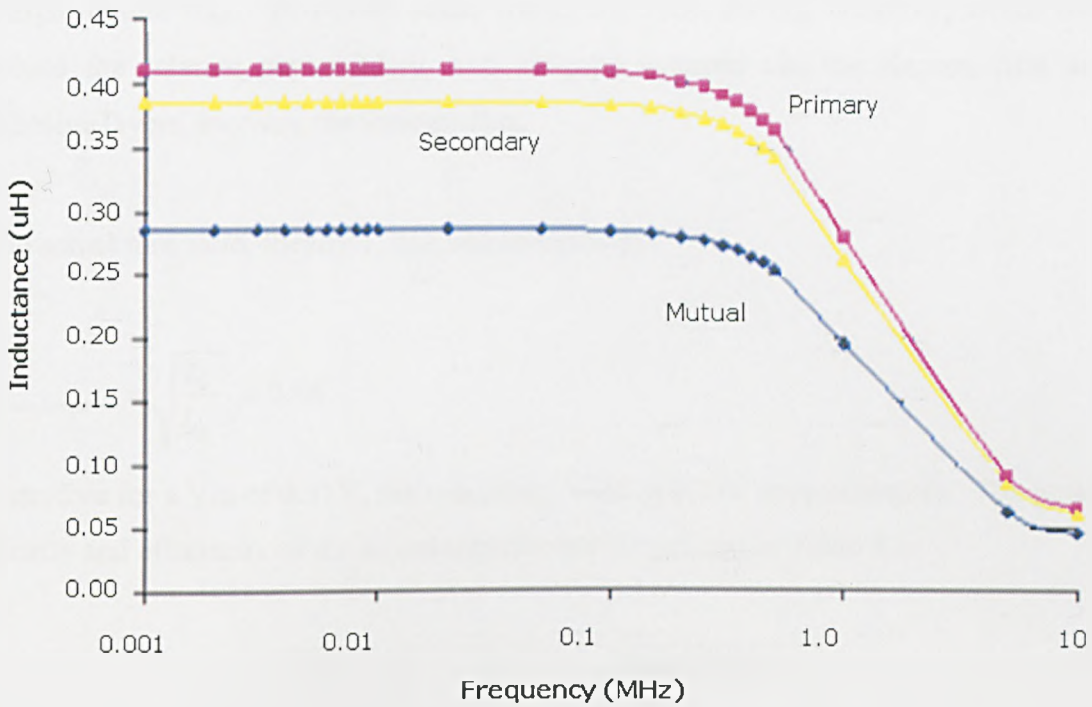


Figure 8.30 Mutual inductance vs. frequency. The mutual inductance is determined by measuring the inductance when the transformer primary and secondary are connected in the same and opposite polarity.

With the measured inductance the coupling factor at no load can be determined;

$$k = \frac{M_L}{\sqrt{L_p L_s}} = 0.72$$

With equal turns and core area the leakage inductance is approximately even for each winding. Therefore, the primary and secondary leakage inductance at 1MHz is, approximately;

$$L_{leakage} = (1 - k) \times L_{primary} = 0.11 \mu H$$

There is only a minor, approximately 10%, difference between this value and the leakage inductance value indicated by the short circuit test as shown in Fig 8.29. For most on-chip transformers,  $k$  is 0.3 to 0.9, due to the leakage of magnetic flux [8.8]. Liakopoulos and Ahn [8.9] showed that interleaved coils had a better transformer coupling constant. The high relative permeability of the permalloy should assist with

a high mutual flux. However, stress within the films during assembly, which may reduce the relative permeability, and air-gaps incurred via the Kapton film and adhesive layers, increase the leakage flux.

The actual turn ratio, ideally 1, can be estimated by:

$$V_{transformation} = \sqrt{\frac{L_s}{L_p}} = 0.96$$

Therefore for a  $V_{in}$  of 0.31V, the secondary  $V_{out}$  is 0.29V approximately. The power density and efficiency of the micro-transformer is outlined in Table 8.5.

Parameter	RaceTrack
$I_{out}(mA)$	86
$L(\mu H)$	0.96
$V_{OUT}$	0.29
$P_{out} (mW)$	25
$P_{eddy} (mW)$	15.79
$P_{phys} (mW)$	4.32
$P_{cu} (mW)$	0.73
Efficiency (%)	54
Power Density ( $W/cm^3$ )	0.36

Table 8.5 Power Density and efficiency of the micro-transformer at 50 kHz.

The power density and efficiency are not sufficient for applications within DC-DC converters. Optimisation is required to reduce the eddy current power loss and a reduction of component footprint. Another test that could have been performed but was not due to difficulties in connecting the load was, testing of the regulation.

## 8.6 Summary

The total AC resistance and total inductance are frequency dependent parameters because of the skin and proximity effects in the winding and the eddy currents in the core. The stray capacitance gives a negligibly small effect over the frequency range used, with values in the pico-farad region. The behaviour of the examined inductors

reveals that the effects due to the eddy currents in the core and to the turn-to-turn and turn-to-core stray capacitances become significant at high frequencies.

The inductance fall-off at higher frequencies is due to the cancellation flux generated by eddy currents and the dependence of the permeability of the alloys frequency.

The air-gap within the core of an inductor increases the value of the DC saturation current and improves the inductance at high operational frequencies as compared to an inductor with no air gap. This is because the effective permeability of the core maintains higher values at high frequencies although the relative permeability of the alloy decreases with frequency. Since the effective permeability of the core can be improved, a larger gap can also improve the inductance at high frequencies.

From these measurements, it is clear that the power handling capabilities and the efficiency of the micro-inductors and micro-transformers have to be improved. The main power loss mechanism in the frequency range of interest is eddy current power loss. Thinner laminate layers or an increase in resistivity whilst maintaining a moderate relative permeability, for example less than 1000, is required.

The solenoid component is a useful vehicle for examining the fabrication process and the potential of various core materials. The solenoid component is clearly more mass manufacturable and performs more favourably.

The following chapter develops a simple optimisation procedure. Components designed and tested to assess gains in power density and efficiency. Modelling is also used to verify some of the assumptions in the optimal design process.

## References

- [8.1] <http://www.buckleys.co.uk/holidayguide.htm>
- [8.2] D. J. Elliott, "Integrated Circuit Fabrication Technology," McGraw-Hill Book Company, page 72, 1982.
- [8.3] E.C. Snelling, "Soft Ferrites, Properties and Applications," Butterworths, 2<sup>nd</sup> edition, 1988.
- [8.4] Agilent Technologies, "Impedance Measurement Handbook", Dec. 2003.
- [8.5] D. H. Lloyd., MAG-100A Unitrode Magnetics Design Handbook, 1999.
- [8.6] C. R. Sullivan and S. R. Sanders. "Measured Performance of a High-Power-Density Microfabricated Transformer in a DC-DC Converter." IEEE Power Electronics Specialists Conference, pp. 287-294, June 1996.
- [8.7] Birchall and Stott, "Electrical principles for installation and craft students," McGraw-Hill, 1971.
- [8.8] T. M. Liakopoulos and C. H. Ahn, "Microfabricated toroidal-type planar inductors for MEMS and power electronic applications," Electrochem. Soc. Proc., vol. 98, no. 20, pp. 402–412, 1998.
- [8.9] H. Gan, "On-chip transformer modelling, characterisation and applications in power and low noise amplifiers," PhD thesis, Stanford University, March 2006.

## Chapter 9

### Modeling-based component optimisation

#### 9.1 Introduction

This chapter outlines a simplified optimization process of the solenoid micro-inductor. Models of magnetic components developed in ANSYS® v.10, are used to model the flux and current distribution within the magnetic components. Simulated results of the solenoid component are compared with experimental and analytical results from Chapter 8 in section 9.2. Section 9.3 investigates the influence of air-gaps on the performance of a theoretical 1-turn pot-core component. An optimisation procedure is then developed with reference to the solenoid components of Chapter 8 and analytical results are presented in section 9.4. The fabrication and characterisation of a prototype solenoid inductor with a laminate core is also presented within this section. Lastly, conclusions are presented based on the simulated, analytical and experimental data.

#### 9.2 Modeling of the solenoid micro-inductor

The work presented in sections 9.2 & 9.3 is the result of collaboration with Dr Hua Lu and Professor Chris Bailey of University of Greenwich. The focus of this section is to compare the simulated and experimental performance of the solenoid micro-inductor of Chapter 8, using core materials of electroformed  $Ni_{80}Fe_{20}$  and the commercial alloy, Vitrovac 6025.

The Finite Element (FE) computer modeling method was used to predict the magnetic field, the eddy losses and inductance of the manufactured micro-inductor. The model is shown in Fig. 9.1 [9.1]. The model is 3D but there is only one layer of element along the out-of-plane direction so the efficiency is close to a 2D model.

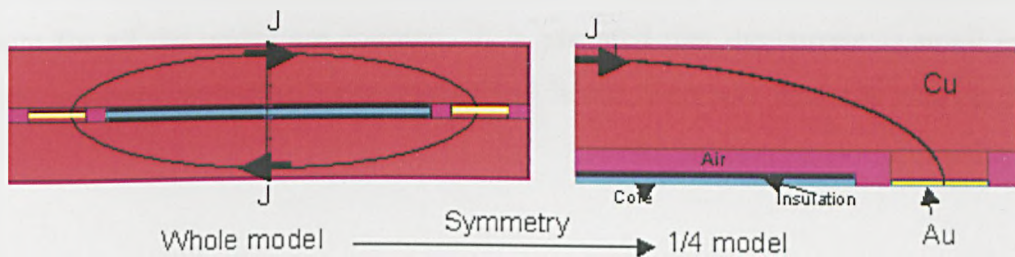
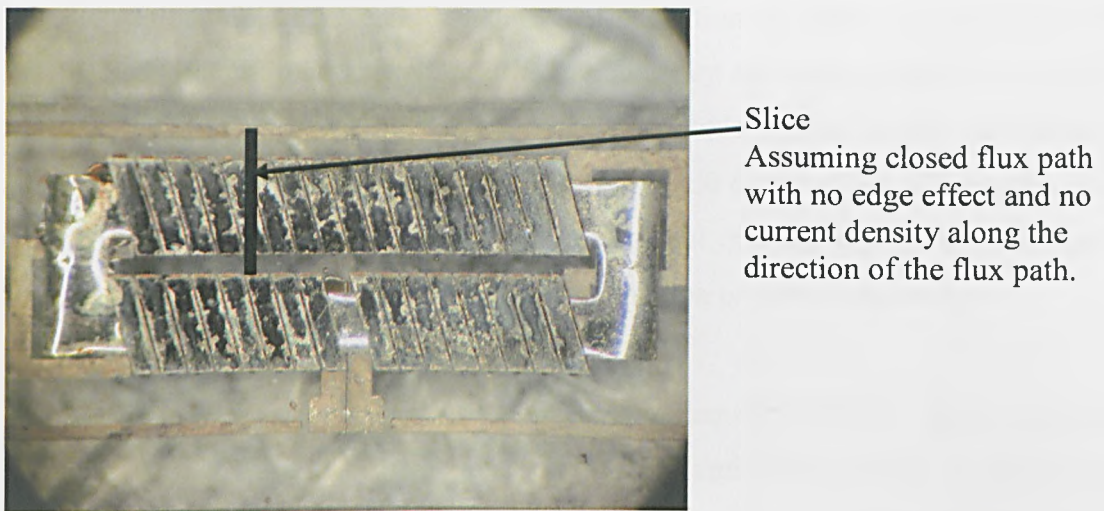


Figure 9.1 Computer model of the solenoid micro-inductor [9.1].

The dimensions, which are identical to the fabricated component, are listed in Table 9.1.

Parameter	Dimension ( $\mu\text{m}$ )
Winding Width	200
Number of Windings	33
Winding Thickness	90
Core Width	500
NiFe Core thickness	10
Vitrovac Core thickness	20

Table 9.1 Micro-Inductor model dimensions.

As with the experimental characterization the highest switching frequency is 10MHz. The low-frequency approximation electromagnetic theory is still valid because even at 10MHz the wave length (30m) in vacuum is still much greater than the dimensions of the inductor. When an AC current passes through the inductor the problem is transient



by nature, to model this phenomenon via transient analysis in the time domain is very time-consuming [9.1]. Instead, for sinusoidal excitation the harmonic analysis method can be used. In harmonic analysis all the variables are assumed to vary sinusoidally in time and all that needs to be solved is the amplitude of the electric and magnetic variables such as the current density and magnetic field distributions. Obviously, in real applications the waveforms are rarely sinusoidal but one can always assume that the sinusoidal wave is a term in the Fourier decomposition of the real waveform.

The 3D slice model was meshed using ANSYS element SOLID117. This element has the magnetic and the electrical degrees of freedom and eddy currents in the core and winding can be modeled. The load in this problem is the total current. It can be applied at a node on the conductor region of the symmetry planes where the voltage degrees of freedom for all the nodes are coupled. It is assumed that the current is small enough that the magnetic core does not saturate and linear harmonic analysis method can be used.

The key parameters of an inductor are the inductance and the losses. The latter can be represented by the resistance factor, loss tangent, or the Q-factor. The inductance per unit length,  $L$ , can be calculated by using its relationship with the magnetic energy and the applied electric current  $E = \frac{1}{2} LI^2$ , where  $E$  and  $I$  are the total energy per unit length and the effective value of the applied current respectively. The voltage drop over a unit length along the conductor has the complex form  $\tilde{U} = (U_r + iU_i)$  and it can be deduced from the ANSYS output of the time-integrated voltage. The voltage and the current can then be used to calculate the complex impedance  $\tilde{Z} = (Z_r + iZ_i)$  and the Q-factor  $Q = Z_i / Z_r$ . In this context, the value of  $Q$  is the reciprocal of the loss tangent and it characterizes the power loss of the inductor [9.2]. The Joule loss density can be defined as  $p = \text{Re} \left( \frac{1}{2\sigma} J_i J_i^* \right)$  where  $J_i$  is the complex current density. This quantity is available directly from the ANSYS' output variable, JHEAT.

The modeled magnetic field distribution and the electric current density distribution for the micro-inductor with  $Ni_{80}Fe_{20}$  core are shown in Fig. 9.2 & 9.3, respectively. It can be seen that at 1MHz, the induced current in the core begins to concentrate at the

surface and the magnetic field in the core centre is reduced in magnitude. In the copper conductor, proximity effect causes the current to concentrate more on the area close to the inner surface. These phenomena are expected because, at  $f=1\text{MHz}$ , the skin depths for  $Ni_{80}Fe_{20}$  and copper are about  $5\mu\text{m}$  and  $66\mu\text{m}$ , respectively.

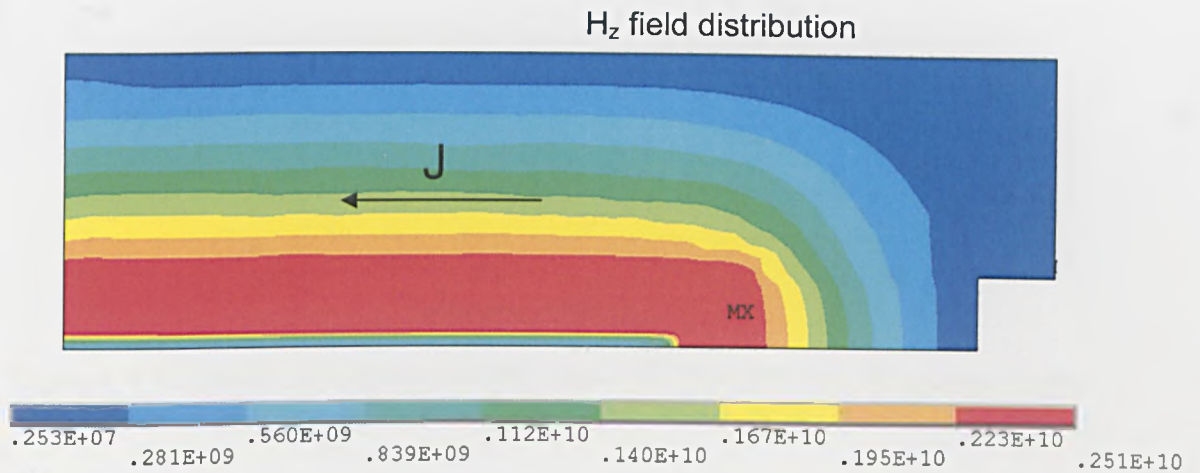


Figure 9.2 H field distribution in the solenoid inductor at  $f=1\text{MHz}$  [9.1].

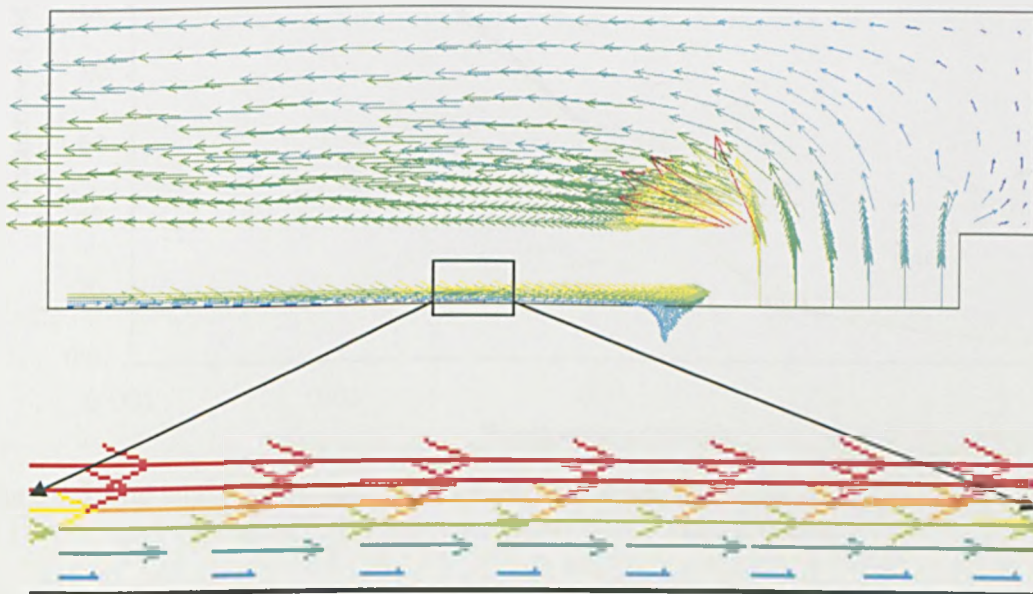


Figure 9.3 Current density in the inductor. The highlight region, at the bottom of the picture, shows the induced currents in the core. The frequency is  $f=1\text{MHz}$  [9.1].

The measured and modeled inductance values for  $Ni_{80}Fe_{20}$  and Vitrovac 6025 cored inductors are presented in Fig. 9.4 & 9.5.

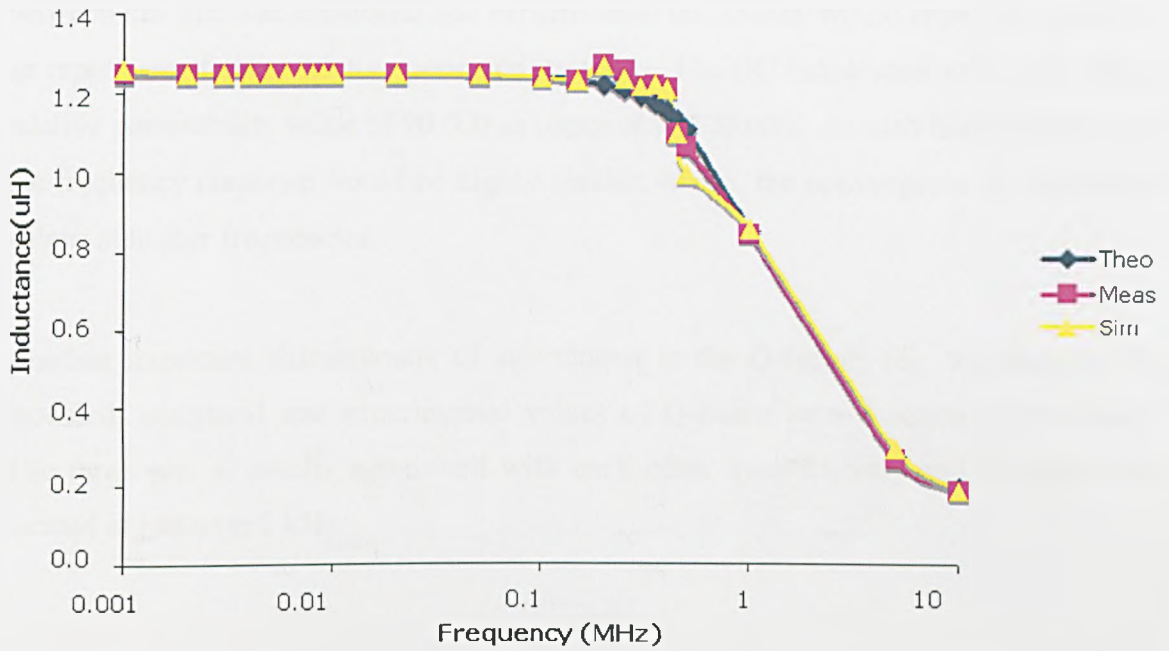


Figure 9.4 The analytical, measured and simulated values of the inductance for the solenoid inductor with 10µm Ni-Fe core material.

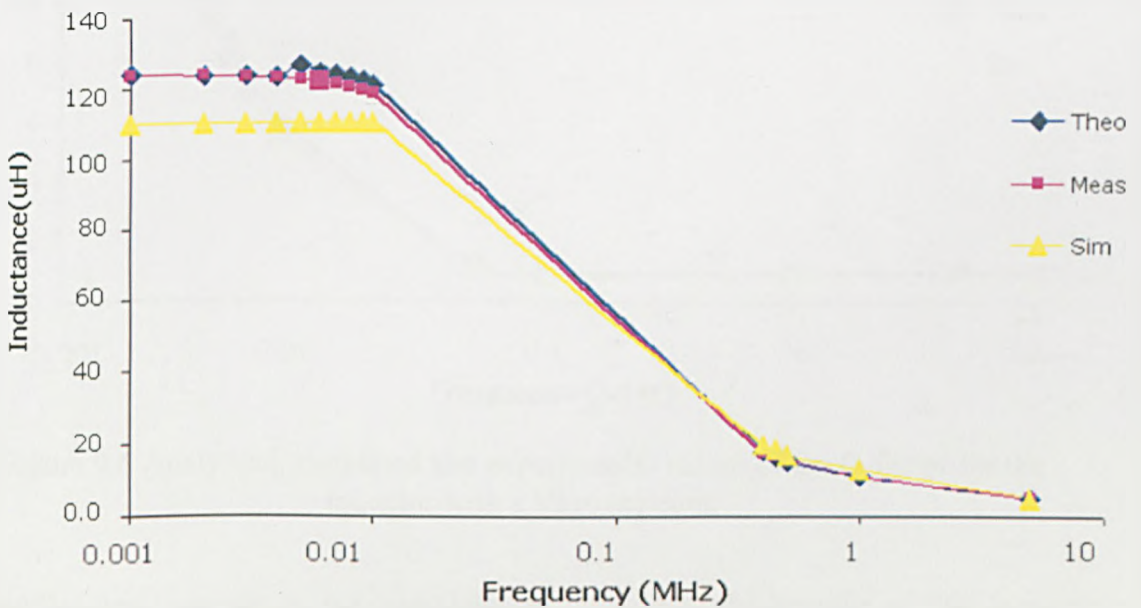


Figure 9.5 The analytical, simulated and experimental values of the inductance for the solenoid inductor with 20µm 6025v core material.

The maximum inductance values for the two core materials differs by about 100 times which is consistent with the fact that the permeability of Vitrovac 6025 is 50 times that of the  $Ni_{80}Fe_{20}$  and the thickness of the former is two times that of the latter. The figures also show that, as the frequency increases, the inductance decreases rapidly but for the Vitrovac 6025 the decline happens at lower frequencies because of its susceptibility to skin effects and permeability frequency response. The initial difference



between the Vitrovac simulated and experimental inductance would appear to be due to an input error for the relative permeability term. The DC inductance value indicates a relative permeability value of 90,000 as opposed to 100,000. At such high permeability the frequency response would be highly similar, hence, the convergence of inductance values at higher frequencies.

Another important characteristic of an inductor is the Q-factor; Fig. 9.6 displays the modeled, analytical and experimental values of Q-factor as a function of frequency. The three sets of results agree well with each other quantitatively and the peaks are located at just over 2 kHz.

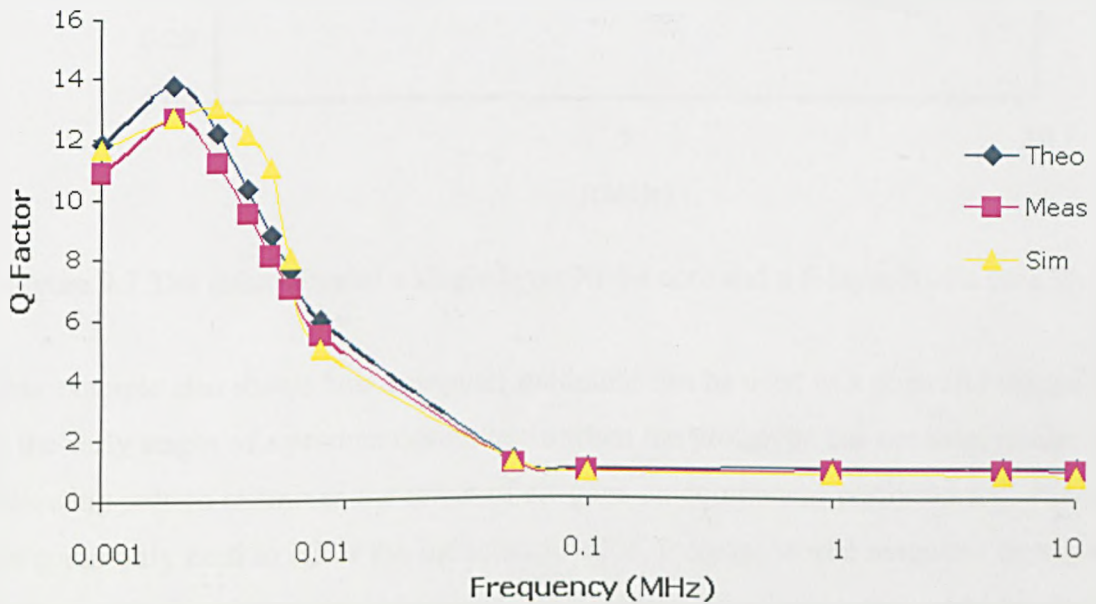


Figure 9.6 Analytical, simulated and experimental values of the Q-factor for the inductor with a Vitrovac core.

A multilayered core design was simulated to investigate the benefits of thin laminate layers. As the frequency increases, the inductance of the solenoid inductor decreases rapidly when the skin depth is comparable to the thickness of the magnetic core. Therefore the thickness of the magnetic film is an important design parameter in micro-inductor/transformer manufacturing and laminate cores have often been used [9.3-9.5]. To demonstrate the effect of core thickness, a computer model with a core which consists of 5 layers of  $Ni_{80}Fe_{20}$  films has been analyzed. The thickness of the film is 5 microns and the total cross-section area is kept the same as a one-layer  $Ni_{80}Fe_{20}$  core with a thickness of 12 $\mu$ m. The values of the inductance are presented in Fig 9.7. The

results show that for the laminate core design the inductance is the same as the single layer core at low frequency but declines at a higher frequency.

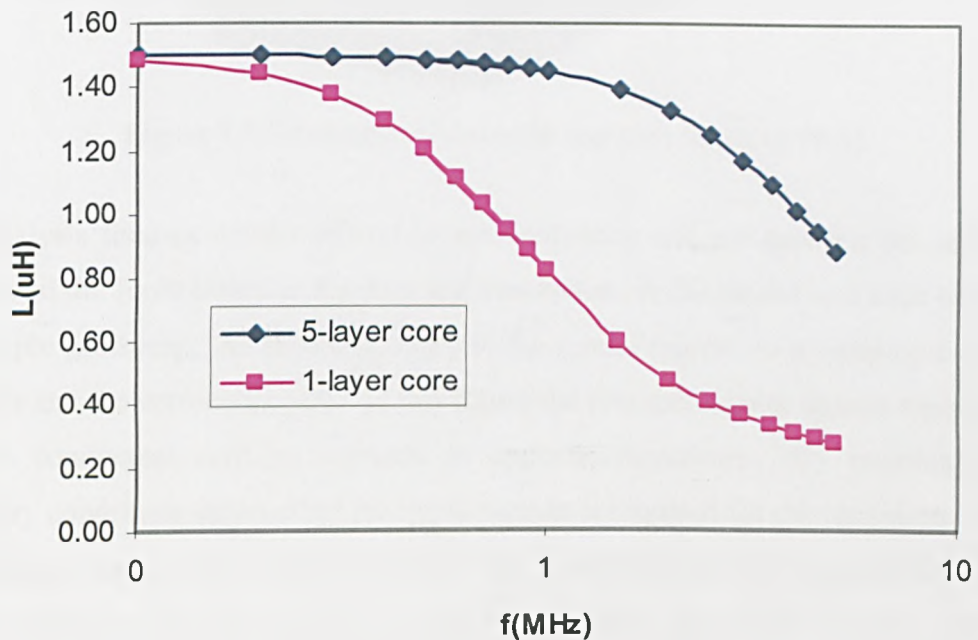


Figure 9.7 The inductance of a single layer Ni-Fe core and a 5-layer Ni-Fe core [9.1].

This example also shows how computer modeling can be used as a powerful design tool in the early stages of a product design cycle when the prototype has not been made. The following section examines the affect of air-gaps on component performance. Air-gaps are commonly used to tailor the inductance value, increase stored magnetic energy and increase the saturation value of current. The simulation of such gaps provides data on the fringing affects of the air-gap.

### 9.3 Computer modeling of a one-turn pot-core micro-inductor

A one-turn magnetic inductor consisting of a copper conductor with a rectangular cross-section coated with an insulation layer and a layer of magnetic core was modelled [9.6]. Fig 9.8 illustrates the modelled component.

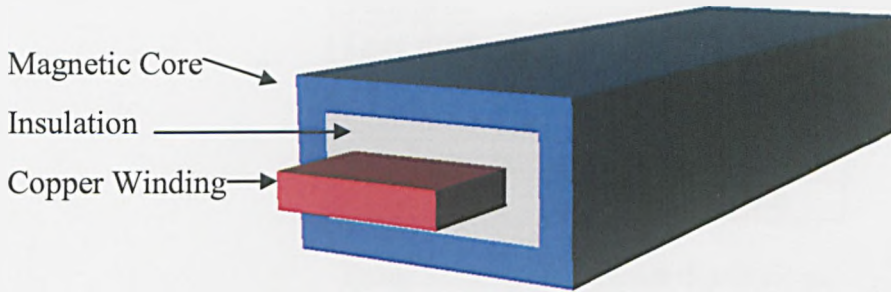


Figure 9.8 Schematic of a simple one-turn inductor [9.6].

The analysis focuses on the effects of the frequency and air gaps on the inductance values and the Joule losses in the core and conductor. A 2D model was used because of the simple geometry. As shown in Fig 9.9, the model represents a cross-section of the inductor and the surrounding air. In this figure the two rectangular shapes represent two parallel conductors carrying currents in opposite directions. By imposing proper boundary conditions only half of the cross-section is required for the modeling. Outside the inductor, some air has been included in the model because the magnetic field is non-zero outside the inductor especially when the core has gaps in it. The cut-off radius  $r_{cutoff}$  is chosen so that the changes in the field do not vary significantly when the cut-off radius changes.

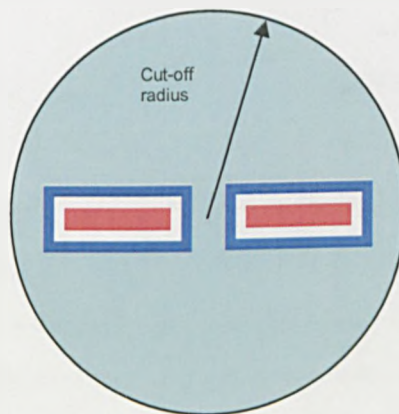


Figure 9.9 Schematic cross-section of the inductor model. Materials are represented by different shades. Only the right hand half needs to be modelled.

The dimensions are listed in Table 9.21.



Parameter	Size
Core thickness	5 $\mu\text{m}$
Insulation thickness	5 $\mu\text{m}$
Conductor width	700 $\mu\text{m}$
Conductor thickness	65 $\mu\text{m}$
$r_{cutoff}$	0.15m

Table 9.2 Inductor model dimensions.

The 2D model was meshed using ANSYS 4-noded 2D element PLANE13. This element has the magnetic and the electrical degrees of freedom and eddy currents can be modelled. Table 9.3 contains the material properties used in this study. The load in this problem is the total current. It can be applied at a point in the conductor region but it is necessary to couple the voltage degrees of freedom of the conductor. It is assumed that the current is small enough that the magnetic core does not saturate and linear harmonic analysis method can be used.

Property	NiFe(80:20)	Cu	Air
$\rho$ ( $\mu\Omega\cdot\text{cm}$ )	20	1.7	$\infty$
$B_{sat}$ (Tesla)	0.85		
$\mu_r$	2000	1	1

Table 9.3 Material properties used in the modelling

As before with the solenoid component, the key parameters of an inductor are the inductance and the losses. The inductance of the one-turn inductor with  $Ni_{80}Fe_{20}$  core is shown in Fig 9.10. The decline of the inductance at high frequency is expected: as the frequency increases, the induced current in the magnetic core produces a cancellation flux that reduces the total flux density. The turning point of about 1MHz coincides with the skin depth of the magnetic core being almost the same as the thickness of the core.

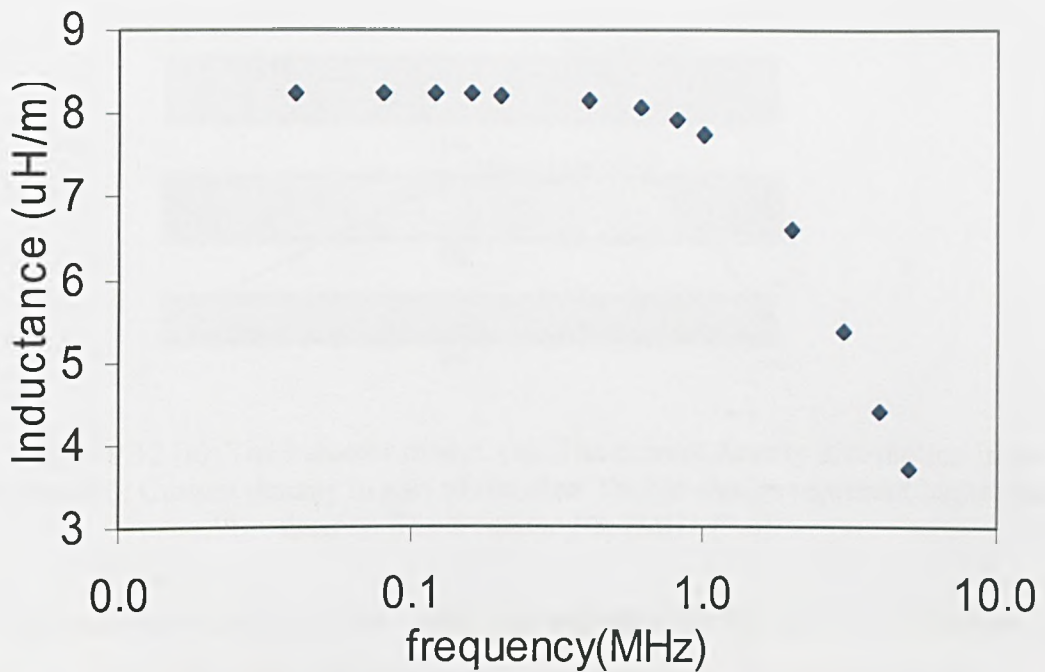


Figure 9.10 Inductance vs. Frequency for the model of a 1-turn pot-core  $Ni_{80}Fe_{20}$  micro-inductor [9.6].

Fig 9.11 shows the flux distributions at a corner of the inductor at two frequencies: 1Hz and 10MHz. At 1Hz the flux is still quite evenly distributed but at 10MHz, the flux lines only appear near the two surfaces of the core: the flux density in the middle has been canceled by the flux density created by the induced currents in the core.

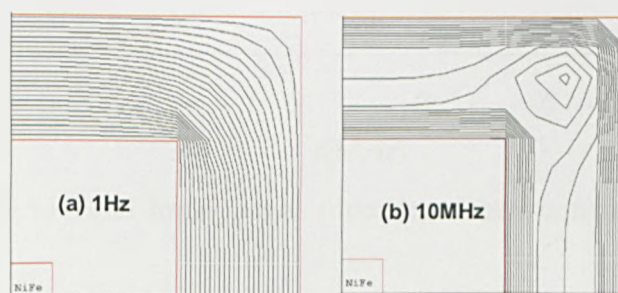


Figure 9.11 Flux line distribution in the core (a)  $f=1\text{Hz}$  and (b)  $f=10\text{MHz}$ .

The current density in both the core and the winding conductor depends on the frequency. As shown in Fig 9.12, because of the skin effect, at  $f=1\text{MHz}$  the currents begin to concentrate at the two ends of the conductor and the two sides of the core. This reduces the effective cross-section of the winding and creates Joule losses in the core.

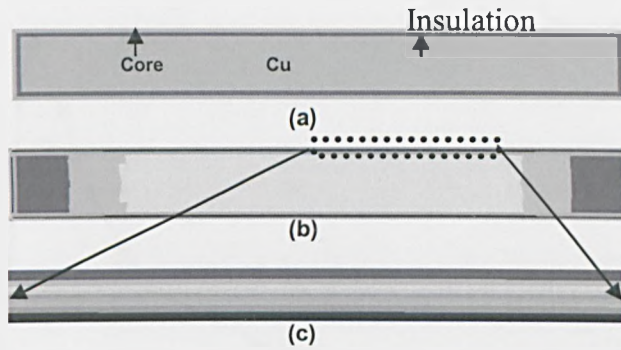


Figure 9.12 (a): The inductor model. (b): The current density distribution in the inductor. (c): Current density in part of the core. Darker shades represent higher current density. The frequency is 1MHz [9.6].

As the inductance decreases the Joule loss increases in the core and windings. At a current amplitude  $I_{\max} = 2A$ , the loss vs. frequency results is shown in Fig 9.13.

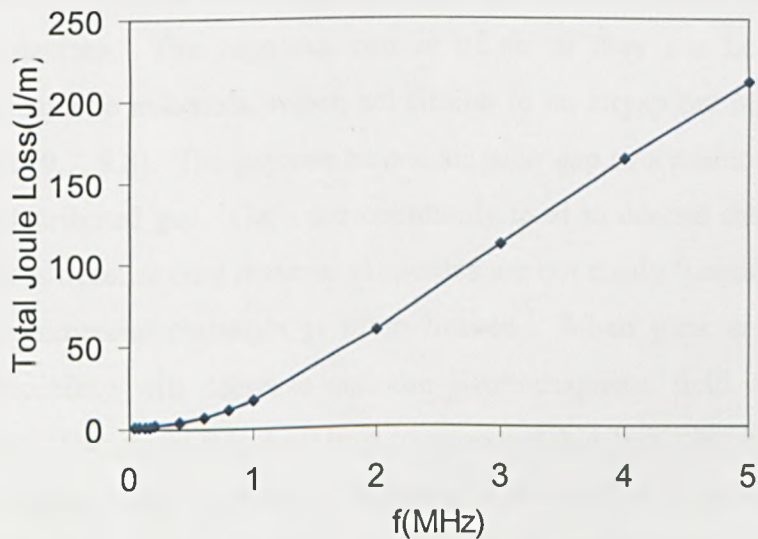


Figure 9.13 Total Joule loss as function of the frequency [9.6].

The Q-factor values are shown in Fig 9.14. The peak is near  $f=0.2MHz$ . This behaviour can be explained by the definition  $Q = \frac{2\pi fL}{R}$  where  $R$  is the total resistance. As the frequency  $f$  increases and so does the  $Q$  value, but as  $f$  increases further  $L$  begins to decrease and  $R$  begins to increase which leads to the decrease of  $Q$ .

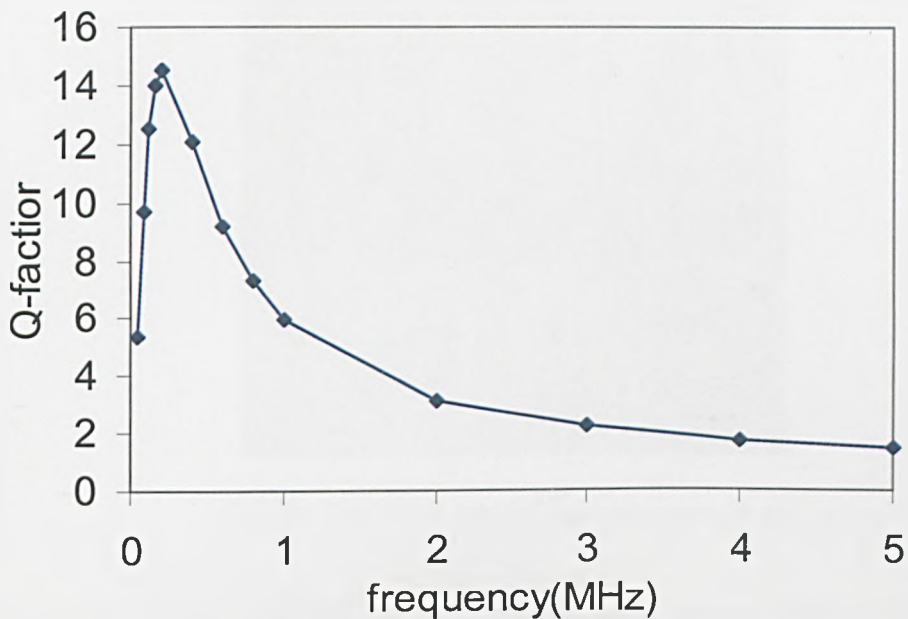


Figure 9.14 Q-factor vs. Frequency [9.6].

The introduction of air gaps in the magnetic path can alter significantly the properties of the magnetic devices. The gaps can consist of air or they can be filled with low permeability magnetic materials, which act similar to an airgap but reduce the amount of leakage flux [9.7, 9.8]. The gap can be one singular gap or a multitude of air gaps to form a quasi-distributed gap. Gaps are commonly used to control the performance of magnetic devices because core material properties are not easily ‘tunable’ and the range of available commercial materials is often limited. When gaps are introduced the effective permeability will decrease and the electromagnetic field distributions will change. At high frequency this may lead to unacceptable flux distributions, hot-spots and excessive overall Joule losses in an inductor. It is therefore important to understand how gaps affect the losses and the inductance as gap design changes. Fig 9.15 shows a model with gaps. It is assumed that the gaps are located on the top part of the core and this is why a one-half rather than a one-quarter model has been used in this work. Since the model is 2D, it should be noted that the gaps actually run the full length of the inductor.



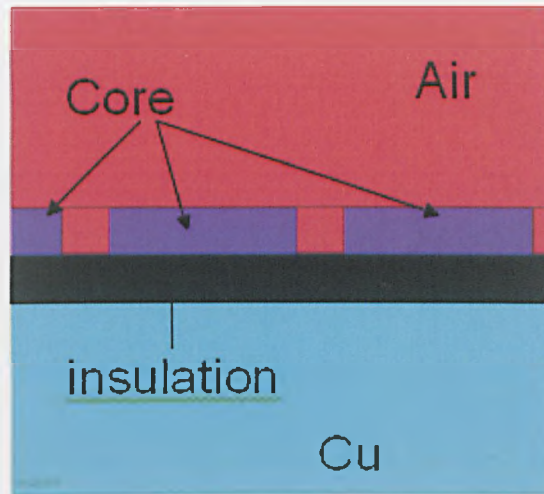


Figure 9.15 FEA Model with air gaps [9.6].

A model with a single gap and a model with ten gaps are modelled and the results are compared. For comparison, the gap width of single-gap model is the same as the sum of the gap widths of the ten-gap model. The gap distance, which is defined as the width of the core between two adjacent gaps in the ten-gap model is  $50\mu\text{m}$ . With the introduction of air gaps in the magnetic path, the magnetic fields and the electric currents change significantly. Fig 9.16 shows that at  $f=1\text{MHz}$  the distribution of flux lines in the models with no gaps, with a single gap and with ten gaps. In the no-gap model almost all the flux concentrates in the core while an insignificant amount of flux exists outside the inductor. Clearly, any model that does not include the air outside the inductor may incur significant errors when gaps are present.

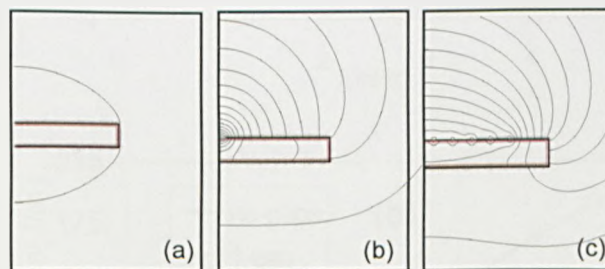


Figure 9.16 Flux lines in and around the inductor with, (a) no gap in the core, (b) single  $50\mu\text{m}$  gap, and (c) ten  $5\mu\text{m}$  gaps [9.6].

Because of the increased reluctance of the magnetic path the magnetic energy that can be stored in the inductor becomes less as gaps are introduced. Fig 9.17 shows the ten-gap model has much smaller inductance than the single-gap inductor and the inductance of the one-gap inductor is much smaller than that of the no-gap model (see Fig 9.10).

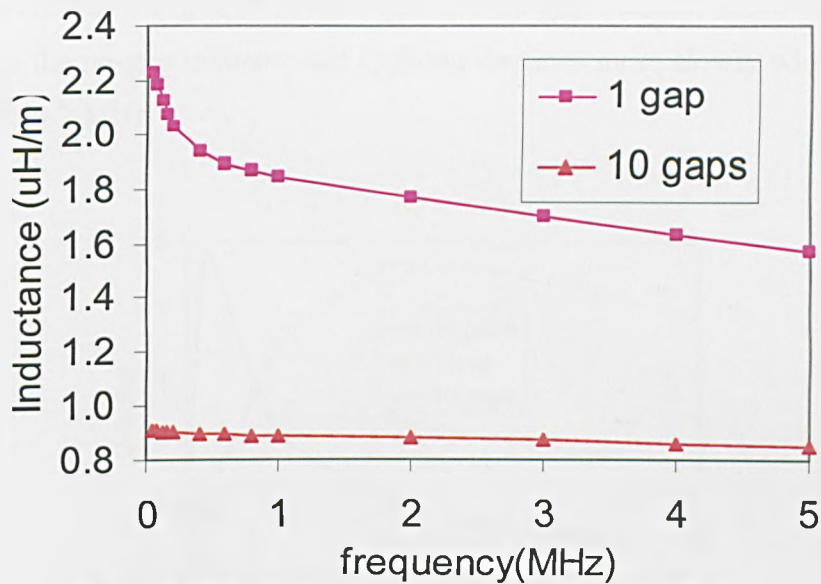


Figure 9.17 Inductance of inductors with gaps [9.6].

The distribution and the intensity of the current density also changes when gaps are introduced. Fig 9.18 shows that for all frequencies the copper losses are the highest in the one-gap model while in the core the losses are the lowest for the ten-gap model.

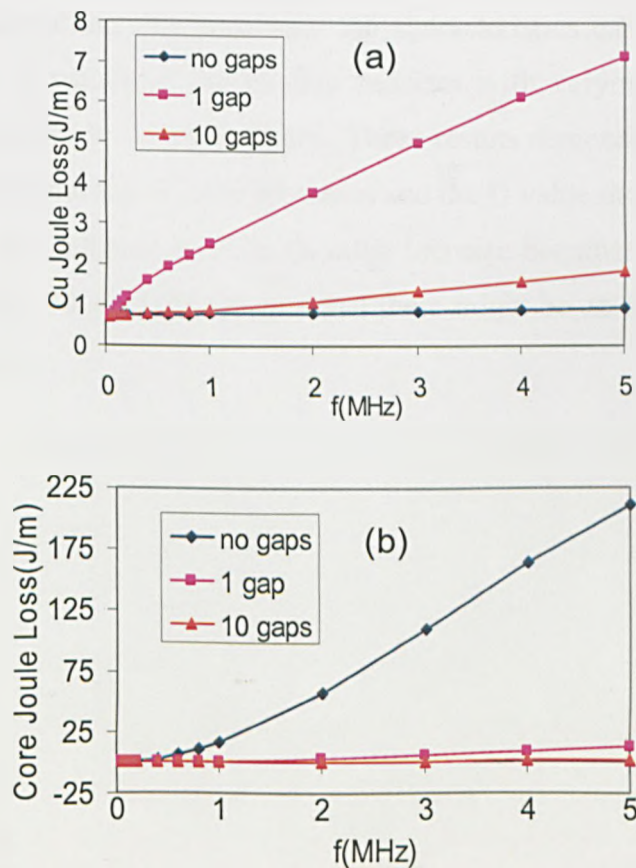


Figure 9.18 (a) Losses in the conductor. (b) Losses in the magnetic core [9.6].



The Q-factor shown in Fig 9.19 reveals that the ten-gap inductor has a value which is comparable to the no-gap inductor and Q-factor declines more slowly when the peak is reached at about 2 MHz.

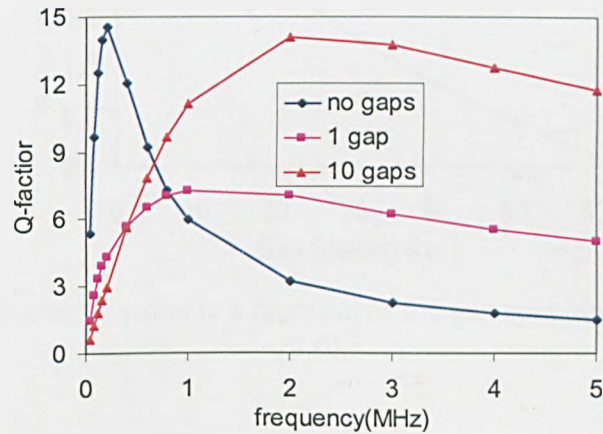


Figure 9.19 Q-factor values of inductors with and without magnetic gaps as a function of frequency [9.6].

In the results presented above, the gap distance, which is the width of the magnetic core between two adjacent gaps in the ten-gap model, is fixed at  $50\mu\text{m}$ . This can be changed of course and by controlling this parameter the characteristics can also be modified. The inductance and Q values of the ten-gap inductor with varying gap distance are shown in Fig 9.20 and Fig 9.21, respectively. These results demonstrate that as the gap distance increases the inductance value decreases and the Q value increases. The results shown in Fig 9.21 also indicate that the Q value increase becomes slower as the gap distance is greater than  $50\mu\text{m}$ . This means that there might be an optimal gap spacing for the one-turn inductor.

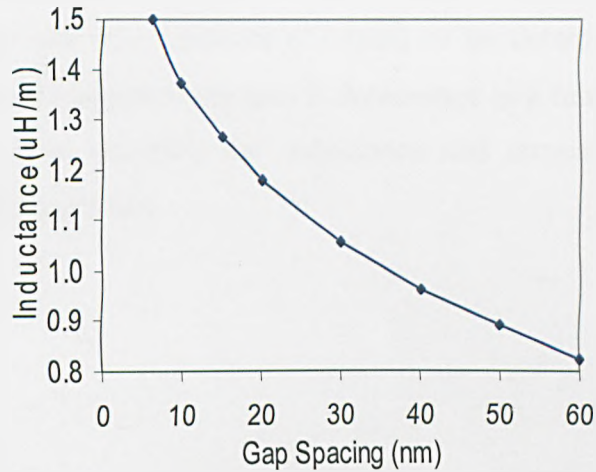


Figure 9.20 The inductance value is a function of the gap spacing of the ten-gap model [9.6].

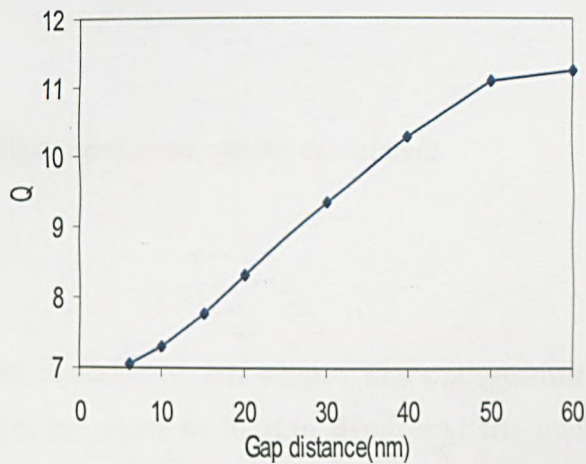


Figure 9.21 The gap-distance dependent Q values of of an inductor with ten-gaps [9.6].

In summary, the key parameters such as the inductance and the Q-factor have been characterised. The introduction of multiple small gaps in the magnetic core has a greater effect on the inductance than that of a single larger gap. Results demonstrate that the losses in the core and the conductor are also lower when multiple gaps are used.

#### 9.4 Optimization & Characterization of the Solenoid Micro-Inductor

Based on its excellent material properties analysed in previous chapters, the CoFeCu alloy is selected for analytical optimization. The optimization is performed with respect to the original prototype component in Chapter 8; (1) to maintain the inductance value with power density being the primary factor over efficiency, and (2) maintain the inductance value with efficiency improvement the main objective.

An operating frequency is selected, in this case 0.5 MHz, allowing skin depth values for the windings (93 $\mu$ m) and core laminate (17.4 $\mu$ m) to be determined. Secondly, the number of windings and magnetic core area is determined as a function of the saturation flux density of the core material, the inductance and current requirement of the application. From Faraday's law

$$V = N \frac{d\Phi}{dt} \quad (9.1)$$

such that

$$VT = NA_e B \quad (9.2)$$

Eq(9.2) can be rewritten as follows

$$VT = LI \quad (9.3)$$

Using (9.2) and substituting into (9.3):

$$LI = NA_e B \quad (9.4)$$

Therefore the area of the component can be calculated:

$$A_e = \frac{LI}{BN} \quad (9.5)$$

Design constraints are included at this stage. The optimization process requires that each CoFeCu laminate be equal to  $\frac{1}{2}$  skin depth and the number of laminations is restricted to 10 for reasons of costs and manufacturability. With the increase in core area, the number of turns, N, is adjusted accordingly. The optimization process maintains also the number of turns to 33. Efficiency is sought to be increased by optimizing the core through the number of laminations. Other known parameters include: the maximum applied current, 1.24A, inductance, 0.3 $\mu$ H, PCB current density, 10A/mm<sup>2</sup>, and winding height is restricted to twice the skin depth. The dimensions and performance of the optimized component can therefore be calculated, following the same procedure within Chapter 8, as shown in Table 9.4.

<b>Dimensions</b>	Optimized Component (1)	Optimized Component (2)	Prototype Component
Number of turns	7	33	33
Turn thickness	180 $\mu\text{m}$	90 $\mu\text{m}$	90 $\mu\text{m}$
Turn width	700 $\mu\text{m}$	200 $\mu\text{m}$	200 $\mu\text{m}$
Turn spacing	40 $\mu\text{m}$	20 $\mu\text{m}$	20 $\mu\text{m}$
Number of laminations	10	10	1
Lamination thickness	8.7 $\mu\text{m}$	1 $\mu\text{m}$	10 $\mu\text{m}$
Lamination width	500 $\mu\text{m}$	500 $\mu\text{m}$	500 $\mu\text{m}$
Lamination insulation	5 $\mu\text{m}$	5 $\mu\text{m}$	5 $\mu\text{m}$
<b>Performance</b>	Optimized Component (1)	Optimized Component (2)	Prototype Component
$V_{in}$ (V)	0.94	0.51	0.51
$P_{out}$ (W)	1.16	0.09	0.09
$B_{pk}$ (T)	1.4	1.4	1.4
$P_{eddy}$ (mW)	0.14	0.22	24.6
$P_{hys}$ (mW)	1	0.11	0.11
$P_{Cu}$ (mW)	7.5	1.62	1.62
Efficiency (%)	<b>88</b>	<b>97</b>	<b>77</b>
Power density ( $\text{W}/\text{cm}^3$ )	<b>170</b>	<b>30.8</b>	<b>24.7</b>

Table 9.4 Performance of optimized and prototype components with CoFeCu cores operating at 500 kHz.

The optimized component (1) produces an 11% increase in efficiency and nearly 7 fold increase in power density. Conventional inductors and transformers will normally operate with efficiency in the range of 90-95%. Hence, the application would have to greatly benefit from the increase in power density to tolerate the level of efficiency. Optimized component (2), similar to (1), uses the data from the prototype to identify eddy current core loss as the main loss mechanism. The core is reduced to ten 1 $\mu\text{m}$  laminates and via this adjustment improves efficiency by 20% and increases power density by 6.13W/cc. Comparing the two optimized components, a trade-off between efficiency and power density is evident.

The analytical data within Table 9.4 and the simulated data in Fig 9.7 indicate the clear benefits of the laminated core. By considering AC losses within the core and winding, and using the new manufacturing processes it is possible to develop microscale magnetic components with high power density and efficiency. Further improvements in power density and efficiency would require a design process encompassing thermal and cooling considerations.

Due to manufacturing restrictions and lack of time, the production of a 10-laminate core via direct and sequential deposition of magnetic and dielectric layers was not possible. However, via a manual stacking fabrication process two components consisting of highly laminated Ni-Fe cores were fabricated to experimentally verify the benefits of the laminated core. The two components consisted of 70 and 105 horizontal 5 $\mu$ m thick Ni-Fe laminate layers. A summarized fabrication sequence is displayed in Fig. 9.22. The dimensions of the laminate are shown in Fig 9.23. The inductor was designed for an inductance value of 1 $\mu$ H. The number of windings was adjusted according to the overall core area. The windings consisted of hand wound copper; this was possible due to the increase in core area.

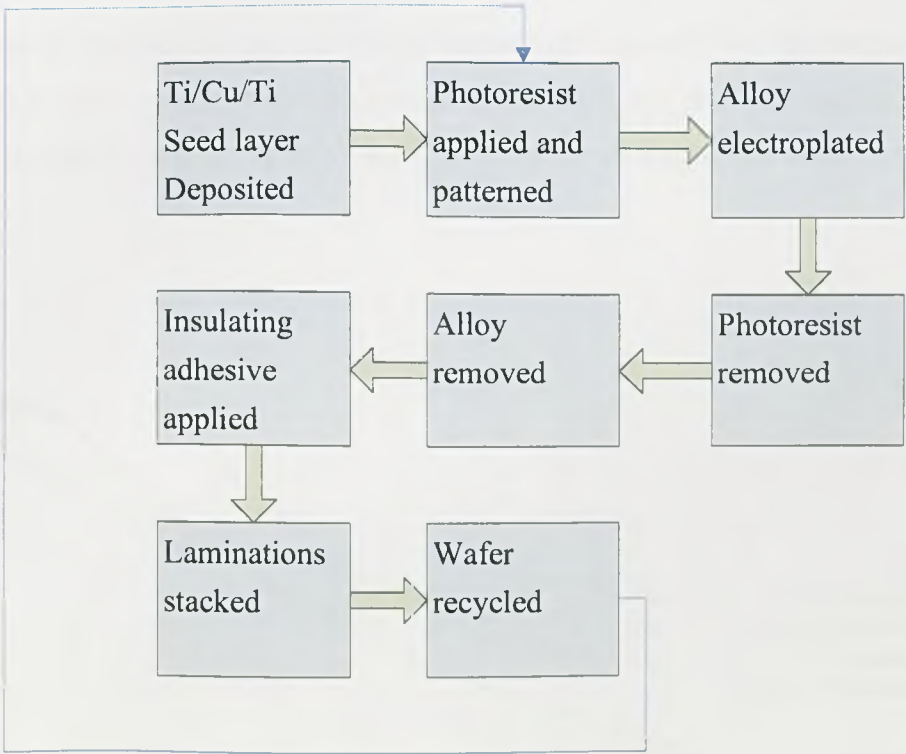


Figure 9.22 Fabrication and assembly process of the laminated core.



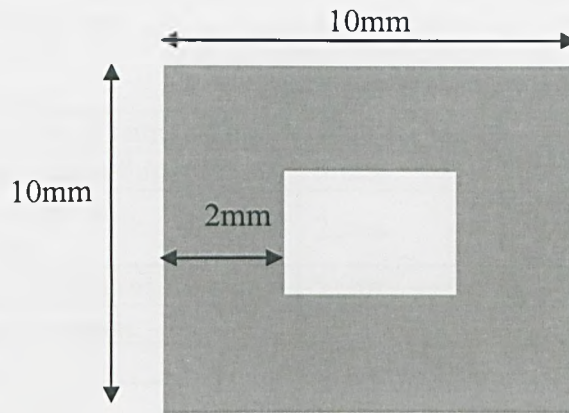


Figure 9.23 Footprint of a laminate layer.

Fig 9.24 displays the inductance values as a function of frequency for the two inductors. The analytical and the experimental results agree well for the two inductors. The experimental values were recorded by Raytheon Systems Limited and were verified by the author.

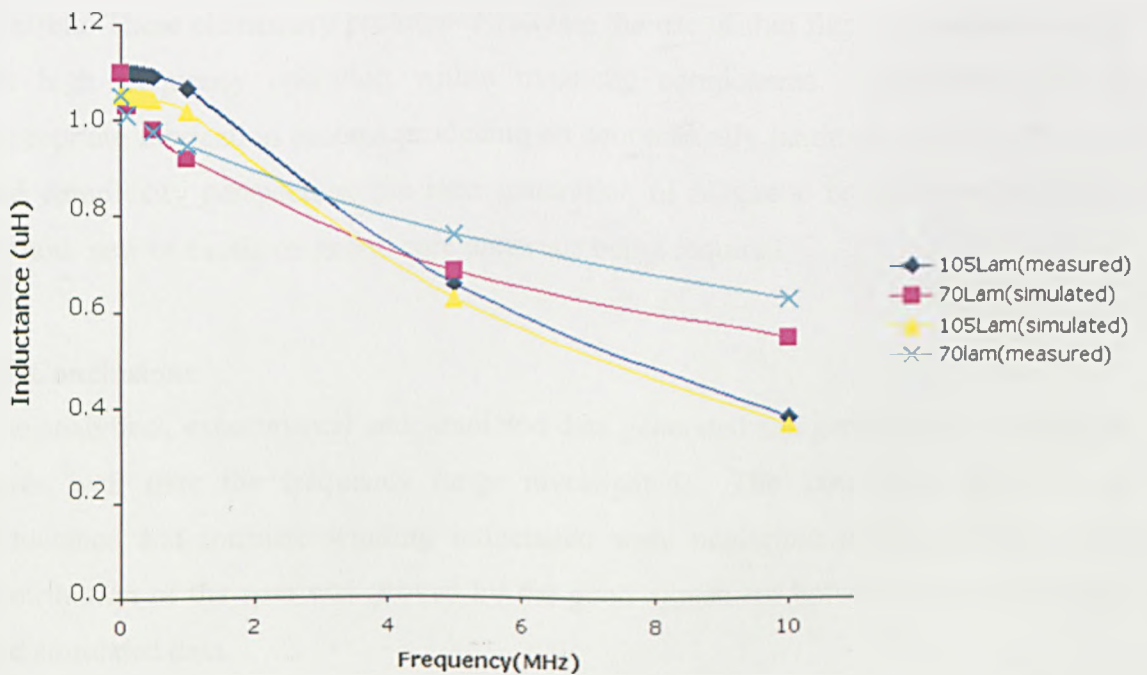


Figure 9.24 Inductance vs. Frequency for laminated hand wound inductors.

The performance of the prototype laminate-core inductors at 500 kHz is outlined in Table 9.5.



<b>Dimensions</b>	component (1)	component (2)
Number of turns	5	4
Number of laminations	70	105
Lamination thickness	5 $\mu\text{m}$	5 $\mu\text{m}$
Lamination width	2 mm	2 mm
Lamination insulation	5 $\mu\text{m}$	5 $\mu\text{m}$
<b>Performance</b>		
$V_{in}$ (V)	6.3	7.45
$P_{out}$ (W)	14.42	21.30
$B_{pk}$ (T)	0.8	0.8
$P_{eddy}$ (mW)	0.829	1.24
$P_{hys}$ (mW)	0.09	0.136
$P_{Cu}$ (mW)	0.27	0.42
Efficiency (%)	<b>92</b>	<b>92</b>
Power density ( $\text{W}/\text{cm}^3$ )	<b>33</b>	<b>49</b>

Table 9.5 Performance of laminated core inductors

The results displayed in Table 9.5 indicate that by considering AC losses within the core and windings high power density components with efficiency greater than 90% are possible. These elementary prototypes validate the use of thin film soft magnetic alloys for high frequency operation within magnetic components. Therefore, with an appropriate fabrication process producing an economically laminated core, from a cost and complexity perspective, the next generation of magnetic components is feasible without new or exotic magnetic core materials being required.

## 9.5 Conclusions

The analytical, experimental and simulated data generated and presented in this chapter agree well over the frequency range investigated. The assumption that leakage inductance and intrinsic winding inductance were negligible in comparison to the contribution of the core was proved by the good agreement between the experimental and simulated data.

The modeling of the magnetic components provided a detailed insight into the behavior and performance of the component. Only by modeling was it possible to identify areas of the components prone to detrimental skin depth and proximity effects. Also, the

internal and external flux path of the components could be visualized and effects of air-gaps examined in detail.

Another advantage of modeling is that it permits the rapid evaluation of material properties and alterations to component geometry. Modeling allowed a comparison of single layer and laminated cores. To perform such an assessment experimentally is labour intensive, expensive and time consuming. Due to the importance of tailoring the magnetic properties of the film this is a highly desirable design tool.

The simplified optimization procedure highlighted that via consideration of AC losses within the component, major gains in terms of component power density and efficiency were attainable. The theoretical results within Table 9.4 and results from the fabricated components produced some of the highest power densities to date. This was achieved with an overall operating efficiency greater than 90%.

In conclusion, the modeling results permitted an evaluation that was quicker and more explanatory than the experimental and analytical approach. The simple laminated core prototypes highlighted the potential of the investigated materials and technology used in their fabrication.

Further improvement in terms of power density is attainable through the development of optimal magnetic core materials or more advanced manufacturing processes. This will influence the cost and manufacturability of the product by reducing the number of core laminations, or time for their production. The following chapter outlines the main conclusions generated by the work within this thesis and details potential fabrication processes that could be used for future developments in microscale magnetic components.

## References

- [9.1] H. Lu, D. Flynn, C. Bailey and M. Desmulliez "An Analysis of a Microfabricated Solenoid Inductor," IEEE Proc. Electronics System-integration Technology Conference (ESTC), vol. 1, pp. 556-561, Dresden, September 2006.
- [9.2] E.C. Snelling, "Soft Ferrites, Properties and Applications," Butterworths, 2<sup>nd</sup> edition, 1988.
- [9.3] M. Brunet, T. O'Donnell, J. O'Brien, P. McCloskey, C. O'Mathuna, "Design Study and Fabrication Techniques for High Power Density Micro-Transformers," IEEE Tran., Magn., pp. 1189-1195, 2001
- [9.4] U. Reggiani, G. Grandi, G. Sancineto, M.K. Kazimierczuk, and A. Massarini, "High-frequency behavior of laminated iron-core inductors for filtering applications," in Proc. IEEE APEC, pp. 654-660, 2000.
- [9.5] J. W. Park and M. G. Allen, "Ultra low-profile micromachined power inductors with highly laminated Ni/Fe Cores: Application to low-Megahertz DC-DC converters," IEEE Trans. Magn., April 2003.
- [9.6] H. Lu, D. Flynn, C. Bailey and M. Desmulliez "Computer Modelling of a Micro-manufactured One-turn Inductor," IEEE Proc. of High Density Packaging Conference, Shanghai, June 2006.
- [9.7] C. R. Sullivan, "AC Resistance of Planar Power Inductors and the Quasidistributed Gap Technique," IEEE Trans. Power Electronics, vol. 16, no. 4, pp. 558-567, July 2001.
- [9.8] N. H. Kutkut and D. M. Divan, "Optimal Air-Gap Design in High-Frequency Foil Windings," IEEE Trans. Power Electronics, vol. 13, no. 5, pp. 942-949, Sept. 1998.

## Chapter 10

### Conclusions and Future Work

#### 10.1 Conclusion

Efficient DC-DC power converters operating in the MHz frequency regime deeply depend on the choice of suitable materials used in the development of their magnetic cores. The needs for faster switching, reduced power losses and smaller components have driven power supply switching frequencies into the range of 500 kHz-10MHz. Prohibitive power losses at higher switching frequencies limit the use of traditional magnetic components such as ferrites. At increased frequencies, the magnetic component becomes smaller, AC resistance losses increase and current handling capability becomes more stringent. Typical ferrite cores suffer from a reduction in useable flux density at these frequencies. Their large core area results in the magnetic component normally being the largest component on the PCB, and high sintering temperatures during fabrication limit their monolithic integration with neighbouring components. New magnetic materials need therefore to be studied to overcome the shortcomings of ferrite based magnetic cores. New core materials must have high resistivity, high saturation flux, permeability of 100-3000 and low coercivity. Moreover, these materials must be suitable for thin film deposition such that cost-effective mass-manufacture can be implemented. In addition, a method of producing small windings requires development.

Previous attempts to develop microscale magnetic components utilizing thin film alloys have demonstrated improvements in device performance. However, these development efforts have suffered from either slow or expensive deposition of the magnetic alloy, limited bandwidth of operation due to film thickness, high relative permeability or low saturation flux density. Therefore, the main objective of this thesis was to research and develop novel fabrication processes for the assembly of microscale magnetic components.

Chapter 1 identified the main motivation of microscale magnetic components; this included an assessment of market trends and technology drivers affecting magnetic components and their applications. The primary technical challenges involved in the miniaturisation of magnetic components were also described.

Chapter 2 reviewed the fundamental magnetic design equations and background theory on magnetic materials and identified the desirable properties for power magnetic components. An explanation of the major loss mechanisms within thin films, hysteresis and eddy current phenomena, were provided, along with a description of anisotropy within magnetic thin films.

Chapter 3 outlined the function of magnetic components operating within DC-DC converters, the chosen application of this thesis. A detailed review of conventional components, including component structure, materials and fabrication processes was presented. The findings of the study into current state of the art of techniques for fabricating microscale magnetic components were also provided. Finally, the performance of conventional and prior micromachined components was presented in order to assess the performance of the components fabricated within this thesis.

Chapter 4 explained the theory behind the process of electrodeposition and the various waveforms that can be applied. Prior work into electrolytes used to investigate the deposition process and properties of Ni-Fe were reviewed. The theory behind magnetic field annealing was presented and applied to the DC deposition of Ni-Fe. Magnetic field annealing produced magnetically anisotropic films with favourable film properties. The anomalous co-deposition effect was experimentally verified. The DC deposition results also indicated a variation of grain size with Fe content.

Chapter 5 presented a Design Of Experiments (DOE) carried out for the manufacturing of magnetic alloys. The effect of alloy properties generated by deposition conditions was examined in terms of the electric and magnetic properties of the thin film. Other magnetic thin film alloys incorporated into the prototype magnetic components were also introduced.

Chapter 6 examined the basic loss mechanisms of the component and derived the equations that impact on the system performance. Various component geometries were described and assessed since the design of the component is application specific. The impact of the component's performance on the operation of the converter was also demonstrated in this chapter.

Chapter 7 detailed the fabrication process of the microinductors and microtransformers. This chapter also introduced the methods used and challenges encountered in developing a laminated core structure.

Chapter 8 explained the experimental procedure used to characterise the components. Results of the characterisation of all the fabricated components were presented, and analysis of the data was provided.

Chapter 9 provides an overview of ANSYS and a description of the methodology of the developed models. A comparison between analytical, experimental and simulated data was performed and conclusions provided.

Within this thesis micromachined inductors and transformers have been fabricated on glass using micromachined techniques borrowed from the LIGA process. From the results, parasitic capacitances do not appear to significantly affect inductor performance over the measured frequency range. Eddy currents and parasitic capacitance become significant at higher frequency. The analytical results using the two dimensional model agree well with the experimental and simulated values of inductance, resistance and Q-factor. The minor increase in resistance of the experimental values is attributed to the hysteresis resistance that is omitted from the model and parasitic resistance induced by leakage flux.

The ANSYS models developed in this thesis provided a valuable insight into the flux density distribution, current density distribution, affect of laminate layers, fringing affects due to air-gap dimension and location, and core material parameters on device performance. Knowledge of the influence of such parameters is a valuable asset in producing highly efficient components at the early stage in the design cycle. Hence the models provide a clear contribution to knowledge in the development of such components.

The DOE presented in Chapter 5 that investigated the influence of the PR variables on NiFe deposit composition, electrical and magnetic properties provided a valuable insight to the influence of grain size on the magnetic and electric properties of the alloy. The variation of grain size via pulse waveform is advantageous over the process utilised



by Herzer. The analysis approach by Herzer involved thermal annealing and the introduction of elements to produce grain refining. With the increase in grain size, associated with thermal annealing, and composition alteration the effects of grain size are ambiguous. The PR approach permits more clarity when assessing the effects of grain size. The incorporation of a PR electrodeposited alloy optimised via DOE and integrated within a flip chip bonded microinductor is also a first in the field of magnetic component development.

The solenoid winding is normally a 3D structure that is difficult to fabricate with micro-machining techniques and can be susceptible to high resistance interconnects. The novel assembly process of the windings using thick film electroplating and flip-chip-bonding, overcomes these challenges. A single layer solenoid component allows near ideal performance, however, this tends not to be realisable with traditional fabrication methods as the number of windings is limited by the cores inner diameter and how tightly the turns are packed together. To increase the inductance multiple winding layers would normally be needed and this leads to an increase in parasitic capacitance and AC resistance loss due to the proximity effect. Therefore, the novel fabrication process developed in this thesis has enabled the utilisation of the optimal geometry previously unattainable.

In addition, the solenoid winding is was also useful as a test vehicle for various alloys, since the flip-chip-bonding of the windings allows a variety of magnetic alloys to be inserted within identical components. As a result a very accurate assessment of the various alloys was possible due to the identical component geometries.

The results indicate that the solenoid winding has a low winding resistance, which is essential to efficient component operation. To maintain component efficiency and constant inductance, the core thickness, or laminate layer, should not be greater than the skin depth for a given frequency.

The performance of the commercial alloy, Vitrovac, is hindered by the thickness and the high relative permeability of the film. Results proved that electrodeposited alloys are better suited to the application due to the ability to vary film thickness and the relative permeability via magnetic field annealing or deposition current waveform. These

processes avoid the need for additives that may greatly reduce saturation flux density, which is a purely compositional dependent value. The PR achieved a higher inductance and the anisotropic permalloy had a greater bandwidth of operation than the “traditional” DC permalloy. Overall, the CoFeCu alloy was the most advantageous film with the highest recorded saturation current and Q-factor.

The microinductors presented in this thesis have proved that an efficient component can be manufactured via an inexpensive UV LIGA and electroplating process. An optimal design process led to the development of some of the most high power density components to date as shown in Table 9.4. The efficiency, size and power density demands highlighted in Chapter 1 are addressed by the optimised components.

The power density and volume of the two prototype Ni-Fe laminated core hand-wound inductors from Chapter 9 are compared against prior components in Fig 10.1. That figure demonstrates that these elementary prototypes validate the use of thin film soft magnetic alloys for high frequency operation within magnetic components when a suitably large core area is realisable. This is a very high impact proof of concept device for magnetic components within power supplies.

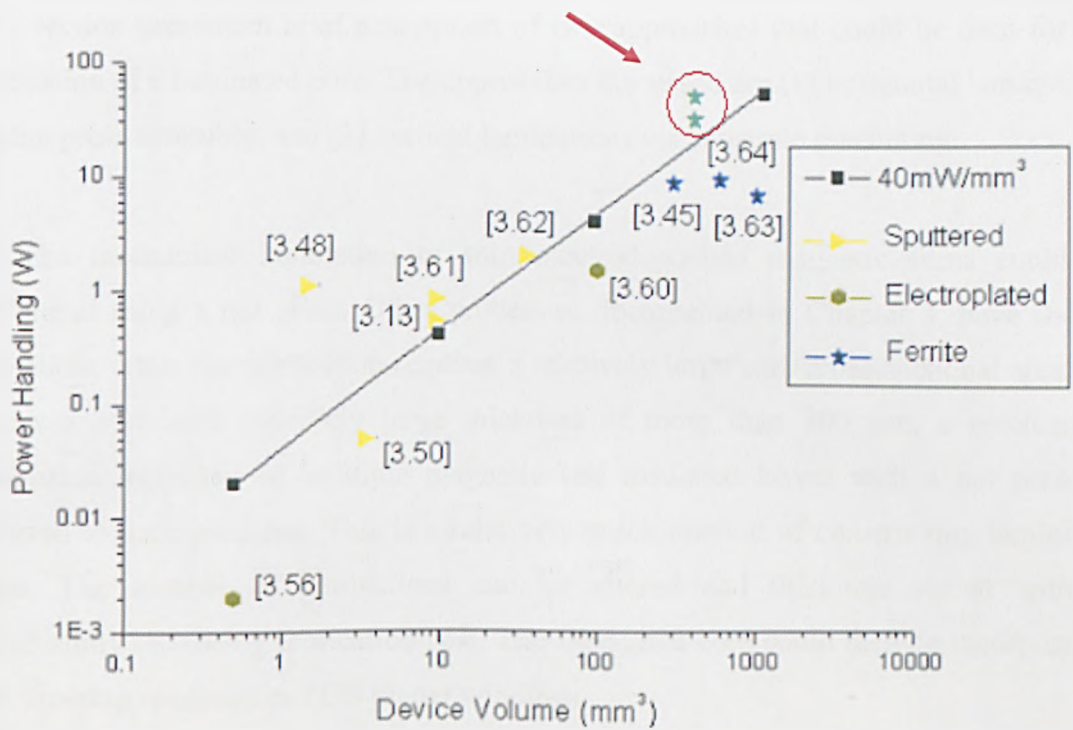


Figure 10.1 Comparison of performance of prototype laminated inductors with prior work (components 1&2 have been circled). Note that both power density and device volume are in logarithmic scales.

The performances of the devices developed within this thesis have been shown to supersede the performance of prior work. This can be attributed to the fact that this thesis provided a very comprehensive investigation into microscale magnetic components. In compassing the electrical and magnetic design of magnetic components, the material science aspect of optimising magnetic alloys, novel manufacturing processes were developed and finite element models were developed.

The challenge to develop inductors and transformers for MHz DC-DC converter operation requires the development of optimal core materials and/or manufacturability of laminated layers. Whilst studying in details the former, this thesis has also provided an insight into the latter, tailoring film properties with either magnetic field annealing or current waveform during the deposition process. Hence, suggestions for future work are focused on optimising the prototypes within this thesis by means of laminated core fabrication methods tailored to mass manufacture.

## 10.2 Future Work

This section presents a brief description of two approaches that could be used for the fabrication of a laminated core. The approaches discussed are (1) horizontal laminations via hot press assembly, and (2) vertical laminations via substrate machining.

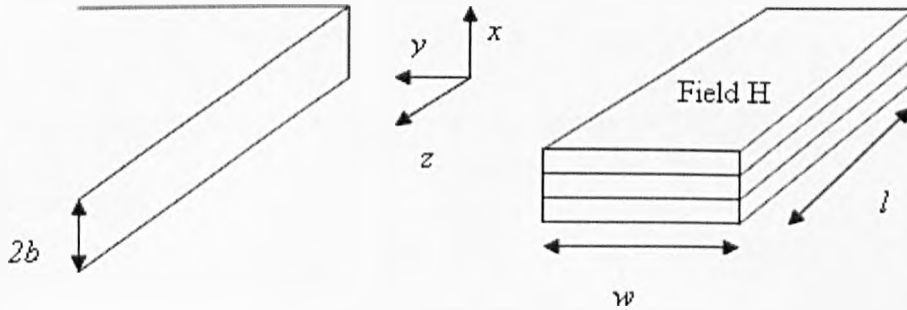
(1) The mechanical lamination of thin electrodeposited magnetic films could be performed using a hot press. Other processes, documented in Chapter 3, have shown limitations when the application requires a relatively large core cross-sectional area. To realise a core with relatively large thickness of more than 500  $\mu\text{m}$ , a mechanical lamination technique of multiple magnetic and insulated layers with a hot press is believed to have potential. This is a relatively quick method of constructing laminated cores. The number of laminations can be altered and thickness varied without significantly increasing fabrication cost. The fabricated core could then be incorporated into flip-chip windings or PCB planar windings.

The manufacture process would involve the electrodeposition of electrically and magnetically optimised magnetic alloys. The alloys would be fabricated to the required dimensions, coated with a thin film spin cast polyimide and cured. The sheets of coated magnetic alloy would then be placed in a hot press with thin layers of epoxy adhesives films, the stacked sheets would then be pressed at a pre-determined temperature, pressure and time. A mechanical milling machine could be used to form any openings required for windings.

(2) Another concept is the manufacturing of vertical laminations which would involve integration of the core into the actual substrate. A substrate material such as Silicon (Si) or Low temperature Co-fired Ceramic (LTCC) could be through etched or machined. The magnetic alloy could then be deposited onto the sidewalls of the vertical trenches and windings could be fabricated via flip-chip-bonding. With a conductive substrate or sidewalls coated with a seed layer, the magnetic alloy could be electrodeposited. Another option could be a polymer loaded with magnetic particles, the polymer could then be screen printed into the vertical trenches.

## Appendix A

### AC Inductance and AC Core Resistance Derivation



The time-varying magnetic field vector ( $H$ ) is directed along the  $z$ -axis and depends only on the  $x$ -coordinate:

$$H(x, y, z, t) = H(x, t) = H(x, t)a_z \quad (\text{A1})$$

Where  $a_z$  is the unit vector in the  $z$ -axis direction. The Maxwell equations

$$\nabla \times H = J + \frac{\partial D}{\partial t} \quad (\text{A2})$$

$$\nabla \times E = -\frac{\partial B}{\partial t} \quad (\text{A3})$$

$$\nabla \cdot B = 0 \quad (\text{A4})$$

combined with the constitutive relations:

$$J = \sigma E \quad (\text{A5})$$

$$B = \mu H \quad (\text{A6})$$

provide the full expression of H alongside the boundary conditions. In the equations above, H is the magnetic field intensity vector, J is the current density vector, D is the electric flux density (electric displacement) vector, E is the electric field intensity vector, B is the magnetic flux density vector,  $\sigma$  is the conductivity of the material, and  $\mu$  is the permeability of material. The displacement current  $\frac{\partial D}{\partial t}$  in Eq (A2) is negligible at the frequencies of interest. Rewriting Eq(A2) & (A3), neglecting the displacement current and using Eq(A6), in terms of vector phasor  $(\hat{H}, \hat{E}, \hat{J})$  for a sinusoidal time-harmonic analysis

$$\nabla \times \hat{H} = \hat{J} \quad (\text{A7})$$

$$\nabla \times \hat{E} = -j\omega\mu \hat{H} \quad (\text{A8})$$

$$\text{As } H(x, y, z, t) = \text{Re} \left\{ \left[ \hat{H}(x, y, z) e^{j\omega t} \right] \right\}$$

The substitution of Eq(A5) into Eq(A8) provides

$$\nabla \times \left( \frac{\hat{J}}{\sigma} \right) = -j\omega\mu \hat{H} \quad (\text{A9})$$

The current density is eliminated from this expression using Eq(A7). Then

$$\nabla \times \left( \frac{\nabla \times \hat{H}}{\sigma} \right) = -j\omega\mu \hat{H} \quad (\text{A10})$$

Since  $\sigma$  and  $\mu$  are assumed as constants, Eq(A10) becomes:



$$\nabla \times \nabla \times \hat{H} = -j\omega\sigma\mu \hat{H} \quad (\text{A11})$$

or

$$\nabla \left( \nabla \cdot \hat{H} \right) - \nabla^2 \hat{H} = -j\omega\sigma\mu \hat{H} \quad (\text{A12})$$

By Eq(A4) and (A6), one obtains the Helmholtz equation

$$\nabla^2 \hat{H} = j\omega\sigma\mu \hat{H} \quad (\text{A13})$$

Recalling  $\nabla^2$  denotes the vectorial Laplacian operator

$$\nabla^2 = \frac{\partial^2}{\partial x^2} + \frac{\partial^2}{\partial y^2} + \frac{\partial^2}{\partial z^2} \quad (\text{A14})$$

in Cartesian coordinates. Since the magnetic field intensity is dependent only on the x coordinate, Eq(A13) becomes a one dimensional diffusion equation:

$$\frac{\partial^2 \hat{H}}{\partial^2 x} = j\omega\sigma\mu \hat{H} \quad (\text{A15})$$

Or

$$\frac{\partial^2 \hat{H}}{\partial^2 x} = k^2 \hat{H} \quad (\text{A16})$$

Where  $k^2 = j\omega\sigma\mu$ . The solution to Eq (A16) is simply:

$$\hat{H} = H_1 e^{\hat{k}x} + H_2 e^{-\hat{k}x} \quad (\text{A17})$$

Recalling that  $\sqrt{j} = (1 + j)/\sqrt{2}$ ,

$$k = \sqrt{j\omega\mu\sigma} = (1 + j)\sqrt{\frac{\omega\mu\sigma}{2}} \quad (\text{A18})$$

In terms of the skin depth,  $\delta$ , defined by

$$\delta = \sqrt{\frac{2}{\omega\mu\sigma}} \quad (\text{A19})$$

Eq(A18) becomes

$$k = \frac{1 + j}{\delta} \quad (\text{A20})$$

Since the field is penetrating from both the top and the bottom side,  $H_{x=b} = H_{x=-b}$

$$H_o = H_1 e^{\hat{k}x} + H_2 e^{-\hat{k}x} \quad (\text{A21})$$

And

$$H_o = H_1 e^{-\hat{k}x} + H_2 e^{\hat{k}x} \quad (\text{A22})$$

Where  $H_o$  is the effective value of the magnetic field intensity. By solving Eq(A21) & (A22)

$$H_1 = H_2 = \frac{H_o}{\cosh kb} \quad (\text{A23})$$

The solution of the magnetic field intensity is

$$\hat{H} = H_o \frac{\cosh k x}{\cosh k b} \quad (\text{A24})$$

The magnetic flux density is then

$$\hat{B} = \mu H_o \frac{\cosh k x}{\cosh k b} \quad (\text{A25})$$

The magnetic flux,  $(\phi)$ , flowing in one sheet is given by the integration of the magnetic flux density over the cross-sectional area

$$\phi = \int_{-b}^{+b} w \hat{B} dx = \frac{2w\delta\mu}{1+j} H_o \tanh\left(\frac{(1+j)b}{\delta}\right) \quad (\text{A26})$$

The total magnetic flux,  $(\phi)_c$ , in the packet of lamination is given by the sum of the partial flux, as in the individual sheets, and for a packet with  $\frac{t}{2b}$  laminations:

$$\phi_c = \frac{wt\delta\mu}{(1+j)b} H_o \tanh\left(\frac{(1+j)b}{\delta}\right) \quad (\text{A27})$$

Where  $t$  is the effective magnetic thickness of the total core excluding insulation thickness. Now, assuming that the magnetic core in the figure is a closed magnetic core and there is a winding with  $N$  turns, for a mean length of core  $l$ , the effective magnetic field intensity at the surface of core is:

$$H_o = \frac{NI}{l} \quad (\text{A28})$$

Where  $I$  is an effective value of current flowing through the winding. Considering a harmonic variation with time, the voltage induced in the winding is:

$$V = j\omega N\phi_c \quad (\text{A29})$$

Now, the impedance of the winding due to the core is:

$$Z = \frac{V}{I} = \frac{j\omega t \omega \delta \mu}{(1+j)lb} N^2 \tanh\left(\frac{(1+j)b}{\delta}\right) \quad (\text{A30})$$

For low frequency,

$$Z = \frac{V}{I} = j\omega \mu \frac{\omega t}{l} N^2 \quad (\text{A31})$$

Where a static inductance,  $L_o$ , can be defined as

$$L_o = \mu \frac{\omega t}{l} N^2 \quad (\text{A32})$$

Eq (A31) becomes

$$Z = L_o \frac{j\omega}{(1+j)b} N^2 \tanh\left(\frac{(1+j)b}{\delta}\right) \quad (\text{A33})$$

Finally, resolving this expression into its real and imaginary parts, the inductance,  $L_{ac}$ , is

$$L_{ac} = L_o \frac{1}{\frac{2b}{\delta}} \times \frac{\sinh \frac{2b}{\delta} + \sin \frac{2b}{\delta}}{\cosh \frac{2b}{\delta} + \cos \frac{2b}{\delta}} \quad (\text{A34})$$

And the resistance,  $R_{ac}$ , representing the eddy current loss

$$i s R_{ac} = \omega L_o \frac{1}{\frac{2b}{\delta}} \times \frac{\sinh \frac{2b}{\delta} - \sin \frac{2b}{\delta}}{\cosh \frac{2b}{\delta} + \cos \frac{2b}{\delta}} \quad (\text{A35})$$

## Appendix B

### Fabrication of Solenoid Micro-Inductor

Fabrication Process: (A) Deposition of seed layer and Patterning of Photoresist, (B) Electrodeposition of windings, (C) Reapplication of photoresist and pattern for interconnecting bumps, (D) Electrodeposition of copper:gold bumps, seed layer etched and photoresist insulation layer applied and pattern, (E) Image of completed lower winding layer. The upper layer is fabricated with the same procedure and the core structure is positioned on the lower windings prior to final assembly with thermo compression flip-chip bonding.



